



2018

M^a Cristina Momblona Rincón

Unconventional materials for light-emitting and photovoltaic applications



VNIVERSITAT DE VALÈNCIA

Doctorado en
Nanociencia y Nanotecnología

PhD Thesis

**Unconventional materials for
light-emitting and photovoltaic applications**

M^a Cristina Momblona Rincón

Supervisors:

Dr. Enrique Ortí Guillén

Dr. Hendrik Jan Bolink

April 2018



VNIVERSITAT ID VALÈNCIA

Doctorado en

Nanociencia y Nanotecnología

Instituto de Ciencia Molecular, Universidad de Valencia

Ph. D. thesis:

Unconventional materials for light-emitting and photovoltaic applications

Ph. D. candidate:

María Cristina Momblona Rincón

Supervisors: Dr. Enrique Ortí Guillén

Dr. Hendrik Jan Bolink

Tutor: Dr. Hendrik Jan Bolink

10 April 2018

Dr. ENRIQUE ORTÍ GUILLÉN, Catedrático de Química Física en la Universidad de Valencia e Investigador de la Universidad de Valencia en el Instituto de Ciencia Molecular (ICMol) y **Dr. HENDRIK JAN BOLINK**, Investigador de la Universidad de Valencia en el Instituto de Ciencia Molecular (ICMol).

CERTIFICAN:

Que el trabajo que presenta la doctoranda María Cristina Momblona Rincón en esta memoria con el título “Unconventional materials for light-emitting and photovoltaic applications” corresponde a su Tesis Doctoral y ha sido realizado bajo nuestra dirección en el Instituto de Ciencia Molecular de la Universidad de Valencia, autorizando mediante este escrito la presentación de la misma.

Dr. Enrique Ortí Guillén
(Director de la tesis doctoral)

Dr. Hendrik Jan Bolink
(Director y tutor de la tesis doctoral)

En Valencia, a 10 de Abril de 2018

Dedicado a mi familia

Agradecimientos

Mis primeros agradecimientos son para mis directores de Tesis, Enrique y Henk. Siempre os estaré agradecida por haber confiado en mí, por vuestro ánimo constante, vuestro respaldo y por inculcarme ese reto de superación. Gracias por haberme hecho el inmenso regalo de poder trabajar en dos líneas de investigación punteras y de alto nivel y de poder haber formado parte de un gran equipo, grande a nivel científico y más grande aún a nivel personal.

A cada uno de los miembros del grupo de investigación MOED: Gracias Olga por enseñarme en los inicios de ese material llamado “perovskita” y por cada uno de los paseos, cenas, que compartimos en mis primeros meses en Valencia. A mi tocaya Cristina. Gracias por tantísimas cosas tanto profesionales como personales. Esas preparaciones de las reuniones, el intento de leer artículos en la playa, viajes y millones de conversaciones, y todo lo que vendrá en el país que sea. Lidón, mi mitad en esta etapa. Gracias por ese tándem perfecto durante todos estos años, por tu paciencia, tu buen hacer. Me llevo conmigo esas alegrías compartidas, esa lucha constante por conseguir los objetivos y muy buenos momentos de viajes, de conversaciones, allá donde esté, siempre tendrás tu casa. Gracias Toni por tu generosidad científica, personal y paciencia infinita conmigo, siempre dispuesto a ayudar con una sonrisa. Porque gracias a ti no solo soy más “sabia” en emisión de luz, sino en multitud de temas de miles de conversaciones. A Michele, gracias por tu constante guía y ánimo durante estos años cuando las cosas iban bien pero más cuando iban mal. Gracias por tus consejos, por compartir tu conocimiento y ayudarme a ver siempre las cosas con otra perspectiva. A María, mi hermana valenciana. Gracias por tantísimas cosas, por tu amistad y ayuda incondicional desde el primer segundo que pisé el ICMol, por tantos buenos momentos vividos, de cenas, teatros, conversaciones, viajes. Gracias por todo. Gracias Giulia por también tantos buenos momentos, quedadas en Valencia, por estar

ahí y escucharme cuando lo necesitaba. Gracias Enrico por los momentos tan divertidos en la sala limpia contigo y por esas pizzas caseras. A Laura, gracias por haber compartido tantísimos buenos momentos y alguno más regular entre esas cuatro paredes de cristal. Gracias por todas las risas, conversaciones, por animarme y me llevo conmigo un montón de momentos contigo tanto en el ICMol como fuera. A Alejandra por tu cercanía, ayuda constante y esa sensación de hacerme sentir en casa. A Ángel y Estrella por muchos momentos vividos con vosotros en Valencia y el gran apoyo en vuestro viaje a mi tierra. Azin, my Iranian sister, always so helpful and kind with me, thanks for sharing too many good moments with me, for taking care of me when I was sick, for our Chinese dinners or teas in the happiness seller. Gracias Dani por todos los momentos tan divertidos y por escucharme y darme tu consejo cuando lo necesitaba, siempre pensaré que fuiste el gran descubrimiento del grupo. Gracias David y Jorge A por los buenos ratos durante estos años con vosotros. María Grazia, sigue con ese ánimo de trabajo constante, gracias por todos los buenos ratos que hemos pasado. Beni, gracias por escucharme cuando estaba regular y por compartir tu forma de ver la vida conmigo. Gracias Jorge F. por ayudarnos siempre cuando las cosas iban mal, he aprendido muchísimo de tí durante estos años. Pablo, gracias por los momentos tan divertidos en las comidas. Ana, nunca pierdas esa sonrisa, esa positividad y esas ganas de sacar el trabajo adelante.

Gracias Paco por tantos buenos momentos fuera del ICMol. A Javi C., Víctor y Mario, por todos los buenos ratos pasados entre esas cuatro paredes de cristal. A Joaquín y Jesús por esas conversaciones y risas cuando iba al despacho. A Pedro y Rafa, Amparo y Begoña, gracias por compartir conmigo vuestra experiencia y por vuestra inestimable ayuda en mis primeros pasos en la docencia.

Gracias Miguel por tu gran apoyo y generosidad que me demostraste desde el primer día que nos conocimos. Cada día estoy más segura de que llegarás muy lejos. Thanks Jarla, Adrien and Ania, for doing my stay in Oxford

so nice, I will never forget our trip to Cornwell and all the adventures we had in Oxford.

A Ruth y Teresa, porque Valencia no habría sido lo mismo sin vosotras. A mis amigos de siempre, tan lejos pero tan cerca. A Silvia, Marimar y Andrés, Maite, Jorge V., Carmen, Adrián, Mapi, Cristina, gracias por todo. En algún momento compensaré esos momentos que no he podido estar de manera presente pero no dudéis que mi mente estaba con vosotros. A los de la pandilla, gracias por cada momento con vosotros, porque aunque pasen los años, cuando nos juntamos todo sigue igual. A Jorge M. por compartir los momentos anteriores y el comienzo de esta etapa. Gracias por animarme a dar el paso.

El mayor agradecimiento es para mi familia. A mis tíos y tías, eternamente agradecida por la familia tan maravillosa que tengo. Cada viernes esperándome o llamándome para preguntar qué tal iba todo. Gracias por estar siempre ahí, por esa ayuda continua, incondicional, apoyo y ese cariño que solo la familia te puede dar.

A mi padre, porque si he llegado hasta aquí y soy como soy, es gracias a él. Gracias por todo el esfuerzo que has tenido que hacer para que yo pudiera llegar a este momento, gracias por todo lo que me has inculcado desde pequeña, por ese esfuerzo de hacer las cosas bien, por confiar en mí y el hacerme sentir contenta por el trabajo bien realizado.

El último agradecimiento es para quien va dedicada cada letra de esta tesis y con quien estará mi pensamiento cada momento el día de la defensa, para mi madre. Gracias por tu comprensión, por esa alegría con la que atendías cada una de mis llamadas contando mi día a día en Valencia y esa gran sonrisa y fuerte abrazo con el que me recibías cada viernes al llegar a casa. Por animarme en esta lucha constante que es la vida, siempre llena de fuerza, cariño y alegría. Esta tesis y todo lo que vendrá después, no es por mí, sino por ti.

Contents

1. General introduction & aim of the thesis	1
1.1. General introduction	3
1.2. Aim of the thesis	5
2. Light-emitting electrochemical cells	7
2.1. Introduction	9
2.1.1. Light-emitting electrochemical cells	9
2.1.2. Iridium(III) iTMC: the core of LECs	10
2.1.3. Photophysics of iTMCs	11
2.1.4. Strategies for colour tuning in Ir-iTMCs	13
2.1.5. Processing and performance of LECs	14
2.1.6. Operation mechanism of LECs	18
2.1.7. Limitations of LECs and state-of-the art	20
2.2. Improving the device stability of red and near-infrared light-emitting electrochemical cells by chemical modification	25
2.2.1. Introduction	25
2.2.2. Experimental and methodology	27
2.2.3. Results and discussion	33
2.2.4. Conclusions	42
2.2.5. Contributions of the author	43
3. Perovskite solar cells	45
3.1. Introduction	47
3.1.1. Metal halide perovskites	47
3.1.2. Processing of perovskite films	52
3.1.3. Basic principles of the operation of solar cells	56
3.1.4. Characterization of solar cells	59

3.1.5. Perovskite solar cells	62
3.1.6. State-of-the-art	64
3.2. Improving light harvesting efficiency in perovskite solar cells by effect of the absorber thickness	65
3.2.1. Introduction	65
3.2.2. Experimental and methodology	66
3.2.3. Results and discussion	70
3.2.4. Conclusions	76
3.2.5. Contributions of the author	77
3.3. Highly efficient and fully vacuum-deposited <i>p-i-n</i> and <i>n-i-p</i> perovskite solar cells	79
3.3.1. Introduction	79
3.3.2. Experimental and methodology	81
3.3.3. Results and discussion	85
3.3.4. Conclusions	99
3.3.5. Contribution of the author	100
4. General conclusions	101
5. Resumen en castellano	107
References	141
Other contributions of the author	165
Index of Figures	169
Index of Tables	175
List of abbreviations	177
Annexes	181

Content of Annexes

A1. Light-emitting electrochemical cells	183
A1.1. Highly stable red-light-emitting electrochemical cells	183
A1.2. Supporting information of Highly stable red-light-emitting electrochemical cells	195
A1.3. Simple design to achieve red-to-near-infrared emissive cationic Ir(III) emitters and their use in light emitting electrochemical cells	209
A1.4. Supporting information of Simple design to achieve red-to-near-infrared emissive cationic Ir(III) emitters and their use in light emitting electrochemical cells	215
A2. Perovskite solar cells	243
A2.1. Efficient methylammonium lead iodide perovskite solar cells with active layers from 300 to 900 nm	243
A2.2. Supporting information of Efficient methylammonium lead iodide perovskite solar cells with active layers from 300 to 900 nm	251
A2.3. Efficient vacuum deposited p-i-n and n-i-p perovskite solar cells employing doped charge transport layers	259
A2.4. Supporting information of Efficient vacuum deposited p-i-n and n-i-p perovskite solar cells employing doped charge transport layers	267

Chapter 1

General introduction & aim of the thesis

1.1. General introduction

The world's energy consumption is experiencing an unstoppable increase as a result of population growth and economic development. In the last ten years, the global primary energy consumption has increased an average of 1.8% per year.¹ Lighting accounts for 15 percent of the global electricity consumption and 5 percent of the worldwide greenhouse gas emissions.² The total replacement of conventional incandescent and fluorescent lamps to solid-state lighting (SSL) for general lighting purpose can reduce energy consumption to less than 10% of the total electricity generated.³ Therefore, solid-state lighting (SSL) based on light-emitting diodes (LEDs), organic light-emitting diodes (OLEDs) or light-emitting electrochemical cells (LECs) plays an important role in achieving the planet's energy consumption targets.

Today, more than 85% of the world's total primary energy consumption is supplied by coal, oil and gas, which in turn produce CO₂. Only 3% of the world annual energy consumption is due to renewable sources (see Figure 1).

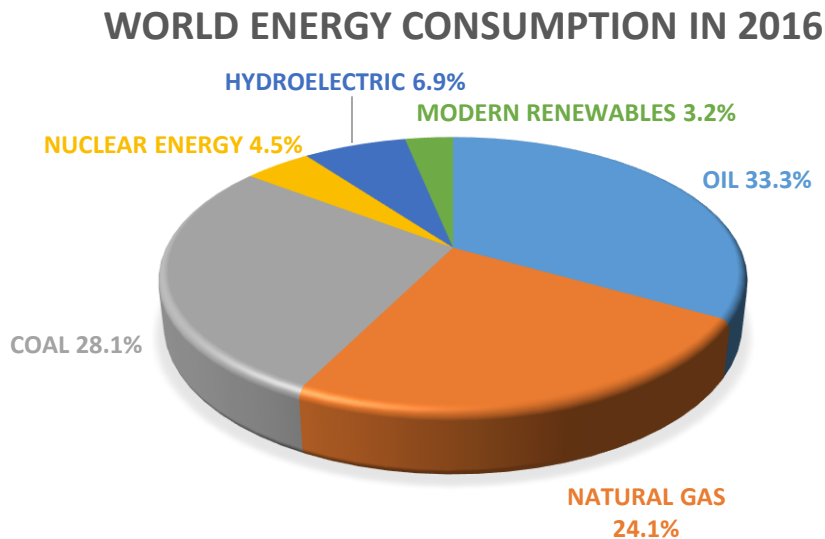


Figure 1. World energy consumption in 2016.¹

Solar energy is the most abundant and permanent renewable energy resource and the only one capable of providing all the energy the world needs. The solar radiation reaching the Earth's surface in one year is an order of magnitude greater than the total estimated non-renewable energy resources, including nuclear.⁴ The enormity of this resource is apparent when it is compared with the limited reservoirs of oil, gas and coal in the Earth. Nowadays, the development of renewable energy sources based on solar energy has become one of the main approaches to solve the energy crisis and environmental problems. Among the technologies available to harvest solar radiation, photovoltaics (solar cells) is the most promising one. Solar cells can efficiently convert sunlight directly into electricity.

In order to have a photovoltaic technology competitive with fossil fuels in utility-scale power generation, it is necessary to focus on reducing the total cost of solar energy, either through increased efficiencies and operational lifetime or lower cost per photovoltaic cell. The photovoltaic market is set by crystalline and polycrystalline silicon solar cells (c-Si and poly-Si, respectively). However, thin-film solar cells, such as cadmium telluride (CdTe) and copper indium gallium diselenide (CIGS) are gaining market due to their lower costs. However, for c-Si, poly-Si and these thin-film photovoltaic technologies, the industrial fabrication requires high energy-input manufacturing, involving high-temperature and complex fabrication processes. Perovskite solar cells (PSCs) have emerged as a potential low-cost alternative photovoltaic technology.

1.2. Aim of the thesis

The global aim of this thesis is the implementation of unconventional materials into light-emitting and photovoltaic devices with high conversion efficiencies.

In particular we aim to:

- ✓ Improve the stability of light-emitting electrochemical cells and extend the emission wavelength to red and near-infrared.
- ✓ Improve the efficiency of perovskite solar cells via vapour phase deposition of the perovskite absorber and by optimizing the interfaces in the device architectures.

Chapter 2

Light-emitting electrochemical cells

2.1. Introduction

2.1.1. Light-emitting electrochemical cells

Light-emitting electrochemical cells (LECs) are solid-state electroluminescent devices made of a single emissive layer consisting of: a conjugated polymer (pLECs),⁵⁻⁹ a non-ionic small fluorescent molecule (SM-LECs),¹⁰ a phosphorescent transition-metal complex (TMC-LECs),¹¹⁻¹⁶ quantum dots (QD-LECs)¹⁷⁻¹⁸ or recently organic-inorganic halide perovskites.¹⁹⁻²⁰ The presence of ions in the active layer is crucial for the device operation due to the working mechanism. Therefore, LECs based on uncharged emitters do require the presence of an additional electrolyte or an ion-conducting polymer. As the use of charged emitters will make the device architecture simpler, the most attractive active materials for LECs are ionic transition-metal complexes (iTMCs). iTMCs, in its anionic and cationic forms, play several key roles: promotion of charge injection from the electrodes, electron and hole transport through the device and radiative recombination, i.e. luminescence. Given the excellent solubility of the cationic complexes in common organic solvents²¹ and the generally low solubility of the anionic ones,^{11-12, 22} the former have been the most widely iTMCs used as electroluminescent materials for LECs.

The first LEC based on iTMCs was reported in 1996 where a polymer based on a Ru(II) complex was used as the single component in the emissive layer.²³ In the following years, a large number of polymer iTMCs or iTMCs based on cationic Ru(II) and Os(II) complexes were implemented into LECs.²⁴⁻³⁴ The limited range of the electroluminescence emission wavelengths from orange to red due to their low ligand-field splitting energies (LFSEs)³⁵⁻³⁶ and the low luminescence efficiencies (5.5% reported in 2002)²⁸ limited their application in light-emitting devices. Other iTMCs with different transition metal cores were investigated and incorporated into LECs, such as rhenium(I),³⁷⁻³⁹ platinum(II)⁴⁰ and copper(I)⁴¹⁻⁴⁶ but iridium(III) was shown to

be a strong candidate. The greater versatility of iridium(III) iTMCs (Ir-iTMCs) in comparison with other iTMCs for light-emitting applications is due to: 1) synthetic versatility forming homo- and heteroleptic complexes, 2) colour emission over the whole visible range, 3) enhance photostability (the non-emissive metal-centred triplet excited states (^3MC) are less accessible) and 4) high efficiency and device stability. The first paper describing a LEC based on a cationic Ir-iTMC was published in 2004 by Slinker *et al.*³⁵ Up to now, more than 100 publications confirm iridium complexes as the best candidates to be used as emitters in light-emitting electrochemical cells. Unfortunately, iridium is expensive and one of the least abundant elements in the Earth's crust and, in the near future, it will need to be replaced by other more abundant and cheaper metals, such as copper.

2.1.2. Iridium(III) iTMCs: the core of LECs

Iridium is a third-row transition element. It has a $5d^6$ electronic configuration where its d orbitals are split by the interaction with the octahedral ligand field into three stabilized t_{2g} (d_{xy} , d_{xz} , d_{yz}) and two destabilized e_g orbitals (d_{z^2} , $d_{x^2-y^2}$). The energy difference between these two groups of orbitals (Δ_o) presents a high splitting because of the presence of the highly charged ion belonging to the third-row transition metal. Therefore, the electronic configuration of the metal centre is always in a low-spin state ($t_{2g}^6e_g^0$) and the ligand-field stabilization energy is maximized. As a result, cationic iridium(III) complexes are generally stable and inert toward ligand substitution. From a spin-statistic point of view, when a hole and an electron recombine and an exciton is formed in the emissive layer, 25% of the cases the excitons correspond to singlet excited states and 75% to triplet excited states. For an organic semiconductor (OS), the light emission results through the singlet state (fluorescence), whereas for an iTMC both the triplets and the singlets can result in light emission (phosphorescence). The high spin-orbit coupling (SOC) of iridium(III) yields almost unitary intersystem crossing (ISC) efficiency from singlet to triplet excited states. Singlet excitons are in Ir-iTMCs efficiently

converted into triplets and therefore, the complexes can efficiently harvest both singlet and triplet excitons. Therefore, Ir-iTMCs are typically phosphorescent triplet emitters that exhibit efficient spin-forbidden phosphorescence emissions. This fact allows for higher electroluminescence efficiencies compared to organic semiconductors (singlet emitters).

The vast majority of cationic iridium complexes are heteroleptic and possess the structure $[\text{Ir}(\text{C}^{\wedge}\text{N})_2(\text{N}^{\wedge}\text{N})]^+$, where the Ir(III) metal centre is coordinated to three ligands, two anionic cyclometalated ligands ($\text{C}^{\wedge}\text{N}$) and one neutral ancillary ($\text{N}^{\wedge}\text{N}$) ligand. In order to balance the positive charge, the presence of a small mobile counteranion is essential, generally hexafluorophosphate (PF_6^-) and tetrafluoroborate (BF_4^-) are the most used in the literature. These counterions have an active role in the operation mechanism, because their displacement to the respective electrode under an applied bias lowers the charge injection barriers. However, the presence of some counterions, such as chloride (Cl^-),⁴⁷ has been demonstrated to be detrimental for the device performance.²⁸ In the Section (2.1.6.), the operation mechanism and the role of the counterions will be explained.

2.1.3. Photophysics of iTMCs

In this section, the photophysics of the iTMCs will be explained through the archetype iTMC $[\text{Ir}(\text{ppy})_2(\text{bpy})][\text{PF}_6]$, where ppy^- is 2-phenylpyridinate and bpy is 2,2'-bipyridine⁴⁸ (see Figure 2a).

In Ir-iTMCs, the atomic orbital composition of the highest-occupied molecular orbital (HOMO) is usually comprised of a mixture of Ir $d\pi$ orbitals (t_{2g}) and the phenyl π orbitals of the $\text{C}^{\wedge}\text{N}$ ligands (Figure 2b), whereas the lowest-unoccupied molecular orbital (LUMO) is localised essentially on the $\text{N}^{\wedge}\text{N}$ ligand (Figure 2c).⁴⁸⁻⁵⁰ In LECs, the energies of the HOMO and LUMO are not so important than in OLEDs, where the energy levels of the emitter must be properly aligned with the adjacent layers. For LECs, these values are only

important in host-guest systems, but not for the “single emitter” devices because the emitter will also act as charge transporter.

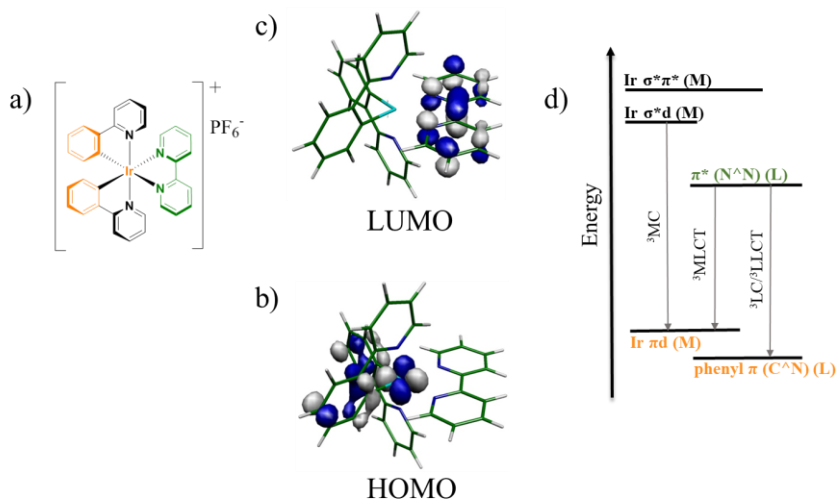


Figure 2. a) Structure of the prototype Ir-iTMC: $[\text{Ir}(\text{ppy})_2(\text{bpy})][\text{PF}_6]$ where $\text{ppy}^- = 2$ -phenylpyridinate and $\text{bpy} = 2,2'$ -bipyridine.⁴⁸ The HOMO is spatially located on the Ir metal centre and the phenyl rings of the cyclometalated ligands (in orange) and the LUMO is located on the ancillary ligand (in green). Schematic representation of the electronic density contours calculated for the frontier molecular orbitals b) HOMO and c) LUMO of $[\text{Ir}(\text{ppy})_2(\text{bpy})][\text{PF}_6]$ complex. d) Electronic energy-level diagram for a generic Ir-iTMC. MC is metal-centred, MLCT is ligand-centred, LLCT are metal-to-ligand and ligand-to-ligand charge transfer, respectively.

As the emission behaviour in iTMCs is determined by the SOC between the lowest-energy triplet excited state (T_1) and the higher-lying singlet and triplet states, the description of the electronic transitions in terms of excitations between the highest occupied and lowest unoccupied molecular orbitals are useful in determining the nature of the excited states. The electronic nature and the relative energy ordering of the low-lying triplet states and, in particular of the emitting excited state T_1 , is essential to understand the photophysical properties of the complex. Theoretical calculations performed with the time-dependent version of the density functional theory (TD-DFT) demonstrated that the lowest-energy triplet excited state (T_1) in Ir-iTMCs generally arises from “mixed” triplet levels, due to the contributions of ${}^3\text{MLCT}$ (metal-to-ligand charge transfer), ${}^3\text{LC}$ (ligand-centred) and sometimes also

³LLCT (ligand-to-ligand charge transfer) states.⁵¹ The energy position of the non-emissive ³MC (metal-centred) states with respect to the emitting triplet state T₁ is relevant because the thermal population of the ³MC states is one of the possible non-radiative deactivation processes that can take place in Ir-iTMCs. Generally, ³MC states are energetically inaccessible⁵² to be thermally populated due to the fact that the ligand-field stabilization energy is enhanced by the use of cyclometalated ligands. However, under particular circumstances, this deactivation process must be thoroughly considered.⁵³⁻⁵⁴ The electronic transfer through ³MC states involve electron promotion from HOMO dπ orbitals (t_{2g}) to the antibonding dσ* orbitals (e_g) of the iridium ion. The latter are characterized by a strong σ-antibonding interaction between the iridium and the nitrogen atoms of the C[^]N ligands.⁴⁸ Then, the population of ³MC states lead to elongation and rupture of the Ir-N(C[^]N) bonds, open the molecular structure of the complex and enhance the reactivity of the complex with the entrance of small nucleophilic molecules facilitating the degradation of the complex.

2.1.4. Strategies for colour tuning in Ir-iTMCs

The spatial separation of the HOMO and the LUMO on different molecular moieties offers the possibility of modulating the HOMO–LUMO energy gap, and therefore of tuning the emission in the whole visible range, from blue to deep-red. Several groups have reviewed the different strategies to colour tuning of iridium complexes.^{13-15, 55-58} The colour emission of Ir-iTMCs can be tuned by changing or chemically modifying the organic ligand framework around the iridium(III) metal. The energy gap can be fine-tuned by playing independently on the cyclometalated (HOMO) or on the ancillary ligand (LUMO), or even on both of them (see Figure 3). As a rule of thumb, it can be said that: 1) the use of electron-withdrawing/donating substituents on the C[^]N ligands reduce/enhance the σ donation to the metal, thus decreasing/increasing the electron density on the iridium core, and lead to a stabilization/destabilization of the HOMO; and 2) the use of electron-

donating/withdrawing substituents on the N[^]N ligand or use of intrinsically electron-rich/poor ligands brings about a destabilization/stabilization of the LUMO.

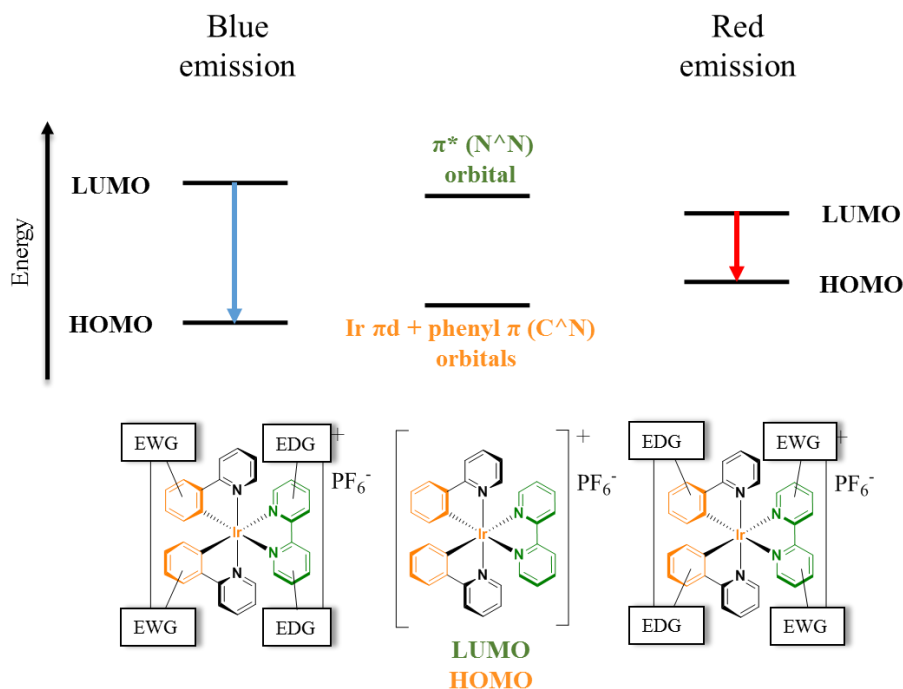


Figure 3. General scheme depicting the different approaches used for tuning the colour emission toward the blue (left) or red (right) of the archetype $[\text{Ir}(\text{ppy})_2(\text{bpy})][\text{PF}_6]$ complex (centre). Up: Energy-level diagram. Bottom: Chemical structure of the $[\text{Ir}(\text{ppy})_2(\text{bpy})][\text{PF}_6]$ complex, where EWG and EDG mean electron-withdrawing groups and electron-donating groups, respectively. Adapted from reference 58.

2.1.5. Processing and performance of LECs

LECs are solution-processed devices where all layers, except from the top electrode (cathode), are deposited from solutions of benign solvents under ambient air. In most cases, the top electrode is thermally evaporated but cathode inks,⁵⁹ liquid top contacts²⁹ or the use of soft contact lamination⁶⁰ can be used for the fabrication of fully solution-processed devices. Most research laboratories fabricate LECs using the laboratory-scale spin-coating technique. The transference from laboratory-scale fabrication to industrial applications is feasible via industry-relevant solvent-based deposition techniques, such as roll-

to-roll (R2R), inkjet printing, spray-sintering, slot-die, blade-coating or gravure coating, among others.⁶¹⁻⁶⁶

The device architectures most often reported are sandwich-type,²⁵ planar-type (with interdigitated electrodes),⁶⁷⁻⁶⁹ and cascade-type (or arrays of LECs).⁷⁰⁻⁷¹ Along this thesis, only sandwich-type LECs were fabricated and this section will focus on them.

The architecture of sandwich-type LECs (Figure 4) consists, as their name indicates, of one or two organic/organometallic layers sandwiched between one transparent conductive oxide (TCO), such as indium tin oxide (ITO) or the less commonly used fluorine-doped tin oxide (FTO), and a high-work-function (air-stable) reflecting metal cathode (Al, Au). One of the great advantages of LECs is that they do not require low work-function metals, which are extremely sensitive to ambient oxygen and water, for electron injection. This insensitivity to the work function of the electrode reduces the requirements for the encapsulation of the devices. Although in other technologies encapsulation has been successfully achieved for devices made on glass, there are unsolved problems for devices processed on flexible substrates.

Double-layer LECs (Figure 4) are composed of a hole injection layer, generally poly(3,4-ethylenedioxythiophene):polystyrenesulfonate (PEDOT:PSS) followed by the layer of the emissive material. PEDOT:PSS is often used to promote hole injection as well as to smooth the ITO surface and increase the yield of device preparation. The emissive layer is composed of the iTMC mixed with a lithium-based salt⁷²⁻⁷⁵ or an ionic liquid (IL).^{71, 76-77} These additional salts increase the density of mobile ions and the ionic mobility, reinforcing the migration of ions and accelerating the device turn-on time (t_{on}). The emissive compound can be dispersed in an inert polymer,²⁷⁻²⁸ such as poly(methyl methacrylate) (PMMA), poly(carbonate) (PC) or poly(styrene) (PS) to improve the homogeneity of the layer and to enhance the photoluminescence quantum yield (PLQY or Φ) decreasing the self-quenching that occurs due to concentration effects (high concentrations favour exciton

hopping and subsequently emission quenching). LECs are less sensitive to the active layer thickness than OLEDs and thickness variations of the active layer are tolerated. By reducing the thickness of the iTMC layer the t_{on} shortens but the efficiency is also decreased due to higher exciton quenching at the electrodes.⁷⁸ Finally, an air-stable cathode is thermally evaporated as the top electrode, such as Ag, Al or Au.

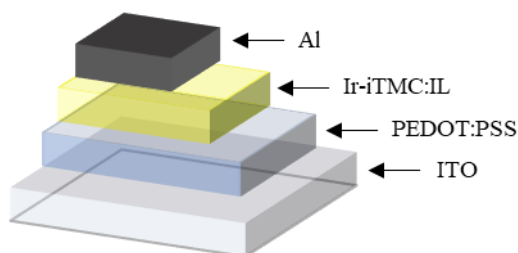


Figure 4. Schematic layout of a double-layer sandwiched-type LEC.

Figures of merit

The most common figures of merit used in the characterization of LECs are the following:

- *Light output*: General term commonly used for flux of light or radiant energy emitted from the device per unit area.
- *Luminance (L)*: Flux of light emitted from the device per unit area. The value of luminance reported for a given device is the maximum observed, defined as *maximum luminance* (L_{max}). The SI unit is the candela per surface unit ($cd\ m^{-2}$).
- *Irradiance (I)*: Flux of radiant energy emitted from the device per unit area, measured in power per unit area ($\mu W\ cm^{-2}$). The value of irradiance reported for a given device is the maximum observed, defined as *maximum irradiance* (I_{max}).
- *Current density (J)*: Flux of current through the device, measured in ampere per surface unit ($A\ m^{-2}$).

- *Voltage (V)*: The voltage applied or measured in a working device. For a pulsed driving cell, the voltage is the average between the on- and off- time of the pulse.
- *Turn-on time (t_{on})*: Time needed to reach $L = 50 \text{ cd m}^{-2}$ (t_{50}) or $L = 100 \text{ cd m}^{-2}$ (t_{100}).
- (t_{max}): Time needed to reach the maximum luminance (L_{max}).
- *Device lifetime ($t_{1/2}$)*: Time to reach half of the maximum luminance.
- *Current efficiency or efficacy*: The flux of light in candelas per electrical ampere. The SI unit is candela per ampere (cd A^{-1}). The value of efficacy reported for a given device is the maximum observed.
- *Power efficiency (PE)*: The flux of light measured in lumens per electric watt. It is measured in lm W^{-1} . The value of power efficiency reported for a given device is the maximum observed.
- *External Quantum Efficiency (EQE_{EL})*: The ratio of photons emerging from the device per injected electrons.

$$EQE_{EL} = \frac{b \cdot \phi}{2 \cdot n^2} \quad (1)$$

Where b is the recombination efficiency (equal to unity for two ohmic contacts),⁷⁹ ϕ is the fraction of excitons that decay radiatively, and n is the refractive index of the glass substrate and is equal to 1.5. The factor $1/(2n^2)$ accounts for the light outcoupling of the device.

- *Commission Internationale de l'Eclairage coordinates (CIE coord.)* (Figure 5): These coordinates can be calculated from the electroluminescence emission spectrum and give a univocal definition of the emission colour according to universally accepted international standards.⁸⁰

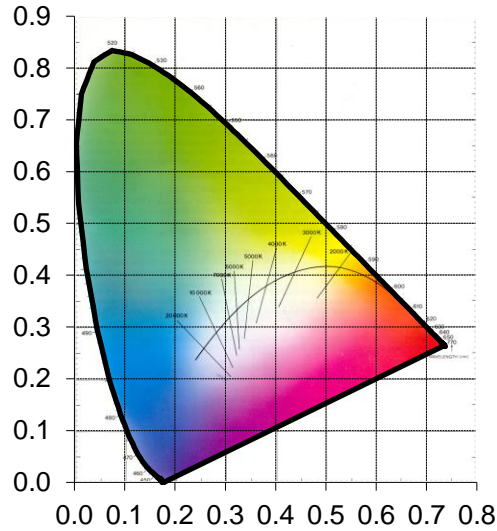


Figure 5. The Commission Internationale de l'Eclairage (CIE) chromaticity diagram.

2.1.6. Operation mechanism of LECs

The operation mechanism of LECs has been the subject of a long-standing debate. Two main different device mechanisms were proposed for explaining the LEC operation (Figure 6): the electrochemical doping model (ECD)(Figure 6a)^{5, 81-82} and the electrodynamic model (ED)(Figure 6b).⁸³⁻⁸⁶ Both models agree that the injection barrier for electrons and holes is reduced by the separation of the positive and negative ions in the emissive layer upon application of a bias, but they differ with respect to the internal distribution of the electric field. In the ECD model (Figure 6a), the charge injection is promoted by the doping of the material near the electrodes forming *p*- and *n*-doped regions that grow over time, and the applied potential drops over the remaining intrinsic region between these doped zones. By contrast, in the ED model (Figure 6b) the electric field drops over a thin electrical double layer (EDLs) at the electrodes.

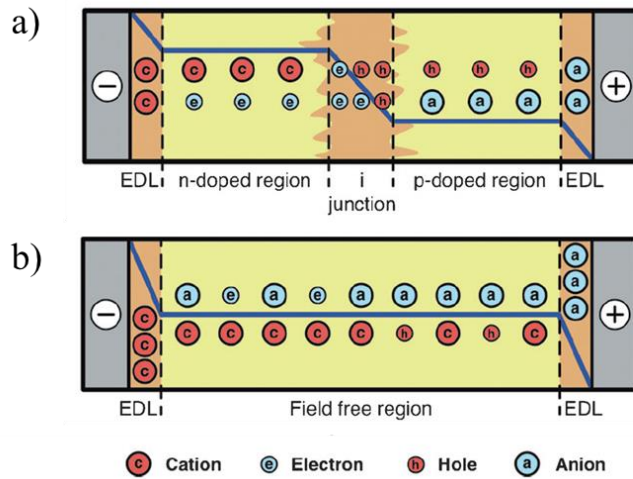


Figure 6. Scheme of the potential profile and the electronic and ionic charge distribution in a LEC during steady-state operation. a) Electrochemical doping model (ECD) and b) electrodynamic model (ED). Thick blue line: potential profile. Cyan and red symbols represent the negatively and positively charges, respectively. Orange and yellow regions correspond to high- and low-field regions in the bulk, respectively. Adapted from reference 13.

In 2010, a unifying model reported by van Reenen *et al.*⁶⁹ and Lenes *et al.*⁸⁷ conclude the debate and a broad consensus emerged. In brief, this model describes that under no bias the intrinsic emitting layer in the LEC device is neutral because charges are randomly distributed. After applying an external bias, anions and cations migrate to the respective electrode interfaces and form thin EDLs thereby reducing the injection barrier. This reduction facilitates charge injection leading to the oxidation and reduction of the emissive material forming *p*- and *n*-doped regions. With the formation of these doped zones, the carrier injection is enhanced and there is a gradually increase of the device current and light output. A *p-i-n* junction is then formed through the device and the emissive species are confined in the intrinsic region “*i*”. These highly conductive doped regions slowly grow at the expense of the neutral (undoped) emitting layer. The speed of the formation of the EDLs is associated with the time needed for the counterions in the LEC to be redistributed under the applied bias and ultimately related to the t_{on} of the device. It was found that the use of smaller counterions reduced the t_{on} compared to large anions.²⁹ The widening

of the doped zones is unavoidable and their growth will increase exciton quenching and consequently decrease the luminance of the LEC until eventually no light is emitted. The operation mechanism implies that LECs are self-limiting devices.

2.1.7. Limitations of LECs and state-of-the art

Initially, LECs suffered from some drawbacks compared to OLEDs, but during the past fifteen years, tremendous progress has been achieved to overcome the primary shortcomings, namely: 1) reduction of turn-on time (t_{on}), 2) enhancement of efficiency together with luminance levels, 3) improvement of device stability, 4) enhancing the colour gamut, to blue and red emission. A brief explanation on these achievements is presented below.

Reduction of turn-on time (t_{on})

The low ionic conductivity in the solid state is the origin of the long t_{on} observed in LECs ranging from a few minutes to several days. For real application in lighting, an instantaneous t_{on} in the sub-second time scale is required. The major breakthroughs in the reduction of t_{on} were the addition of ionic liquids (ILs) in the active layer and the operation of the device using a current driving mode.

The former was proposed by Malliaras *et al.* in 2005 with the addition of the ionic liquid 3-butyl-1-methylimidazolium hexafluorophosphate [Bmim][PF₆] to the Ir-iTMC.⁷⁶⁻⁷⁷ The ionic conductivity in the emissive layer is improved due to the higher density of mobile ions in the film. They found that small amounts of this IL significantly reduced the t_{on} of LECs from several hours to several minutes, whereas the luminance was increased.

The performance of LECs depend on several factors, among which the driving mode used to operate the device is one of the most important. In general, current driving shows a faster t_{on} compared with voltage driving due to the higher voltages in the first instants of operation. In addition, pulsed driving

gives better-performing devices compared with constant driving. Therefore, the use of pulsed-current driving resulted in LECs with virtually instantaneous t_{on} .⁸⁸⁻⁸⁹

Enhancement of efficiency together with luminance levels

The excitons in the triplet excited states in Ir-iTMC have long lifetimes with long diffusion lengths. Excitons are quenched when they encounter a reactive species such as an electron or a hole or radical cations and anions in the doped layers. Hence, the long diffusion lengths and the efficient quenching of excitons makes it difficult to achieve high brightness and high efficiency in LECs. For real applications, high efficiency together with high luminance is desired during the device operation.

Higher current efficacies at high brightness were obtained using pulsed-current driving⁹⁰ compared to conventional constant driving.⁹¹⁻⁹³ However, a multi-component system based on a host:guest:electrolyte active material, where the guest is an iTMC, has recently boosted the efficiency operation to 99.2 cd A⁻¹ at the significant high luminance of 1910 cd m⁻². In the device, an outcoupling structure was also employed.⁹⁴ In the host-guest system, the exciton is trapped on the triplet-emitting iTMC guest suppressing the exciton diffusion and confining the exciton quenching in the central recombination zone.

Improvement of device stability

Friend *et al.* mentioned in 1999 that the most critical performance characteristic for OLEDs is the device lifetime, operational and storage. For most applications, operating lifetimes in excess of 3,000 hours, and, generally, in excess of 10,000 hours are necessary. Related to storage times, 5 or more years are required.⁹⁵

The commonly observed trade-off between fast t_{on} and long device lifetimes³⁶ was overcome using the above-mentioned pulsed-current driving

approach. Under operation, the device has time to relax in the off-state after each current pulse which leads to a reduction of the growth of the doped zones. However, the device lifetime is often limited by the stability of the emitter. Several chemical modifications were reported that enhanced the device stability. Generally speaking, an enhancement of stability is achieved by spatial separation of the iTMCs and by providing a rigid and stable coordination environment for the metal cation. Recently, two families of iTMC complexes were reported by our group with long stabilities and short t_{on} . One family contains arylazole ancillary ligands⁹⁶ and the other uses benzothiazole ancillary ligands, with device lifetimes greater than 2700 h and 6000 h, respectively. Other strategy consists on the use of ligands capable of intramolecular π - π stacking.⁹⁷⁻⁹⁹ The supramolecular cage is formed and due to the stack of the ligand limits the attack of nucleophilic molecules to the Ir metal core and the degrading of the emitter is hindered. The first example reported using this strategy showed an extraordinary stability of around 2000 h.⁹⁷

Due to the breakthrough in the device stability obtained with the benzothiazole-based iTMC family, the processing and performance of these LECs will be more extensively described in the next section of this thesis.

Colour: blue and red emission

The “Energy gap law” (EGL)¹⁰⁰⁻¹⁰¹ states that a series of compounds with similar ground- and excited-state vibrational modes will show a linear correlation between nonradiative decay rates with the emission energy. Ir-iTMCs typically follow the EGL behaviour, then the nonradiative decay rate increases as the energy gap decreases (toward red emission). Since the PLQY is defined as:

$$PLQY = \frac{k_r}{k_r + k_{nr}} \quad (2)$$

where k_r and k_{nr} are the radiative and nonradiative rates, respectively, PLQY decreases as the energy gap decreases. Ultimately, the PLQY is related to the

device efficiency in terms of the EQE_{EL} . As the PLQY of red-emitting Ir-iTMCs is typically low, the EQE_{EL} will be low (see Equation (1)). Moreover, re-absorption of the low energy emission by red Ir-iTMCs for excitation of molecular vibrations is one of the reasons for the low efficiency and/or device lifetime of red LECs.¹⁰²

In addition to the lower efficiency, a small number of red-emitting LECs have been reported and only few of them have CIE coordinates close to the ideal red value (CIE 0.66, 0.33) showing poorer stability compared to yellow/orange LECs.

However, the greatest challenge for organometallic synthetic chemists is still the design of iTMCs with deep-blue and blue emission. Up to now, only a few examples have been reported and they also exhibit poorer stability compared to yellow and orange LECs. The low stability is normally attributed to the degradation of the emitter via an over-charge injection process¹⁰³⁻¹⁰⁶ or the population of the non-emissive metal-centred (^3MC) triplet in the Ir complex.^{48, 98-99, 107-108}

2.2. Improving the device stability of red and near-infrared light-emitting electrochemical cells by chemical modification

2.2.1. Introduction

Red (620–660 nm) and deep-red (660–700 nm) emitting devices are widely used in applications such as signage and automotive. Moreover, pure-red emitters together with pure-green and -blue emitters are needed for full-colour applications and as key components for obtaining white light. Near infrared emission (> 700 nm) is interesting for applications in sensing, telecommunications or bioimaging. LECs based on red- and near-infrared emitters could serve as a low-cost alternative to be successfully applied in light-emitting sources in the near future.

Device lifetime is the most critical performance characteristic for LECs employed in lighting applications. The device stability of LECs mainly depends on the current applied through the device and the nature of the iTMC employed (structural, chemical and electrochemical stability). The device stability decreases with increasing current density due to a number of reasons: 1) fast growing of the doped regions, 2) chemical degradation of the iTMC, 3) quenching of excitons by the injected charges and excitons presented in the doped layers, 4) saturation of the phosphorescent emissive centres and 5) Joule heating of the device. Therefore, the application of low currents seems to be beneficial for device stability, whereas the use of high currents leads to acceleration of the device degradation due to the higher stress that the materials are subjected to.

The iTMC stability can be enhanced with the use of rigid ligands.¹⁰² This rigidity prevents degradation of the complex (rupture of weak bonds), reduces the intramolecular vibrations in the complex and less heat is generated via non-radiation relaxation processes. In addition, a large energy difference between the emitting $^3\text{MLCT}$ triplet and the ^3MC triplet prevents the complex from reaching the unstable ^3MC states.

While stable green- and yellow-emissive LECs have been widely reported, there are few examples of red-to-near infrared (NIR)-emissive iridium iTMC-based LECs.^{93, 102, 109-116} In general, red-emitting LECs exhibit lifetimes of a few hours or less. In cyclometalated $[\text{Ir}(\text{C}^{\wedge}\text{N})_2(\text{N}^{\wedge}\text{N})]^+$ complexes, Tamayo *et al.* reported the complex $[\text{Ir}(\text{tbutyl-ppz})_2(\text{biq})][\text{PF}_6]$ ($\text{tbutyl-ppz}^- = 4'$ -tert-butylphenyl)pyrazolato, $\text{biq} = 2,2'$ -biquinoline) that was incorporated into LECs showing its maximum electroluminescence wavelength ($\lambda_{em,EL}^{max}$) at 635 nm with a luminance of 7500 cd m^{-2} but no lifetime data was presented.¹⁰⁹ Zhang *et al.* reported the most efficient red-emitting LEC up to now ($\lambda_{em,EL}^{max}$ at 624 nm) with an EQE_{EL} of 9.51% using the $[\text{Ir}(\text{ppy})_2(\text{pyoxd})][\text{PF}_6]$ complex ($\text{ppy}^- = 2$ -phenylpyridinate, $\text{pyoxd} = 2$ -phenyl-5-(2-pyridyl)-1,3,4-oxadiazole). This red-emitting LEC showed a device lifetime of 490 min under operation at 5 V.⁹³ Hu *et al.* introduced in a host-guest configuration a benzoimidazole moiety in the $\text{N}^{\wedge}\text{N}$ ligand in the $[\text{Ir}(\text{ppy})_2(\text{qIbi})][\text{PF}_6]$ ($\text{qIbi} = 2$ -(1-phenyl-1*H*-benzoimidazol-2-yl)quinoline) complex producing a LEC with a deep-red emission ($\lambda_{em,EL}^{max}$ at 650 nm).¹¹⁷ Recently, Namanga *et al.* demonstrated a lifetime of 280 h for the $[\text{Ir}(\text{bzq})_2(\text{biq})][\text{PF}_6]$ ($\text{bzq}^- = \text{benzo}[h]\text{quinolato}$ and $\text{biq} = 2,2'$ -biquinoline) ($\lambda_{em,EL}^{max}$ at 662 nm), with maximum luminance of 33.65 cd m^{-2} and efficiency of 0.33 cd A^{-1} , which is among the longest device lifetimes reported for any deep-red LEC.¹⁰²

The benzothiazole moiety has previously been used in iTMCs as part of the cyclometalated $\text{C}^{\wedge}\text{N}$ ligand.¹¹⁸⁻¹²⁰ In particular, 2-(pyridin-2-yl)benzo[*d*]thiazole (btzpy) has been coordinated to other metal ions¹²¹⁻¹²² and there is only one example with iridium using the related $\text{N}^{\wedge}\text{N}$ domain ($\text{N}^{\wedge}\text{N} = 2$ -(pyridin-2-yl)-4,5-dihydrothiazole) but the complex was only evaluated as a photosensitizer for catalytic water reduction.¹²³

In this chapter, the study of the thin-film photophysical characterization, fabrication and characterization of LECs using a series of ionic iridium(III) complexes (**1–8**) based on the $[\text{Ir}(\text{ppy})_2(\text{btzpy})][\text{PF}_6]$ complex having ppy^- as the $\text{C}^{\wedge}\text{N}$ cyclometalated ligand and btzpy as the $\text{N}^{\wedge}\text{N}$ ancillary

ligand is presented. The incorporation of substituents, replacement for other ligands, and the role of the heteroatom in the benzothiazole unit are analysed. All the LECs studied here exhibit deep-red to infrared electroluminescence.

2.2.2. Experimental and methodology

Ir(III)-iTMC complexes

The Ir-iTMCs used in this thesis for the fabrication of LECs were synthesized, purified and characterized by the groups of Prof. Dr. Edwin C. Constable and Prof. Dr. Catherine E. Housecroft at the Department of Chemistry of the University of Basel (Switzerland) or by the group of Prof. Dr. Eli Zysman-Colman at the Organic Semiconductor Centre, EaStCHEM School of Chemistry of the University of St. Andrews (United Kingdom). The chemical structures of the red and near-infrared emitters studied in the thesis are depicted in Figure 7. Complexes **1–6** were synthesized by Dr. Cathrin D. Ertl at the University of Basel. Complexes **7** and **8** were synthesized by Dr. Amlan K. Pal at the University of St. Andrews.

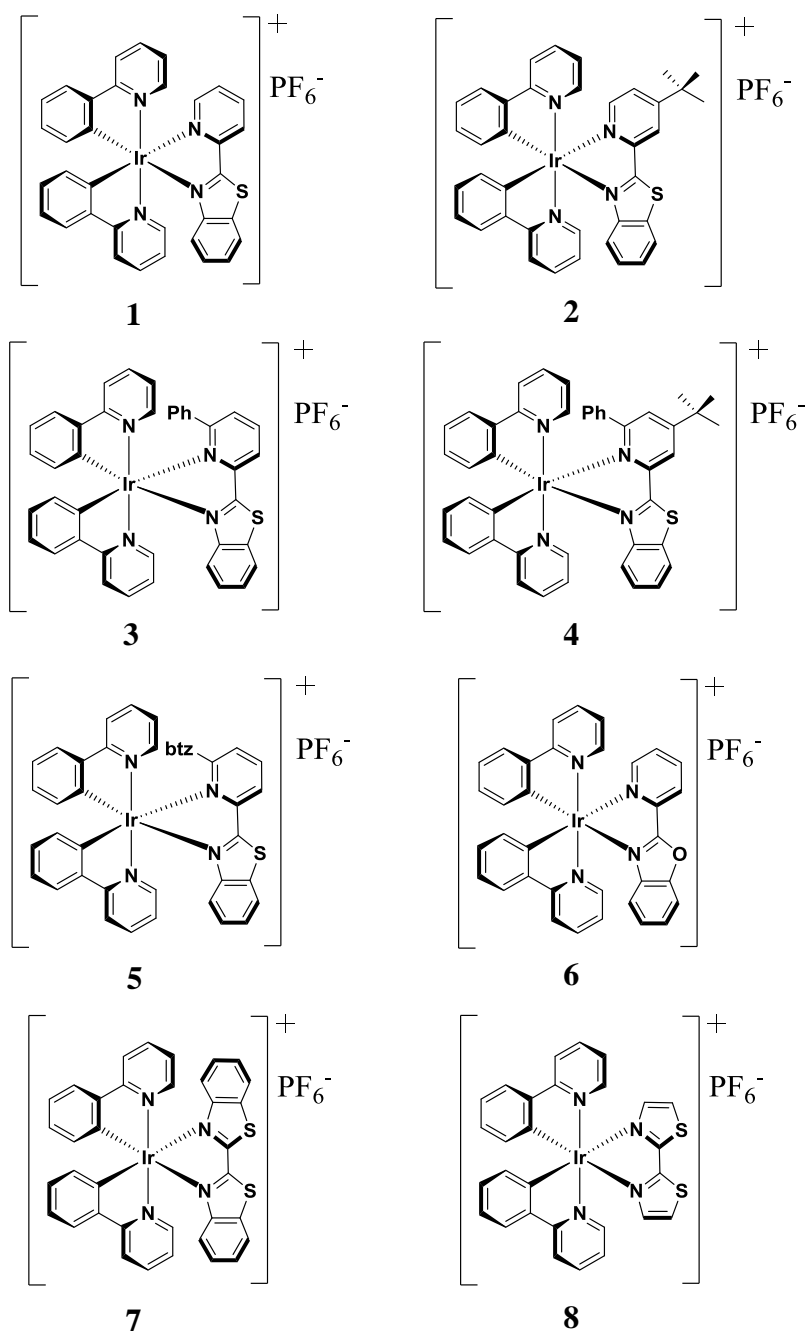


Figure 7. Chemical structures of the red and near-infrared Ir-iTMC emitters (complexes 1-8) studied in this thesis.

Processing, preparation and characterization of the LECs were carried out in a class 10000 cleanroom (Figure 8). The cleaning of the substrates and coating of the layers were done inside the cleanroom in atmospheric conditions, and the thermal annealing, evaporation of the cathode and characterization of the device, were carried out under inert conditions in an MBRAUN glovebox (< 0.1 ppm H₂O and O₂).



Figure 8. Photograph of the class 10000 cleanroom at the Instituto de Ciencia Molecular (ICMol) of the Universidad de Valencia.

Materials

All the materials were used as received. Poly(3,4-ethylenedioxythiophene):polystyrenesulfonate (PEDOT:PSS, Clevios P VP Al 4083, aqueous dispersion, 1.3–1.7% solid content) was purchased from Heraeus. The ionic liquid 1-butyl-3-methylimidazolium hexafluoridophosphate ([Bmim][PF₆]) (> 98%) and the poly(methyl methacrylate) (PMMA, M_w = 120,000 g mol⁻¹) were purchased from Sigma-Aldrich. The solvents acetonitrile, dichloromethane, methyl ethyl ketone and anisol were purchased from Sigma-Aldrich. The photolithography-patterned indium tin oxide (ITO)

($15 \Omega \square^{-1}$) glass substrates and the quartz substrates were purchased from Naranjo Substrates (www.naranjosubstrates.com) and UQG Optics, respectively.

Processing of samples for thin-film photoluminescence characterization

In order to evaluate the suitability of the iTMCs as emitters in LEC devices, the solid-state photophysical properties of the emitters were characterized. The photoluminescence (PL) spectrum and the PLQY were determined in a thin-film configuration. The PL spectrum gives information about the spectral region where the complex emits when excited by a light source. For clarity, the emission intensity (in counts) is normalized to unity. The PLQY (in 100% or in a scale 0 to 1) is the relation between the photons emitted per photons absorbed by the emitter or emitter-containing film. As mentioned above, Ir-iTMCs can harvest both singlet and triplet excitons, therefore the PLQY should resemble the solid-state PL efficiency. Hence, the device efficiency is mainly determined by the solid-state PLQY of the iTMC emitter.

The samples for thin-film PL measurements had the same composition and thickness than the emissive layer used in the LECs. Each complex was mixed with the IL [Bmim][PF₆] in a 4-to-1 molar ratio. A 100 nm thick film was deposited from a solution of complexes **1**, **5** and **6** in acetonitrile and complexes **2-4**, **7** and **8** in dichloromethane. Prior to deposition, all solutions were filtered with a polytetrafluoroethylene (PTFE) filter with 0.22 μm pore size and spin-coated at 1000 rpm for 30 s in air onto cleaned quartz substrates. As the films obtained from the filtered solutions of complexes **2** and **4** in the LEC layout were inhomogeneous, the complexes were dispersed with a small amount (2 wt.% with respect to the other components of the light-emitting layer) of polymethylmethacrylate (PMMA) to improve the homogeneity of the layer.

LEC preparation

All the devices studied in this thesis have the stack architecture (see Figure 4): ITO/PEDOT:PSS/active layer/Al. The composition of each active layer was a mixture consisting of the light-emitting iTMC and the IL in a 4-to-1 molar ratio, except for complexes **2** and **4**, which were dispersed with a small amount (2 wt.% with respect to the other components of the light-emitting layer) of PMMA.

LECs were prepared as follows. The substrates were cleaned by subsequently 5-minute sonication steps in water-soap, water and 2-propanol baths, in that order. After drying, the substrates were placed in a UV-ozone cleaner (Jelight 42-220) for 20 minutes. Onto the clean ITO substrates, a 80 nm layer of PEDOT:PSS was spin-coated at 1000 rpm for 60 s and dried at 150 °C for 15 min. The PEDOT:PSS was added from a syringe and filtered with a polypropylene (PP) 0.45 µm pore size filter. The purpose of this layer is to flatten the ITO, improving the reproducibility of the devices and hence preventing the formation of pinholes that can lead to shorts. Then, a 100 nm thick film of the emissive layer was deposited in the same conditions that were described for thin-film samples for photoluminescence measurements. In brief, solutions of complex:IL in a 4-to-1 molar ratio were filtered and spin-coated at 1000 rpm for 30 s. The IL was added to reduce the t_{on} defined as the time to reach a luminance of 50 or 100 cd m⁻² (t_{50} or t_{100}) and to increase the performance of the devices.⁷⁶ The devices were transferred to the inert atmosphere glovebox for annealing at 100 °C for 1 h. Finally, a 70 nm thick film of aluminium was thermally evaporated using a shadow mask under vacuum ($< 1 \times 10^{-6}$ mbar) with an Edwards Auto500 evaporator integrated into the glovebox. The active area of the cells was 6.34 mm². The devices were not encapsulated and were characterized inside the glovebox at room temperature.

Thin-film photoluminescence and LEC characterization and equipment.

All devices were tested without encapsulation and were characterized inside the glovebox at room temperature. For each device configuration, we evaluated eight cells to ensure meaningful statistics.

The thin-film PL spectrum and solid-state PLQY were measured in air with a Hamamatsu C9920-02 Absolute PL Quantum Yield Measurement System. The system consists of an excitation light source (a xenon lamp linked to a monochromator), an integration sphere and a multi-channel spectrometer.

LECs are intrinsically dynamic devices and their characterization is made in a different way than what is usual for OLEDs. OLEDs are frequently characterized by monitoring the luminance and current density *versus* voltage in scans with different scan speeds. Due to the slow ionic motion occurring in LECs, their operation changes with different scan speeds and therefore this method is not suitable. Therefore, LECs are generally studied by applying either a fixed voltage or a fixed current density over time. As mentioned above, our group has shown the benefits of operating the devices under pulsed-current driving and this mode has been chosen for the characterization of the devices studied in this thesis. Therefore, LECs using complexes **1–8** were tested by applying a pulsed current and by monitoring the voltage and the luminance with a True Colour Sensor (MTCSiCT Sensor, MAZeT GmbH) using a Lifetime Test System (Botest OLT OLED Lifetime-Test System, Botest System GmbH). LEC using complex **7** was also evaluated by applying a pulsed current with the Botest Lifetime Test System, but due to NIR emission the irradiance was monitored using an integrating sphere (UDT Instruments, model 2525LE) coupled to a Radiometric Sensor (UDT Instruments, model 247) and an optometer (UDT Instruments, model S370).

The pulsed current consisted of a block wave at 1000 Hz frequency with a duty cycle of 50%. The peak current density of the pulse was 200 A m⁻² and the average current density was 100 A m⁻² for LECs **1–6**. For further

understanding of the device stability of the LEC using complex **1**, this device was driven at average current densities of 300, 700, 1250 and 1500 A m⁻². For LECs using complexes **7** and **8**, the current densities applied to the devices were 800 A m⁻², which corresponds to an average current density of 400 A m⁻².

Electroluminescence spectra were recorded using an Avantes fiber optics photospectrometer.

2.2.3. Results and discussion

The thin-film photophysical properties of the complexes **1–8**, such as the photoluminescence (PL) spectrum and PLQY, were determined under illumination at 320 nm (Table 1). All the complexes emit in the red – near-infrared region with maximum emission wavelengths ($\lambda_{em,PL}^{max}$) ranging from 625 nm for complex **6** to 707 nm for complex **7**. The PLQY values are low (<18%), with the highest PLQY obtained for complex **2** (PLQY = 17.6%) and the lowest values obtained for complexes with the lowest emission energies of the series: complex **3** (PLQY = 9.7%, $\lambda_{em,PL}^{max}$ = 651 nm), complex **5** (PLQY = 5.8%, $\lambda_{em,PL}^{max}$ = 658 nm) and complex **7** (PLQY = 5.0%, $\lambda_{em,PL}^{max}$ = 707 nm), presumable as a consequence of the EGL.

Table 1. Thin-film photophysical characterization of complexes **1–8** (λ_{exc} = 320 nm).

Complex	λ_{em}^{max} (nm)	PLQY (%)
1	645	11.0
2	642	17.6
3	651	9.7
4	626	12.5
5	658	5.8
6	625	12.3
7	707	5.0
8	658	14.0

Simple two-layer LECs were prepared to evaluate the electroluminescent properties of complexes **1–8** in a sandwich-type structure. LECs fabricated using complexes **1–8** will be referred as LECs **1–8** for clarity. The device layout is as follows, ITO/PEDOT:PSS/complex(**1–8**):IL/Al, as explained in the experimental and methodology section (Section 2.2.2.). In brief, LECs were prepared by spin-coating a 80 nm thick film of PEDOT:PSS on pre-cleaned ITO substrates. The active layer (100 nm thick film) was then deposited by spin-coating from a filtered solution of complexes **1–8**, mixed with the IL [Bmim][PF₆] in a 4-to-1 molar ratio. For complexes **2** and **4**, a 2 wt.% of PMMA (with respect to the other components of the light-emitting layer) was added to improve the film coverage and homogeneity of the layer. After the active layer deposition, a 70 nm thick film of aluminium was thermally evaporated to finish the device. As mentioned before, the IL was added to reduce the t_{on} defined as the time to reach a luminance of 50 or 100 cd m⁻² (t_{50} or t_{100}) and to increase the performance of the devices.⁷⁶

As mentioned earlier, the operation of the device under pulsed-current driving shows better device performance than under the typical constant-voltage driving. Therefore, in this study LECs **1–8** were evaluated using a pulsed-current driving, consisting of a block wave at a 1000 Hz frequency with a duty cycle of 50% and an average current density of 100 A m⁻² for LECs **1–6**. LEC **1** was also evaluated at different average current densities of 300, 700, 1250, and 1500 A m⁻². A current density of 400 A m⁻² was used for LECs **7** and **8**.

The electroluminescence (EL) spectra of LECs **1–8** are shown in Figure 9. LECs **1–6** and **8** are red-emitting devices (Figure 9a) ($\lambda_{em,EL}^{max}$ centred at 636, 642, 651, 648, 655 and 598 nm for LECs **1–6**, respectively, and 661 nm for LEC **8**), whereas LEC **7** emits in the near-infrared region (Figure 9b) ($\lambda_{em,EL}^{max}$ centred at 705 nm). The Commission Internationale de l’Eclairage coordinates (CIE coord.) for LECs **1–6** and **8** were determined from the electroluminescence spectra and are collected in Table 2. The EL spectra for

LECs **1**, **2**, **3**, **5**, **7** and **8** are similar to the solid-state PL spectra indicative of the similar excited states being involved in the light emission process. LEC **4** shows a red-shift of 22 nm ($\lambda_{em,EL}^{max} = 648$ nm) and LEC **6** has a blue-shift of 27 nm ($\lambda_{em,EL}^{max} = 598$ nm), for reasons currently not yet understood. These electroluminescence spectra are very interesting because, up to now, red and deep-red emitting LECs based on cyclometalated $[\text{Ir}(\text{C}^{\wedge}\text{N})_2(\text{N}^{\wedge}\text{N})]^+$ complexes are scarce and only few pure-red LECs have been reported. The colour of device **3** CIE coord. (0.64, 0.35) and LECs **5** and **8**, both with CIE coord. (0.65, 0.34), essentially coincide with the pure-red CIE coord. (0.66, 0.33).

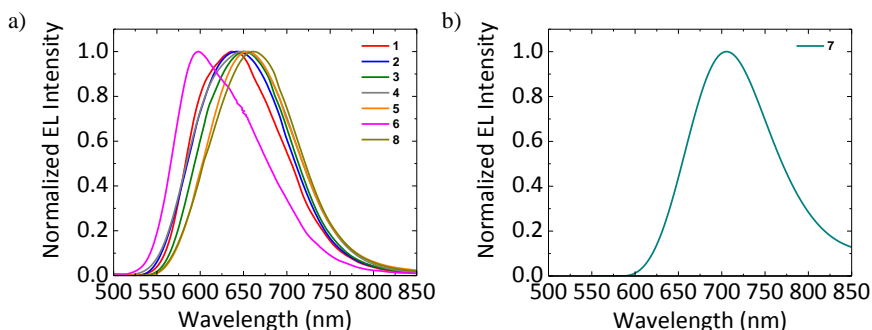


Figure 9. Electroluminescence spectra of a) LECs **1–6** and **8** driven at an average pulsed-current density of 100 A m^{-2} for **1–6** and 400 A m^{-2} for **8** and b) LEC **7** driven at an average pulsed-current density of 400 A m^{-2} . (1000 Hz, 50% duty cycle, block wave).

The luminance and operating average voltage *versus* time dependence of LECs **1–6** driven at the average current density of 100 A m^{-2} and of LECs **7** and **8** driven at 400 A m^{-2} are shown in Figure 10. The key parameters that represent the performances of LECs **1–8** are summarized in Table 2. All LECs present the typical behaviour under pulsed-current mode operation. The luminance rises while the operating voltage rapidly diminishes because the ionic motion over operation decreases the electrical resistance and start to grow the *p*- and *n*-doped regions in the active layer. Once the maximum luminance is attained, the luminance starts to decrease and the operating average voltage remains constant.

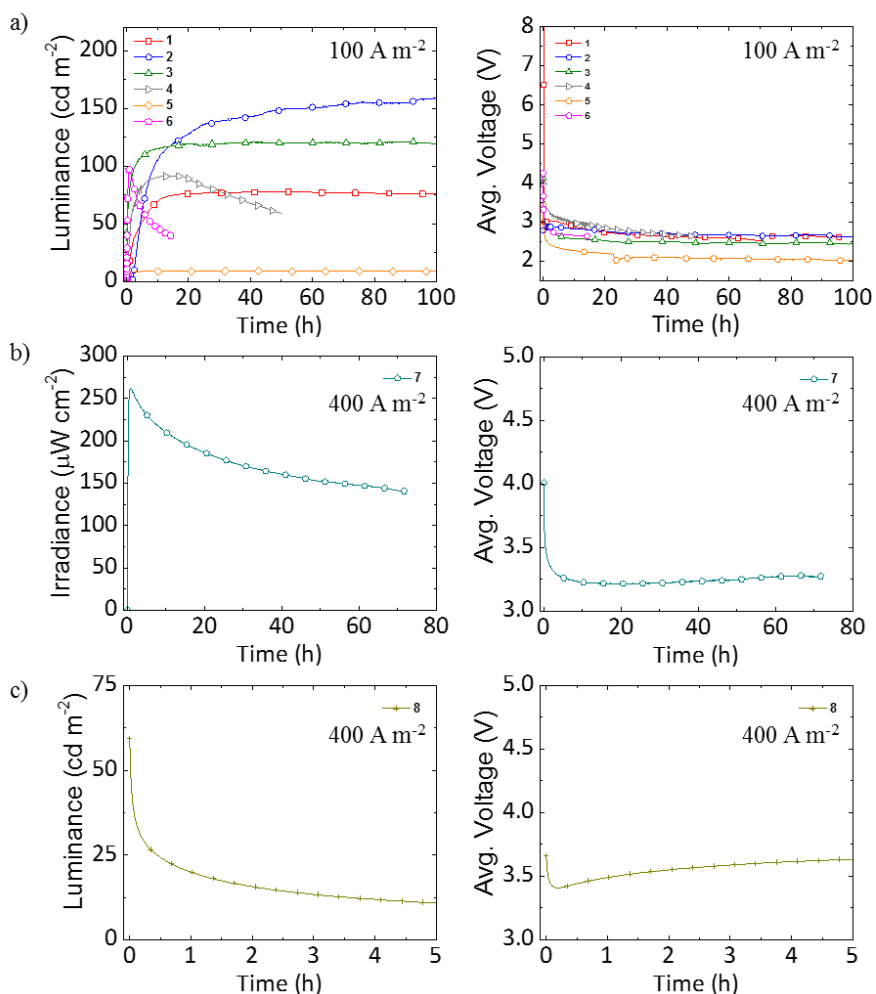


Figure 10. Left: Time-dependent luminance or irradiance. Right: Time-dependent operating average voltage. a) LECs **1–6**, b) LEC **7** and c) LEC **8**. Devices operated under an average pulsed-current density of 100 A m⁻² in a) and 400 A m⁻² in b) and c). (1000 Hz, 50% duty cycle, block wave).

LEC **1** exhibits a maximum luminance (L_{\max}) of 77 cd m⁻² reached after 54 h (t_{\max}) under operation and a device lifetime ($t_{1/2}$) exceeding 1000 h (estimated by extrapolation from the time-dependent luminance curve, Figure 10a). The long time required for reaching the maximum luminance together with the long device lifetime obtained in LEC **1**, imply that the ionic movement in the device and the growing of the doped zones is slow. LEC **2** containing the complex with the *tert*-butyl group in the pyridyl ring (see Figure 7) shows the

highest maximum luminance value of the series with 200 cd m⁻² (t_{\max} at 870 h) and a further enhanced device stability exceeding 6000 h compared to LEC **1** ($t_{1/2} > 1000$ h) becoming the best device of the series and the most stable red-emitting LEC reported up-to-date. For the extrapolation of the device lifetime of LEC **2**, an extended time-dependent luminance graph is depicted in Figure 11. The turn-on time (t_{50}) of LECs **1** (4.6 h) and **2** (4.3 h) are similar, but the luminance in LEC **2** continues to increase over a long time indicating that the optimum charge injection and charge balance are slowly obtained. This could indicate that the slow ionic motion leads to a very slow growing over time of the doped zones becoming beneficial for the device lifetime.¹²⁴⁻¹²⁵ The higher luminance obtained for LEC **2** is due to the higher thin-film PLQY measured for complex **2** (17.6%) compared with complex **1** (11%) (see Table 1).

Table 2. Device performance parameters and electroluminescence data obtained for LECs **1–8** operated under pulsed-current driving (1000 Hz, 50% duty cycle, block wave).

PC ^a / A m ⁻²	Complex	L_{\max} ^b / cd m ⁻²	t_{50} ^c / h	t_{\max} ^d / h	$t_{1/2}$ ^e / h	EQE _{EL,max} ^f / %	λ_{em}^{max} _{EL} / nm	CIE ^g (x,y)
100	1	77	4.6	54	>1000*	0.70	636	0.63, 0.37
	2	200	4.3	870	>6000*	2.00	642	0.63, 0.37
	3	119	0.2	63	>4500*	1.49	651	0.64, 0.35
	4	91	1.3	18	63*	1.04	648	0.62, 0.37
	5	9		4.8	>150*	0.14	655	0.65, 0.34
	6	97	0.2	0.84	9	0.55	598	0.59, 0.41
400	7	262 [#]		0.8	80	0.37	705	
	8	59			0.24	0.23	661	0.65, 0.34

^aAverage pulsed-current density. ^bMaximum luminance reached. ^cTime to reach 50 cd m⁻² luminance. ^dTime to reach the maximum light emission. ^eTime to reach one-half of the maximum light emission. ^fMaximum external quantum efficiency reached. ^gThe Commission Internationale de l'Éclairage (CIE) colour coordinates. [#]This value is expressed in $\mu\text{W cm}^{-2}$ since the EL signal is partially out of the visible spectrum. *Extrapolated values.

LEC **3** incorporating the complex with the pendant phenyl group attached to the N[^]N ligand also shows a higher luminance ($L_{\max} = 119$ cd m⁻² at 63 h) and a longer lifetime ($t_{1/2} > 4500$ h) than LEC **1** ($L_{\max} = 77$ cd m⁻², $t_{1/2} > 1000$ h) although its thin-film PLQY is lower (complex **3** = 9.7%, complex **1** =

11%). However, when the size of the substituents is increased beyond that of complex **3**, as in complexes **4** and **5**, the corresponding LECs have a significantly reduced stability, and the device lifetime decay on a timescale of tens of hours. The replacement of the sulphur heteroatom in the benzothiazole unit (LEC **1**) by an oxygen heteroatom in the benzoxazole unit (LEC **6**) leads to similar luminance ($L_{\max} = 77$ and 97 cd m^{-2} , respectively), but produces a detrimental effect in terms of device stability with a decrease from exceeding 1000 h for LEC **1** to 150 h for LEC **6**. Generally, the time to reach the maximum luminance (t_{\max}) and the t_{50} for LECs **4–6** are almost four times faster than for LECs **1–3**, which support the hypothesis that the device lifetime is mainly affected by the growth of the doped zones, which increases the quenching of excitons.

LEC **7** was deposited from a solution of the complex in methyl ethyl ketone/anisole 3:2. The device did not emit light under pulsed-driving operation most likely related to the poorer film quality of complex **7** resulting from its low solubility. Then, a different solvent (dichloromethane) was used to improve the solubility of the complex, which led to uniform layers completely covering the substrates after spin-coating. Under pulsed-driving operation at an average current density of 400 A m^{-2} , LEC **7** exhibits a maximum irradiance (I_{\max}) of $262 \mu\text{W cm}^{-2}$ and a device lifetime ($t_{1/2}$) of 80 h (Figure 10b). Under the same driving conditions, LEC **8** shows a maximum luminance (L_{\max}) of 59 cd m^{-2} and the device stability ($t_{1/2}$) is considerably reduced to 0.24 h (Figure 10c). The presence of the annulated benzenes in the ancillary ligand (LEC **7**) seems to be beneficial for device stability. The presence of the larger cation in complex **7** compared to complex **8** (see Figure 7) reduces the ionic movement in the active layer during operation, which decreases the exciton quenching and increases the device lifetime. t_{\max} is significantly longer for LEC **7** (0.8 h) than for LEC **8** ($< 5 \text{ s}$), also indicative of the slower ionic movement in LEC **7** compared to LEC **8**. As mentioned above, the device stability is a result of the stable luminance resulting from the Ir-iTMC and the pulsed-current driving approach.

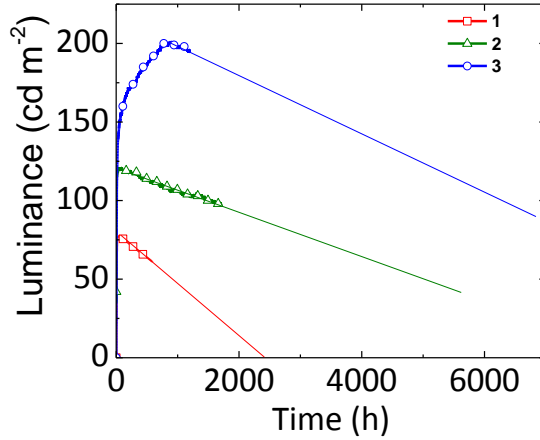


Figure 11. Extended graph of the time-dependent luminance of LECs **1–3** operated under an averaged pulsed-current density of 100 A m^{-2} . (1000 Hz, 50% duty cycle, block wave).

In view of the red and deep-red emission wavelength, the device efficiency expressed as current efficiency is not adequate due to the emission wavelength, which is only in part visible to the human eye. Therefore, the device efficiency is better to be expressed in terms of the EQE_{EL} . The EQE_{EL} values of LECs **1–8** are presented in Table 2. The maximum EQE_{EL} calculated from equation (1) that can be obtained with a thin-film PLQY of 11% (complex **1**) without special outcoupling structures is roughly 2.4%. Experimentally, under 100 A m^{-2} operation, a maximum EQE_{EL} of 0.70% for LEC **1** was obtained. However, due to the higher luminance achieved for LECs **2** and **3**, the maximum experimental EQE_{EL} values for LECs **2** and **3** were 2.00 and 1.49%, respectively. LEC **4** reached an EQE_{EL} of 1.04%, whereas LECs **5** and **6** have EQE_{EL} values of 0.14 and 0.55%, respectively. At 400 A m^{-2} , LEC **7** exhibits an improved EQE_{EL} (0.37%) compared to that based on **8** (0.23%). Considering the low thin-film PLQY of complex **7** (5%) and the high current density applied (up to 400 A m^{-2}) the achieved efficiency for LEC **7** is noticeable.

To the best of our knowledge, the most efficient red-emitting LEC led to a champion peak EQE_{EL} of 9.51%.⁹³ Few examples of near-infrared emitting LECs exhibiting low EQE_{EL} values ($\text{EQE}_{\text{EL}} < 0.1\%$)⁵⁸ have been reported due

to the EGL. An EQE_{EL} value of 1% has now been overcome for near-infrared emitting LECs using host:guest systems or tandem devices with cationic iTMCs.^{114, 126-127}

As commented before, the best way to attain stable devices is to use a pulsed-current driving and, to the best of our knowledge, the best device lifetime for red-emitting LECs has been reported with a device lifetime of 280 h.¹⁰² Therefore, the LECs 1–3 studied in this thesis show stabilities ranging from 4 to 20 times longer than those reported previously. These high lifetime values are exceptional and are only comparable to those obtained for a very few orange emitting LECs operated under the same driving conditions.¹²⁸ The performance of LECs 1–3 are limited by the moderate luminance and the rather slow response. This performance is dependent on the applied current and directly related to the device stability. For further understanding on the device stability, LEC 1 was driven at higher current densities that permits to study the device degradation in accelerated conditions due to the higher stress that the device is subjected to. LEC 1 was selected for this more in-depth analysis due to its good performing characteristics and its simplest chemical structure. Moreover, complex 1 was obtained in sufficient large quantities to prepare a number of devices to be operated under increasing average current densities.

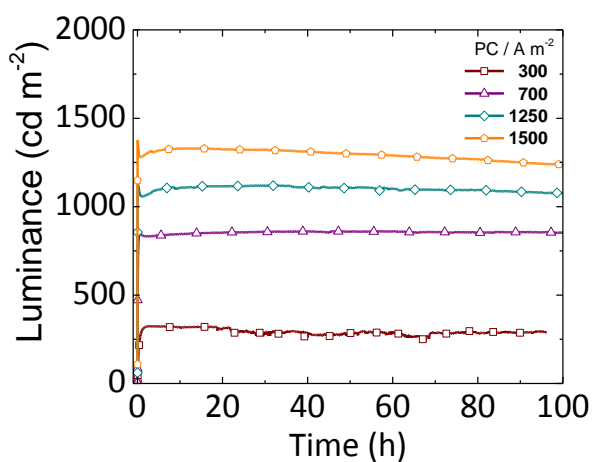


Figure 12. Luminance *versus* time of LEC 1 operated under different average pulsed-current densities from 300 to 1500 A m⁻² (1000 Hz, 50% duty cycle, block wave).

The luminance *versus* time measured for LEC **1** operated using pulsed-current densities of 300, 700, 1250, and 1500 A m⁻² (block wave, 1000 Hz, and 50% duty cycle) are shown in Figure 12. At high driving currents, the luminance decay slowly and, surprisingly, it does not depend very strongly on the applied current density. As mentioned before, a strong dependency of the device lifetime on the current density is normally observed in electroluminescent devices. There is virtually no luminance decay over the first 100 h when driving LEC **1** under the pulsed conditions at average current densities of 300 and 700 A m⁻², and only a moderate decrease of approximately 10% is observed when the average current density is set at 1250 and 1500 A m⁻² after 100 h. The quasi steady-state luminance that is reached at each current density increases linearly in the range from 100 to 700 A m⁻² (the luminance curve for 100 A m⁻² is not depicted for clarity), whereas at higher applied current densities the luminance values still increase but less than linearly. This linear dependence has been previously observed in LECs under pulsed-current driving at very low current densities.¹²⁹ However, this linearity is not usually observed at high current densities, which indicates that there is little exciton-exciton or exciton-polaron quenching up to high current densities of 700 A m⁻². Moreover, the luminance intensity can be tuned from 77 to exceeding 1250 cd m⁻² by the current density applied.

The time to reach the maximum luminance (t_{\max}) and the time to reach 100 cd m⁻² (t_{100}) are also affected by the applied current density. Interestingly, t_{100} is substantially reduced to the second scale, from 500 s at 300 A m⁻² to 5 s at 1500 A m⁻² (Figure 13). For lower current densities, the maximum luminance takes longer to be achieved. This is related to the voltage that is applied, which is lower for lower applied current densities.

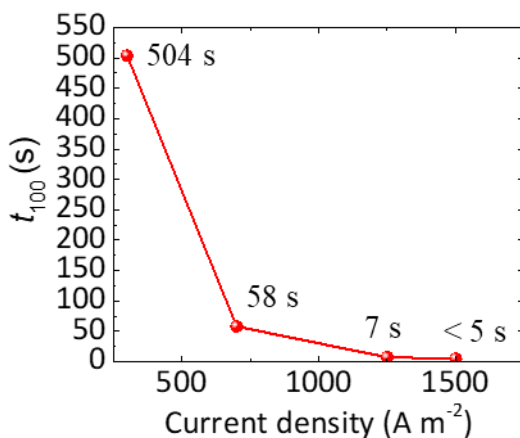


Figure 13. Time to reach 100 cd m⁻² (t_{100}) versus applied current density for LEC 1. (1000 Hz, 50% duty cycle, block wave).

2.2.4. Conclusions

The thin-film photophysical and electroluminescent properties of complexes **1–8** were characterized and analysed and the results have been presented and discussed in this chapter.

Complexes **1–6** were synthesized and characterized by Dr. Cathrin D. Ertl at the University of Basel and complexes **7** and **8** were synthesized and characterized by Dr. Amlan K. Pal at the University of St. Andrews. The complexes are based on the [Ir(ppy)₂(btzpy)][PF₆] complex having 2-phenylpyridinate (ppy⁻) as the C[^]N cyclometalated ligand and 2-(pyridin-2-yl)benzo[*d*]thiazole (btzpy) as the N[^]N ancillary ligand.

The thin-film photophysical properties of complexes **1–8** show photoluminescent emission in the red – near-infrared region with maximum emission wavelength ranging from 625 nm to 707 nm. The PLQY values of the series are low (<18%) due to the energy gap law.¹⁰⁰⁻¹⁰¹

All complexes were incorporated into light-emitting electrochemical cells (LECs) as single emitters to study their electroluminescent properties. LECs **1–6** and **8** shows red emission, whereas LEC **7** present infrared emission.

The colour of devices **3**, **5** and **8** essentially coincide with the pure red CIE coordinate (0.66, 0.33).

Although the maximum luminance presents a moderate value for LECs **1–3**, up to 200 cd m⁻² for LEC **2**, they exhibit lifetimes in excess of 1000, 6000 and 4000 h, respectively, becoming the most stable red-emitting LECs reported up-to-date.

The EQE_{EL} values obtained are moderate with a highest EQE_{EL} value of 2% for LEC **2**. However, the relatively high EQE_{EL} of 0.37% for the near-infrared LEC **7** is impressive due to its low thin-film PLQY value of 5% and the high current density applied (up to 400 A m⁻²).

The possibility of tuning the luminance levels has been demonstrated, having a fast response with almost no lost in device stability, by increasing the average current density applied from 100 A m⁻² to 1500 A m⁻². This proves that these complexes are highly interesting to be further explored in lighting devices and that they constitute a step forward in the demand for red-light applications.

2.2.5. Contributions of the author

Article 1. Ertl, C. D.;[‡] **Momblona, C.**;[‡] Pertegás, A.; Junquera-Hernández, J. M.; La-Placa, M.-G.; Prescimone, A.; Ortí, E.; Housecroft, C. E.; Constable, E. C.; Bolink, H. J., Highly stable red-light-emitting electrochemical cells. *Journal of the American Chemical Society* **2017**, *139* (8), 3237-3248. ([‡] equally contributed). (IF: 13.858, Q1).

Article 2. Pal, A. K.; Cordes, D. B.; Slawin, A. M. Z.; **Momblona, C.**; Pertegás, A.; Ortí, E.; Bolink, H. J.; Zysman-Colman, E., Simple design to achieve red-to-near-infrared emissive cationic Ir(III) emitters and their use in light-emitting electrochemical cells. *RSC Advances* **2017**, *7* (51), 31833-31837. (IF: 3.108, Q1).

IF = Impact factor (Science Citation Reports, Web of Science), Q = Quartile.

Chapter 3

Perovskite solar cells

3.1. Introduction

Metal halide perovskites have emerged as revolutionary optoelectronic semiconductors, and are promising materials for applications such as photovoltaics, light-emitting diodes, photodetectors or lasers, among others.¹³⁰⁻¹³⁴ The rapid evolution of the certified efficiency of perovskite solar cells (PSCs) exceeding 22%¹³⁵ and the low cost of the perovskite precursors and processing methods make these devices appealing for commercialization. Devices with a similar architecture have led to very efficient light-emitting diodes (LEDs) reaching external quantum efficiencies exceeding 13%,¹³⁶ further increasing their market prospects.

The unique and superior optical and electrical properties of the organic-inorganic (hybrid) perovskites establish them as excellent candidate for absorbers/emitters and charge transport materials. These properties are: high optical absorption coefficient with sharp onset,¹³⁷ ambipolar conduction with balanced electron and hole mobilities,¹³⁸ long photogenerated carrier diffusion lengths and lifetimes,¹³⁹⁻¹⁴¹ low trap densities¹⁴² and low exciton binding energies.¹⁴³⁻¹⁴⁵

3.1.1. Metal halide perovskites

Crystal structure

The exceptional tuning that offers their structure enables metal halide perovskites to possess zero- (0D), one- (1D), two- and quasi-two- (2D), and three- (3D) dimensional structures.¹⁴⁶⁻¹⁴⁸ This thesis focuses on the study of 3D perovskites.

3D metal halide perovskites are a family of bulk materials that can be described with the general formula ABX_3 . This crystal structure (Figure 14) consists of a framework of corner-sharing metal halide (BX_6) octahedra that extend in the three dimensions, with small cations (A) fitting into the void spaces between the octahedra. In the archetype organic-inorganic perovskite, A

is an organic (methylammonium (CH_3NH_3^+ or MA^+) or formamidinium ($\text{NH}_2\text{CH}=\text{NH}_2^+$ or FA^+)) or inorganic monovalent cation (cesium Cs^+), B is a divalent cation (Pb^{2+} or Sn^{2+} or to a less extent Ge^{2+}) and X is a halide (Cl^- , Br^- , I^-).¹⁴⁸⁻¹⁵⁰

These materials are known for more than a century and have been studied extensively in the 1990's in transistor applications.¹⁵¹ Most of the perovskite materials that were studied in the previous century were prepared as small crystals that were used to determine their structural, chemical and optical properties. Only a rather small number of these materials were processed into thin films which explains the un-noticed photovoltaic properties up to recently.

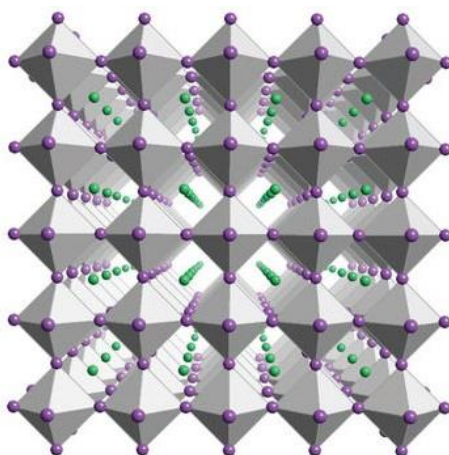


Figure 14. Crystal structure of ABX_3 3D-perovskite. Pb are placed at the centre of the grey octahedrons, lavender spheres represent iodine atoms and green spheres represent the methylammonium cations. Adapted from reference 152.

The empirical index Goldschmidt tolerance factor (t),¹⁵³ typically used for oxide and sulphide-based perovskites, is a measure of the fit of the A-site cation to the cubic corner-sharing octahedral network, where the lattice is treated as an array of close-packed spheres. This predicts the stable crystal structure of perovskite materials in terms of the ionic packing.

$$t = \frac{r_A + r_X}{\sqrt{2} \cdot (r_B + r_X)} \quad (3)$$

Where r_A , r_B and r_X are the ionic radii of A, B and X, respectively. With t values between 0.8 and 1.0, the formation of a cubic perovskite structure is favourable. Values of the tolerance factor larger than 1 or smaller than 0.8 usually result in nonperovskite structures. More refined models have also been proposed that take into account other space-filling considerations enabling a better prediction for the specific case of organic-inorganic metal halide perovskites.¹⁵⁴⁻¹⁵⁷

The prototypical perovskite photovoltaic absorber methylammonium lead iodide (MAPbI₃) has three crystal structures depending on the temperature:¹⁵⁸ an orthorhombic *Pnma* phase below 160 K, a tetragonal *I4/mcm* phase from 160 to 330 K and a cubic *Pm-3m* phase above 330 K. These transitions need to be considered because they may alter the electronic band structure and ultimately the optoelectronic properties of the material.^{150, 159}

Electronic structure

The electronic structure presents similar characteristics for all metal halide perovskites. The valence band (VB) consists of admixed np^6 (n is the principal quantum number, Cl: $n = 3$, Br $n = 4$, I $n = 5$) and ns^2 orbitals from the metal (Ge: $n = 4$, Sn $n = 5$, Pb $n = 6$) whereas the conduction band (CB) consists of the empty np^6 orbitals from the metal. The electronic states of the organic or inorganic cation in the A-site of the perovskite structure lie far away from the VB and CB and provide no direct electronic contribution near the band gap.¹⁶⁰⁻¹⁶² Qualitatively, the band structure is almost material independent (excluding differences in the band gap) and it is strongly dependent on the symmetry the perovskite adopts.

All the perovskites are direct band gap semiconductors,¹⁶³⁻¹⁶⁴ leading to efficient light absorption with high absorption coefficients.

Optical properties

The large absorption coefficients^{140, 165} reported in the order of 10^4 – 10^5 cm^{-1} are a consequence of the direct band gap transition. The sharp absorption onset demonstrates the high quality of the material without the presence of imperfections or defects typically observed as a tail in the absorption onset.¹⁶⁶ Moreover, the absorption spectra provides information about the nature of photogeneration: excitonic materials often exhibit a characteristic excitonic peak that distinguishes them from band-like materials.

The band gap of metal halide perovskites can be tuned over a range spanning the near-infrared to near-ultraviolet wavelengths by simple compositional substitution of the three lattice positions: A, B or/and X sites.¹⁶⁷ As the electronic structure is determined by the inorganic framework, the halide substitution has a strong effect on the VB of the perovskite and the band gap. In contrast, the replacement of MA with FA makes only a slight change to the band gap.

The prototypical perovskite MAPbI_3 has a band gap located between 1.5 and 1.6 eV.¹⁶⁸ The replacement of the A cation of MA^+ for FA^+ in MAPbI_3 decreases the band gap from 1.55 (pure MA^+) to 1.47 eV (pure FA^+),¹⁶⁹ whereas the substitution of the B cation of Pb^{2+} by Sn^{2+} decreases the band gap to 1.2 eV.^{150, 170-172} Alternatives for the toxic Pb^{2+} and eco-toxic Sn^{2+} while maintaining the low direct band gaps of the resulting perovskites are not easy to find. When the iodine in MAPbI_3 is replaced with a halide with a smaller ionic size (Br^- and Cl^-), the band gap is increased (2.3 eV for MAPbBr_3 and 3.1 eV for MAPbCl_3).¹⁷³ The organic cation substitution is hard to determine because they occupy the same crystallographic site and the effects are only observed indirectly by the induced distortion of the inorganic lattice.¹⁷⁴⁻¹⁷⁵ Therefore, perovskite benefit from spectral tuning making them suitable for the top- and bottom-cell application in tandem solar cells, respectively.¹⁷⁶

Electrical properties

Knowledge of the perovskite's electrical properties such as the charge carrier mobilities, diffusion lengths and lifetimes, as well as the nature of the photogenerated species, are crucial for the fabrication of optoelectronic devices.

The charge carrier mobility, μ , describes the ability of electrons and holes to move within a semiconductor under an applied field. The mobility depends on the morphology and on the material composition. Mobilities exceeding $10 \text{ cm}^2 \text{ V}^{-1} \text{ s}^{-2}$ have been measured in perovskite films.^{138, 141, 177-178}

The charge carrier diffusion length is another characteristic that describes the charge transport ability of a material. It describes the motion of charges by diffusion from regions of high carrier population in the semiconductor to areas with lower populations. Charge carrier diffusion lengths ranging from $0.1 \text{ }\mu\text{m}$ to exceeding $10 \text{ }\mu\text{m}$ have been reported for perovskites depending on their composition and thin film morphology.^{139-140, 177, 179-182}

The carrier lifetime (t) is the time that the charges take to recombine under non thermodynamic equilibrium situation, such as under photoexcitation. Carrier lifetime is related to the diffusion length and to the number of traps within the semiconductor. Therefore, it is often used to assess the quality of materials. Carrier lifetimes in excess of $1 \text{ }\mu\text{s}$ have been reported for perovskite films, demonstrating the low amount of charge transport affecting defects in these films (t is directly dependent on the defects).¹³⁹

After light absorption, the primary photogenerated species presented in the absorber are excitons (bound electron-hole pairs). It is vital to understand if these excitons will remain in the material or will dissociate to give rise to free charge transport (see Section 3.1.3.).

3.1.2. Processing of perovskite films

A variety of processing routes have been reported employing solution or vacuum-based deposition techniques or a combination of both. Although analysis *a posteriori* suggests that the compound is exactly the same in all cases, as mentioned above, the properties of the films vary significantly depending on the deposition method used. The differences are so relevant that the motto “same compound, different material”¹⁸³ can be applied to perovskites. Therefore, a precise description of the preparation method is essential for a better understanding of the materials. In addition, the environmental conditions (vacuum, dry nitrogen, dry air or humid air) during deposition and annealing will influence the perovskite layer and hence its properties.

Solution-based deposition methods

For solution-based processing the perovskite precursors are dissolved in an organic solvent and deposited using coating or printing methods, such as spin-, dipping- or doctor blade- coating and gravure coating.¹⁸⁴

Spin-coating is the most popular method for small-area perovskite deposition in the photovoltaic academic community. In brief, a small amount of precursor solution in a volatile solvent is added on the centre of the substrate and is rotated at high speed. The material is spread by centrifugal force and the solvent is simultaneously evaporated during the high-speed rotation. After rotation a semi-dry film with a uniform thickness is obtained.

The solution-based deposition methods using spin-coating can be grouped into two main categories: one- and two-step solution deposition.

- One-step solution deposition

The perovskite film is directly deposited from solution of the precursors in polar and high-boiling solvents, such as γ -butyrolactone (GBL),¹⁸⁵ dimethylformamide (DMF)¹⁸⁶ and dimethylsulfoxide (DMSO).¹⁸⁷⁻¹⁸⁸ The perovskite is deposited by spin-coating of the precursor solution followed by a

post-annealing treatment.¹⁸⁹⁻¹⁹¹ The layers processed by this method are not homogeneous due to uncontrolled crystal growth and therefore have a high roughness. In order to improve the homogeneity, the use of several additives have been explored to enhance the quality of the layer, such as methylammonium chloride (MACl),¹⁹² HI¹⁷⁹ or HBr/H₂O,¹⁹³ I₂,¹⁹⁴ NH₄Cl,¹⁹⁵ 1,8-diiodooctane,¹⁹⁶ or phosphonic acid ammonium.¹⁹⁷ Another approach to improve the quality of the perovskite layer is the addition of a solvent that does not dissolve the perovskite film (e.g. toluene, diethyl ether, chlorobenzene, benzene or xylene) during the last few seconds of the spin process. High-quality perovskite films with smooth morphology and large grains are obtained by this method, generally referred to as solvent exchange or solvent engineering.¹⁹⁸⁻²⁰⁰

- Two-step solution deposition

In this method, first a PbI₂ layer is spin-coated and subsequently converted into a perovskite by dipping/spin-coating of the methylammonium iodide (MAI) solution.²⁰¹⁻²⁰² Therefore, the MAI has to intercalate into the solid PbI₂ layer in a heterogeneous reaction. The morphology of the final perovskite film is determined by the morphology of the PbI₂ film and the reaction rate is determined by the diffusion of MAI into the PbI₂ lattice.

- Vapour-assisted solution deposition

This method differs from the two-step solution deposition method in the incorporation of MAI through a vapour deposition technique. Although the perovskite films present uniform surface coverage, large grain size and full conversion, the process is less rapid and the highest efficiency obtained is only 12%.²⁰³⁻²⁰⁴

Vacuum-based deposition methods

In vacuum- or vapour-based deposition the perovskite precursors are placed separately in ceramic crucibles that are positioned in temperature controlled heating sources (see Figure 15). After reducing the pressure in the

chamber to a base pressure of $1 \times 10^{-5} - 1 \times 10^{-6}$ mbar, they are heated to their corresponding sublimation temperatures. To monitor the nominal thickness of the film, a quartz crystal microbalance (QCM) sensor is employed. The QCM consists of a thin quartz crystal sandwiched between two metal electrodes. An alternating electric field is applied across the crystal, causing vibrational motion of the crystal at its resonant frequency. Mass changes deposited in the crystal surface can be monitored due to the change in its oscillation frequency.

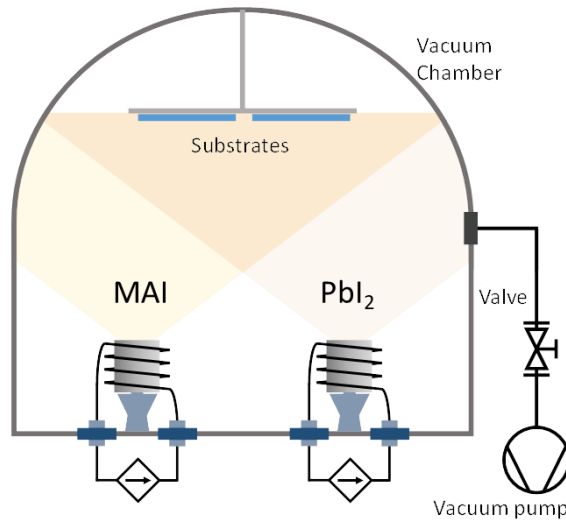


Figure 15. Schematic representation of a vacuum chamber with two thermal sources.

Prior to perovskite deposition, an initial calibration of each precursor material is performed to determine the tooling factor. The tooling factor is a correction for the difference in material deposited on the substrate versus the QCM due to the different source-to-substrate and source-to-QCM distance. A film of the corresponding material is deposited on a flat substrate recording the nominal thickness measured by the QCM with a previous tooling factor value (Tooling1). This nominal thickness is then compared to the real thickness determined using another technique, such as AFM, surface profilometry or cross-section SEM. The linear relationship provides the new tooling factor of the evaporation system (Tooling 2).

$$Tooling2 = Tooling1 \cdot \frac{thickness_{actual}}{thickness_{QCM}} \quad (4)$$

For a correct calibration, the material density (ρ), the acoustic impedance (or Z-ratio), and the tooling factor are required for the determination of the thickness and evaporation rate (measured in \AA s^{-1}) of the material being sublimated. The stoichiometry (chemical composition) of the deposited film is controlled by the ratio of the evaporation rates of the precursors, whereas the morphology of the deposited film can be controlled by the overall evaporation rate used.

The substrates are placed above the thermal sources (see Figure 15) and are held at room-temperature during perovskite deposition. This makes this deposition method compatible with plastic substrates.

The first deposition of thermally evaporated perovskite was demonstrated by Era *et al.* using dual source thermal evaporation.²⁰⁵ In 2013, Snaith *et al.*²⁰⁶ and Bolink *et al.*¹⁵² prepared the first planar $\text{MAPbI}_{3-x}\text{Cl}_x$ and MAPbI_3 perovskite solar cells, respectively, by dual-source thermal evaporation with an efficiency that exceeded 15%. The former reported a direct comparison between solution- and vacuum-deposited perovskite. In that study, the vacuum-deposited film showed a full coverage, extremely uniform and crystalline with crystal sizes of hundreds of nanometers, whereas the solution-processed film exhibited large variations in film thickness. In both cases, the diffraction pattern was identical, indicating that both techniques generated a similar perovskite.²⁰⁶ Bolink *et al.*¹⁵² implemented the perovskite layer between organic layers avoiding the high temperature required for sintering metal oxides (Al_2O_3 , TiO_2 or ZrO_2). In both cases, the perovskite films are extremely uniform and pinhole-free.

Currently, vacuum-deposited solar cells have reached efficiencies exceeding 20%, demonstrating the promise for real applications.²¹⁵⁻²¹⁷

Other vapour-based deposition techniques, such as closed space vapour transport (CSVST),²⁰⁷ chemical vapour deposition (CVD),²⁰⁸⁻²⁰⁹ flash

evaporation,²¹⁰⁻²¹² or atomic layer deposition (ALD),²¹³⁻²¹⁴ have been employed to prepare perovskite thin films used to built up photovoltaic devices.

Vacuum-deposition techniques have the following benefits:

- i. intrinsic purity of sublimed materials,
- ii. fine control over film thickness, stoichiometry and morphology,
- iii. compatibility with large areas,
- iv. intrinsically additive: multilayer devices can be fabricated without chemical modifications of the underlying layers or the use of orthogonal solvents,
- v. low substrate-fabrication temperature: compatible with plastic electronics and with inorganic solar cells in the form of tandem devices,
- vi. avoid of toxic solvents,
- vii. use of a consolidated technique widely adopted in the coating and semiconductor industry, such as organic light-emitting diodes (OLEDs), being mass produced in the form of fully evaporated devices.

3.1.3. Basic principles of the operation of solar cells

The operation of solar cells is determined by three processes: light harvesting, charge separation and charge transport and collection.

Light harvesting

A good light absorber material should have a direct band gap and high absorption coefficient. The band gap is determined by the composition of the semiconductor and the absorption coefficient depends on the material and on the wavelength of the light that is being absorbed. A semiconductor can only absorb photons whose energy is equal or higher than its band gap E_g . Photons with higher energy than E_g can excite electrons to energy levels above the conduction band (CB) and these electrons rapidly relax to the CB by releasing the extra energy as heat.

Charge separation

The photogenerated electron and hole must be dissociated to avoid recombination. Depending on the permittivity of the material, the charges will be attracted forming an exciton or free carriers. The degree of binding is determined by the exciton binding energy (E_b). Low exciton E_b (lower than the thermal energy at room temperature ($kT = 26$ meV)) are beneficial for having free electrons and holes that will contribute to the photocurrent. A broad range of low E_b values, from 2 meV to 62 meV at room temperature have been experimentally obtained for MAPbI₃. However, it is widely accepted that the species generated after photoexcitation in MAPbI₃ are free charges. The progression in the halide series from iodide to chlorine increases the E_b .²¹⁸⁻²¹⁹

Charge transport and collection

Once the charges are dissociated, the charges move within the semiconductor. To direct the flow of electrons and holes to the respective electrodes, a $p-n$ junction formed by joining n -type and p -type semiconductor materials or using charge selective layers (or charge transport layers) adjacent to the absorber are two different strategies. In this thesis, we will employ the latter one. The charge selective layers block one type of charges and transport the other one. Due to this fact, the layers are also referred as charge selective or extracting layers. These layers are fabricated with electron-blocking (hole transporting) and hole-blocking (electron transporting) materials, HTM and ETM, respectively. A schematic energy-level diagram with the absorber and the HTM and ETM is shown in Figure 16. The HOMO of the HTM and the LUMO of the ETM will be aligned with the VB and the CB of the absorber, respectively. This allows a good transport of holes and electrons, respectively. To block the electrons, the LUMO of the HTM is closer to vacuum compared with the CB of the absorber, and to block the holes, the HOMO of the ETM is further to vacuum compared with the VB of the absorber.

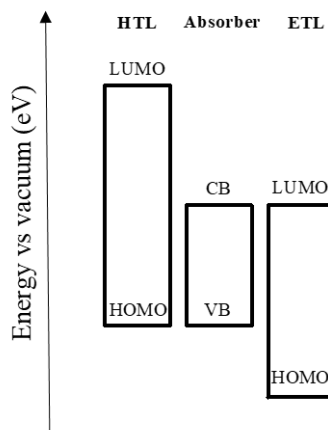


Figure 16. Schematic energy-level diagram with absorber and adjacent selective charge layers with adequate energy alignment with the absorber.

Despite the charges are directed towards the respective electrodes, charge recombination in the absorber occurs. Therefore, identifying the mechanism of recombination is important for increasing the device performance. The main types of mechanisms of recombination dominating in perovskites (Figure 17) are:²²⁰⁻²²¹

1. Monomolecular (or trap-assisted or trap-mediated) recombination

This mechanism (Figure 17a) involves the capture of an electron or a hole in a specific trap state and subsequently the non-radiative recombination with a hole (or electron). These trap states are energetic states whose energy level is in the band gap of the perovskite, and arise from defects or impurities in the crystal structure. They can be shallow or deep states, being shallow traps the most predominant type in perovskite.^{178, 222-224} It is highly dependent on the material processing.

2. Bimolecular recombination

This mechanism (Figure 17b) occurs between electrons and holes from direct band-to-band electron-hole recombination, from the relaxed state conduction band minimum (CBM) of CB1 to the valence band minimum (VBM) of the VB1 (CBM \rightarrow VBM) or states higher in the bands CB1 and VB1, respectively.

This can lead to emission of light, which can be re-absorbed by the material in a process called photon recycling.

3. Auger recombination

This mechanism (Figure 17c) involves at least three particles. The energy of an electron (or hole) is transferred to another electron (or hole) to allow non-radiative recombination with a hole (or electron). This mechanism bears little importance for photovoltaic applications as it requires a high light intensity (only obtained when light is focussed and thus amplified in so-called concentrated solar cells).

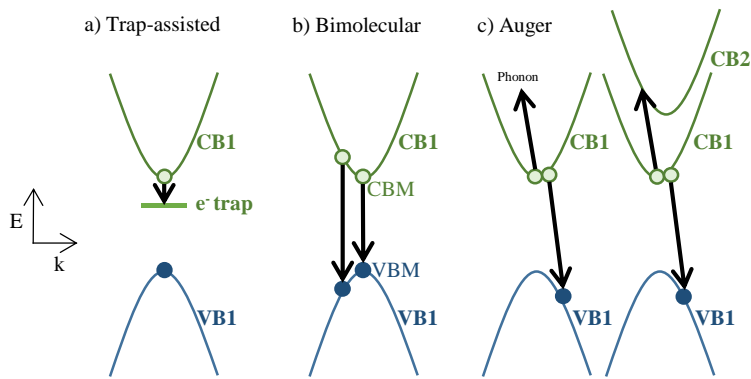


Figure 17. Schematic representation of the different recombination mechanisms active in perovskites. a) Trap-assisted recombination. b) Bimolecular recombination. c) Auger recombination. VB: valence band, CB: conduction band. Adapted from reference 221.

3.1.4. Characterization of solar cells

External quantum efficiency (EQE_{PV}) or incident photon-to-electron conversion efficiency (IPCE) is the fraction of incident photons that are converted to electrical current as a function of wavelength, and internal quantum efficiency (IQE) is the fraction of absorbed photons that are converted to electrical current as a function of wavelength. EQE_{PV} and IQE are related by the following expression:

$$IQE = \frac{EQE}{(1-R-T)} \quad (5)$$

where R and T are the reflectance and transmittance of the solar cell, respectively.

The efficiency of conversion of sun light into electrical power, also referred as power conversion efficiency (PCE or η), is defined as the ratio of the output electricity to the input energy of sunlight. In practice, the PCE of a solar cell is defined as the ratio of the maximum power output, P_{\max} , generated by the solar cell to the power input, P_{in} , based on the measurement of current density – voltage (J – V) curve (Figure 18).

$$PCE = \eta = \frac{P_{\max}}{P_{\text{in}}} = \frac{J_{\text{mpp}} \cdot V_{\text{mpp}}}{P_{\text{in}}} = \frac{J_{\text{sc}} \cdot V_{\text{oc}} \cdot FF}{P_{\text{in}}} \quad (6)$$

Where,

- J_{mpp} and V_{mpp} are the current density and voltage at the maximum power point (mpp)
- J_{sc} is the short-circuit current density. The current density through the terminals when the cell is operated at short circuit ($V = 0$ V)
- V_{oc} is the open-circuit voltage. The voltage across the output terminals when the cell is operated at open circuit ($J = 0$ mA cm⁻²)
- FF is the fill factor and is defined as the ratio of the maximum power point to the product of the open-circuit voltage and the short-circuit current density. Graphically, is the ratio of the areas of the two rectangles defined by J_{mpp} and V_{mpp} and by J_{sc} and V_{oc} .
- P_{in} is 100 mW cm⁻² for standard AM 1.5 G illumination.

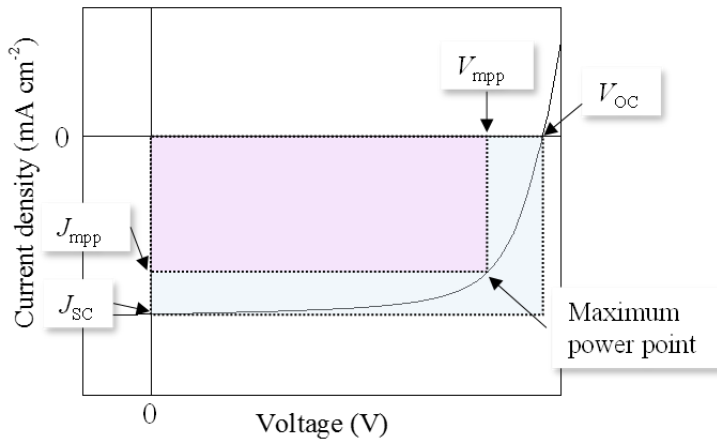


Figure 18. Typical J - V characteristics of a solar cell.

The V_{oc} depends on the band gap of absorber and is determined by the energy difference of the quasi-Fermi levels that are generated upon absorption of photons in the semiconductor (at solar illumination, these levels are very close to the CB and VB, respectively). The J_{sc} is a product of three aspects of efficiency: light harvesting, charge separation and charge collection.

Depending on the conditions of the measurements, the J - V curves exhibit hysteresis-like distortions between forward (negative to positive bias) and reverse (positive to negative bias) scans for some perovskite solar cells.²²⁵ This is an undesired feature and complicates the analysis of the devices. The presence of hysteresis denotes that the device performance is strongly affected by the measurement method. The origin and the presence/absence of this hysteretic phenomena have been widely debated. Although several explanations have been proposed in terms of ion migration,²²⁶⁻²²⁷ charge trapping/detrapping²²⁸⁻²²⁹ or ferroelectric polarization,²³⁰ this issue is still under debate.

The theoretical maximum power conversion efficiency attainable for a single junction solar cell depending on the band gap of the absorber is calculated in the detailed balance or Shockley - Queisser limit (Figure 19).²³¹

These calculations were performed for a cell operated at 298.15 K (25 °C) and under illumination by an AM 1.5G spectral irradiance according to ASTM G173-03 standard. The sun spectrum was approximated by the emission of a black body with a surface temperature (T_s) of 6000 K.

They assumed that in an ideal solar cell the only recombination path which cannot be reduced to zero is the radiative recombination. For the generation of electron-hole pairs it was assumed that photons with an energy below the energy band gap do not interact with the solar cell, while photons with an energy above the band gap are converted into electron-hole pairs with a quantum efficiency of 100%. For a material with a band gap of ~ 1.5 eV (MAPbI₃), a maximum theoretical efficiency of 31% can be attained.²³²⁻²³³

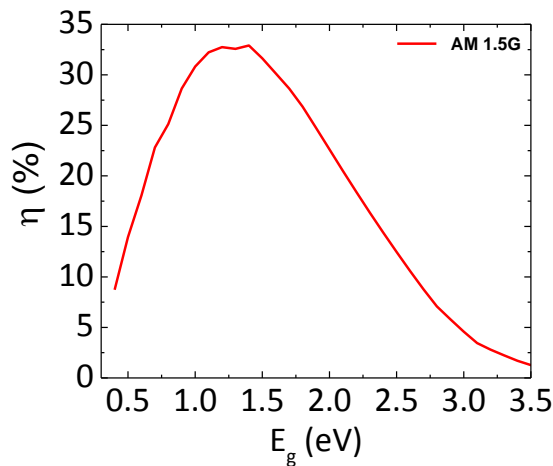


Figure 19. The maximum power conversion efficiency for a solar cell operated at 298.15 K and illuminated with an AM 1.5 G spectral irradiance (ASTM 173-03) in accordance with standard solar test conditions as a function of the band gap energy. Graph depicted from tabulated data from reference 234.

3.1.5. Perovskite solar cells

In a single-junction perovskite solar cell, the perovskite film is typically sandwiched between thin layers of charge transport materials, which efficiently extract photogenerated charges from the perovskite layer (Figure 16). As mentioned before, these films are hole transport layer (HTL, p -type) and electron transport layer (ETL, n -type). Each contact offers a potential barrier to

selectively allow the transport of the corresponding charges to the electrodes. The HTL/ETL layer will allow the transport of holes/electrons, whereas electrons/holes will be blocked. The choice of the proper HTL and ETL will take into account the diffusivity, chemical reactivity and energetic levels matching with perovskite.

Single junction PSCs architectures can be catalogued into two different categories depending on the sequence of functional layers in the device starting from the layer onto which light is incident, $p-i-n$ or $n-i-p$ (Figure 20).²³⁵ “ p ” and “ n ” are the hole and electron transport layers, respectively, and “ i ” is the perovskite layer. The $p-i-n$ (or “inverted”) structure (Figure 20a and 20b) is derived from organic solar cells or organic photovoltaics (OPV), where traditionally uses PEDOT:PSS at the front as hole transport layer and PCBM in the back side of the device as electron transport layer. The $n-i-p$ (or “regular”) structure (Figure 20c and 20d) has been transferred from dye sensitized solar cells (DSSC), where TiO_2 is the front electron transport layer and spiro-OMeTAD is the back hole transport layer. For both $p-i-n$ and $n-i-p$ configurations, the absorber layer is essentially intrinsic “ i ”.

Moreover, two different types of perovskite solar cells have been reported: mesoscopic and planar. In the former, a mesoscopic metal oxide scaffold is used, such as titanium oxide (TiO_2) or aluminium oxide (Al_2O_3) into which the perovskite is infiltrated (Figure 20a and 20d),²³⁶ whereas in the latter, a compact thin film of charge selective material is used (Figure 20b and 20c).

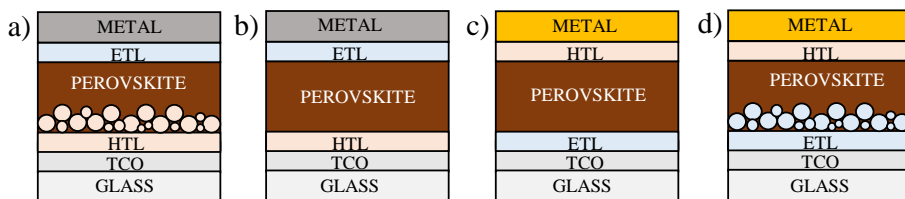


Figure 20. Schematic layout of single-junction perovskite solar cells. a) Mesoscopic and b) planar $p-i-n$ solar cells. c) Planar and d) mesoscopic $n-i-p$ solar cells. TCO: transparent conductive oxide, HTL: hole transport layer, ETL: electron transport layer.

3.1.6. State-of-the-art

In few years, perovskite solar cells have reached efficiencies similar to crystalline silicon solar cells, whose efficiencies exceed 26%.²³⁷ Up to date, the most efficient certified perovskite solar cells exhibit 22.1% in small cells (0.09 cm²),²³⁸ 19.7% in a 1 cm² cell²³⁸ and 12.1% in a 36.1 cm² module²³⁹ as well as a perovskite/Si monolithic tandem with efficiency of 23.6%.²⁴⁰ In terms of flexible solar cells, an efficiency exceeding 18% in an area of 0.1 cm² has been reported.²⁴¹ Perovskite solar cells eliminate the problems of high-cost manufacturing, heavyweight and rigidity of conventional silicon solar cells. Moreover, easy of fabrication, variety of processing and low-cost of the perovskite precursors makes perovskite as a promising material for optoelectronic applications.

However, the demonstration of highly efficient large-area devices and with flexible, lightweight substrates together with the toxicity and long-term stability are considerable concerns for their real applications. The transition to multi-component perovskite compounds with multi-cation/multi-halide composition has represented a breakthrough in device efficiency and stability.²⁴²⁻²⁴⁵ However, the replacement of lead by a non-toxic metal in perovskite solar cells is still a big challenge. These drawbacks open a new avenue for exploration of potentially low-toxic and long-term stable metal halide perovskite solar cells.

3.2. Improving light-harvesting efficiency in perovskite solar cells by effect of the absorber thickness

3.2.1. Introduction

Most of the perovskite solar cells that were reported in the first years after their emerging on the scene were using a mesoscopic metal-oxide electron-transport scaffold. These layers require a high-temperature processing and are therefore incompatible with plastic substrates.^{185, 246-249} Solar cells using a *p-i-n* (inverted) structure, where the perovskite was sandwiched between organic materials, avoiding the use of high temperature during device fabrication, are an alternative as reported by Bolink *et al.*¹⁵² In these devices, a MAPbI₃ film was vacuum-deposited between thin layers of charge selective materials, poly(3,4-ethylenedioxythiophene):poly(styrenesulfonic acid) (PEDOT:PSS) and poly(N,N'-bis(4-butylphenyl)-N,N'-bis(phenyl)benzidine (polyTPD) as hole transport materials and (6,6)-phenyl C₆₁-butyric acid methyl ester (PCBM) as the electron transport material. PolyTPD and PCBM were selected due to their ability to block electrons and holes, respectively, and the well aligned HOMO and LUMO energies with the VB and CB of the perovskite, respectively. The device exhibited an efficiency exceeding 12%, and showed hysteresis-free *J-V* characteristics with a *J*_{SC} of 16.12 mA cm⁻², a *V*_{OC} of 1.05 V and a FF of 67%, with a rather thin (285 nm) perovskite absorber. In view of the good photovoltaic performance, an in-depth study of the photovoltaic efficiency by modifying the perovskite thickness was performed. This should lead to an increase in the photocurrent obtained if the charge carrier diffusion length is sufficiently long. If the diffusion length of one of the charge carriers is below the absorber layer thickness, charge recombination will occur limiting the achievable photocurrent and reducing the open circuit voltage.

Depending on the type of perovskite and preparation method, very different charge diffusion lengths have been reported for MAPbI₃, from 100 to 1000 nm.^{139-140, 250} Assuming that the upper limit of 1 micrometer is valid,

thicknesses of the absorber layer reaching these values should be possible. Only a few studies on perovskite thickness dependence have been performed to determine the optimal thickness. These studies did not use perovskite films with thickness above 600 nm due to limitations in the perovskite fabrication via solution process²⁵¹ or PbI₂ vacuum-deposited and perovskite conversion after dipping in a CH₃NH₃I (MAI) solution.²⁵² These studies reported optimum J_{SC} at a perovskite layer thickness of ranging from 330 to 450 nm. One of the advantages of perovskite deposition by vacuum-deposition is the control over the layer thickness. Therefore, to extend the available layer thicknesses vacuum deposition was used to prepare perovskite layers with thicknesses ranging from 160 to 900 nm. These layers were implemented into *p-i-n* solar cells and the photovoltaic response was evaluated. It was demonstrated that the J_{SC} of the solar cells increases with increasing perovskite thickness up to 300 nm and more slowly for devices with 300 to 900 nm thick perovskite films. Due to the decrease of the FF for devices with perovskite layers exceeding 300 nm, the PCE is reduced for thicker devices. However, the partial oxidation of the polyTPD increasing its conductivity in cells with 900 nm perovskite thick film leads to the recovery of the FF and efficiency. Hence, similar efficiencies are reached with 300 nm than with 900 nm perovskite thin films. The maintenance of the efficiency demonstrates that with non-limiting organic layers, the solar cell performance is rather independent on perovskite layer thickness demonstrating that the charge carrier diffusion length is not limiting.

3.2.2. Experimental and methodology

Materials

All the chemicals and solvents were used as received. Poly(3,4-ethylenedioxythiophene):polystyrenesulfonate (PEDOT:PSS Clevios P VP Al 4083, aqueous dispersion, 1.3–1.7% solid content) was purchased from Heraeus. Poly[N,N'-bis(4-butylphenyl)-N,N'-bis(phenyl)benzidine (polyTPD) and [6,6]-phenyl C₆₁-butyric acid methyl ester (PCBM) were purchased from

American Dye Source and Solenne B. V., respectively. PbI_2 , AgSbF_6 and chlorobenzene were purchased from Sigma Aldrich. $\text{CH}_3\text{NH}_3\text{I}$ was synthesized before each set of experiments following the procedure previously reported.²⁵³ In brief, $\text{CH}_3\text{NH}_3\text{I}$ was synthesized by reacting 26 mL of methylamine (40 wt.% in water, Sigma Aldrich) and 10 mL of hydroiodic acid (57 wt.% in water, Sigma Aldrich) in a 250 mL round-bottomed flask at 0 °C for 2 h under magnetic stirring. The white precipitate was recovered by evaporation at 50 °C for 1 h. The product was dissolved in ethanol (Sigma Aldrich), filtered and recrystallized from diethyl ether (Sigma Aldrich) and dried at 70°C in an oven for 24 h. The photolithography-patterned indium tin oxide (ITO) ($15 \Omega \square^{-1}$) glass substrates were purchased from Naranjo Substrates (www.naranjosubstrates.com).

Perovskite deposition

The perovskite precursors (PbI_2 and $\text{CH}_3\text{NH}_3\text{I}$) were contained in ceramic crucibles placed in CreaPhys evaporation sources and were heated to their corresponding sublimation temperature at a base pressure of 1×10^{-6} mbar. The substrates were placed at 20 cm from the top of the ceramic crucibles (Figure 15). A shutter was present below the substrate holder, which was kept closed until the adequate $\text{PbI}_2:\text{CH}_3\text{NH}_3\text{I}$ ratio was achieved. The calibration of the evaporation rate for the $\text{CH}_3\text{NH}_3\text{I}$ was found to be difficult due to non-uniform layers and the soft nature of the material, which impeded accurate thickness measurements. Hence, the source temperature of the $\text{CH}_3\text{NH}_3\text{I}$ was kept constant at 70 °C and once the sensor reading was stable, PbI_2 was heated. The $\text{PbI}_2:\text{CH}_3\text{NH}_3\text{I}$ ratio was controlled off line using grazing incident X-ray diffraction by adjusting the PbI_2 deposition temperature. The optimum deposition temperatures were found to be 250 °C for PbI_2 and 70 °C for $\text{CH}_3\text{NH}_3\text{I}$. The process was followed by three QCM sensors placed in the chamber, two for monitoring the thickness/evaporation rate of the perovskite precursors and one for monitoring the thickness/evaporation rate of the

perovskite deposition. Up to 5 substrates can be coated with the perovskite in one single co-evaporation step.

Fabrication of perovskite solar cells

In this work, vacuum-deposited MAPbI₃ thin films were implemented into *p-i-n* solar cells with the following layout: ITO/PEDOT:PSS/polyTPD/MAPbI₃/PCBM/Au (Figure 21a) and ITO/PEDOT:PSS/doped-polyTPD/MAPbI₃/PCBM/Au (Figure 21b).

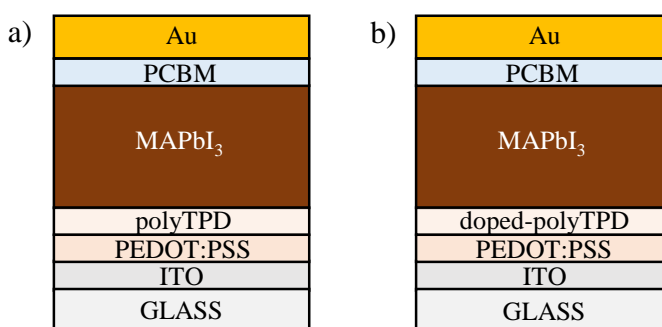


Figure 21. Scheme of the device layouts studied in this thesis a) ITO/PEDOT:PSS/polyTPD/MAPbI₃/PCBM/Au and b) ITO/PEDOT:PSS/doped-polyTPD/MAPbI₃/PCBM/Au.

The solar cells were prepared as follows: the pre-patterned ITO substrates were subsequently cleaned by 5-minute sonication steps in water-soap, water and 2-propanol baths, in that order. After drying, the substrates were placed in a UV-ozone cleaner (Jelight 42-220) for 20 minutes. A 80 nm thick film of PEDOT:PSS was spin-coated at 1200 rpm for 30 s onto the clean ITO substrates and thermally annealed at 150 °C during 15 min. The PEDOT:PSS was added from a syringe and filtered with a polypropylene (PP) filter with a 0.45 μm pore size. This layer smoothens the ITO, increases the device yield and acts as hole transport layer. Then, a 20 nm thick film of polyTPD or doped-polyTPD was deposited from a chlorobenzene solution (7 mg mL⁻¹) incorporating 0.05 molar % in AgSbF₆ in the case of doped-polyTPD solution. Both of them were deposited from a syringe and filtered with a polytetrafluoroethylene (PTFE) 0.22 μm pore size filter and spin-coated at 3000

rpm for 30 s. Then, the devices were transferred inside a vacuum chamber (MBRAUN) integrated into the inert atmosphere glovebox (<0.01 ppm O_2 and <0.1 ppm H_2O). Perovskite layers were vacuum-deposited with different thicknesses ranging from 210 to 900 nm. (See section of perovskite deposition for a more detailed procedure). After perovskite deposition, the samples were finished with 20 nm thick film of PCBM deposited using a meniscus coater and a coating speed of 2.5 mm s^{-1} . Finally, a film of 60 nm of gold was thermally evaporated as a top electrode using a shadow mask under vacuum ($< 1 \times 10^{-6}$ mbar) with an Edwards Auto500 evaporator integrated into the glovebox. The active area of the cells were 0.06 cm^2 and typically 4 cells are present on each substrate. The devices were not encapsulated and were characterized inside the glovebox at room temperature.

Characterization of perovskite solar cells

Absorption measurements were done using a fibre optics based Avantes Avaspec 2048 spectrometer. All layer thickness was measured with a mechanical profilometer (Ambios XP1). The perovskite films were characterized by using grazing incidence X-ray diffraction (GIXRD) after its evaporation. The measurements were done at room temperature in the 2θ range 5° – 50° on an Empyrean PAN analytical powder diffractometer, using Cu K α radiation. Typically, four repeated measurements were collected and merged into a single diffractogram.

Current density – voltage (J – V) curves and the EQE_{PV} were recorded in a MiniSun simulator by ECN the Netherlands. The EQE_{PV} was estimated using the cell response at different wavelength (measured with a white-light halogen lamp in combination with band-pass filters). During J – V measurements, the devices were illuminated by a white-light halogen lamp and using a mask overlaying the sample which only illuminated the active area of the cells. Before each measurement, the exact light intensity was determined using a calibrated Si reference diode equipped with an infrared cut-off filter

(KG-3, Schott). An estimation of the J_{SC} under standard test conditions was calculated by convoluting the EQE_{PV} spectrum with the AM1.5G reference spectrum, using the premise of a linear dependence of J_{SC} on light intensity. The J - V curves were measured using a Keithley 2400 source measure unit. The scan was performed with steps of 0.01 V starting from -0.2 to 1.1 V with a time delay between each point set of 0.01 s. Light intensity dependence measurements were done by placing 0.1, 1, 10, 20, 50% neutral density filters (LOT-QuantumDesign GmbH) between the light source and the device. All the characterizations, except the UV-Vis absorption spectra, X-ray diffraction and profilometer measurements, were performed in a nitrogen-filled glovebox (<0.01 ppm O_2 and <0.1 ppm H_2O) without exposure to ambient.

3.2.3. Results and discussion

The optical properties and crystallinity of the vacuum-deposited $MAPbI_3$ films with different thicknesses were characterized to evaluate their suitability as light absorbers prior to their implementation into solar cells. The percent absorption of the perovskite films with different thicknesses deposited on glass are depicted in Figure 22.

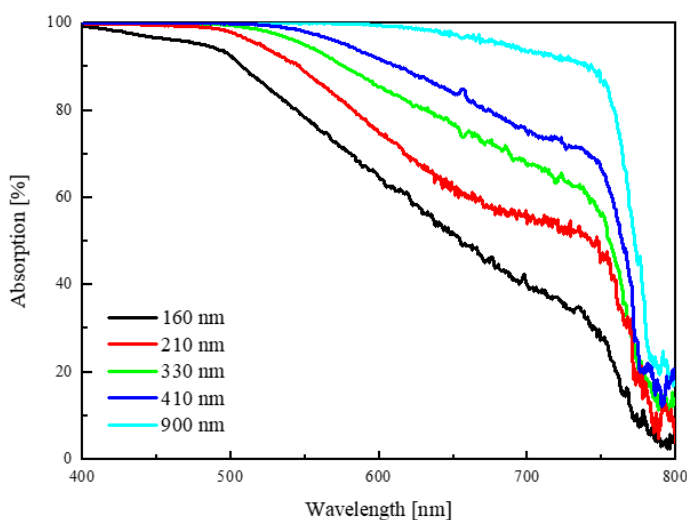


Figure 22. Percent absorption spectra of vacuum-deposited $MAPbI_3$ films with thicknesses ranging from 160 to 900 nm.

All films showed an absorption onset at 790 nm, in good agreement with the band gap value of ~ 1.5 eV reported for MAPbI₃.^{170, 254-255} The absorption in percentage increases almost linearly with the perovskite film thickness. Notably, a single pass of the light (at 760 nm) through the thinner film of the series (210 nm) leads to more than 30% absorption whereas the thicker film (900 nm) absorbs almost 90%.

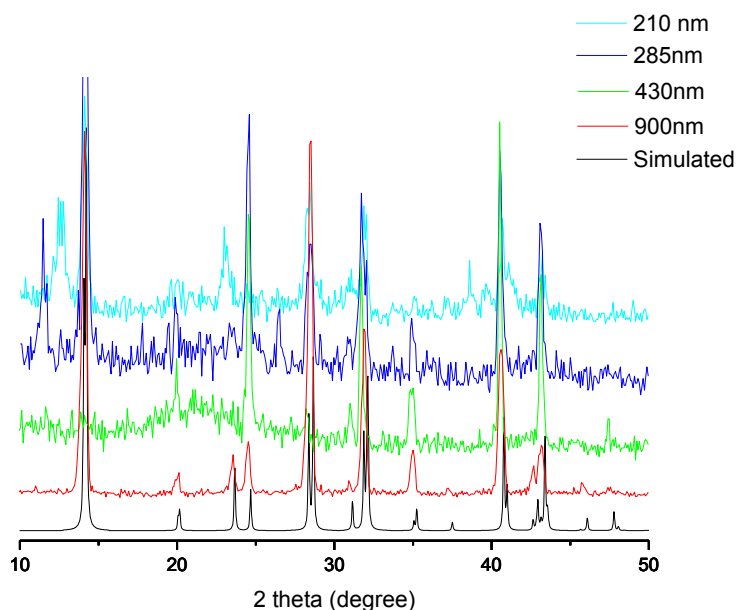


Figure 23. X-ray diffraction patterns of perovskite layers with different layer thicknesses.

The X-ray diffraction patterns of perovskite layers from 210 to 900 nm are depicted in Figure 23. The typical peaks corresponding to the MAPbI₃ perovskite tetragonal structure appears at 2θ values of 14.1, 28.4, 31.9, 40.6 and 43.2° assigned to the (110), (220), (310), (224) and (330) planes, respectively. Minor peaks also appear at 2θ values of 19.9, 23.5, 24.5 and 34.9° related to the (200), (211), (202) and (312) planes. However, slight variation in the diffraction patterns between different perovskite films are observed. Nowadays, it is known that the perovskite is tolerant to slight compositional variations.²⁵⁶⁻²⁵⁷ Therefore, given the good properties of the vacuum-deposited perovskite thin films, they were implemented into *p-i-n* solar cells.

A set of *p-i-n* solar cells with the layout ITO/PEDOT:PSS/polyTPD/MAPbI₃/PCBM/Au were fabricated (see Figure 21a). In brief, 80 nm thick film of PEDOT:PSS and 20 nm thick film of polyTPD were spin-coated on top of a pre-patterned ITO contact. In the following, the MAPbI₃ perovskite layer was vacuum-deposited with thicknesses ranging from 210 to 900 nm. On top of the perovskite layers, a layer of 20 nm of PCBM was deposited and the devices were finished by thermally evaporating 60 nm of Au. The energy-level diagram of the device and a cross-section SEM image of a device with 900 nm perovskite thick film are shown in Figure 24. In Figure 24a, a mismatch in the energy levels of the PCBM layer and the metal contact (Au) can be observed in the energy level diagram, but the formation of a strong interface dipole layer between PCBM and Au reduce the extraction barrier.²⁵⁸ The cross-section SEM image was obtained by collaboration with Dr. Eran Edri from Weizmann Institute of Science, Israel. The cross-section SEM image (Figure 24b) shows the growth of the perovskite layer, as a planar, pin-hole free and compact film. All the layers, except the thin blocking layers are visible. In this *p-i-n* structure, the ITO acts as anode and hole-collecting contact, whereas the Au is the cathode and top electron-collecting electron. Au was selected as its superior performing and more stable devices compared to other devices employing other top contact electrodes.

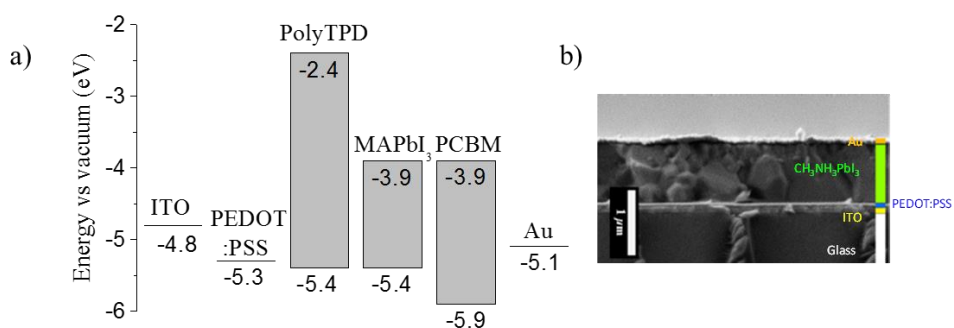


Figure 24. a) Flat band energy level diagram. b) Cross-section SEM of a device with 900 nm perovskite thick film (in collaboration with Weizmann Institute of Science, Israel).

The J - V curves for the perovskite solar cells with increasing perovskite film thickness were measured under 1 sun illumination (100 mW cm^{-2}) and the key parameters were extracted and summarizes graphically in Figure 25 and in Table 3.

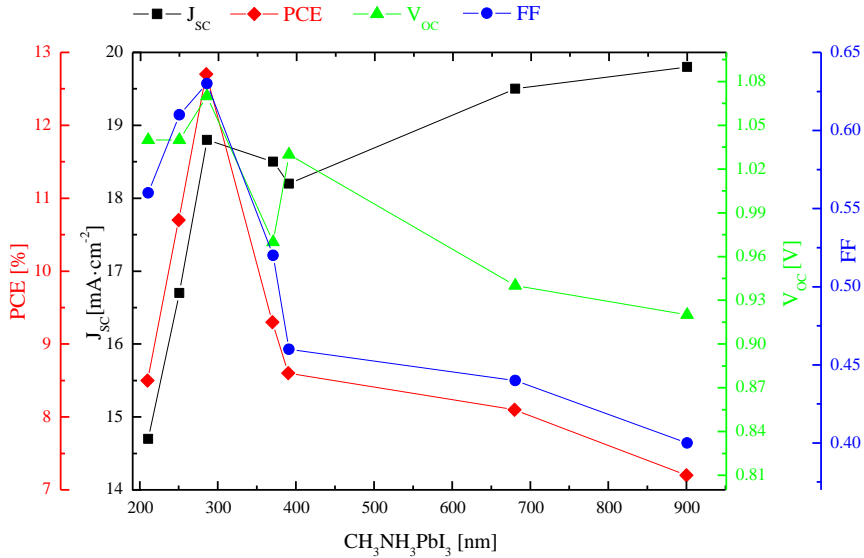


Figure 25. Thickness dependence of the photovoltaic parameters (J_{sc} , V_{oc} , FF and PCE) extracted from their respective J - V curves.

In Figure 25 it can be observed that there is a significant gain in photocurrent generation due to increased light absorption when going from 200 to 400 nm perovskite thickness and continues to increase slowly up to 900 nm thick perovskite film. The increase in J_{sc} in devices from 400 to 900 nm is 5%, whereas 25% more light is absorbed in the perovskite layer (see Figure 22). It seems that the absorption efficiency is enhanced in thicker devices whereas the collection efficiency is reduced. The V_{oc} remains constant for devices with perovskite thickness from 200 to 400 nm and decreases by nearly 10% for devices with thicker perovskite layer. The FF is the main parameter that is negatively affected by the increase of the perovskite thickness. The FF drops strongly for devices with a perovskite layer thickness exceeding 300 nm. As a

result of this strong decrease in the FF, the PCE is also negatively affected decreasing with perovskite layer thicknesses.

Table 3. Key parameters extracted from J - V curves of p - i - n devices with perovskite thickness from 210 to 900 nm.

CH ₃ NH ₃ PbI ₃ [nm]	J_{SC} [mA cm ⁻²]	V_{OC} [V]	FF [%]	PCE [%]
210	14.7	1.04	56	8.6
250	16.7	1.04	61	10.6
285	18.8	1.07	63	12.7
370	18.5	0.97	52	9.3
390	18.2	1.03	46	8.6
680	19.5	0.94	44	8.1
900	19.8	0.92	40	7.2
900*	19.5	0.94	65	12.0

*Doped-polyTPD.

When the incident light is reduced in a device with a thick perovskite layer (400 nm) (see Table 4), the FF improves from 49% (1 sun illumination) to 61% (0.01 sun illumination) reaching similar values to the best (thin perovskite layer) devices (FF = 63% for device with 285 nm perovskite thick film). Therefore, at lower illumination intensity, lower charge carrier densities are photogenerated and the FF increases. This highlights the high quality of the perovskite layer indicating that the level of traps is low, yet the limiting factor is the efficiency of charge extraction. This is likely due to the difference in the hole mobility in the polyTPD layer compared to that in the perovskite layer. Typically, organic semiconductors, such as spiro-OMeTAD, polyhexylthiophene (P3HT) or other polymer derivatives exhibit much lower hole mobility (in the range of 10^{-7} to $1 \text{ cm}^2 \text{ V}^{-1} \text{ s}^{-1}$) than MAPbI₃.²⁵⁹

Table 4. FF values of a device with 400 nm perovskite thick film at different % of light intensity illumination.

1 Sun intensity illumination [%]	FF [%]
100	48.7
50	52.6
20	55.9
10	58.6
1	63.4

From previous experience in organic light-emitting diodes (OLEDs), it is known that the conductivity of the polyTPD layer increases superlinearly when it is partially oxidized (doped-polyTPD).²⁶⁰ However, high doping levels may hamper the layer's ability to block electrons. In this study, in order to enhance the charge extraction, we replaced the pristine polyTPD with a slightly oxidized polyTPD (0.05 % oxidized with AgSbF₆). A *p-i-n* solar cell with a 900 nm thick perovskite film was fabricated with the layout: ITO/PEDOT:PSS/doped-polyTPD/MAPbI₃/PCBM/Au (Figure 21b).

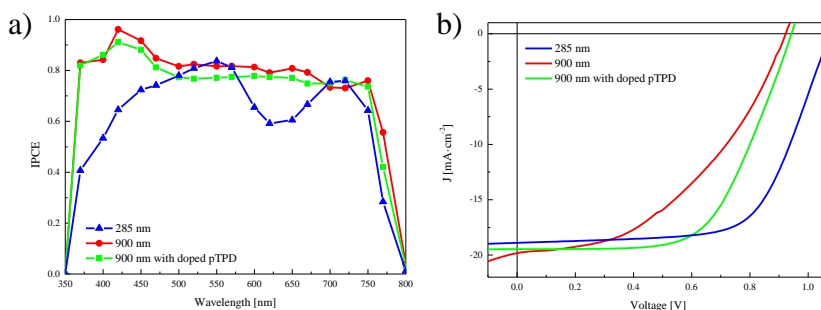


Figure 26. a) IPCE and b) J - V -curves of ITO/PEDOT:PSS/polyTPD/MAPbI₃/PCBM/Au devices with 285 and 900 nm perovskite thickness and ITO/PEDOT:PSS/polyTPD/MAPbI₃/PCBM/Au with 900 nm perovskite thickness.

The EQE spectra and J - V curves of the devices with 285 and 900 nm layer of perovskite are shown in Figure 26. An increased in the EQE spectra in the region of 350 to 500 nm is observed by increasing in the device the perovskite thickness from 285 nm to 900 nm (Figure 26a). At the same perovskite film thickness of 900 nm, a device with partially oxidized polyTPD showed an enhanced FF, similar V_{OC} and J_{SC} compared with the device with the

undoped polyTPD (Figure 26b). Due to the enhanced PV characteristics of the device with 900 nm thick film of perovskite, it reaches similar efficiencies than the most efficient device of the series, 12.7% for 285 nm thick film perovskite and 12.0% for the 900 nm thick film perovskite with doped-polyTPD layer. The effect of the doped polyTPD layer on cells employing a thinner perovskite layer was also studied but the effect was negligible. This is an example of the high electronic quality of organic-inorganic lead halide perovskite materials. As explained in the introduction of this chapter, long diffusion lengths have been reported for solution-processed MAPbI₃ perovskites. As these values depend on the preparation method, this study is a demonstration of long diffusion lengths in vacuum-processed MAPbI₃ perovskites reaching high efficiency with 900 nm absorber thick film.

3.2.4. Conclusions

To optimize the absorber (MAPbI₃ perovskite) thickness, in this work a series of methylammonium lead iodide perovskite solar cells with a *p-i-n* structure have been prepared with a wide range of active layer thicknesses. The device layout was ITO/PEDOT:PSS/(doped-)polyTPD/MAPbI₃/PCBM/Au. With undoped hole transport layers, the best performance was obtained for solar cells with 300 nm perovskite thick film, reaching a PCE of 12.7%. The efficiency was negatively affected for devices with thicker perovskite thin films of 900 nm with a PCE of 7.2%. However, if the hole transport material (polyTPD) was slightly doped, the device with a perovskite layer thickness of 900 nm reached a PCE of 12%, only slightly below that of the best device of the series with a perovskite layer thickness of 300 nm.

These results demonstrate that the photogenerated charges in perovskite do not suffer from significant recombination losses even in such very thick layers, corroborating long carrier diffusion lengths. Therefore, in this study we demonstrate that the solar cell performance is almost independent on perovskite layer thickness in the range of 300 to 900 nm.

3.2.5. Contributions of the author

Article. **Momblona, C.**; Malinkiewicz, O.; Roldán-Carmona, C.; Soriano, A.; Gil-Escrig, L.; Bandiello, E.; Scheepers, M.; Edri, E.; Bolink, H. J., Efficient methylammonium lead iodide perovskite solar cells with active layers from 300 to 900 nm. *APL Materials* **2014**, 2 (8), 081504. (IF: 4.335, Q1).

IF = Impact factor (Science Citation Reports, Web of Science), Q = Quartile.

3.3. Highly efficient and fully vacuum-deposited *p-i-n* and *n-i-p* perovskite solar cells

3.3.1. Introduction

Perovskite thin films are typically sandwiched between thin layers of charge transport materials, which ideally only allow one type of carrier to pass. Understanding the properties and limitations of these selective layers is of great importance for the development of highly efficient solar cells. The charge transport layers should have the following characteristics:²⁵⁹ a) suitable band alignment with the perovskite allowing the transport of one carrier while blocking the other, 2) sufficient charge carrier mobilities, 3) homogeneous film formation generating full and intimate contact with the perovskite, 4) sufficient thermal, photo, and chemical stability (also against reactions with the perovskite) and 5) optical transparency to prevent parasitic absorption of sunlight. It was reported that the charge extraction layers are the major limiting factors of perovskite solar cells.²⁶¹ In order to enhance the charge extraction, several approaches have been reported, such as the use of thinner extraction layers or enhancing the conductivity of the charge transport layers through partial oxidation or reduction (referred to as doping). Inorganic charge transport layers, such as TiO₂ or ZnO, can be doped with lithium salts^{247, 262} or other metal ions²⁶³⁻²⁶⁷ leading to an enhanced conductivity. An alternative strategy to increase the conductivity of the charge extraction layers is the use of doped organic semiconductors. The use of molecular dopants reduces the tendency to diffuse in the organic semiconductor compared to halides and alkali metals. By doping an evaporated organic layer with a molecular dopant, using co-evaporation, the conductivity of the layer can be varied over several orders of magnitude by varying the doping concentration. These dopants typically evaporate at a suitable temperature range between 100 and 400 °C in vacuum and enable more stable doping. These molecular dopants have been widely

studied for organic light-emitting diodes (OLEDs) and organic solar cells (OPVs).

In this work, we have selected 2,2'-(perfluoronaphthalene-2,6-diylidene) dimalononitrile (F₆-TCNNQ) as the molecular dopant (*p*-dopant) for the hole transport material N4,N4,N4'',N4''-tetra([1,1'-biphenyl]-4-yl)-[1,1':4',1''-terphenyl]-4,4''-diamine (TaTm) and N1,N4-bis(tri-*p*-tolylphosphoranylidene) benzene-1,4-diamine (PhIm) as the dopant (*n*-dopant) for the electron transport material (C₆₀) because of their possibility to be sublimated.

Most of the solar cells using a vacuum-deposited perovskite layer employ charge transport layers processed from solution.^{152, 206, 268-269} Polander *et al.* demonstrated a fully vacuum-deposited cell, for which high open-circuit voltages V_{OC} of 1.1 V were obtained, using a doped HTM and undoped ETL in the device layout.²⁷⁰ The most efficient fully vacuum-deposited perovskite solar cell until the publication of the results of the work developed in this thesis was 15.4% exhibiting high hysteresis between the forward and reverse scan of the *J-V* curves. In that report the perovskite layer was sandwiched between two undoped organic molecules functioning as charge extraction layers.²⁷¹⁻²⁷²

In this part of the thesis, fully vacuum-deposited planar perovskite solar cells, with a similar structure to that reported by our team mentioned above, that is, the MAPbI₃ perovskite layer is deposited between two charge extraction layers, is presented. Each charge extraction layer is composed by a thin layer of a pristine organic semiconductor acting as charge transport layer and a thicker layer consisting of the same semiconductor material that are partially oxidized (in the case of the hole transporter) or reduced (in the case of the electron transport layers) by its respective *p*- and *n*-dopant. This multilayer stack has been prepared in planar-type solar cells both with the *p-i-n* and *n-i-p* architectures allowing for the first time a direct comparison between these two device types. In the following part of the thesis, the role and effect of the undoped and doped layers on the device performance is described. This study

highlights the unprecedented high power conversion efficiencies exceeding 16.5% and 20% obtained for vacuum-deposited MAPbI₃-based *p-i-n* and *n-i-p* solar cells, respectively, which is among the highest efficiencies reported for MAPbI₃-based solar cells.^{217, 273-275}

3.3.2. Experimental and methodology

Materials

All the chemicals and solvents were used as received. 2,2'-(perfluoronaphthalene-2,6-diylidene) dimalononitrile (F₆-TCNNQ), N₄,N₄,N₄'',N₄''-tetra([1,1'-biphenyl]-4-yl)-[1,1':4',1''-terphenyl]-4,4''-diamine (TaTm) and N1,N4-bis(tri-*p*-tolylphosphoranylidene)benzene-1,4-diamine (PhIm) were obtained from Novaled GmbH. Fullerene (C₆₀) was purchased from Sigma Aldrich. PbI₂ was purchased from Tokyo Chemical Industry CO (TCI), and CH₃NH₃I (MAI) from Lumtec. The photolithography-patterned indium tin oxide (ITO) (15 Ω □⁻¹) glass substrates were purchased from Naranjo Substrates.

Fabrication of perovskite solar cells.

Two different planar-type *p-i-n* and *n-i-p* solar cells were fabricated with the structures: ITO/TaTm:F₆-TCNNQ/TaTm/MAPbI₃/C₆₀/C₆₀:PhIm/Ag (Figure 27a) and ITO/C₆₀:PhIm/C₆₀/MAPbI₃/TaTm/TaTm:F₆-TCNNQ/Au (Figure 27b). For clarity, the TaTm:F₆-TCNNQ layer will be referred in the text as *p*-HTL and the C₆₀:PhIm layer will be referred as *n*-ETL.

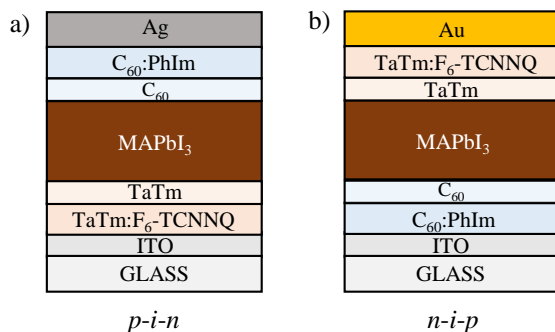


Figure 27. Scheme of the a) *p-i-n* and b) *n-i-p* devices studied in this work.

The devices were prepared as follows. ITO-coated glass substrates were subsequently cleaned with soap, water and isopropanol in an ultrasonic bath, 5 minutes each, followed by 20 minutes of UV-ozone treatment. Then, the substrates were transferred to a vacuum chamber integrated into a nitrogen-filled glovebox (MBRAUN, H₂O and O₂ < 0.1 ppm) and evacuated to a pressure of 1×10^{-6} mbar. The vacuum chamber is equipped with six temperature controlled evaporation sources (Creaphys) fitted with ceramic crucibles. The sources were directed upwards with an angle of approximately 90° with respect to the bottom of the evaporator. The substrate holder to evaporation sources distance is approximately 20 cm. Three QCM sensors are used, two monitoring the deposition rate of each evaporation source and a third one close to the substrate holder monitoring the total deposition rate. Prior to do co-deposition, for thickness calibration, we first individually sublimed the charge transport materials and their dopants (TaTm and F₆-TCNNQ, C₆₀ and PhIm). A calibration factor (tooling factor) was obtained by comparing the thickness inferred from the QCM sensors with that measured with a mechanical profilometer (Ambios XP1). Once the tooling factor was determined, these materials were co-sublimed at temperatures ranging from 135–160 °C for the dopants to 250 °C for the pure charge transport molecules, and the evaporation rate was controlled by separate QCM sensors and adjusted to obtain the desired doping concentration. For doping concentration optimization, the deposition rate for TaTm and C₆₀ was kept constant at 0.8 \AA s^{-1} while varying the

deposition rate of the dopants during co-deposition. This method allows for a precise control of the ratios of each molecule in the sublimed film by carefully monitoring the evaporation rate using QCM sensors during the evaporation process. Pure TaTm and C₆₀ layers were deposited at a rate of 0.5 Å s⁻¹.

For the *p-i-n* configuration (Figure 27a), 40 nm of the *p*-HTL (TaTm:F₆-TCNNQ) capped with 10 nm of the pure TaTm were deposited. On the other hand, for the *n-i-p* configuration (Figure 27b), 40 nm of the *n*-ETL (C₆₀:PhIm) capped with 10 nm of the pure C₆₀ were deposited.

Once completed the deposition of the respective charge selective contacts, the chamber was vented with dry N₂ to replace the *p*-HTL or *n*-ETL crucibles, respectively, with those containing the starting materials for the perovskite deposition, PbI₂ and CH₃NH₃I. The vacuum chamber was evacuated again to a pressure of 1 × 10⁻⁶ mbar, and the perovskite films were deposited by co-deposition of the two precursors (Figure 27). The calibration of the deposition rate for the CH₃NH₃I was found to be difficult due to non-uniform layers and the soft nature of the material, which impeded accurate thickness measurements. Hence, the source temperature of the CH₃NH₃I was kept constant at 70 °C and the CH₃NH₃I:PbI₂ ratio was controlled off line using grazing incident x-ray diffraction by adjusting the PbI₂ deposition temperature. The optimum deposition temperatures were found to be 250 °C for PbI₂ and 70 °C for CH₃NH₃I. After deposition of a 500 nm thick perovskite film, the chamber was vented and the crucibles replaced with those containing C₆₀ and PhIm, or TaTm and F₆-TCNNQ and evacuated again to a pressure of 1 × 10⁻⁶ mbar. The devices were completed by depositing a 10 nm thick film of pure C₆₀ and a 40 nm thick film of the *n*-ETL (C₆₀:PhIm) (*p-i-n*, Figure 27a) or 10 nm thick film of pure TaTm and a 40 nm thick film of *p*-HTL (TaTm:F₆-TCNNQ) (*n-i-p*, Figure 27b). This process of exchanging crucibles was done to evaluate the effect of changes in the type of charge selective contact for an identical perovskite layer. In one evaporation run, we can prepare 5 substrates (3 by 3 cm²) each containing 4 cells. Generally, one substrate was reserved for a

reference configuration allowing to evaluate 4 variations in the transport layers per perovskite evaporation. It is also possible to prepare the complete stack without breaking vacuum as we have 6 sources available. Finally, the substrates were transferred to a second vacuum chamber where the metal top contact (100 nm thick) was deposited, Ag for the *p-i-n* (Figure 27a) and Au for the *n-i-p* devices (Figure 27b).

Characterization of perovskite solar cells.

The perovskite thin films were characterized as follows. Grazing incident X-ray diffraction (GIXRD) patterns were collected in air at room temperature on an Empyrean PANalytical powder diffractometer using the Cu K α 1 radiation. Typically, three consecutive measurements were collected and averaged into a single spectra. Cross-section Scanning Electron Microscopy (SEM) images were performed on a Hitachi S-4800 microscope operating at an accelerating voltage of 2 kV over Platinum-metallized samples. Absorption spectra were collected in air using a fiber optics based Avantes Avaspec2048 Spectrometer.

The characterization of the solar cells was performed as follows. The EQE_{PV} was estimated using the cell response at different wavelengths (measured with a white-light halogen lamp in combination with band-pass filters), where the solar spectrum mismatch is corrected using a calibrated Silicon reference cell (MiniSun simulator by ECN, the Netherlands). The *J-V* characteristics were obtained using a Keithley 2400 source measure unit and under white light illumination, and the J_{SC} was corrected taking into account the device EQE_{PV}. The electrical characterization was validated using a solar simulator by Abet Technologies (model 10500 with an AM1.5G xenon lamp as the light source). Before each measurement, the exact light intensity was determined using a calibrated Si reference diode equipped with an infrared cut-off filter (KG-3, Schott). Importantly, no difference in the *J-V* characteristics was observed as a function of evaluation method. The *J-V* curves were

recorded between -0.2 and 1.2 V with 0.01 V steps, integrating the signal for 20 ms after a 10 ms delay. This corresponds to a speed of about 0.3 V s $^{-1}$. The devices layout has four equal areas (0.0653 cm 2 , defined as the overlap between the ITO and the top metal contact) and measured through a shadow masks with 0.01 cm 2 aperture. For hysteresis study, different scan rates (0.1 , 0.5 and 1 V s $^{-1}$) were used, biasing the device from -0.2 to 1.2 V with 0.01 V steps and *vice versa*. Light intensity dependence measurements were done by placing 0.1 , 1 , 10 , 20 and 50% neutral density filters (LOT-QuantumDesign GmbH) between the light source and the device.

3.3.3. Results and discussion

A single layer of 500 nm of MAPbI $_3$ was deposited in vacuum on top of glass and the crystallinity, morphology and optical properties were characterized (Figure 28). The XRD pattern (Figure 28a) shows the typical peaks of the tetragonal phase of MAPbI $_3$ with the main peaks at 2θ values of 14.1 and 28.4° attributed to the (110) and (220) planes. The top-view SEM image (Figure 28b) shows a pinhole-free and compact film with crystal grains with grain size around 100 nm. The UV-Vis absorption spectrum (Figure 28c) exhibits an absorption onset around 790 nm corresponding to the reported band gap of 1.55 eV.^{170, 254-255}

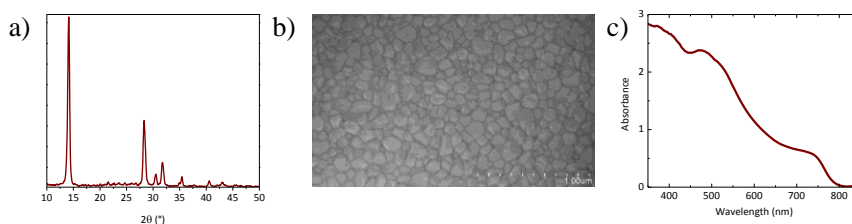


Figure 28. a) XRD diffraction pattern, b) top-view SEM image and c) UV-Vis spectrum of 500 nm thick film of MAPbI $_3$ deposited on top of glass.

The vacuum-deposited MAPbI₃ was implemented into *p-i-n* solar cells, employing the simplest structure of the perovskite layer sandwiched between single thin films (10 nm) of hole and electron extraction molecules (without any molecular dopant): ITO/TaTm/MAPbI₃/C₆₀/Ag. The photovoltaic response under 1 sun illumination is rather poor (Figure 29), showing a pronounced s-shape in the *J-V* curve, leading to poor FF and hence low PCE values. This indicates that the charge carrier extraction is severely hindered, either due to the high resistance of the organic charge transport layers or to the presence of an extraction barrier at the electrode interfaces.

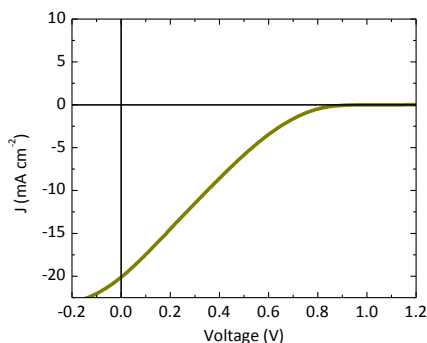


Figure 29. *J-V* curve of the *p-i-n* device with the layout ITO/TaTm/MAPbI₃/C₆₀/Ag illuminated under 1 sun illumination (100 mW cm⁻²).

Optimization of dopant concentration in p-i-n devices

To reduce the series resistance in the device and to ensure an ohmic contact between them and the electrodes, a partially oxidized HTL (*p*-HTL) and reduced ETL (*n*-ETL) was implemented in the previous layout by co-evaporation of the charge transport molecule with a dopant between the pure HTL or ETL and the electrode. Figure 30 shows the *p-i-n* device structure and the energy-level diagram of the stack.

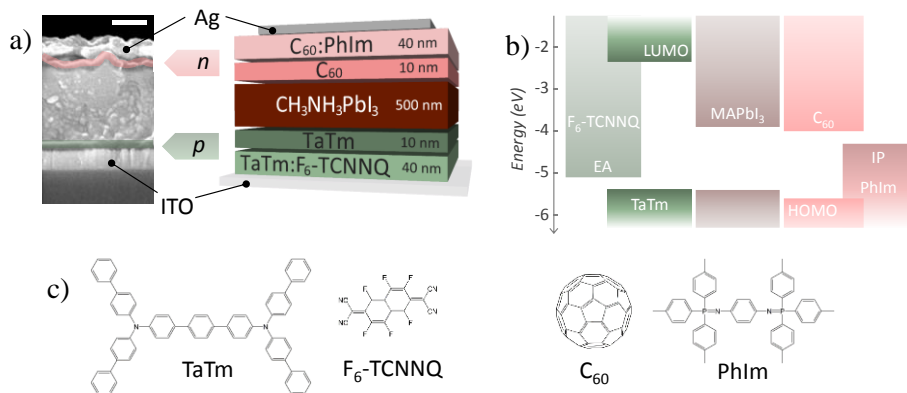


Figure 30. *p-i-n* solar cell: a) cross-section SEM (scale bar 200 nm) and scheme of the device layout, b) flat-band energy level diagram (EA electron affinity, IP ionization potential of the dopants) and c) chemical structures of the organic molecules and molecular dopants used to prepare the charge transport layers.

As can be observed in Figure 30, an undoped HTL and ETL was placed between the perovskite and the doped charge transport layers to prevent any negative interaction (chemical reaction) between the radical cations and anions presented in the doped charge transport layers and the photogenerated charge carriers in the perovskite.

First, the conductivity and absorption of *p*-HTL and *n*-ETL were characterized at different doping concentration. The conductivity of the layers was measured with interdigitated electrodes and the absorption spectra were collected from the layer deposited on top of glass. The corresponding absorption spectra and conductivity data are presented in Figure 31.

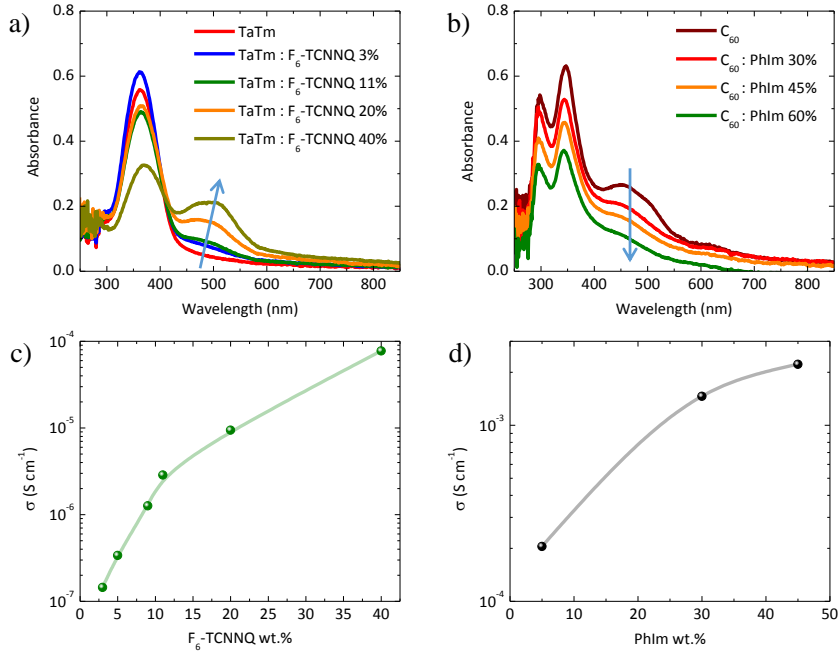


Figure 31. a) Absorption spectra of different p -HTLs as a function of F_6 -TCNNQ dopant concentration, b) absorption spectra of different n -ETLs as a function of PhIm dopant concentration, c) conductivity of the p -HTLs as a function of F_6 -TCNNQ dopant concentration and d) conductivity of the n -ETLs as a function of PhIm dopant concentration.

The conductivity of the layers increases at increasing dopant concentration (Figure 31c for p -HTL and Figure 31d for n -ETL). In terms of absorption of the films, they show an opposite trend. Whereas the p -HTL absorbs more at higher dopant concentrations (Figure 31a), the n -ETL absorbs more at lower dopant concentrations (Figure 31b). It is important to mention that the p -HTL conductivity is two orders of magnitude lower compared to the n -ETL, for the different dopant concentrations evaluated.

In p - i - n devices, to optimize the dopant concentration in the p -HTL (front contact), the dopant of the p -HTL was modified whereas the dopant concentration in the n -ETL was kept constant at 30 wt.%. The J - V curves, the EQE_{PV} and the evolution of the key parameters extracted from the respective J - V curves with the F_6 -TCNNQ dopant concentration are depicted in Figure 32. In the p -HTL, the main effect of increasing the dopant concentration of F_6 -

TCNNQ is the increase in the FF from 55% for a dopant concentration of 3 wt.% to a maximum of 74% at a dopant concentration of 11 wt.% (Figure 32a and 32c). The charges are more efficiently extracted as the p -HTL conductivity increases for increasing doping levels. The V_{OC} increases with increasing dopant concentration going from 1053 to 1082 mV (Figure 32a and 32c). This effect is likely to be a consequence of a reduction in the charge recombination due to the more efficient charge extraction from the perovskite to the external contacts. However, the J_{SC} decreases slightly when the dopant concentration is increased. This effect is due to the higher absorption of the p -HTL at higher dopant concentration, diminishing the light intensity reaching the perovskite absorber and hence decreasing the EQE_{PV} (Figure 32b). Due to this reduction in J_{SC} the optimum F_6 -TCNNQ dopant concentration of 11 wt.% was found with an average PCE of 15.9%.

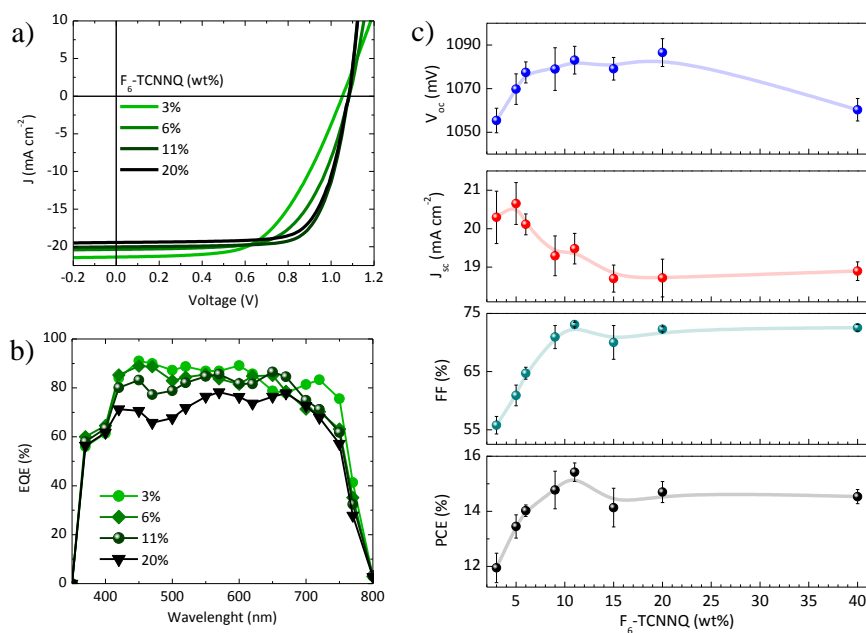


Figure 32. p - i - n solar cells operated under 1 sun illumination (100 mW cm^{-2}) as a function of F_6 -TCNNQ dopant concentration. a) J - V curves, b) external quantum efficiency (EQE_{PV}), c) evolution of the key parameters deduced from the J - V curves (V_{OC} , J_{SC} , FF and PCE) with F_6 -TCNNQ dopant concentration.

Once optimized the F₆-TCNNQ dopant concentration in the *p*-HTL (front contact) at 11 wt.%, this dopant concentration was maintained constant and the dopant concentration in the *n*-ETL (PhIm) (rear contact) was varied. In contrast to the strong effect of the dopant concentration in the *p*-HTL, the effect of the dopant concentration in the *n*-ETL at the rear part of the device was not very pronounced. The PV performances were similar and this indicate that in the dopant range studied, the conductivity of the *n*-ETL is high enough to ensure an efficient electron extraction to the electrode (Ag). Indeed, the conductivity in the *n*-ETL dopant range studied is higher than in *p*-HTL. Due to the similar performance, the graphs are not shown in this chapter.

Optimization of dopant concentration in n-i-p devices

As mentioned above, *n-i-p* devices were fabricated using the same materials than in *p-i-n* devices but inverting the order of the deposition of the layers. In this configuration, Au was chosen as top contact electrode due to its higher work function compared to Ag, metal used as top contact electrode in *p-i-n* devices.

To optimize the dopant concentration in the *n*-ETL (front contact), the dopant concentration in the *p*-HTL was kept constant at 11 wt.%. The *J-V* curves as a function of *n*-ETL dopant concentration is shown in Figure 33. The *J*_{SC} increases slightly with increasing PhIm dopant concentration and reaches 20.28 mA cm⁻² for the highest *n*-dopant concentration. This increase is also observed in EQE_{PV} with increasing PhIm content (Figure 33a). This is a consequence of the reduced C₆₀ content in the film and subsequent higher transmittance in *n*-ETL (Figure 31b). The *V*_{OC} and FF do not change in the range of dopant concentration evaluated, maintaining values as high as 1.1 V and 80%, respectively. These high values lead to average PCEs of 18% and exceeding 20% for the record *n-i-p* cells obtained with a *n*-ETL dopant concentration of 60 wt.% (Figure 33d). This high efficiency is the record not only for vacuum-deposited perovskite cells, but also the highest observed for

devices incorporating the MAPbI₃ absorber. Such high efficiency is somehow contradicting to the commonly accepted belief on the need of large crystals so as to have long charge diffusion lengths and efficient charge collection in perovskite solar cells.²⁷⁶

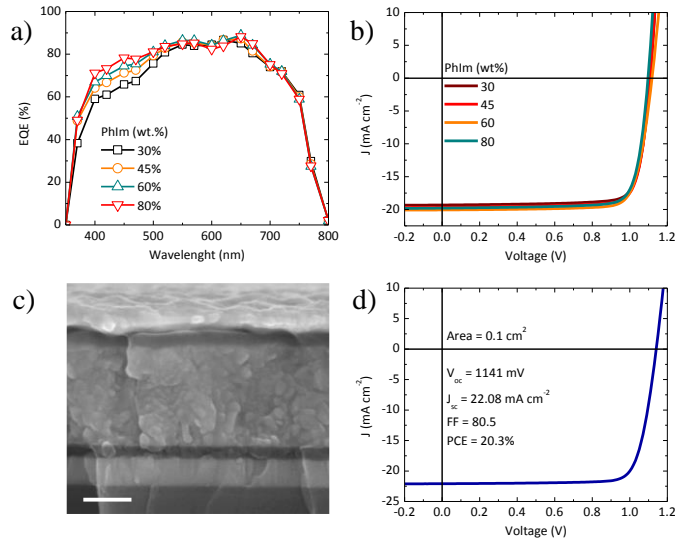


Figure 33. *n-i-p* devices: a) external quantum efficiency (EQE_{PV}) and b) *J-V* curves obtained under 1 sun illumination (100 mW cm⁻²) as a function of PhIm dopant concentration. c) Cross-section SEM image of a representative *n-i-p* solar cell. d) *J-V* curve of the champion *n-i-p* solar cell.

p-i-n vs n-i-p: the importance of the front contact

The results show a strongly enhancement of the performance in *n-i-p* solar cells compared to that of the devices in the *p-i-n* configuration (Figure 34). This enhancement is due to the increased FF value, which is above 80% in the *n-i-p*, compared to the FF around 70% registered in the *p-i-n* configuration. A possible reason for the enhanced FF, when going from the *p-i-n* to the *n-i-p* configuration, is likely related to the difference in conductivity of the doped charge transport layers at the front contact. As mentioned above, the conductivity of the *n*-ETL is two orders of magnitude higher than the conductivity of the *p*-HTL, for the different dopant concentrations evaluated.

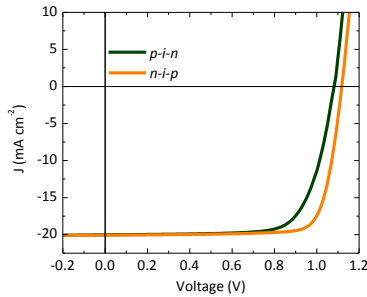


Figure 34. J - V curves obtained under 1 sun illumination (100 mW cm^{-2}) of the champion p - i - n and n - i - p solar cells obtained in this work.

To shed light on the difference of the PV performance between p - i - n and n - i - p devices, the light intensity dependence on the FF is evaluated in both configurations (Figure 35a and 35b). The light intensity-FF dependence shows two different regimes for both devices, one from 1 to 0.1 sun illumination and the other from 0.1 to 0.001 sun illumination. The FF of p - i - n cells increases at lower light intensities in the first regime, whereas decreases in the second one, even for cells using the optimum 11 wt.% dopant concentration in the p -HTL (Figure 35a). However, in n - i - p devices, the FF is virtually independent on light intensity (it is not affected) in the first regime and decreases in the second one (Figure 35b). This trend therefore, confirms that in the p - i - n configuration a barrier for hole extraction exists.

The external quantum efficiency of electroluminescence for p - i - n and n - i - p devices was measured (Figure 35c and 35d). In p - i - n devices (Figure 35c), the radiant flux saturates at about 1.7 V and then decrease, whereas the n - i - p devices (Figure 35d), show enhanced electroluminescence without saturation. This difference confirms a more efficient and balance charge carrier injection in n - i - p devices. The ability to efficiently inject holes when the p -HTL is placed between the HTL and the top metal electrode (n - i - p devices) can be understood considering that the metal electrode is thermally evaporated on top of the p -HTL, which leads to an improved contact because the metal atoms slightly penetrate the soft organic layer and hence increase its conductivity. The EQE

for electroluminescence (EQE_{EL}) of the best performing $n-i-p$ cell presented in this work is $\text{EQE}_{\text{EL}} = 0.36\%$, being this value among the highest reported for light-emitting diodes employing MAPbI_3 as the emitting layer.²⁷⁷⁻²⁷⁸

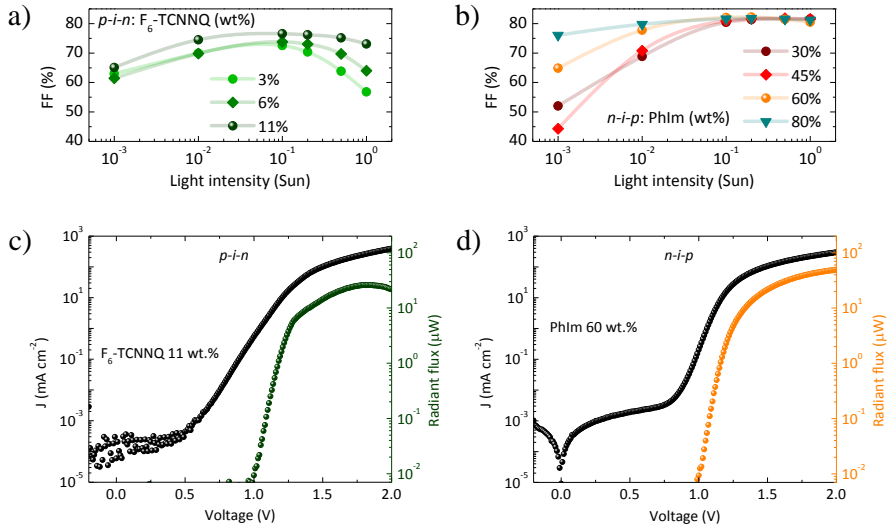


Figure 35. FF dependence on light intensity of a) $p-i-n$ and b) $n-i-p$ at different dopant concentrations of $\text{F}_6\text{-TCNNQ}$ and PhIm, respectively. $J-V$ and radiant flux-voltage curves of c) $p-i-n$ and d) $n-i-p$ champion solar cells.

The hysteresis of the devices was evaluated at different $J-V$ scan speeds (Figure 36). Very small hysteresis between forward and reverse $J-V$ scans is observed only for $p-i-n$ devices (Figure 36a), where small fluctuations in the V_{OC} and FF are present due to possible extraction issues at the ITO/ p -HTL contact (the overall variation of the PCE was limited to 0.1%). On the other hand, highly efficient $n-i-p$ devices are essentially hysteresis-free, independently on the scan speed used (Figure 36b).

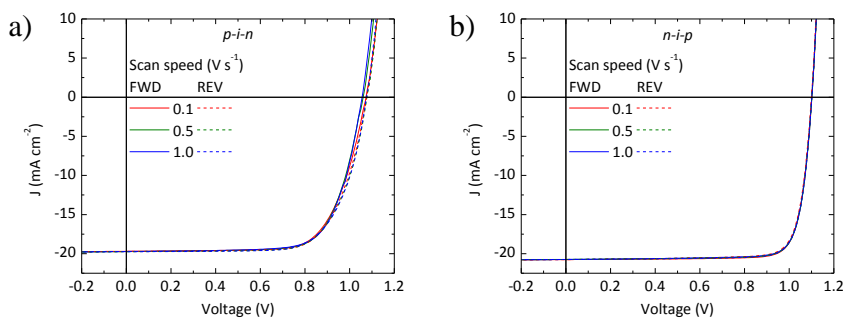


Figure 36. J - V curves obtained under 1 sun illumination (100 mW cm^{-2}) at different scan speeds for a) p - i - n and b) n - i - p solar cells.

Role of the intrinsic transport layers

Intrinsic (undoped) HTL and ETL were placed between the p -HTL and n -ETL and the perovskite to the purpose of avoiding negative interactions. However, it is not obvious whether such a negative interaction in fact occurs, since in perovskites electrons and holes are spontaneously formed after photon absorption without long-living intermediate excitonic states and, additionally, the absorber layer is very thick compared with organic photovoltaic devices. Therefore, a series of p - i - n and n - i - p devices with selective removal of one of the two undoped charge transport layers (HTL or ETL) were fabricated, evaluated and its performance (J - V characteristics) was compared with the reference cell in which both undoped layers are present (green curve) (Figure 37). For comparison, the key parameters extracted from the J - V curves for p - i - n and n - i - p devices with one of the two or both undoped charge transport layers are shown in Table 5.

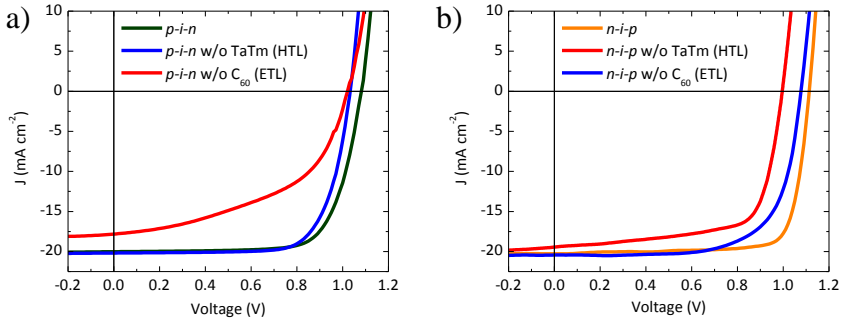


Figure 37. a) J - V curves obtained under 1 sun illumination (100 mW cm^{-2}) for p - i - n devices with both undoped charge transport layers (green line) or without one of the undoped charge transport layers (blue and red). b) J - V curves obtained under 1 sun illumination (100 mW cm^{-2}) for n - i - p devices with both undoped charge transport layers (orange line) or without one of the undoped charge transport layers.

Table 5. Key PV performance data extracted from J - V curves of representative p - i - n and n - i - p devices with one of the two undoped charge selective layers or with both undoped layers.

	Device structure	V_{OC} [mV]	J_{SC} [mA cm^{-2}]	FF [%]	PCE [%]
<i>p</i>-<i>i</i>-<i>n</i>	<i>p</i> -HTL/TaTm/MAPbI ₃ /C ₆₀ / <i>n</i> -ETL	1082	20.02	73.1	15.8
	<i>p</i> -HTL/MAPbI ₃ /C ₆₀ / <i>n</i> -ETL	1033	20.19	73.3	15.3
	<i>p</i> -HTL/TaTm/MAPbI ₃ / <i>n</i> -ETL	1032	17.82	45.0	8.3
<i>n</i>-<i>i</i>-<i>p</i>	<i>n</i> -ETL/C ₆₀ /MAPbI ₃ /TaTm/ <i>p</i> -HTL	1115	20.28	79.8	18.0
	<i>n</i> -ETL/MAPbI ₃ /TaTm/ <i>p</i> -HTL	1084	20.45	68.8	15.2
	<i>n</i> -ETL/C ₆₀ /MAPbI ₃ / <i>p</i> -HTL	998	19.44	68.7	13.3

In p - i - n devices, the dopant concentrations were fixed at the optimum 11 and 30 wt.% for the p -HTL and n -ETL, respectively. The performance of the devices without the undoped ETL is significantly worse (lower FF, J_{SC} and V_{OC}) than for the reference cell. Without the undoped C₆₀ layer, the perovskite film is in close contact with the n -ETL, therefore electron-hole recombination can occur at the interface causing the simultaneous reduction of the PV performance. In contrast, the solar cells without the undoped HTL perform only slightly worse compared to the reference cell, most likely due to the low dopant content and hence low conductivity of the p -HTL (compared to the n -ETL).

However, this layer (*p*-HTL) can still confine the electrons in the perovskite layer and inhibit charge recombination at the *p*-HTL/MAPbI₃ interface. The slight decrease in V_{OC} observed without the undoped TaTm layer can be attributed to the lower Fermi level of the *p*-HTL compared to the HOMO of the TaTm.

Also in the *n-i-p* configuration the effect of the undoped charge transport layers was evaluated (Figure 37b). The selective removal of the undoped layers leads to a decrease in device performance, as observed in the *p-i-n* devices. The effect of the removal of the C₆₀ between the *n*-ETL and the perovskite substantially reduces the V_{OC} and FF, while the removal of the undoped HTL has a limited effect on the device performance, in agreement with what was observed for *p-i-n* devices and with the conductivity trend among the *p*-HTL and the *n*-ETL. Therefore, the presence of the undoped layers between the perovskite and the doped charge transport layers is required for highly efficient solar cells, independently on the device configuration.

Role of the doped transport layers

Additionally, the effect of the selective removal of one of the doped organic layers on the device performances was studied. In both configurations, *p-i-n* and *n-i-p*, *p*-HTL and *n*-ETL are required to avoid severe charge extraction issues. Whereas the devices with only a thin layer of pure TaTm and no doped layer between the ITO and the TaTm shows a strong extraction issue (Figure 38a), devices with only a thin layer of pure C₆₀ and no doped layer between the fullerene and the metal show lower (FF especially) but still appreciable reported photovoltaic behaviour (Figure 38b).^{152, 279} An interface dipole is created at the interface between C₆₀ and noble metals (Au or Ag) enhancing the electron extraction through the contact.

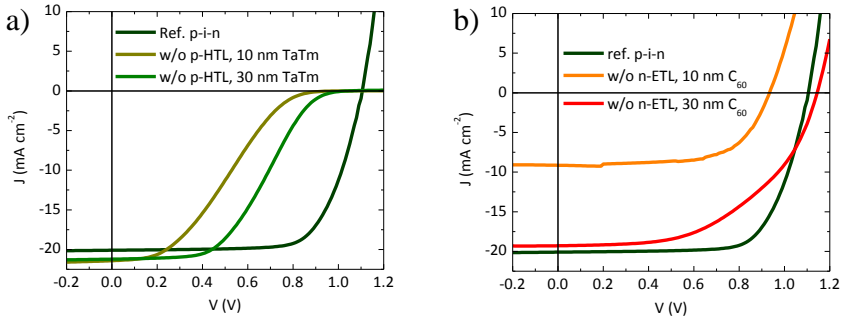


Figure 38. J - V curves obtained under 1 sun illumination (100 mW cm^{-2}) for p - i - n devices a) without p -HTL or b) without n -ETL.

Stability and reproducibility

The stability of the solar cells was analysed without encapsulation under continuous illumination of a white LED light inside a nitrogen-filled glovebox. The light intensity was adjusted by setting the J_{SC} of the solar cells equal to the value obtained under the 1.5 AM illumination. The temperature of the cells reached approximately 40°C during the first 10 minutes of the test and remains constant afterwards. All cells were illuminated under short-circuit conditions and at fixed time intervals J - V scans were taken to extract the key performance indicator of the cells from which the evolution of the PCE was derived. In Figure 39, the stability of both configuration, p - i - n and n - i - p , is shown and no substantial difference in PCE lifetime exists between them. The parameter that causes the PCE decay in p - i - n cells is the current density, whereas in the n - i - p cells the decay is caused by the decrease of the FF.

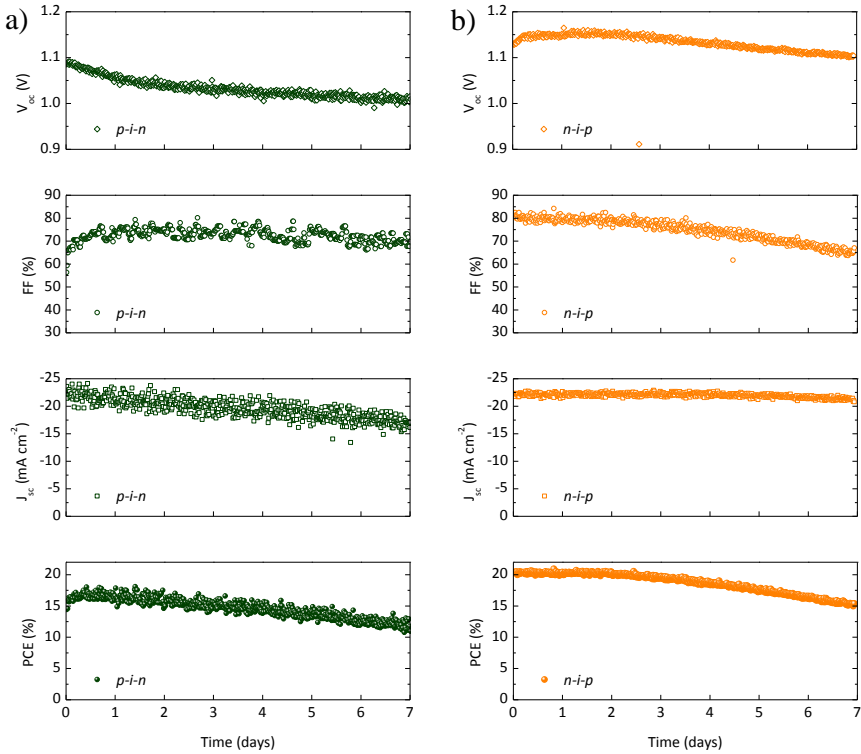


Figure 39. Time-dependent V_{OC} , FF, J_{SC} and PCE of a) $p-i-n$ and b) $n-i-p$ solar cells.

The statistics of the PV performance of $p-i-n$ and $n-i-p$ devices is shown in Figure 40. This chart clearly shows the enhanced PV performance of $n-i-p$ respect to $p-i-n$ solar cells.

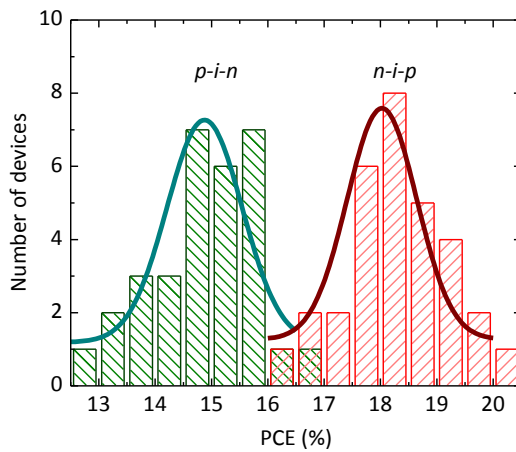


Figure 40. Statistics of the PCE measured for $p-i-n$ (green) and $n-i-p$ (red) devices. Green and red solid lines represent the Gaussian distribution fitting for the PCE.

3.3.4. Conclusions

In this work, fully vacuum-deposited perovskite solar cells were fabricated by depositing methylammonium lead iodide between intrinsic and doped organic charge transport layers.

Two different configurations, one inverted with respect to the other, *p-i-n* and *n-i-p*, are prepared and optimized leading to planar solar cells without hysteresis and very high efficiencies, 16.5% and 20%, respectively. A direct comparison between these two opposite device configurations has been carried out for the first time, with the same materials just inverting the order of the layers.

The results obtained in this work demonstrate that the PV performance of *n-i-p* devices is enhanced compared to the *p-i-n* configuration. This increase in the PV performance in *n-i-p* devices is due to its enhanced FF and likely related to the higher conductivity of the *n*-ETL (C₆₀:PhIm) placed at the front contact than the *p*-HTL (TaTm:F₆-TCNNQ) in *p-i-n* devices. In *n-i-p* devices, the extraction and injection of charge carriers is more efficient and more balanced than in *p-i-n* devices.

The optimization of the dopant concentration at the front contact in both configurations was carried out. After a trade-off between absorption and conductivity of the layers, and the PV performances of the respective devices, the optimum values of dopant concentration in *p-i-n* devices were 11 wt.% of F₆-TCNNQ for the *p*-HTL and 60 wt.% for the *n*-ETL in *n-i-p* devices.

In order to study the effect of the intrinsic and doped charge transport layers in the PV performance of the solar cells, *p-i-n* and *n-i-p* devices were built up without one of the both intrinsic or doped charge transport layers and further characterized.

The PV performance of *p-i-n* devices without intrinsic ETL was significantly worse compared to *p-i-n* devices without intrinsic HTL. Without the ETL, the perovskite film is in close contact with the *n*-ETL and electron-

hole recombination can occur at the interface causing the simultaneous reduction of the PV performance. However, in the solar cells without the intrinsic HTL due to the low dopant content and hence low conductivity of the *p*-HTL (compared to the *n*-ETL), the electrons in the perovskite layer can still be confined and the charge recombination at the *p*-HTL/MAPbI₃ interface is inhibited. The study of the effect of the selective removal of one of the doped organic layers on the device performances led to in both configurations, *p-i-n* and *n-i-p*, *p*-HTL and *n*-ETL are required to avoid severe charge extraction issues. However, the PV performance of *p-i-n* solar cells without the *n*-ETL is still appreciable due to the presence of an interface dipole created at the interface between C₆₀ and noble metals (Au or Ag) enhancing the electron extraction through the contact.

The high efficiency obtained this work in *n-i-p* devices (exceeding 20%) is the record not only for vacuum-deposited perovskite cells, but also the highest observed for devices incorporating the MAPbI₃ absorber. In addition, the EQE for electroluminescence (EQE_{EEL}) of the best performing *n-i-p* cell (EQE_{EEL} = 0.36%) is among the highest reported for light-emitting diodes employing MAPbI₃ as the emitting layer

The fully vacuum-deposited solar cells presented in this work allow to fine tune the device properties by controlling the individual layer thicknesses and composition for specific applications including tandem configurations.

3.3.5. Contribution of the author

Article. **Momblona, C.**;[‡] Gil-Escrig, L.;[‡] Bandiello, E.; Hutter, E. M.; Sessolo, M.; Lederer, K.; Blochwitz-Nimoth, J.; Bolink, H. J.; Efficient vacuum deposited *p-i-n* and *n-i-p* perovskite solar cells employing doped charge transport layers. *Energy & Environmental Science* **2016**, 9 (11), 3456-3463. ([‡] equally contributed). (IF: 29.518, Q1).

IF = Impact factor (Science Citation Reports, Web of Science), Q = Quartile.

Chapter 4

General conclusions

The aim of this thesis is the implementation of unconventional materials into light-emitting and photovoltaic devices.

The motivation of this thesis, as commented in Chapter 1, is to reduce the energy consumption to generate illumination and the amount of fuel fossil employed in the generation of energy. For this purpose, novel, efficient and low-cost electroluminescent and photovoltaic devices need to be developed.

In the introduction of the Chapter 2, Section 2.1.7., is mentioned that the small number of red-emitting LECs reported and their poor stability compared to yellow/orange LECs are two of the principal limitations of LECs. With this in mind, the work developed in Section 2.2. was focused on the development of red- and near-infrared LECs and the improvement of the device stability.

The iTMCs studied in this work were based on the $[\text{Ir}(\text{ppy})_2(\text{btzpy})][\text{PF}_6]$ complex (ppy = 2-phenylpyridinate and btzpy = 2-(pyridin-2-yl)benzo[*d*]thiazole) and all of the complexes studied showed red- and near-infrared photoluminescence in the solid-state with moderate PLQYs values (<18%). The LECs prepared with these complexes also exhibit red to near-infrared electroluminescence. Although the maximum luminance values were moderate, they exhibited extremely high device stability with lifetimes in the range of 1000 – 6000 h, being the most stable red-emitting LECs reported up to date. The EQE_{EL} values obtained were moderate (EQE_{EL} values up to 2%), however, these values were impressive in view of its low thin-film PLQY values and the high current density applied in some cases. Moreover, the possibility of tuning the luminance levels was demonstrated, having a fast response with almost no loss in device stability, maintaining its impressive characteristics by increasing the average current density up to the extremely high value of 1500 A m^{-2} .

The results obtained in this work confirm the potential of the [Ir(ppy)₂(btzpy)][PF₆] type complexes for lighting systems and this work constitutes a step forward in their application in commercial red-light applications. The results presented in this Chapter were published in two different publications (Section 2.2.5.).

In Chapter 3 (Section 3.1.2.) the benefit of the precise control over the film thickness when employing vacuum-deposition techniques was highlighted.

In view of the good photovoltaic performance with perovskite absorbers obtained previously in our group, in Section 3.2. an in-depth study of the photovoltaic efficiency by increasing the photocurrent obtained through modification of the perovskite thickness was performed. In this study, a series of vacuum-deposited MAPbI₃ layers with a wide range of layer thicknesses ranging from 210 to 900 nm were fabricated by co-evaporation and then characterized. Given the good properties of the layers, the perovskite layers were implemented into *p-i-n* devices where the perovskite layer was sandwiched between undoped organic charge transport layers. The photogenerated J_{SC} was enhanced when the perovskite thickness was increased, however, at the same time a reduction in the FF and hence in the PCE was observed. This reduction was linked to the low mobility of the undoped polyTPD layer. The partial oxidation of the polyTPD layer increases its conductivity and the device that contains the doped polyTPD layer with the thicker perovskite thick film recovers the FF (65%) and the PCE (12.0%) reaching the same high efficiency than the most efficient device of the series with thinner perovskite films (PCE = 12.7%). Therefore, in this work was demonstrated that with non-limiting organic layers, the PV performance of vacuum-deposited perovskite solar cells is rather independent on the perovskite layer thickness and also demonstrating that the charge carrier diffusion length

is not limiting in the devices. The results presented in this Section were published in one publication (Section 3.2.5.).

In Section 3.3., the fabrication and characterization of fully vacuum-deposited planar perovskite solar cells, employing a MAPbI₃ perovskite layer deposited between a double layer of an intrinsic and doped *n*- or *p*- type organic charge transport layers, respectively, were described. Two different configurations, one inverted with respect to the other, *p-i-n* and *n-i-p*, were prepared using the same materials in both layouts. This was the first time where a direct comparison between the two device types was described. The optimization of the dopant concentration was carried out and it was found that the presence of the undoped layers between the perovskite and the doped charge transport layers were required for high efficiency cells, independently on the device configuration.

The optimized solar cells lead to planar solar cells hysteresis-free and very high efficiencies exceeding 16.5% (*p-i-n*) and 20% (*n-i-p*), at the time the highest efficiencies reported for vacuum-deposited perovskite and in general with MAPbI₃-based solar cells. The improved performance in *n-i-p* solar cells compared to that of the devices in the *p-i-n* configuration is primarily caused by the higher FF value. This is likely related to the difference in conductivity of the doped charge transport layers at the front contact leading to a more efficient and balance charge carrier extraction/injection of the charges. When used as a light-emitting diode these structures also presented the highest EQE_{EL} reported for MAPbI₃ based diodes. The results presented in this Section were published in one publication (Section 3.3.5.).

Chapter 5
Resumen en Castellano

Capítulo uno: Introducción general y objetivos de la tesis

1.1. Introducción general

En los últimos años se ha producido un incremento en el consumo energético mundial debido al aumento de la población y el desarrollo económico.¹ En concreto, la iluminación constituye más de un 15% del consumo eléctrico global y un 5% de las emisiones de gas invernadero a nivel mundial.² Con el completo reemplazo de la iluminación convencional, basada en luces incandescentes y fluorescentes, por un sistema de iluminación de estado sólido (SSL), el consumo energético en iluminación se vería reducido a menos del 10% del consumo eléctrico global.³ Por lo tanto, la iluminación en estado sólido (SSL) basada en diodos emisores de luz (LEDs), diodos orgánicos emisores de luz (OLEDs) o células electroquímicas emisoras de luz (LECs) ha emergido como la mejor alternativa para promover el ahorro energético en iluminación.

Respecto a la generación de energía anual, las fuentes de energía no renovables (combustibles fósiles: carbón, petróleo y gas) representan más del 85% de la generación energética global, mientras que solo un 3% son las energías renovables (ver Figura 1). Indiscutiblemente, la mayor fuente de energía renovable, la más limpia y permanente, es el sol. La radiación solar que alcanza la superficie de la Tierra en un año es de un orden de magnitud mayor a la de todos los recursos estimados de energías no renovables, incluyendo la energía nuclear.⁴ Por lo tanto, es indiscutible la superioridad de este recurso energético cuando se compara con las reservas limitadas de carbón, petróleo y gas que existen en la Tierra. En la actualidad, el desarrollo de la energía solar se ha convertido en una alternativa viable a los combustibles fósiles para aliviar la crisis energética y solventar problemas medioambientales. La energía solar fotovoltaica puede convertir directamente y de manera eficaz la luz solar en electricidad. Sin embargo, para que sea competitiva con los combustibles fósiles, es necesario reducir su coste global mediante el incremento de la

eficiencia y el tiempo de vida operacional y la reducción de costes por célula fotovoltaica. En la actualidad, el mercado fotovoltaico está liderado por células solares cuyo material absorbente de luz es el silicio cristalino o policristalino (c-Si y poly-Si, respectivamente). Recientemente, células solares cuyo material absorbente de luz son materiales tipo perovskita han emergido como una nueva generación de células solares de bajo coste y con un menor factor de emisión de CO₂ en comparación con los demás sistemas fotovoltaicos, siendo competitivas en sí mismas o en combinación con el silicio cristalino.

1.2. Objetivos de la tesis

El objetivo global de la tesis es la implementación de materiales no convencionales en dispositivos emisores de luz y fotovoltaicos con altas eficiencias de conversión.

En particular, los objetivos de esta tesis consisten en:

- ✓ Mejora de la estabilidad de células electroquímicas emisoras de luz y ampliación de su longitud de onda de emisión desde el rojo hasta el infrarrojo cercano.
- ✓ Mejora de la eficiencia de células solares basadas en perovskitas mediante la deposición en fase vapor del absorbente de luz y la optimización de las interfaces en la estructura del dispositivo fotovoltaico.

Capítulo dos: Células electroquímicas emisoras de luz

2.1. Introducción

Las células electroquímicas emisoras de luz (LECs) son dispositivos emisores de luz basados en la utilización de una monocapa de un material electroluminiscente como elemento emisor de luz.^{5, 10-11, 17, 19} La presencia de iones en la capa emisora de luz es crucial para el mecanismo de operación del dispositivo LEC, por lo que los emisores basados en complejos iónicos de metales de transición (iTMCs) se han convertido en el material electroactivo más prometedor en la tecnología LEC.¹³⁻¹⁵

El primer LEC publicado en 1996 empleaba un polímero de un complejo de Ru(II) como material electroluminiscente.²³ Sin embargo, debido al limitado rango de emisión desde el naranja hasta el rojo y a las bajas eficiencias obtenidas con los complejos de Ru(II),^{28, 35-36} otros iTMCs de Re(I),³⁷ Pt(II),⁴⁰ Cu(I)⁴⁴ o Ir(III)⁵² empezaron a ser implementados en dispositivos LEC. Los complejos de Ir(III) (Ir-iTMCs) han destacado debido a: 1) su versatilidad sintética formando complejos homo- y heterolépticos, 2) su color de emisión en todo el rango visible, 3) su mejor fotoestabilidad (el estado excitado triplete no emisor (³MC) es menos accesible) y 4) la mayor eficiencia y estabilidad del dispositivo. Desafortunadamente, debido a la escasez del iridio en la corteza terrestre y a su alto precio, es deseable el reemplazo del mismo por otros materiales más abundantes y baratos, como el cobre.

La mayoría de los Ir-iTMCs utilizados en dispositivos LEC tienen la estructura $[\text{Ir}(\text{C}^{\wedge}\text{N})_2(\text{N}^{\wedge}\text{N})]^+$, donde el metal central Ir(III) está coordinado a dos ligandos ciclometalantes aniónicos ($\text{C}^{\wedge}\text{N}$) y un ligando secundario neutro ($\text{N}^{\wedge}\text{N}$) (Figura 2a). La carga positiva está neutralizada con un contraión pequeño y móvil, generalmente hexafluorofosfato o tetrafluoroborato. Al contrario que los semiconductores orgánicos, de naturaleza fluorescente, el alto acoplamiento spin-órbita presente en los Ir-iTMCs debido a la presencia de átomos pesados promueve que la eficiencia del cruce intersistema (ISC) entre

los estados excitados singlete y triplete sea máxima resultando en emisión fosforescente. En los Ir-ITMCs, los orbitales moleculares frontera HOMO y LUMO residen en diferentes entornos moleculares. El HOMO está formado por una mezcla de orbitales $d\pi$ del metal y de orbitales π del fenilo de los ligandos C^N (Figura 2b), mientras que el LUMO está localizado en el ligando N^N (Figura 2c).⁴⁸⁻⁴⁹ Esta distribución espacial de los orbitales moleculares frontera permite modificar independientemente la energía de ambos mediante la modificación química de los ligandos. El uso de sustituyentes atrayentes/dadores de electrones en los ligandos C^N estabiliza/desestabiliza la energía del HOMO, mientras que el uso de sustituyentes dadores/atrayentes de electrones en el ligando N^N desestabiliza/estabiliza la energía del LUMO (ver Figura 3).^{13, 15, 57-58}

Todas las capas de un dispositivo LEC son depositadas desde disolución de los componentes en disolventes benignos a excepción del electrodo superior metálico, el cual es depositado mediante evaporación térmica en vacío. Para la deposición de las capas a escala de laboratorio, se usa un “*spin coater*”, cuyo equivalente a nivel industrial serían las técnicas de roll-to-roll (R2R), “inkjet printing”, “spray-sintering”, “slot-die” o “blade-coating” entre otras.⁶¹⁻⁶⁵ Entre las estructuras más usadas en los dispositivos LEC destacan las de tipo sándwich,²⁵ plana⁶⁷⁻⁶⁹ o en cascada.⁷⁰ La estructura tipo sándwich consiste en una o dos capas orgánicas/organometálicas intercaladas entre un óxido conductor transparente (TCO) y un electrodo metálico de alta función de trabajo (estable al aire) como el aluminio o el oro. Una de las ventajas de los dispositivos LEC, en contraste a la tecnología OLED, es que no se requiere el uso de metales de baja función de trabajo, los cuales son extremadamente inestables en aire, y por lo tanto no es necesaria la encapsulación del dispositivo. En concreto, un dispositivo LEC con estructura tipo sándwich (Figura 4) está constituido por una capa inyectora de huecos formada por el polímero poli(3,4-etilendioxitiofeno):poliestirenosulfonato (PEDOT:PSS), que ayuda a hacer plana la superficie del TCO (ITO) y aumenta

el rendimiento de la preparación de los dispositivos, seguido por una capa del material emisor de luz. La capa emisora de luz está compuesta por una mezcla de iTMC y una sal de litio⁷²⁻⁷⁵ o líquido iónico (IL).⁷⁶⁻⁷⁷ La adición de estas sales aumenta la densidad de iones móviles, así como la movilidad iónica, ayudando a la migración de iones y acelerando el tiempo de encendido de los dispositivos. Para aumentar la homogeneidad de las capas y aumentar el rendimiento cuántico de fotoluminiscencia disminuyendo la desactivación de la emisión (*quenching*) que ocurre debido a altas concentraciones empleadas, el iTMC puede ser dispersado en un polímero inerte, como polimetilmetacrilato (PMMA).²⁷

El mecanismo de operación que rige el comportamiento de los dispositivos LEC^{69, 87} consiste en la disociación y migración de los iones presentes en la capa emisora hacia los respectivos electrodos al aplicar una diferencia de potencial. Estos iones forman una doble capa eléctrica (EDL) en ambos electrodos reduciendo la barrera energética de inyección de las cargas en ambos electrodos y facilitando la inyección de las mismas. La capa emisora se empieza a oxidar y reducir formando regiones dopadas altamente conductoras tipo *p*- y *n*-. Tras la formación de estas capas dopadas, la inyección de carga está favorecida y gradualmente la corriente en el dispositivo y la emisión de luz se incrementan. Durante la operación del dispositivo, es inevitable el crecimiento de las capas dopadas en detrimento de la zona neutra central produciendo un incremento de la desactivación de los excitones y disminuyendo la luminancia en el dispositivo hasta que finalmente no se produce emisión de luz. Por lo tanto, el mecanismo de operación de los dispositivos LEC conlleva que estos dispositivos sean autolimitantes.

A día de hoy la tecnología LEC todavía presenta una serie de limitaciones que tienen que ser superadas como: 1) la reducción del tiempo de encendido, 2) el aumento de la eficiencia del dispositivo junto con los niveles de luminancia, 3) la mejora de la estabilidad del dispositivo y 4) la obtención de emisión en el azul y en el rojo.

Debido a que la estabilidad de un dispositivo LEC es el resultado de una luminancia estable en el tiempo procedente del complejo iónico de Ir y del empleo de corriente pulsada como modo de operación,⁸⁸⁻⁸⁹ en este capítulo se trató de mejorar la estabilidad de dispositivos LEC emisores en el rojo mediante modificación del ligando secundario y la aplicación de corriente pulsada.

2.2. Método experimental

En este capítulo de la tesis se han fabricado y caracterizado dispositivos LEC a partir de Ir-iTMCs sintetizados, purificados y caracterizados por los grupos del Profesor Dr. Edwin C. Constable y la Profesora Dra. Catherine E. Housecroft de la Universidad de Basel (Suiza) (complejos **1–6**) y por el grupo del Profesor Eli Zysman Colman de la Universidad de St. Andrews (Reino Unido) (complejos **7** y **8**) (ver Figura 7).

El procesado, preparación y caracterización de los dispositivos LEC fue llevado a cabo en una sala limpia de clase 10000 (Figura 8). Todos los materiales empleados en este trabajo están disponibles comercialmente y se utilizaron sin purificación posterior a su adquisición. El estudio de las propiedades fotofísicas de los complejos **1–8** se llevó a cabo en estado sólido, depositando el material sobre un sustrato de cuarzo obteniendo capas delgadas de igual composición y espesor que la capa activa usada en los dispositivos LEC. Una vez preparada la muestra, el espectro de fotoluminiscencia y el rendimiento cuántico fueron obtenidos excitando cada muestra en una esfera integradora modelo C9920-02 Absolute PL Quantum Yield Measurements.

Los dispositivos LEC fabricados en este estudio tienen la siguiente arquitectura tipo sándwich (ver Figura 4): ITO/PEDOT:PSS(80 nm)/complejo(**1–8**):IL(100 nm)/Al(80 nm). El proceso de preparación consistió en la deposición de una capa de 80 nm de PEDOT:PSS mediante *spin-coating* sobre un sustrato de ITO previamente limpiado, seguido de la deposición de la capa activa de 100 nm de espesor. La capa activa fue depositada también por *spin-coating* desde una disolución de los complejos (**1–**

8) mezclados con el líquido iónico [Bmim][PF₆] en una relación molar complejo:IL de 4 a 1. El líquido iónico fue utilizado para reducir el tiempo de encendido del dispositivo y mejorar su rendimiento.⁷⁶ Además, en las disoluciones de los complejos **2** y **4** se añadió PMMA (2% en peso respecto a los demás componentes de la disolución) para mejorar el recubrimiento y homogeneidad de la capa. Para terminar el dispositivo, una capa de aluminio de 70 nm fue depositada mediante evaporación térmica en vacío. La caracterización de los dispositivos LEC se realizó utilizando corriente pulsada (onda cuadrada, 1000 Hz, 50% ciclo de trabajo). Los dispositivos LEC **1–6** fueron estudiados a una densidad de corriente media de 100 A m⁻², el dispositivo LEC **1** a 300, 700, 1250 y 1500 A m⁻² y los dispositivos LEC **7** y **8** a 400 A m⁻². La aplicación de la corriente y la medida de la luminancia y el voltaje frente al tiempo fueron realizadas en el equipo Botest OLT OLED Lifetime-Test System, y la irradiancia fue medida usando una esfera integradora (UDT Instruments, modelo 2525LE) acoplada a un sensor radiométrico (UDT Instruments, modelo 247) y un optómetro UDT Instruments, modelo S370).

2.3. Resultados y discusión

El estudio se llevó a cabo utilizando una familia de Ir-iTMCs derivados del complejo [Ir(ppy)₂(btzpy)][PF₆] (Hppy = 2-fenilpiridina; btzpy = 2-(piridin-2-il)benzo[*d*]tiazol). Los espectros de fotoluminiscencia de las capas delgadas correspondientes a los complejos **1–8** obtenidos bajo iluminación ($\lambda_{exc} = 320$ nm) presentaron longitudes de onda máximas de emisión desde el rojo (625 nm para el complejo **6**) hasta el infrarrojo cercano (707 nm para el complejo **7**) (Tabla 1). Los correspondientes rendimientos cuánticos de fotoluminiscencia son bajos en todas las muestras (< 18%), correspondiendo el mayor valor de PLQY observado al complejo **2** (PLQY de 17,6%) y los menores a los complejos **3**, **5** y **7** (PLQYs de 9,7, 5,8 y 5%, respectivamente) (Tabla 1). Estos bajos valores de PLQY pueden ser consecuencia de la ley de banda de energía prohibida (“energy gap law”).¹⁰⁰⁻¹⁰¹

Los espectros de electroluminiscencia (EL) de los dispositivos estudiados presentan emisión en el rojo para los LECs **1–6** y **8** con $\lambda_{em,EL}^{max}$ a 636, 642, 651, 648, 655 y 598 (LECs **1–6**), respectivamente, y 661 nm para el LEC **8** (Figura 9a) y emisión en el infrarrojo para el LEC **7** con $\lambda_{em,EL}^{max}$ a 705 nm (Figura 9b). Estos dispositivos electroluminiscentes son interesantes ya que hasta la fecha muy pocos ejemplos de LECs emisores en el rojo y en infrarrojo cercano han sido publicados, y muy pocos ejemplos presentan emisión en el rojo puro. Las coordenadas de la *Commission Internationale de l’Eclairage* (CIE coord.) obtenidas para los dispositivos **3**, **5** y **6** presentan coordenadas CIE coincidentes con las del rojo puro (0,66; 0,33).

La evolución temporal de la luminancia y el voltaje del dispositivo fue evaluada bajo aplicación de corriente pulsada (Figura 10). Los parámetros clave del rendimiento de los dispositivos LEC **1–8** están presentados en la Tabla 2. El dispositivo LEC **1** presenta una luminancia máxima de 77 cd m⁻² alcanzada a las 54 h junto con un tiempo de vida ($t_{1/2}$) que excede las 1000 h. El largo tiempo requerido para alcanzar la luminancia máxima junto con el largo tiempo de vida implican que el movimiento iónico en el dispositivo y el crecimiento de las capas dopadas es lento. El dispositivo LEC **2** presenta la luminancia máxima más alta de la serie con 200 cd m⁻² alcanzada a las 870 h junto con un notable aumento en estabilidad con un tiempo de vida que alcanza las 6000 h. Las superiores prestaciones del dispositivo LEC **2** determinan que este dispositivo no sólo es el mejor de la serie, sino que es el dispositivo LEC emisor en el rojo más estable publicado hasta la fecha, ya que el dispositivo emisor en el rojo más estable publicado hasta ese momento presentaba un tiempo de vida de 280 h.¹⁰² El tiempo de encendido en ambos dispositivos (LECs **1** y **2**) es similar; sin embargo, la luminancia en el LEC **2** continúa aumentando con el tiempo, indicando que la inyección de carga no es óptima y que el balance entre las cargas se alcanza lentamente. Este hecho podría indicar que el movimiento iónico es lento y produce un crecimiento muy lento de las zonas dopadas en el tiempo llegando a ser beneficioso para la estabilidad del dispositivo. La mayor

luminancia obtenida en el LEC **2** es debido al mayor valor de PLQY medido en estado sólido para el complejo **2** (17,6%) en comparación con el complejo **1** (11%). El dispositivo **3** presenta una luminancia máxima (119 cd m⁻²) y un tiempo de vida mayor ($t_{1/2} > 4500$ h) que el complejo **1**, aunque el complejo **1** presente menor PLQY en estado sólido (9,7%) en comparación con el complejo **1** (11%). Sin embargo, cuando el tamaño de los sustituyentes aumenta (complejos **4** y **5**), la estabilidad de los correspondientes dispositivos se ve reducida cayendo a valores de decenas de horas. El reemplazo del átomo de azufre en la unidad de benzotiazol (LEC **1**) por un átomo de oxígeno (LEC **6**) no afecta a la luminancia máxima alcanzada ($L_{\max} = 77$ and 97 cd m⁻², respectivamente) pero sí afecta negativamente a la estabilidad y la eficiencia del dispositivo. En los dispositivos LEC **4–6**, el tiempo requerido para alcanzar la máxima luminancia y el tiempo de encendido son casi cuatro veces más rápidos que los LECs **1–3**, corroborando la hipótesis de que el rápido crecimiento de las capas dopadas incrementa la desactivación de los excitones.

El dispositivo LEC **7** fue fabricado desde una disolución en metil etil cetona/anisol 3:2. Sin embargo, este dispositivo no emitió luz al aplicar la corriente pulsada probablemente debido a la mala calidad de la capa que se obtiene como consecuencia de la baja solubilidad del complejo en el disolvente. El uso de diclorometano como disolvente mejoró la solubilidad del complejo produciendo una capa más uniforme después de su deposición por *spin-coating*. El dispositivo **7** accionado con una densidad de corriente media de 400 A m⁻² presentó una irradiancia máxima de 262 $\mu\text{W cm}^{-2}$ y un $t_{1/2}$ de 80 h (LEC **7**), mientras que el LEC **8** presentó una luminancia máxima de 59 cd m⁻² y un $t_{1/2}$ de 0,24 h. La presencia de bencenos fusionados en el ligando secundario (LECs **1–6**, **8**) parece ser beneficiosa para la estabilidad del dispositivo. Por otra parte, la presencia de un catión más grande (complejo **7**) en comparación con el complejo **8**, reduce el movimiento iónico en la capa activa durante la operación, disminuyendo la desactivación del excitón y aumentando el tiempo de vida. Además, el tiempo requerido para alcanzar la luminancia máxima es

significativamente mayor en el LEC **7** (0,8 h) en comparación con el LEC **8** (< 5 s), indicando un movimiento iónico más lento y favoreciendo la estabilidad.

Debido a que los dispositivos LEC emiten en el rojo, solo una parte de la emisión es visible al ojo humano, por lo que la eficiencia del dispositivo se expresa más adecuadamente en términos de eficiencia cuántica externa (EQE_{EL}). Los mayores valores obtenidos para la serie de complejos estudiada, medidos a densidad de corriente media de 100 A m^{-2} , corresponden a los LECs **2** y **3** con valores de EQE_{EL} de 2 y 1,49%, respectivamente, mientras que los LECs **1**, **4**, **5** y **6** presentan valores de EQE_{EL} de 0,7, 1,04, 0,14 y 0,55%, respectivamente. Los LECs **7** y **8** evaluados a 400 A m^{-2} , obtienen valores de EQE_{EL} de 0,37 y 0,23%, respectivamente. Aunque los valores obtenidos son bajos en comparación al máximo de 9,51% publicado para el LEC emisor en el rojo más eficiente,⁹³ estas eficiencias son considerablemente altas si se tienen en cuenta los bajos valores de PLQY que presentan los complejos en estado sólido.

El dispositivo LEC **1** fue seleccionado para estudiar su estabilidad en condiciones de operación extremas, empleando altas densidades de corriente medias desde 300 hasta 1500 A m^{-2} (Figura 12). Se observó que en los dispositivos que operaban a las más altas densidades de corriente, el decaimiento de la luminancia era mínimo en el intervalo de tiempo estudiado, presentando una dependencia lineal en el rango de 100 a 700 A m^{-2} y aumentando, aunque de manera no lineal, a más altas densidades de corriente. Este tipo de tendencia lineal ya se había observado a bajas diferencias de corriente, pero nunca a valores tan altos, indicando que en el dispositivo LEC **1** existe poca desactivación excitón-excitón o excitón-polarón hasta altas densidades de corriente de 700 A m^{-2} . Además, la luminancia puede verse modificada por la densidad de corriente aplicada.

También se observó que, aumentando la densidad de corriente aplicada al dispositivo, el tiempo de encendido se puede reducir desde 500 s hasta 5 s al incrementar la densidad de corriente media de 300 a 1500 A m^{-2} (Figura 13).

2.4. Conclusiones

En este capítulo de la tesis se han fabricado y estudiado ocho dispositivos LEC emisores de luz en el rojo. En la serie estudiada, han destacado los dispositivos **1–3**, los cuales presentan una estabilidad muy alta con tiempos de vida que exceden las 1000, 6000 y 4000 horas, respectivamente. Estos valores de tiempo de vida son los más largos publicados hasta la fecha en dispositivos LEC emisores en el rojo. Además, se ha demostrado la posibilidad de aumentar los niveles de luminancia del dispositivo aumentando la densidad de corriente aplicada a valores extremos, sin que dicho aumento conlleve una pérdida de estabilidad y, además, obteniendo una respuesta rápida de encendido.

Los resultados obtenidos en este trabajo se publicaron en los siguientes artículos científicos (FI = Factor de impacto (Science Citation Reports, Web of Science), Q = Cuartil):

Artículo 1. Ertl, C. D.;[‡] **Momblona, C.**;[‡] Pertegás, A.; Junquera-Hernández, J. M.; La-Placa, M.-G.; Prescimone, A.; Ortí, E.; Housecroft, C. E.; Constable, E. C.; Bolink, H. J., Highly stable red-light-emitting electrochemical cells. *Journal of the American Chemical Society* **2017**, *139* (8), 3237-3248. ([‡] igualmente contribuido). (FI: 13.858, Q1).

Artículo 2. Pal, A. K.; Cordes, D. B.; Slawin, A. M. Z.; **Momblona, C.**; Pertegás, A.; Ortí, E.; Bolink, H. J.; Zysman-Colman, E., Simple design to achieve red-to-near-infrared emissive cationic Ir(III) emitters and their use in light-emitting electrochemical cells. *RSC Advances* **2017**, *7* (51), 31833-31837. (FI: 3.108, Q1).

Capítulo tres: Células solares basadas en perovskita

3.1. Introducción

Las perovskitas de haluro metálico han emergido en los últimos años como un revolucionario material semiconductor para aplicaciones optoelectrónicas.¹³⁰⁻¹³⁴ En menos de una década de su aplicación en células solares, las células solares de perovskita han alcanzado eficiencias superiores al 22%.¹³⁵ Las altas eficiencias alcanzadas junto con el bajo coste de los materiales de partida y los múltiples métodos de procesamiento existentes hacen factible la pronta comercialización de este tipo de dispositivos.

Las perovskitas orgánicas-inorgánicas poseen propiedades eléctricas y ópticas excepcionales que las convierte en excelentes candidatos como materiales semiconductores absorbentes/emisores de luz. En concreto, las perovskitas poseen un alto coeficiente de absorción con un comienzo abrupto de la absorción,¹³⁷ conducción ambipolar con movilidades de electrones y huecos balanceadas,¹³⁸ altas longitudes de difusión de las cargas fotogeneradas,¹³⁹⁻¹⁴¹ bajos niveles de densidad de defectos o trampas¹⁴² y una baja energía de enlace del excitón.¹⁴³⁻¹⁴⁵ Las perovskitas 3D tienen una fórmula general ABX_3 , en la que el octaedro formado por una unidad de haluro metálico (BX_6) se extiende en las tres dimensiones, y un catión pequeño A se introduce en los huecos intersticiales (Figura 14). La perovskita arquetipo está compuesta por un catión A monovalente orgánico o inorgánico (metilamonio $CH_3NH_3^+$ o MA^+ , formamidinio $NH_2CH=NH_2^+$ o FA^+ , cesio Cs^+), un catión B divalente (Pb^{2+} o Sn^{2+}) y un haluro X (Cl^- , Br^- , I^-),¹⁴⁸⁻¹⁵⁰ siendo la composición $MAPbI_3$ la más ampliamente estudiada y aplicada en células solares.

La estructura electrónica viene determinada por una mezcla de orbitales np^6 , siendo n el número cuántico principal ($Cl: n = 3$, $Br n = 4$, $I n = 5$) y orbitales ns^2 del metal ($Ge: n = 4$, $Sn n = 5$, $Pb n = 6$) en la banda de valencia y la banda de conducción por los orbitales np^6 vacíos del metal. Por lo tanto, el catión orgánico/inorgánico no afecta a la estructura electrónica de manera

directa.¹⁶⁰⁻¹⁶² La banda prohibida puede ser modulada desde el infrarrojo cercano hasta el ultravioleta cercano sustituyendo la composición de alguna de las tres posiciones: A, B y/o X.

Las perovskitas pueden ser sintetizadas mediante una amplia variedad de técnicas, que incluyen desde disolución hasta su deposición en vacío o una combinación de ambas. Las propiedades de las capas varían dependiendo del método de deposición empleado, por lo que para comprender las propiedades, una descripción exhaustiva del proceso de preparación es necesaria.

En la deposición por disolución, los precursores son disueltos en un disolvente orgánico y la capa es depositada por métodos de revestimiento como *spin-*, *dipping-* y *doctor blade-coating* o de impresión.¹⁸⁴ Este proceso puede hacerse por deposición en un paso o en dos. En la deposición en un paso, los precursores son disueltos en disolventes polares de alta temperatura de ebullición y la disolución es depositada mediante *spin-coating*. Posteriormente, un tratamiento térmico es necesario para la conversión a perovskita.¹⁸⁹⁻¹⁹¹ Para mejorar la calidad de la capa, normalmente se añade, junto con los precursores un aditivo^{179, 192-197} o se adiciona un disolvente que no disuelva la perovskita en los últimos segundos del proceso de *spin-coating*.¹⁹⁸⁻²⁰⁰ En la deposición en dos pasos, primero se deposita una capa de PbI_2 y posteriormente se convierte a perovskita mediante exposición a una disolución o vapor de MAI.²⁰¹⁻²⁰⁴

En la deposición en vacío, los precursores son situados en crisoles cerámicos y calentados en vacío ($1 \times 10^{-5} - 1 \times 10^{-6}$ mbar) hasta su temperatura de sublimación (Figura 15). Los espesores y velocidades de evaporación son monitorizados mediante microbalanzas de cuarzo (QCM) situadas en el interior de la cámara de vacío. La composición química de la capa depositada es controlada mediante la relación entre las velocidades de evaporación de cada uno de los precursores, mientras que la morfología es controlada por la velocidad total de evaporación usada. Diferentes técnicas de deposición en vacío han sido utilizadas para preparar capas de perovskita, entre ellas se encuentran el *closed space vapour transport* (CSV_T),²⁰⁷ la deposición química

en fase vapor (CVD),²⁰⁸⁻²⁰⁹ la evaporación flash²¹⁰⁻²¹¹ o deposición de capa atómica (ALD).²¹³⁻²¹⁴

Las principales ventajas de utilizar las técnicas de deposición en vacío son: uso de materiales sublimados intrínsecamente más puros, control preciso sobre espesor, estequiometría y morfología de la capa, compatible con deposición en áreas grandes, fabricación de multicapas, baja temperatura en el sustrato durante fabricación, eliminación de disolventes y empleo de una técnica ampliamente en la industria semiconductor.

El principio básico de operación de una célula solar consiste en tres procesos: absorción de luz, separación de cargas y transporte y extracción de cargas.

Un buen absorbente de luz debe tener una banda prohibida directa y un alto coeficiente de absorción. Dependiendo de la permitividad del material, las cargas estarán atraídas formando un excitón o como cargas libres. A pesar del amplio rango de valores de energía de enlace del excitón publicados (de 2 a 62 meV a temperatura ambiente),^{145, 280-283} todo parece indicar que las especies generadas después de la fotoexcitación en MAPbI₃ son cargas libres. Una vez que las cargas están disociadas, hay que dirigir el flujo de electrones y huecos hacia los respectivos electrodos. Para ello, hay dos estrategias, la presencia de una unión *p-n* o el uso de capas selectivas de cargas depositadas en contacto con la capa absorbente de luz. Durante la tesis se utilizará la segunda estrategia, donde la capa de perovskita estará depositada entre una capa transportadora de huecos (HTL) y otra transportadora de electrones (ETL) (Figura 16). Estas capas tienen que estar formadas por materiales con una energía del HOMO, en el caso del HTL, y del LUMO, en el del ETL, que estén alineadas con la banda de valencia (VB) y la de conducción (CB) de la capa absorbente de luz, respectivamente.

Dependiendo de la secuencia de las capas en el dispositivo, las células solares se pueden catalogar en *p-i-n* o *n-i-p* empezando por la capa por la que

incide la luz. “*p*” y “*n*” se refieren a las capas transportadoras de huecos y de electrones, respectivamente, e “*i*” a la capa de perovskita. La estructura *p-i-n* (o “invertida”) (Figura 20a y 20b) deriva de las células solares orgánicas, donde una capa de PEDOT:PSS es utilizada como HTL como contacto frontal y una capa de PCBM como ETL. La estructura *n-i-p* (o “regular”) (Figura 20c y 20d) deriva de las células solares sensibilizadas por colorantes, donde el óxido TiO₂ es el ETL como contacto frontal y el spiro-OMeTAD es utilizado como HTL.

Estado del arte

Las células solares de perovskita están alcanzando las eficiencias de células solares fabricadas con silicio cristalino (26%).²³⁷ Hasta la fecha, las células solares más eficientes tienen eficiencias del 22,1% en áreas pequeñas (0,09 cm²),²³⁸ del 12,1% en un módulo de 36,1 cm²,²³⁹ y del 23,6% en el caso de una célula solar tándem monolítica perovskita/Si.²⁴⁰ Además, se ha obtenido el 18% de eficiencia en una célula solar flexible con área 0,1 cm².²⁴¹ Sin embargo, su estabilidad a largo plazo y la toxicidad del plomo empleado en su fabricación son dos problemas a resolver para su aplicación. La transición a perovskitas con composición multicomponente (multicatión/multihaluro) representa una vía para aumentar la estabilidad.²⁴²⁻²⁴⁵ Sin embargo, el reemplazo del plomo por otro metal menos tóxico es todavía un reto y está dando lugar a nuevas líneas de investigación.

3.2. Mejora de la eficiencia de las células solares de perovskita mediante el aumento de la luz absorbida por efecto del espesor de la capa absorbente

3.2.1. Introducción

La mayoría de las células solares de perovskita publicadas en los primeros años de estudio utilizaban una estructura mesoscópica (ver Figura 20a y 20d) de un óxido metálico transportador de electrones (Figura 20d), la cual requiere un tratamiento térmico a alta temperatura, siendo incompatible con su deposición en sustratos plásticos. La alternativa utilizada actualmente es la fabricación de células solares tipo *p-i-n* donde la perovskita se deposita entre capas orgánicas planas cuyo procesamiento no requiere alta temperatura (Figura 20b). Anteriormente nuestro grupo de investigación depositó en vacío una capa de perovskita MAPbI₃ entre finas capas de materiales selectivos de carga, PEDOT y polyTPD como materiales transportadores de huecos y PCBM como material transportador de electrones.¹⁵² PolyTPD y PCBM fueron seleccionados para bloquear electrones y huecos, respectivamente, debido al buen alineamiento de sus niveles energéticos HOMO y LUMO con las bandas de valencia y de conducción de la perovskita, respectivamente, alcanzando valores de eficiencia mayores de 12%.¹⁵²

Debido al buen rendimiento fotovoltaico obtenido con una capa relativamente fina de MAPbI₃ de 285 nm, un aumento de la fotocorriente generada sería esperable con mayores espesores si la longitud de difusión de las cargas es suficientemente alta en la capa de perovskita. Dependiendo del método de preparación, valores muy diferentes de longitud de difusión de cargas han sido publicados para MAPbI₃, desde 100 a 1000 nm.^{139-140, 250} Aceptando el valor máximo de 1000 nm, una célula solar con una capa absorbente de luz de ese espesor podría ser posible.

Una de las ventajas de la deposición de perovskita en vacío es el control preciso sobre el espesor de la capa. Por lo tanto, en este trabajo se han preparado

capas de entre 210 y 900 nm de MAPbI_3 en vacío y se han implementado en células tipo *p-i-n*. El efecto del espesor de MAPbI_3 en la respuesta fotovoltaica fue evaluado observando un aumento de J_{SC} y una disminución de FF al aumentar el espesor de la capa absorbente de luz. La oxidación parcial de la capa de polyTPD en celdas con 900 nm de perovskita favoreció la recuperación del FF y de la eficiencia obteniéndose valores similares a los máximos alcanzados con espesores menores de perovskita. El mantenimiento de la eficiencia demuestra que con capas orgánicas no limitantes, el rendimiento de la célula solar es independiente de la capa absorbente de luz y que la longitud de difusión de carga no es limitante en la capa de perovskita.

3.2.2. Método experimental

Los materiales empleados en este trabajo, a excepción del $\text{CH}_3\text{NH}_3\text{I}$, están disponibles comercialmente y se utilizaron sin purificación posterior a su adquisición.

La capa de perovskita fue depositada por coevaporación térmica en vacío de los precursores PbI_2 y $\text{CH}_3\text{NH}_3\text{I}$. Los materiales fueron introducidos en crisoles cerámicos, colocados sobre fuentes de evaporación y calentados a sus correspondientes temperaturas de sublimación en una cámara de vacío a $1 \times 10^{-5} - 1 \times 10^{-6}$ mbar (Figura 15). Los sustratos están colocados 20 cm por encima de los crisoles cerámicos. Por debajo de los sustratos, se dispone un obturador “*shutter*” que se mantiene cerrado hasta que la proporción óptima de $\text{PbI}_2:\text{CH}_3\text{NH}_3\text{I}$ es alcanzada. Debido a que el material $\text{CH}_3\text{NH}_3\text{I}$ forma capas no uniformes y blandas, la temperatura del $\text{CH}_3\text{NH}_3\text{I}$ fue mantenida constante a 70 °C y, una vez la lectura en el sensor está estabilizada, se calienta el PbI_2 . La proporción $\text{PbI}_2:\text{CH}_3\text{NH}_3\text{I}$ óptima se determinó mediante la caracterización de la capa depositada mediante difracción de rayos X. Las temperaturas óptimas de deposición obtenidas fueron 250 °C para el PbI_2 y 70 °C para el $\text{CH}_3\text{NH}_3\text{I}$. El proceso fue controlado mediante tres microbalanzas de cuarzo (QCM) situadas en el interior de la cámara, dos para monitorizar el espesor/velocidad

de evaporación de los precursores y una para la deposición de la capa de perovskita.

Las capas finas de MAPbI₃ evaporadas en vacío fueron implementadas en células solares tipo *p-i-n* con la estructura: ITO/PEDOT:PSS/polyTPD(o polyTPD-dopado)/MAPbI₃/PCBM/Au (Figura 21). El proceso de preparación consistió en la deposición de una capa de 80 nm de PEDOT:PSS mediante *spin-coating* sobre un sustrato de ITO previamente limpiado, seguida de la deposición de una capa de 20 nm de polyTPD o polyTPD dopado con AgSbF₆ (0,05% molar). Posteriormente, se depositó en vacío una capa evaporada de perovskita con un rango de espesores entre 210 y 900 nm en el correspondiente dispositivo. Para terminar el dispositivo, se depositaron 20 nm de una capa de PCBM mediante *meniscus coater* y 70 nm de una capa de aluminio mediante evaporación térmica en vacío.

La absorción óptica de las distintas capas se midió con un espectrofotómetro Avantes Avaspec 2048, y el espesor de las mismas con un perfilómetro Ambios XP1. Las capas se caracterizaron por difracción de rayos X de haz rasante (GIXRD) en un difractómetro de polvo analítico PAN Empyrean, usando radiación Cu K α . Las curvas *J-V* y la EQE_{PV} se midieron en un Simulador MiniSum de ECN the Netherlands. Las medidas en función de la intensidad de luz se realizaron colocando filtros neutros (LOT-QuantumDesign GmbH) entre la fuente de luz y el dispositivo. Todas las caracterizaciones fueron realizadas en atmósfera de nitrógeno.

3.2.3. Resultados y discusión

Las propiedades ópticas y la cristalinidad de las capas evaporadas de MAPbI₃ fueron medidas para evaluarlas como capas absorbentes de luz antes de implementarlas en células solares. Todas las capas evaporadas de MAPbI₃ presentaron un principio de absorción a 790 nm, correspondiente a un valor de banda prohibida de ~1,5 eV. En la Figura 22 se observa que el aumento de la absorción (a 760 nm) es prácticamente lineal con el espesor de la capa de

perovskita. El difractograma de rayos X (Figura 23) presenta los picos típicos de la estructura tetragonal de la perovskita. Aunque existen pequeñas variaciones entre los difractogramas, es conocido que la MAPbI₃ tolera pequeñas variaciones de su composición por lo que el rendimiento del dispositivo no se verá afectado por dichas variaciones.²⁵⁶⁻²⁵⁷

Debido a las buenas propiedades de las capas evaporadas de MAPbI₃, éstas fueron implementadas en células solares tipo *p-i-n* con la estructura: ITO/PEDOT:PSS/polyTPD/MAPbI₃/PCBM/Au (Figura 21a). Si se observa el diagrama de niveles de energía (Figura 24a), el desajuste energético entre la capa de PCBM y el electrodo superior (Au) se minimiza debido a que se produce un dipolo interfacial favoreciendo la extracción de las cargas. El rendimiento fotovoltaico de las células solares fue evaluado mediante curvas *J-V* bajo iluminación de 1 sol (100 mW cm⁻²) y los parámetros extraídos de las curvas se presentaron en la Figura 25 y Tabla 3. La fotocorriente generada (*J*_{SC}) aumenta al aumentar la absorción de luz al aumentar el espesor de la capa absorbente de luz de 200 a 400 nm, y continúa aumentando más lentamente hasta alcanzar un espesor de 900 nm (Figura 25). El incremento de *J*_{SC} es de un 5% frente a un aumento del 25% de la absorbancia de luz al aumentar el espesor en el rango de 400 nm a 900 nm (Figura 22), indicando que la eficiencia de absorción se incrementa en dispositivos con espesores más grandes mientras que la eficiencia de recolección se reduce. El *V*_{OC} permanece constante para dispositivos con espesores de perovskita entre 200 y 400 nm y disminuye cerca de un 10% para dispositivos con espesores mayores. Sin embargo, el FF es el parámetro que más se ve afectado, disminuyendo al aumentar el espesor de la capa de perovskita, lo cual influye negativamente en la eficiencia del dispositivo.

Al disminuir la intensidad de luz incidente en un dispositivo con una capa de perovskita relativamente gruesa (Tabla 4), el FF mejora desde un 49% a un 61%, lo cual indica que el factor limitante de la eficiencia es la extracción de carga y no la densidad de defectos o trampas presentes en la perovskita. Esta

limitación en la extracción de carga puede deberse a la diferencia de movilidad de los huecos en la capa de polyTPD en comparación con la capa de perovskita. Para aumentar la extracción de cargas, la capa de polyTPD fue parcialmente oxidada aumentando así su movilidad. Para ello, se fabricó una célula solar tipo *p-i-n* con 900 nm de espesor y estructura ITO/PEDOT:PSS/polyTPD dopado/MAPbI₃/PCBM/Au (Figura 21b). El dispositivo presenta una recuperación del FF, un valor similar de V_{OC} y J_{SC} comparado con el dispositivo con la capa de polyTPD sin dopar (Figura 26). Debido a esta mejora en el rendimiento del dispositivo, se obtuvo una eficiencia del 12% alcanzando los mejores valores reportados para dispositivos con una capa de perovskita de 285 nm.

3.2.4. Conclusiones

En este estudio se fabricaron una serie de dispositivos tipo *p-i-n* con diferentes espesores para la capa de perovskita absorbente de luz (MAPbI₃) depositada en vacío. El dispositivo más eficiente (12,7%) con una capa no dopada transportadora de huecos se obtuvo con un espesor de capa de perovskita de 300 nm. Al aumentar el espesor de la capa absorbente de luz hasta 900 nm, la eficiencia del dispositivo se vio negativamente afectada disminuyendo hasta un valor de 7,2%. Sin embargo, si el material transportador de huecos (polyTPD) se dopa ligeramente, el dispositivo recupera la eficiencia (12%) comparado con la célula solar más eficiente de la serie (12,7%) fabricada con una capa de perovskita más fina.

Los resultados obtenidos demuestran que las cargas fotogeneradas en la capa de perovskita no se ven afectadas por pérdidas de recombinación significativas en capas muy gruesas, corroborando los altos valores de longitudes de difusión de las cargas. En este trabajo se demuestra que el rendimiento de la célula solar es prácticamente independiente del espesor de la capa de perovskita para valores entre 300 y 900 nm.

Los resultados obtenidos en este trabajo se publicaron en el siguiente artículo científico (FI = Factor de impacto (Science Citation Reports, Web of Science), Q = Cuartil):

Artículo. **Momblona, C.**; Malinkiewicz, O.; Roldán-Carmona, C.; Soriano, A.; Gil-Escrig, L.; Bandiello, E.; Scheepers, M.; Edri, E.; Bolink, H. J., Efficient methylammonium lead iodide perovskite solar cells with active layers from 300 to 900 nm. *APL Materials* **2014**, 2 (8), 081504. (FI: 4.335, Q1).

3.3. Células solares totalmente evaporadas altamente eficientes tipo *p-i-n* y *n-i-p*

3.3.1. Introducción

La comprensión de las propiedades y limitaciones de las capas selectivas de cargas adyacentes a la capa de perovskita es de gran importancia para el desarrollo de células solares de alta eficiencia. Las estrategias utilizadas para mejorar la extracción de cargas han sido el uso de capas muy finas o el aumento de la movilidad de las cargas mediante oxidación o reducción parcial (dopado) de la capa. Una alternativa para aumentar la conductividad de las capas de extracción de cargas consiste en el uso de capas de semiconductores orgánicos dopados. El uso de dopantes moleculares mediante coevaporación reduce la tendencia a difundir en el semiconductor y la conductividad puede aumentar del orden de varios órdenes de magnitud variando la concentración de dopante. Los dopantes moleculares han sido típicamente utilizados en OLEDs y en células solares orgánicas, ya que presentan temperaturas de sublimación apropiadas entre 100 y 400 °C y proporcionan un dopado más estable.

En esta parte de la tesis, se han fabricado células solares donde todas sus capas han sido depositadas en vacío, donde la capa de MAPbI₃ ha sido depositada entre dos capas dobles de extracción de cargas. Cada una de las capas está compuesta por una fina capa intrínseca de material semiconductor actuando como capa transportadora de cargas y una capa más gruesa consistente en el mismo material semiconductor parcialmente oxidado (en el caso del transportador de huecos) o reducido (en el caso de la capa transportadora de electrones). Esta secuencia de capas ha sido preparada en células solares tipo *p-i-n* y *n-i-p* permitiendo por primera vez una comparación directa entre ambos tipos de dispositivos. El efecto y función de las capas no dopadas y dopadas en el rendimiento del dispositivo fue estudiado de forma exhaustiva.

3.3.2. Método experimental

Todos los materiales empleados en este trabajo están disponibles comercialmente y se utilizaron sin purificación posterior a su adquisición. Se seleccionó el F₆-TCNNQ como dopante molecular del material transportador de huecos TaTm y el PhIm como el dopante para el material transportador de electrones C₆₀, debido a sus adecuadas temperaturas de sublimación en vacío.

Se fabricaron dos tipos diferentes de células solares planas, tipo *p-i-n* y *n-i-p*, con las siguientes configuraciones (Figura 27): ITO/TaTm:F₆-TCNNQ(40 nm)/TaTm(10 nm)/MAPbI₃(500 nm)/C₆₀(10 nm)/C₆₀:PhIm(40 nm)/Ag(100 nm) (Figura 27a) e ITO/C₆₀:PhIm(40 nm)/C₆₀(10 nm)/MAPbI₃(500 nm)/TaTm(10 nm)/TaTm:F₆TCNNQ(40 nm)/Au(100 nm) (Figura 27b). La capa dopada compuesta por TaTm:F₆-TCNNQ se referirá en el texto como *p*-HTL y la capa dopada compuesta por C₆₀:PhIm se referirá como *n*-ETL. Los dispositivos se fabricaron en una cámara de vacío, la cual contiene seis fuentes térmicas para evaporación de moléculas. La estructura de la cámara de vacío y monitorización del proceso son los mismos descritos en el capítulo anterior. Previamente a la deposición de las capas, cada material fue calibrado individualmente y se obtuvo un factor de calibración para la diferencia de lectura de espesor en el sensor y el espesor real de la capa depositada. Una vez obtenido el factor de calibración, los materiales fueron co-evaporados en el rango de temperaturas de 135–160 °C para los dopantes y 250 °C para las moléculas transportadoras de carga. Para la optimización de la concentración de dopante en las capas dopadas, la velocidad de deposición para los materiales TaTm y C₆₀ fue mantenida constante a 0,8 Å s⁻¹ mientras se variaba la velocidad de deposición de los dopantes durante la co-deposición. Las capas puras de TaTm y C₆₀ fueron depositadas a una velocidad de evaporación de 0,5 Å s⁻¹.

En la fabricación de los dispositivos *p-i-n* (Figura 27a) se depositaron 40 nm de *p*-HTL (TaTm:F₆-TCNNQ) y 10 nm de TaTm puro, mientras que en la fabricación de los dispositivos *n-i-p* (Figura 27b) se depositaron una capa de

40 nm de *n*-ETL (C_{60} :PhIm) y 10 nm de C_{60} puro. Una vez depositados los respectivos contactos selectivos de carga, se depositó una capa de perovskita de 500 nm de espesor siguiendo el mismo procedimiento al descrito en la Sección 3.2.2. de este capítulo. A continuación, se depositaron una capa de 10 nm de C_{60} puro y una capa de 40 nm de *n*-ETL (C_{60} :PhIm) (*p-i-n*, Figura 27a) o 10 nm de TaTm y 40 nm de *p*-HTL (TaTm:F₆-TCNNQ) (*n-i-p*, Figura 27b). Se completaron los dispositivos con la deposición de una capa de 100 nm del respectivo electrodo superior (Ag para *p-i-n* y Au para *n-i-p*) mediante evaporación térmica en vacío.

Las capas de perovskita y los dispositivos fueron caracterizados de igual manera a la descrita en la Sección 3.2.2. de este capítulo.

3.3.3. Resultados y discusión

Como etapa previa se depositó una capa de 500 nm de perovskita sobre vidrio y se estudiaron sus propiedades ópticas, morfológicas y cristalinas. El difractograma de rayos X presenta los picos típicos de la fase tetragonal de MAPbI₃ (Figura 28a). La morfología superficial de la capa observada por SEM presenta una capa compacta, libre de huecos y con un tamaño de grano de entorno a 100 nm (Figura 28b). El espectro de absorción exhibe absorción que comienza de forma abrupta a 790 nm correspondiente a una banda prohibida de ~1.5 eV (Figura 28c).

Una vez caracterizada la capa, ésta se implementó en células solares tipo *p-i-n* con la configuración ITO/TaTm/MAPbI₃/ C_{60} /Ag. La respuesta fotovoltaica de la célula solar bajo iluminación de 1 sol es muy baja presentando un pronunciado efecto *s-shape*, el cual indica que la extracción de las cargas está impedida debido a una alta resistencia de las capas transportadoras de cargas o a la existencia de una barrera de extracción de las cargas en las interfaces con los electrodos.

Para reducir la resistencia en serie del dispositivo y asegurar un contacto óhmico entre las capas orgánicas y los electrodos, se introdujo una

capa parcialmente oxidada y reducida entre las interfaces TCO/HTL y ETL/metál, respectivamente (Figura 27). La conductividad y absorción de las capas *p*-HTL y *n*-ETL se midieron para diferentes concentraciones de dopante, observando que la conductividad y absorción de la capa *p*-HTL aumenta al aumentar la concentración de dopante (Figura 31a y 31c). Sin embargo, en la capa *n*-ETL la conductividad aumenta pero la absorbancia disminuye al aumentar la concentración de dopante (Figura 31b y 31d). Hay que resaltar que la conductividad de la capa *p*-HTL es dos órdenes de magnitud menor que la de la capa *n*-ETL en el rango de concentración de dopantes estudiado.

En células solares tipo *p-i-n*, para optimizar la concentración de dopante en la capa *p*-HTL, se mantuvo constante la concentración de dopante en el contacto *n*-ETL a 30% en peso. A partir de los datos obtenidos de las curvas *J-V* medidas bajo iluminación de 1 sol en dispositivos con diferentes cantidades de dopante en la capa *p*-HTL (Figura 32), se observó un aumento en el FF de 55% a 74% cuando se aumenta la concentración de dopante en la capa *p*-HTL desde un 3% a un 11% en peso. Las cargas se extraen más eficientemente al aumentar la conductividad en la capa. Además, el V_{OC} también aumenta debido a una reducción de la recombinación de carga al verse favorecida la extracción de cargas hacia los electrodos. Sin embargo, el J_{SC} disminuye al aumentar la concentración de dopante debido a que la capa *p*-HTL absorbe más al aumentar la concentración de dopante, disminuyendo la luz que incide en la capa de perovskita. Se obtuvo una concentración óptima de dopante en la capa *p*-HTL del 11% en peso obteniendo células solares con PCE del 15,9%. Una vez optimizada la concentración de dopante de la capa *p*-HTL, ésta se mantuvo constante a la óptima concentración de 11% en peso y la concentración de dopante en la capa *n*-ETL fue modificada. En este caso, el efecto de la concentración de dopante en la capa *n*-ETL no es significativo y se obtuvieron rendimientos similares en el rango de concentraciones de dopante estudiado, debido a que la conductividad de la capa *n*-ETL es suficientemente alta para la extracción de cargas hacia el electrodo (Ag).

En los dispositivos tipo *n-i-p*, el electrodo superior elegido fue el Au debido a su función de trabajo más alta en comparación con la Ag. Para optimizar la concentración de dopante en la capa *n*-ETL, ésta se varió mientras que la concentración de dopante *p*-HTL se mantuvo constante e igual a un 11% en peso (Figura 33). El J_{SC} aumenta al aumentar la concentración de dopante debido a la menor absorción de la capa *n*-ETL. El V_{OC} y el FF se mantuvieron constantes en el rango de concentraciones de dopante evaluado, presentando altos valores de 1,1 V y 80%, respectivamente. Estos valores dan lugar a valores de PCE del 18% y a una célula solar con un 20% de eficiencia, la cual constituye el record no sólo de células solares con perovskita depositadas en vacío, sino también de células solares basadas en MAPbI₃.

Los resultados demuestran un fuerte aumento en el rendimiento de las células solares *n-i-p* respecto a las *p-i-n*, debido a un mayor valor de FF en *n-i-p* (80%) en comparación con *p-i-n* (70%) (Figura 34). El aumento de FF puede ser debido a la diferencia de conductividad de las capas transportadoras de cargas dopadas en el contacto frontal con el ITO, ya que la conductividad de la capa *n*-ETL es dos órdenes de magnitud mayor que la conductividad de la capa *p*-HTL. Para esclarecer esta diferencia, se realizaron medidas de dependencia de FF frente a la intensidad de luz incidente en ambas configuraciones (Figura 35). El FF de las células solares *p-i-n* aumenta al disminuir la intensidad de luz y luego disminuye (Figura 35a), mientras que en los dispositivos *n-i-p* el FF no se ve afectado por la intensidad de luz incidente al comienzo y luego disminuye (Figura 35b). Esta tendencia confirma que en la configuración *p-i-n* existe una barrera de extracción de los huecos. Las medidas de la eficiencia cuántica externa de electroluminiscencia (Figuras 35c y 35d) demostraron una mayor eficiencia y una inyección de cargas más balanceada en los dispositivos *n-i-p*. La habilidad de inyectar más eficientemente huecos cuando la capa *p*-HTL está situada entre la capa de HTL y el electrodo superior Au (*n-i-p*) se puede explicar considerando que el electrodo metálico es evaporado térmicamente encima de la capa *p*-HTL, lo cual da lugar a un contacto más eficiente debido a que átomos

metálicos pueden penetrar ligeramente en las capas orgánicas y aumentar su conductividad. La mejor celda tipo *n-i-p* presenta un valor de $EQE_{EL} = 0,36\%$, el cual es uno de los mayores valores publicados para diodos emisores de luz empleando como capa emisora $MAPbI_3$.

La histéresis de los dispositivos fue evaluada a diferentes velocidades de barrido en curvas $J-V$ (Figura 36). Se observó una histéresis mínima en dispositivos *p-i-n* con pequeñas fluctuaciones en V_{OC} y FF debidas a un posible problema de extracción de las cargas en la interface ITO/*p*-HTL (Figura 36a). Sin embargo, los dispositivos *n-i-p* no presentan histéresis a ninguna de las velocidades de barrido estudiadas (Figura 36b).

Para estudiar el efecto de las capas HTL y ETL en el dispositivo, se fabricaron y evaluaron una serie de células solares *p-i-n* sin la presencia de una de las dos capas intrínsecas (Figura 37a y Tabla 5). El rendimiento de la célula solar que no contiene la capa intrínseca ETL es significativamente peor que la célula solar de referencia que contiene ambas capas debido a que recombinación entre electrones y huecos puede ocurrir en la interface causando la reducción simultánea de todos los parámetros de la célula solar. Sin embargo, para las células solares que no contienen la capa intrínseca HTL, su rendimiento empeora ligeramente en comparación con la célula de referencia, debido a la menor conductividad de la capa *p*-HTL (comparado con la capa *n*-ETL), la cual puede confinar los electrones en la capa de perovskita y disminuir la recombinación de carga en la interface *p*-HTL/ $MAPbI_3$.

El efecto de la eliminación de las capas intrínsecas en dispositivos *n-i-p* también fue evaluado (Figura 37b y Tabla 5). La supresión de la capa de C_{60} reduce el rendimiento de la célula solar en los parámetros V_{OC} y FF, mientras la supresión de la capa de TaTm tiene un efecto mínimo. Por lo tanto, la presencia de las capas intrínsecas entre la capa de perovskita y las capas dopadas es necesaria para la obtención de células solares altamente eficientes independientemente de la configuración del dispositivo.

Por último, se evaluó el efecto de las capas dopadas en el rendimiento de las células solares (Figura 38). En ambas configuraciones, las capas *p*-HTL y *n*-ETL son esenciales para evitar problemas severos en la extracción de cargas. Sin embargo, dispositivos tipo *p-i-n* con una capa fina de C₆₀ y el electrodo superior (Ag) presentan un apreciable rendimiento fotovoltaico debido al dipolo que se crea en la interface C₆₀/Ag aumentando la extracción de las cargas hacia el electrodo.

3.3.4. Conclusiones

En este trabajo se han fabricado células solares de perovskita cuyas capas han sido depositadas por deposición en vacío. La capa absorbente de luz (MAPbI₃) se depositó entre capas intrínsecas y dopadas compuestas por moléculas orgánicas transportadoras de cargas. En concreto, se fabricaron y evaluaron dos tipos diferentes de configuraciones, una invertida respecto a la otra, *p-i-n* y *n-i-p* produciendo células solares planas sin histéresis y con muy altas eficiencias, 16,5% and 20%, respectivamente.

Los resultados demostraron que las prestaciones de las células solares tipo *n-i-p* eran superiores a las obtenidas en la configuración *p-i-n*. Este aumento, debido al incremento en el FF, está probablemente relacionado con la diferencia de conductividad en la capa transportadora de cargas dopada en el contacto frontal, siendo mayor la conductividad de la capa *n* produciendo una extracción e inyección de cargas más eficiente con la interface del ITO y presentando un mayor balance entre las cargas.

En este trabajo se optimizó la concentración de dopante que contiene la capa dopada del contacto frontal. La optimización se realizó mediante medidas de absorbancia y conductividad de las capas con diferentes concentraciones de dopante, junto con su evaluación en la respuesta fotovoltaica de los correspondientes dispositivos mediante curvas *J-V*. Los valores óptimos de concentración de dopante fueron de 11% en peso de dopante tipo *p* (F₆-TCNNQ) para la capa *p*-HTL (configuración *p-i-n*) y 60% en peso

de dopante tipo n (PhIm) para la capa n -ETL (configuración n - i - p). En ambas configuraciones, la concentración de dopante en la capa dopada del contacto superior se mantuvo constante a 30% en peso de dopante tipo n (PhIm) (configuración p - i - n) y a 11% en peso de dopante tipo p (F₆-TCNNQ) (configuración n - i - p).

Se estudió el efecto de las capas intrínsecas y dopadas transportadoras de huecos en el rendimiento fotovoltaico de las células solares. Para ello, se fabricaron células solares tipo p - i - n y n - i - p sin la presencia de una de las dos capas intrínsecas o sin una de las dos capas dopadas.

El rendimiento fotovoltaico de las células solares p - i - n sin capa intrínseca ETL se vio significativamente afectada en comparación con células solares sin la capa intrínseca HTL. Esto es debido a que la menor conductividad de la capa p -HTL puede confinar los electrones en la capa de perovskita reduciendo la recombinación de carga en la interface p -HTL/MAPbI₃. Mientras que en dispositivos n - i - p , la supresión de la capa de ETL reduce el rendimiento de la célula solar mientras que la supresión de la capa de HTM tiene un mínimo efecto.

En el estudio de la supresión de las capas dopadas se observó un mayor efecto negativo en el rendimiento de las células solares. En ambas configuraciones, las capas p -HTL y n -ETL son esenciales para evitar problemas severos en la extracción de cargas. Sin embargo, en dispositivos tipo p - i - n con una capa fina de C₆₀ y el electrodo superior (Ag) presentan un apreciable rendimiento fotovoltaico debido al dipolo que se crea en la interface aumentando la extracción de las cargas hacia el electrodo.

Por lo tanto, la presencia de las capas intrínsecas entre la capa de perovskita y las capas dopadas es necesaria para la obtención de células solares altamente eficientes independientemente de la configuración del dispositivo.

Este trabajo representó el poder realizar por primera vez una comparación directa entre estas dos configuraciones, p - i - n y n - i - p , utilizando

los mismos materiales en su fabricación e invirtiendo únicamente el orden de deposición de los mismos. Tras la optimización, las células solares no presentaron histéresis y se obtuvieron muy altas eficiencias, mayores de 16.5% (*p-i-n*) y 20% (*n-i-p*), siendo no solo las eficiencias más altas publicadas en células solares depositadas en vacío sino también entre las células solares cuya capa absorbente de luz es MAPbI₃. También, los dispositivos fueron evaluados como diodos emisores de luz obteniendo el máximo valor de EQE_{EL} (EQE_{EL}=0,36%) entre los diodos emisores de luz basados en MAPbI₃ publicados.

Además, la fabricación de estos dispositivos cuyas capas han sido depositadas en vacío, demuestran que se puede realizar una modificación de las propiedades del dispositivo controlando la composición de las capas, permitiendo el uso de este tipo de células solares en una específica aplicación de los mismos en configuración tipo tándem.

Los resultados obtenidos en este trabajo se publicaron en el siguiente artículo científico (FI = Factor de impacto (Science Citation Reports, Web of Science), Q = Cuartil):

Artículo. **Momblona, C.**;[‡] Gil-Escrig, L.;[‡] Bandiello, E.; Hutter, E. M.; Sessolo, M.; Lederer, K.; Blochwitz-Nimoth, J.; Bolink, H. J.; Efficient vacuum deposited p-i-n and n-i-p perovskite solar cells employing doped charge transport layers. *Energy & Environmental Science* **2016**, 9 (11), 3456-3463. ([‡] igualmente contribuido). (FI: 29.518, Q1).

References

1. <http://www.bp.com/statisticalreview>.
2. <https://www.energy.gov/>.
3. Shinde, K. N.; Dhoble, S. J.; Swart, H. C.; Park, K., Current progress in solid-state lighting. In *Phosphate phosphors for solid-state lighting*, Springer Berlin Heidelberg: Berlin, Heidelberg, 2012; pp 249-264.
4. <https://www.worldenergy.org>.
5. Pei, Q.; Yang, Y.; Yu, G.; Zhang, C.; Heeger, A. J., Polymer light-emitting electrochemical cells: In situ formation of a light-emitting p-n junction. *Journal of the American Chemical Society* **1996**, *118* (16), 3922-3929.
6. Yang, Y.; Pei, Q., Voltage controlled two color light-emitting electrochemical cells. *Applied Physics Letters* **1996**, *68* (19), 2708-2710.
7. Sun, M.; Zhong, C.; Li, F.; Cao, Y.; Pei, Q., A fluorene-oxadiazole copolymer for white light-emitting electrochemical cells. *Macromolecules* **2010**, *43* (4), 1714-1718.
8. Tang, S.; Pan, J.; Buchholz, H. A.; Edman, L., White light from a single-emitter light-emitting electrochemical cell. *Journal of the American Chemical Society* **2013**, *135* (9), 3647-3652.
9. Hu, Y.; Zhang, Y.; Gao, J., Strong electroluminescence from polymer films with heavily quenched photoluminescence. *Advanced Materials* **2006**, *18* (21), 2880-2883.
10. Tang, S.; Tan, W.-Y.; Zhu, X.-H.; Edman, L., Small-molecule light-emitting electrochemical cells: evidence for in situ electrochemical doping and functional operation. *Chemical Communications* **2013**, *49* (43), 4926-4928.
11. Chen, H.-F.; Wu, C.; Kuo, M.-C.; Thompson, M. E.; Wong, K.-T., Anionic iridium complexes for solid state light-emitting electrochemical cells. *Journal of Materials Chemistry* **2012**, *22* (19), 9556-9561.
12. Matteucci, E.; Baschieri, A.; Mazzanti, A.; Sambri, L.; Ávila, J.; Pertegás, A.; Bolink, H. J.; Monti, F.; Leoni, E.; Armaroli, N., Anionic cyclometalated Iridium(III) complexes with a bis-tetrazolate ancillary ligand for light-emitting electrochemical cells. *Inorganic Chemistry* **2017**, *56* (17), 10584-10595.
13. Costa, R. D.; Ortí, E.; Bolink, H. J.; Monti, F.; Accorsi, G.; Armaroli, N., Luminescent ionic transition-metal complexes for light-emitting electrochemical cells. *Angewandte Chemie - International Edition* **2012**, *51* (33), 8178-8211.
14. Henwood, A. F.; Zysman-Colman, E., Luminescent iridium complexes used in light-emitting electrochemical cells (LEECs). *Topics in Current Chemistry* **2016**, *374* (4), 1-41.
15. Housecroft, C. E.; Constable, E. C., Over the LEC rainbow: Colour and stability tuning of cyclometallated iridium(III) complexes in light-emitting electrochemical cells. *Coordination Chemistry Reviews* **2017**, *350*, 155-177.
16. Shin, I. S.; Lim, H. C.; Oh, J. W.; Lee, J. K.; Kim, T. H.; Kim, H., Fast-response light-emitting electrochemical cells based on neutral iridium(III) complex. *Electrochemistry Communications* **2011**, *13* (1), 64-67.

17. Norell Bader, A. J.; Ilkevich, A. A.; Kosilkin, I. V.; Leger, J. M., Precise color tuning via hybrid light-emitting electrochemical cells. *Nano Letters* **2011**, *11* (2), 461-465.
18. Wang, D.; Wang, H.; Wang, Q.; Yang, W.; Ding, Y., Amidate-ancillary benzothienyl iridium(III) complexes: Synthesis, structures, photophysical properties and DFT calculations studies. *Journal of Organometallic Chemistry* **2014**, *749*, 41-46.
19. Puscher, B. M. D.; Aygüler, M. F.; Docampo, P.; Costa, R. D., Unveiling the dynamic processes in hybrid lead bromide perovskite nanoparticle thin film devices. *Advanced Energy Materials* **2017**, *7* (15), 1602283.
20. Aygüler, M. F.; Weber, M. D.; Puscher, B. M. D.; Medina, D. D.; Docampo, P.; Costa, R. D., Light-emitting electrochemical cells based on hybrid lead halide perovskite nanoparticles. *The Journal of Physical Chemistry C* **2015**, *119* (21), 12047-12054.
21. Yang, C.-H.; Beltran, J.; Lemaire, V.; Cornil, J. r. m.; Hartmann, D.; Sarfert, W.; Fröhlich, R.; Bizzarri, C.; De Cola, L., Iridium metal complexes containing N-heterocyclic carbene ligands for blue-light-emitting electrochemical cells. *Inorganic Chemistry* **2010**, *49* (21), 9891-9901.
22. Dumur, F.; Yuskevitch, Y.; Wantz, G.; Mayer, C. R.; Bertin, D.; Gigmes, D., Light-emitting electrochemical cells based on a solution-processed multilayered device and an anionic iridium (III) complex. *Synthetic Metals* **2013**, *177*, 100-104.
23. Maness, K. M.; Terrill, R. H.; Meyer, T. J.; Murray, R. W.; Wightman, R. M., Solid-state diode-like chemiluminescence based on serial, immobilized concentration gradients in mixed-valent poly[Ru(vbpy)₃](PF₆)₂ films. *Journal of the American Chemical Society* **1996**, *118* (43), 10609-10616.
24. Slinker, J.; Bernards, D.; Houston, P. L.; Abruña, H.; Bernhard, S.; Malliaras, G. G., Solid-state electroluminescent devices based on transition metal complexes. *Chemical Communications* **2003**, *0* (19), 2392-2399.
25. Lee, J. K.; Yoo, D. S.; Handy, E. S.; Rubner, M. F., Thin film light emitting devices from an electroluminescent ruthenium complex. *Applied Physics Letters* **1996**, *69* (12), 1686-1688.
26. Gao, F. G.; Bard, A. J., High-brightness and low-voltage light-emitting devices based on trischelated ruthenium(II) and tris(2,2'-bipyridine)osmium(II) emitter layers and low melting point alloy cathode contacts. *Chemistry of Materials* **2002**, *14* (8), 3465-3470.
27. Rudmann, H.; Rubner, M. F., Single layer light-emitting devices with high efficiency and long lifetime based on tris(2,2' bipyridyl) ruthenium(II) hexafluorophosphate. *Journal of Applied Physics* **2001**, *90* (9), 4338-4345.
28. Rudmann, H.; Shimada, S.; Rubner, M. F., Solid-state light-emitting devices based on the tris-chelated ruthenium(II) complex. 4. High-efficiency light-emitting devices based on derivatives of the tris(2,2'-bipyridyl) ruthenium(II) complex. *Journal of the American Chemical Society* **2002**, *124* (17), 4918-4921.
29. Buda, M.; Kalyuzhny, G.; Bard, A. J., Thin-film solid-state electroluminescent devices based on tris(2,2'-bipyridine)ruthenium(II)

- complexes. *Journal of the American Chemical Society* **2002**, *124* (21), 6090-6098.
30. Elliott, C. M.; Pichot, F.; Bloom, C. J.; Rider, L. S., Highly efficient solid-state electrochemically generated chemiluminescence from ester-substituted trisbipyridineruthenium(II)-based polymers. *Journal of the American Chemical Society* **1998**, *120* (27), 6781-6784.
 31. Bernhard, S.; Barron, J. A.; Houston, P. L.; Abruña, H. D.; Ruglovksy, J. L.; Gao, X.; Malliaras, G. G., Electroluminescence in ruthenium(II) complexes. *Journal of the American Chemical Society* **2002**, *124* (45), 13624-13628.
 32. Bernhard, S.; Gao, X.; Malliaras, G. G.; Abruña, H. D., Efficient electroluminescent devices based on a chelated osmium(II) complex. *Advanced Materials* **2002**, *14* (6), 433-436.
 33. Hosseini, A. R.; Koh, C. Y.; Slinker, J. D.; Flores-Torres, S.; Abruña, H. D.; Malliaras, G. G., Addition of a phosphorescent dopant in electroluminescent devices from ionic transition metal complexes. *Chemistry of Materials* **2005**, *17* (24), 6114-6116.
 34. Gao, F. G.; Bard, A. J., Solid-state organic light-emitting diodes based on tris(2,2'-bipyridine)ruthenium(II) complexes. *Journal of the American Chemical Society* **2000**, *122* (30), 7426-7427.
 35. Slinker, J. D.; Gorodetsky, A. A.; Lowry, M. S.; Wang, J.; Parker, S.; Rohl, R.; Bernhard, S.; Malliaras, G. G., Efficient yellow electroluminescence from a single layer of a cyclometalated iridium complex. *Journal of the American Chemical Society* **2004**, *126* (9), 2763-2767.
 36. Slinker, J. D.; Rivnay, J.; Moskowitz, J. S.; Parker, J. B.; Bernhard, S.; Abruña, H. D.; Malliaras, G. G., Electroluminescent devices from ionic transition metal complexes. *Journal of Materials Chemistry* **2007**, *17* (29), 2976-2988.
 37. Gong, X.; Ng, P. K.; Chan, W. K., Trifunctional light-emitting molecules based on rhenium and ruthenium bipyridine complexes. *Advanced Materials* **1998**, *10* (16), 1337-1340.
 38. Li, F.; Zhang, M.; Cheng, G.; Feng, J.; Zhao, Y.; Ma, Y.; Liu, S.; Shen, J., Highly efficient electrophosphorescence devices based on rhenium complexes. *Applied Physics Letters* **2004**, *84* (1), 148-150.
 39. Ranjan, S.; Lin, S.-Y.; Hwang, K.-C.; Chi, Y.; Ching, W.-L.; Liu, C.-S.; Tao, Y.-T.; Chien, C.-H.; Peng, S.-M.; Lee, G.-H., Realizing green phosphorescent light-emitting materials from rhenium(I) pyrazolato diimine complexes. *Inorganic Chemistry* **2003**, *42* (4), 1248-1255.
 40. Lu, W.; Chan, M. C. W.; Zhu, N.; Che, C.-M.; Li, C.; Hui, Z., Structural and spectroscopic studies on Pt···Pt and π - π interactions in luminescent multinuclear cyclometalated platinum(II) homologues tethered by oligophosphine auxiliaries. *Journal of the American Chemical Society* **2004**, *126* (24), 7639-7651.
 41. Costa, R. D.; Tordera, D.; Ortí, E.; Bolink, H. J.; Schönle, J.; Graber, S.; Housecroft, C. E.; Constable, E. C.; Zampese, J. A., Copper(I) complexes for sustainable light-emitting electrochemical cells. *Journal of Materials Chemistry* **2011**, *21* (40), 16108-16118.

42. Elie, M.; Sguerra, F.; Di Meo, F.; Weber, M. D.; Marion, R.; Grimault, A.; Lohier, J.-F.; Stallivieri, A.; Brosseau, A.; Pansu, R. B.; Renaud, J.-L.; Linares, M.; Hamel, M.; Costa, R. D.; Gaillard, S., Designing NHC–copper(I) dipyriddyamine complexes for blue light-emitting electrochemical cells. *ACS Applied Materials and Interfaces* **2016**, *8* (23), 14678-14691.
43. Armaroli, N.; Accorsi, G.; Holler, M.; Moudam, O.; Nierengarten, J. F.; Zhou, Z.; Wegh, R. T.; Welter, R., Highly luminescent Cu^I complexes for light-emitting electrochemical cells. *Advanced Materials* **2006**, *18* (10), 1313-1316.
44. Keller, S.; Constable, E. C.; Housecroft, C. E.; Neuburger, M.; Prescimone, A.; Longo, G.; Pertegás, A.; Sessolo, M.; Bolink, H. J., [Cu(bpy)(P[^]P)]⁺ containing light-emitting electrochemical cells: improving performance through simple substitution. *Dalton Transactions* **2014**, *43* (44), 16593-16596.
45. Murray, N. S.; Keller, S.; Constable, E. C.; Housecroft, C. E.; Neuburger, M.; Prescimone, A., [Cu(N[^]N)(P[^]P)]⁺ complexes with 2,2':6',2''-terpyridine ligands as the N[^]N domain. *Dalton Transactions* **2015**, *44* (16), 7626-7633.
46. Weber, M. D.; Viciano-Chumillas, M.; Armentano, D.; Cano, J.; Costa, R. D., σ -Hammett parameter: a strategy to enhance both photo- and electro-luminescence features of heteroleptic copper(I) complexes. *Dalton Transactions* **2017**, *46* (19), 6312-6323.
47. Schneider, G. E.; Bolink, H. J.; Constable, E. C.; Ertl, C. D.; Housecroft, C. E.; Pertegás, A.; Zampese, J. A.; Kanitz, A.; Kessler, F.; Meier, S. B., Chloride ion impact on materials for light-emitting electrochemical cells. *Dalton Transactions* **2014**, *43* (5), 1961-1964.
48. Costa, R. D.; Ortí, E.; Bolink, H. J.; Graber, S.; Schaffner, S.; Neuburger, M.; Housecroft, C. E.; Constable, E. C., Archetype cationic iridium complexes and their use in solid-state light-emitting electrochemical cells. *Advanced Functional Materials* **2009**, *19* (21), 3456-3463.
49. Hay, P. J., Theoretical studies of the ground and excited electronic states in cyclometalated phenylpyridine Ir(III) complexes using density functional theory. *The Journal of Physical Chemistry A* **2002**, *106* (8), 1634-1641.
50. Lowry, M. S.; Goldsmith, J. I.; Slinker, J. D.; Rohl, R.; Pascal, R. A.; Malliaras, G. G.; Bernhard, S., Single-layer electroluminescent devices and photoinduced hydrogen production from an ionic iridium(III) complex. *Chemistry of Materials* **2005**, *17* (23), 5712-5719.
51. Flamigni, L.; Barbieri, A.; Sabatini, C.; Ventura, B.; Barigelletti, F., Photochemistry and Photophysics of Coordination Compounds: Iridium. In *Photochemistry and Photophysics of Coordination Compounds II*, Balzani, V.; Campagna, S., Eds. Springer Berlin Heidelberg: Berlin, Heidelberg, 2007; pp 143-203.
52. Lowry, M. S.; Bernhard, S., Synthetically Tailored Excited States: Phosphorescent, Cyclometalated Iridium(III) Complexes and Their Applications. *Chemistry – A European Journal* **2006**, *12* (31), 7970-7977.
53. Costa, R. D.; Monti, F.; Accorsi, G.; Barbieri, A.; Bolink, H. J.; Ortí, E.; Armaroli, N., Photophysical properties of charged cyclometalated Ir(III)

- complexes: a joint theoretical and experimental study. *Inorganic Chemistry* **2011**, *50* (15), 7229-7238.
54. Sajoto, T.; Djurovich, P. I.; Tamayo, A. B.; Oxgaard, J.; Goddard, W. A.; Thompson, M. E., Temperature dependence of blue phosphorescent cyclometalated Ir(III) complexes. *Journal of the American Chemical Society* **2009**, *131* (28), 9813-9822.
55. Hu, T.; He, L.; Duan, L.; Qiu, Y., Solid-state light-emitting electrochemical cells based on ionic iridium(III) complexes. *Journal of Materials Chemistry* **2012**, *22* (10), 4206-4215.
56. Xu, H.; Chen, R.; Sun, Q.; Lai, W.; Su, Q.; Huang, W.; Liu, X., Recent progress in metal-organic complexes for optoelectronic applications. *Chemical Society Reviews* **2014**, *43* (10), 3259-3302.
57. Ma, D.; Tsuboi, T.; Qiu, Y.; Duan, L., Recent progress in ionic iridium(III) complexes for organic electronic devices. *Advanced Materials* **2017**, *29* (3), 1603253.
58. Henwood, A. F.; Zysman-Colman, E., Lessons learned in tuning the optoelectronic properties of phosphorescent iridium(III) complexes. *Chemical Communications* **2017**, *53* (5), 807-826.
59. Carter, S. A.; Victor, J. G.; Tuttle, S.; Breeden, J., Screen printable electroluminescent polymer ink. Google Patents: 2003.
60. Bernards, D. A.; Biegala, T.; Samuels, Z. A.; Slinker, J. D.; Malliaras, G. G.; Flores-Torres, S.; Abruña, H. D.; Rogers, J. A., Organic light-emitting devices with laminated top contacts. *Applied Physics Letters* **2004**, *84* (18), 3675-3677.
61. Sandström, A.; Dam, H. F.; Krebs, F. C.; Edman, L., Ambient fabrication of flexible and large-area organic light-emitting devices using slot-die coating. *Nature Communications* **2012**, *3*, 1002.
62. Lindh, E. M.; Sandström, A.; Edman, L., Inkjet printed bilayer light-emitting electrochemical cells for display and lighting applications. *Small* **2014**, *10* (20), 4148-4153.
63. Sandström, A.; Asadpoordarvish, A.; Enevold, J.; Edman, L., Spraying light: ambient-air fabrication of large-area emissive devices on complex-shaped surfaces. *Advanced Materials* **2014**, *26* (29), 4975-4980.
64. Hernandez-Sosa, G.; Tekoglu, S.; Stolz, S.; Eckstein, R.; Teusch, C.; Trapp, J.; Lemmer, U.; Hamburger, M.; Mechau, N., The compromises of printing organic electronics: a case study of gravure-printed light-emitting electrochemical cells. *Advanced Materials* **2014**, *26* (20), 3235-3240.
65. Lindh, E. M.; Sandström, A.; Andersson, M. R.; Edman, L., Luminescent line art by direct-write patterning. *Light: Science & Applications* **2016**, *5*, e16050.
66. Mauthner, G.; Landfester, K.; Köck, A.; Brückl, H.; Kast, M.; Stepper, C.; List, E. J. W., Inkjet printed surface cell light-emitting devices from a water-based polymer dispersion. *Organic Electronics* **2008**, *9* (2), 164-170.
67. Gao, J.; Dane, J., Visualization of electrochemical doping and light-emitting junction formation in conjugated polymer films. *Applied Physics Letters* **2004**, *84* (15), 2778-2780.

68. Shin, J.-H.; Edman, L., Light-emitting electrochemical cells with millimeter-sized interelectrode gap: low-voltage operation at room temperature. *Journal of the American Chemical Society* **2006**, *128* (49), 15568-15569.
69. van Reenen, S.; Matyba, P.; Dzwilewski, A.; Janssen, R. A. J.; Edman, L.; Kemerink, M., A unifying model for the operation of light-emitting electrochemical cells. *Journal of the American Chemical Society* **2010**, *132* (39), 13776-13781.
70. Bernards, D. A.; Slinker, J. D.; Malliaras, G. G.; Flores-Torres, S.; Abruña, H. D., Cascaded light-emitting devices based on a ruthenium complex. *Applied Physics Letters* **2004**, *84* (24), 4980-4982.
71. Slinker, J. D.; Rivnay, J.; DeFranco, J. A.; Bernards, D. A.; Gorodetsky, A. A.; Parker, S. T.; Cox, M. P.; Rohl, R.; Malliaras, G. G.; Flores-Torres, S.; Abruña, H. D., Direct 120 V, 60 Hz operation of an organic light emitting device. *Journal of Applied Physics* **2006**, *99* (7), 074502.
72. Lin, K. Y.; Bastatas, L. D.; Suhr, K. J.; Moore, M. D.; Holliday, B. J.; Minary-Jolandan, M.; Slinker, J. D., Influence of lithium additives in small molecule light-emitting electrochemical cells. *ACS Applied Materials and Interfaces* **2016**, *8* (26), 16776-16782.
73. Suhr, K. J.; Bastatas, L. D.; Shen, Y.; Mitchell, L. A.; Holliday, B. J.; Slinker, J. D., Enhanced luminance of electrochemical cells with a rationally designed ionic iridium complex and an ionic additive. *ACS Applied Materials and Interfaces* **2016**, *8* (14), 8888-8892.
74. Bandiello, E.; Sessolo, M.; Bolink, H. J., Lithium salt additives and the influence of their counterion on the performances of light-emitting electrochemical cells. *Journal of Materials Chemistry C* **2016**, *4* (46), 10781-10785.
75. Shen, Y.; Kuddes, D. D.; Naquin, C. A.; Hesterberg, T. W.; Kusmierz, C.; Holliday, B. J.; Slinker, J. D., Improving light-emitting electrochemical cells with ionic additives. *Applied Physics Letters* **2013**, *102* (20), 203305.
76. Parker, S. T.; Slinker, J. D.; Lowry, M. S.; Cox, M. P.; Bernhard, S.; Malliaras, G. G., Improved turn-on times of iridium electroluminescent devices by use of ionic liquids. *Chemistry of Materials* **2005**, *17* (12), 3187-3190.
77. Slinker, J. D.; Koh, C. Y.; Malliaras, G. G.; Lowry, M. S.; Bernhard, S., Green electroluminescence from an ionic iridium complex. *Applied Physics Letters* **2005**, *86* (17), 173506.
78. Lee, K. W.; Slinker, J. D.; Gorodetsky, A. A.; Flores-Torres, S.; Abruña, H. D.; Houston, P. L.; Malliaras, G. G., Photophysical properties of tris(bipyridyl)ruthenium(II) thin films and devices. *Physical Chemistry Chemical Physics* **2003**, *5* (12), 2706-2709.
79. Malliaras, G. G.; Scott, J. C., The roles of injection and mobility in organic light emitting diodes. *Journal of Applied Physics* **1998**, *83* (10), 5399-5403.
80. Schanda, J., CIE Colorimetry. In *Colorimetry*, John Wiley & Sons, Inc.: 2007; pp 25-78.

81. Pei, Q.; Yu, G.; Zhang, C.; Yang, Y.; Heeger, A. J., Polymer light-emitting electrochemical cells. *Science* **1995**, *269* (5227), 1086-1088.
82. Smith, D. L., Steady state model for polymer light-emitting electrochemical cells. *Journal of Applied Physics* **1997**, *81* (6), 2869-2880.
83. deMello, J. C.; Tessler, N.; Graham, S. C.; Friend, R. H., Ionic space-charge effects in polymer light-emitting diodes. *Physical Review B* **1998**, *57* (20), 12951-12963.
84. deMello, J. C.; Halls, J. J. M.; Graham, S. C.; Tessler, N.; Friend, R. H., Electric field distribution in polymer light-emitting electrochemical cells. *Physical Review Letters* **2000**, *85* (2), 421-424.
85. deMello, J. C., Interfacial feedback dynamics in polymer light-emitting electrochemical cells. *Physical Review B* **2002**, *66* (23), 235210.
86. Malliaras, G. G.; Slinker, J. D.; Defranco, J. A.; Jaquith, M. J.; Silveira, W. R.; Zhong, Y. W.; Moran-Mirabal, J. M.; Craighead, H. G.; Abruña, H. D.; Marohn, J. A., Operating mechanism of light-emitting electrochemical cells. *Nature Materials* **2008**, *7* (3), 167-168.
87. Lenes, M.; García-Belmonte, G.; Tordera, D.; Pertegás, A.; Bisquert, J.; Bolink, H. J., Operating modes of sandwiched light-emitting electrochemical cells. *Advanced Functional Materials* **2011**, *21* (9), 1581-1586.
88. Tordera, D.; Meier, S.; Lenes, M.; Costa, R. D.; Ortí, E.; Sarfert, W.; Bolink, H. J., Simple, fast, bright, and stable light sources. *Advanced Materials* **2012**, *24* (7), 897-900.
89. Shavaleev, N. M.; Scopelliti, R.; Grätzel, M.; Nazeeruddin, M. K.; Pertegás, A.; Roldán-Carmona, C.; Tordera, D.; Bolink, H. J., Pulsed-current versus constant-voltage light-emitting electrochemical cells with trifluoromethyl-substituted cationic iridium(III) complexes. *Journal of Materials Chemistry C* **2013**, *1* (11), 2241-2248.
90. Tordera, D.; Frey, J.; Vonlanthen, D.; Constable, E.; Pertegás, A.; Ortí, E.; Bolink, H. J.; Baranoff, E.; Nazeeruddin, M. K., Low current density driving leads to efficient, bright and stable green electroluminescence. *Advanced Energy Materials* **2013**, *3* (10), 1338-1343.
91. Bolink, H. J.; Cappelli, L.; Coronado, E.; Grätzel, M.; Ortí, E.; Costa, R. D.; Viruela, P. M.; Nazeeruddin, M. K., Stable single-layer light-emitting electrochemical cell using 4,7-diphenyl-1,10-phenanthroline-bis(2-phenylpyridine)iridium(III) hexafluorophosphate. *Journal of the American Chemical Society* **2006**, *128* (46), 14786-14787.
92. Bolink, H. J.; Coronado, E.; Costa, R. D.; Lardiés, N.; Ortí, E., Near-quantitative internal quantum efficiency in a light-emitting electrochemical cell. *Inorganic Chemistry* **2008**, *47* (20), 9149-9151.
93. Zhang, J.; Zhou, L.; Al-Attar, H. A.; Shao, K.; Wang, L.; Zhu, D.; Su, Z.; Bryce, M. R.; Monkman, A. P., Efficient light-emitting electrochemical cells (LECs) based on ionic iridium(III) complexes with 1,3,4-oxadiazole ligands. *Advanced Functional Materials* **2013**, *23* (37), 4667-4677.
94. Tang, S.; Sandström, A.; Lundberg, P.; Lanz, T.; Larsen, C.; Van Reenen, S.; Kemerink, M.; Edman, L., Design rules for light-emitting

- electrochemical cells delivering bright luminance at 27.5 percent external quantum efficiency. *Nature Communications* **2017**, *8*, 1190.
95. Friend, R. H.; Gymer, R. W.; Holmes, A. B.; Burroughes, J. H.; Marks, R. N.; Taliani, C.; Bradley, D. D. C.; Santos, D. A. D.; Brédas, J. L.; Lögdlund, M.; Salaneck, W. R., Electroluminescence in conjugated polymers. *Nature* **1999**, *397*, 121-128.
 96. Martínez-Alonso, M.; Cerdá, J.; Momblona, C.; Pertegás, A.; Junquera-Hernández, J. M.; Heras, A.; Rodríguez, A. M.; Espino, G.; Bolink, H.; Ortí, E., Highly stable and efficient light-emitting electrochemical cells based on cationic iridium complexes bearing arylazole ancillary ligands. *Inorganic Chemistry* **2017**, *56* (17), 10298-10310.
 97. Costa, R. D.; Ortí, E.; Bolink, H. J.; Graber, S.; Housecroft, C. E.; Constable, E. C., Intramolecular pi-stacking in a phenylpyrazole-based iridium complex and its use in light-emitting electrochemical cells. *Journal of the American Chemical Society* **2010**, *132* (17), 5978-5980.
 98. Graber, S.; Doyle, K.; Neuburger, M.; Housecroft, C. E.; Constable, C.; Costa, R. D.; Ortí, E.; Repetto, D.; Bolink, H. J., A supramolecularly-caged ionic iridium(III) complex yielding bright and very stable solid-state light-emitting electrochemical cells. *Journal of the American Chemical Society* **2008**, *130* (45), 14944-14945.
 99. Bolink, H. J.; Coronado, E.; Costa, R. D.; Ortí, E.; Sessolo, M.; Graber, S.; Doyle, K.; Neuburger, M.; Housecroft, C. E.; Constable, E. C., Long-living light-emitting electrochemical cells - Control through supramolecular interactions. *Advanced Materials* **2008**, *20* (20), 3910-3913.
 100. Englman, R.; Jortner, J., The energy gap law for radiationless transitions in large molecules. *Molecular Physics* **1970**, *18* (2), 145-164.
 101. Caspar, J. V.; Kober, E. M.; Sullivan, B. P.; Meyer, T. J., Application of the energy gap law to the decay of charge-transfer excited states. *Journal of the American Chemical Society* **1982**, *104* (2), 630-632.
 102. Namanga, J. E.; Gerlitzki, N.; Mallick, B.; Mudring, A.-V., Long term stable deep red light-emitting electrochemical cells based on an emissive, rigid cationic Ir(III) complex. *Journal of Materials Chemistry C* **2017**, *5* (12), 3049-3055.
 103. Fang, J.; Matyba, P.; Robinson, N. D.; Edman, L., Identifying and alleviating electrochemical side-reactions in light-emitting electrochemical cells. *Journal of the American Chemical Society* **2008**, *130* (13), 4562-4568.
 104. Tang, S.; Edman, L., Quest for an appropriate electrolyte for high-performance light-emitting electrochemical cells. *The Journal of Physical Chemistry Letters* **2010**, *1* (18), 2727-2732.
 105. Tang, S.; Mindemark, J.; Araujo, C. M. G.; Brandell, D.; Edman, L., Identifying key properties of electrolytes for light-emitting electrochemical cells. *Chemistry of Materials* **2014**, *26* (17), 5083-5088.
 106. Mindemark, J.; Tang, S.; Wang, J.; Kaihovirta, N.; Brandell, D.; Edman, L., High-performance light-emitting electrochemical cells by electrolyte design. *Chemistry of Materials* **2016**, *28* (8), 2618-2623.

107. Shan, G.-G.; Li, H.-B.; Zhu, D.-X.; Su, Z.-M.; Liao, Y., Intramolecular π -stacking in cationic iridium(III) complexes with a triazole-pyridine type ancillary ligand: synthesis, photophysics, electrochemistry properties and piezochromic behavior. *Journal of Materials Chemistry* **2012**, *22* (25), 12736-12744.
108. Zhang, F.; Duan, L.; Qiao, J.; Dong, G.; Wang, L.; Qiu, Y., The intramolecular π - π stacking interaction does not always work for improving the stabilities of light-emitting electrochemical cells. *Organic Electronics: physics, materials, applications* **2012**, *13* (11), 2442-2449.
109. Tamayo, A. B.; Garon, S.; Sajoto, T.; Peter, I.; Tsyba, I. M.; Bau, R.; Thompson, M. E.; Djurovich, P. I., Cationic bis-cyclometalated iridium(III) diimine complexes and their use in efficient blue, green, and red electroluminescent devices. *Inorganic Chemistry* **2005**, *44* (24), 8723-8732.
110. He, L.; Duan, L.; Qiao, J.; Wang, R.; Wei, P.; Wang, L.; Qiu, Y., Blue-emitting cationic iridium complexes with 2-(1*H*-pyrazol-1-yl)pyridine as the ancillary ligand for efficient light-emitting electrochemical cells. *Advanced Functional Materials* **2008**, *18* (14), 2123-2131.
111. He, L.; Qiao, J.; Duan, L.; Dong, G.; Zhang, D.; Wang, L.; Qiu, Y., Toward highly efficient solid-state white light-emitting electrochemical cells: blue-green to red emitting cationic iridium complexes with imidazole-type ancillary ligands. *Advanced Functional Materials* **2009**, *19* (18), 2950-2960.
112. Kessler, F.; Costa, R. D.; Di Censo, D.; Scopelliti, R.; Ortí, E.; Bolink, H. J.; Meier, S.; Sarfert, W.; Grätzel, M.; Nazeeruddin, M. K.; Baranoff, E., Near-UV to red-emitting charged bis-cyclometallated iridium(III) complexes for light-emitting electrochemical cells. *Dalton Transactions* **2012**, *41* (1), 180-191.
113. Bolink, H. J.; Coronado, E.; Costa, R. D.; Gaviña, P.; Ortí, E.; Tatay, S., Deep-red-emitting electrochemical cells based on heteroleptic bis-chelated ruthenium(II) complexes. *Inorganic Chemistry* **2009**, *48* (9), 3907-3909.
114. Ho, C.-C.; Chen, H.-F.; Ho, Y.-C.; Liao, C.-T.; Su, H.-C.; Wong, K.-T., Phosphorescent sensitized fluorescent solid-state near-infrared light-emitting electrochemical cells. *Physical Chemistry Chemical Physics* **2011**, *13* (39), 17729-17736.
115. Ross, D. A. W.; Scattergood, P. A.; Babaei, A.; Pertegás, A.; Bolink, H. J.; Elliott, P. I. P., Luminescent osmium(II) bi-1,2,3-triazol-4-yl complexes: photophysical characterisation and application in light-emitting electrochemical cells. *Dalton Transactions* **2016**, *45* (18), 7748-7757.
116. Zeng, Q.; Li, F.; Guo, T.; Shan, G.; Su, Z., Synthesis of red-emitting cationic Ir(III) complex and its application in white light-emitting electrochemical cells. *Organic Electronics: physics, materials, applications* **2017**, *42*, 303-308.
117. Hu, T.; Duan, L.; Qiao, J.; He, L.; Zhang, D.; Wang, L.; Qiu, Y., Efficient doped red light-emitting electrochemical cells based on cationic iridium complexes. *Synthetic Metals* **2013**, *163* (1), 33-37.

118. Lo, K. K.-W.; Li, C.-K.; Lau, J. S.-Y., Luminescent cyclometalated iridium(III) arylbenzothiazole biotin complexes. *Organometallics* **2005**, *24* (19), 4594-4601.
119. Yuan, Y.-J.; Yu, Z.-T.; Chen, X.-Y.; Zhang, J.-Y.; Zou, Z.-G., Visible-light-driven H₂ generation from water and CO₂ conversion by using a zwitterionic cyclometalated iridium(III) complex. *Chemistry – A European Journal* **2011**, *17* (46), 12891-12895.
120. Lo, K. K.-W.; Leung, S.-K.; Pan, C.-Y., Luminescent iridium(III) arylbenzothiazole complexes: Photophysics, electrochemistry, bioconjugation, and cellular uptake. *Inorganica Chimica Acta* **2012**, *380*, 343-349.
121. Choudhary, C. K.; Choudhary, R. K.; Mishra, L. K., *Complexes of rhodium(III), palladium(II) and platinum(II) with 2-(2'-pyridyl)benzothiazole*. Indian Chemical Society: Calcutta, INDE, 2002; p 2.
122. Richardson, C.; Keene, F. R.; Steel, P. J., Ruthenium(II) complexes of chelating ligands containing benzoxazole and benzothiazole subunits: synthesis, X-Ray crystallography, spectroscopy, and electrochemistry. *Australian Journal of Chemistry* **2008**, *61* (3), 183-188.
123. Gärtner, F.; Cozzula, D.; Losse, S.; Boddien, A.; Anilkumar, G.; Junge, H.; Schulz, T.; Marquet, N.; Spannenberg, A.; Gladiali, S.; Beller, M., Synthesis, characterisation and application of iridium(III) photosensitisers for catalytic water reduction. *Chemistry – A European Journal* **2011**, *17* (25), 6998-7006.
124. Meier, S. B.; Hartmann, D.; Tordera, D.; Bolink, H. J.; Winnacker, A.; Sarfert, W., Dynamic doping and degradation in sandwich-type light-emitting electrochemical cells. *Physical Chemistry Chemical Physics* **2012**, *14* (31), 10886-10890.
125. AlTal, F.; Gao, J., Long-term testing of polymer light-emitting electrochemical cells: reversible doping and black spots. *Organic Electronics* **2015**, *18*, 1-7.
126. Hsu, J.-H.; Su, H.-C., Host-only solid-state near-infrared light-emitting electrochemical cells based on interferometric spectral tailoring. *Physical Chemistry Chemical Physics* **2016**, *18* (6), 5034-5039.
127. Lee, C.-L.; Cheng, C.-Y.; Su, H.-C., Enhancing device efficiencies of solid-state near-infrared light-emitting electrochemical cells by employing a tandem device structure. *Organic Electronics* **2014**, *15* (3), 711-720.
128. Tordera, D.; Pertegás, A.; Shavaleev, N. M.; Scopelliti, R.; Ortí, E.; Bolink, H. J.; Baranoff, E.; Grätzel, M.; Nazeeruddin, M. K., Efficient orange light-emitting electrochemical cells. *Journal of Materials Chemistry* **2012**, *22* (36), 19264-19268.
129. Bünzli, A. M.; Constable, E. C.; Housecroft, C. E.; Prescimone, A.; Zampese, J. A.; Longo, G.; Gil-Escrig, L.; Pertegás, A.; Ortí, E.; Bolink, H. J., Exceptionally long-lived light-emitting electrochemical cells: multiple intra-cation p-stacking interactions in [Ir(C^N)₂(N^N)](PF₆) emitters. *Chemical Science* **2015**, *6* (5), 2843-2852.

130. Dong, R.; Fang, Y.; Chae, J.; Dai, J.; Xiao, Z.; Dong, Q.; Yuan, Y.; Centrone, A.; Zeng, X. C.; Huang, J., High-gain and low-driving-voltage photodetectors based on organolead triiodide perovskites. *Advanced Materials* **2015**, *27* (11), 1912-1918.
131. Stranks, S. D.; Snaith, H. J., Metal-halide perovskites for photovoltaic and light-emitting devices. *Nature Nanotechnology* **2015**, *10* (5), 391-402.
132. Veldhuis, S. A.; Boix, P. P.; Yantara, N.; Li, M.; Sum, T. C.; Mathews, N.; Mhaisalkar, S. G., Perovskite materials for light-emitting diodes and lasers. *Advanced Materials* **2016**, *28* (32), 6804-6834.
133. Dou, L.; Yang, Y.; You, J.; Hong, Z.; Chang, W.-H.; Li, G.; Yang, Y., Solution-processed hybrid perovskite photodetectors with high detectivity. *Nature Communications* **2014**, *5*, 5404.
134. Harwell, J. R.; Whitworth, G. L.; Turnbull, G. A.; Samuel, I. D. W., Green perovskite distributed feedback lasers. *Scientific Reports* **2017**, *7* (1), 11727.
135. Green, M. A.; Hishikawa, Y.; Dunlop, E. D.; Levi, D. H.; Hohl-Ebinger, J.; Ho-Baillie, A. W. Y., Solar cell efficiency tables (version 51). *Progress in Photovoltaics: Research and Applications* **2018**, *26* (1), 3-12.
136. Chin, X. Y.; Perumal, A.; Bruno, A.; Yantara, N.; Veldhuis, S.; Martínez-Sarti, L.; Chandran, B.; Chirvony, V. S.; Lo, S.-Z. A.; So, J.; Soci, C.; Grätzel, M.; Bolink, H. J.; Mathews, N.; Mhaisalkar, S. G., Self-assembled hierarchical nanostructured perovskites enable highly efficient LEDs via energy cascade. *Energy & Environmental Science* **2018**.
137. De Wolf, S.; Holovsky, J.; Moon, S.-J.; Löper, P.; Niesen, B.; Ledinsky, M.; Haug, F.-J.; Yum, J.-H.; Ballif, C., Organometallic halide perovskites: sharp optical absorption edge and its relation to photovoltaic performance. *The Journal of Physical Chemistry Letters* **2014**, *5* (6), 1035-1039.
138. Ponceca, C. S.; Savenije, T. J.; Abdellah, M.; Zheng, K.; Yartsev, A.; Pascher, T.; Harlang, T.; Chabera, P.; Pullerits, T.; Stepanov, A.; Wolf, J.-P.; Sundström, V., Organometal halide perovskite solar cell materials rationalized: ultrafast charge generation, high and microsecond-long balanced mobilities, and slow recombination. *Journal of the American Chemical Society* **2014**, *136* (14), 5189-5192.
139. Stranks, S. D.; Eperon, G. E.; Grancini, G.; Menelaou, C.; Alcocer, M. J. P.; Leijtens, T.; Herz, L. M.; Petrozza, A.; Snaith, H. J., Electron-hole diffusion lengths exceeding 1 micrometer in an organometal trihalide perovskite absorber. *Science* **2013**, *342* (6156), 341-344.
140. Xing, G.; Mathews, N.; Sun, S.; Lim, S. S.; Lam, Y. M.; Grätzel, M.; Mhaisalkar, S.; Sum, T. C., Long-range balanced electron- and hole-transport lengths in organic-inorganic CH₃NH₃PbI₃. *Science* **2013**, *342* (6156), 344-347.
141. Wehrenfennig, C.; Eperon, G. E.; Johnston, M. B.; Snaith, H. J.; Herz, L. M., High charge carrier mobilities and lifetimes in organolead trihalide perovskites. *Advanced Materials* **2014**, *26* (10), 1584-1589.
142. Shi, D.; Adinolfi, V.; Comin, R.; Yuan, M.; Alarousu, E.; Buin, A.; Chen, Y.; Hoogland, S.; Rothenberger, A.; Katsiev, K.; Losovyj, Y.; Zhang,

- X.; Dowben, P. A.; Mohammed, O. F.; Sargent, E. H.; Bakr, O. M., Low trap-state density and long carrier diffusion in organolead trihalide perovskite single crystals. *Science* **2015**, *347* (6221), 519-522.
143. Tanaka, K.; Takahashi, T.; Ban, T.; Kondo, T.; Uchida, K.; Miura, N., Comparative study on the excitons in lead-halide-based perovskite-type crystals $\text{CH}_3\text{NH}_3\text{PbBr}_3$ $\text{CH}_3\text{NH}_3\text{PbI}_3$. *Solid State Communications* **2003**, *127* (9), 619-623.
144. D'Innocenzo, V.; Grancini, G.; Alcocer, M. J. P.; Kandada, A. R. S.; Stranks, S. D.; Lee, M. M.; Lanzani, G.; Snaith, H. J.; Petrozza, A., Excitons versus free charges in organo-lead tri-halide perovskites. *Nature Communications* **2014**, *5*, 3586.
145. Even, J.; Pedesseau, L.; Katan, C., Analysis of multivalley and multibandgap absorption and enhancement of free carriers related to exciton screening in hybrid perovskites. *The Journal of Physical Chemistry C* **2014**, *118* (22), 11566-11572.
146. Lin, H.; Zhou, C.; Tian, Y.; Siegrist, T.; Ma, B., Low-dimensional organometal halide perovskites. *ACS Energy Letters* **2018**, *3* (1), 54-62.
147. Boix, P. P.; Agarwala, S.; Koh, T. M.; Mathews, N.; Mhaisalkar, S. G., Perovskite solar cells: beyond methylammonium lead iodide. *The Journal of Physical Chemistry Letters* **2015**, *6* (5), 898-907.
148. Saporov, B.; Mitzi, D. B., Organic-inorganic perovskites: structural versatility for functional materials design. *Chemical Reviews* **2016**, *116* (7), 4558-4596.
149. Mitzi, D. B., Synthesis, structure, and properties of organic-inorganic perovskites and related materials. In *Progress in Inorganic Chemistry*, John Wiley & Sons, Inc.: 2007; Vol. 48, pp 1-121.
150. Stoumpos, C. C.; Malliakas, C. D.; Kanatzidis, M. G., Semiconducting tin and lead iodide perovskites with organic cations: phase transitions, high mobilities, and near-infrared photoluminescent properties. *Inorganic Chemistry* **2013**, *52* (15), 9019-9038.
151. Kagan, C. R.; Mitzi, D. B.; Dimitrakopoulos, C. D., Organic-inorganic hybrid materials as semiconducting channels in thin-film field-effect transistors. *Science* **1999**, *286* (5441), 945-947.
152. Malinkiewicz, O.; Yella, A.; Lee, Y. H.; Espallargas, G. M.; Graetzel, M.; Nazeeruddin, M. K.; Bolink, H. J., Perovskite solar cells employing organic charge-transport layers. *Nature Photonics* **2013**, *8*, 128-132.
153. Goldschmidt, V. M., Die Gesetze der Kristallochemie. *Naturwissenschaften* **1926**, *14* (21), 477-485.
154. Liang, L.; Wencong, L.; Nianyi, C., On the criteria of formation and lattice distortion of perovskite-type complex halides. *Journal of Physics and Chemistry of Solids* **2004**, *65* (5), 855-860.
155. Travis, W.; Glover, E. N. K.; Bronstein, H.; Scanlon, D. O.; Palgrave, R. G., On the application of the tolerance factor to inorganic and hybrid halide perovskites: a revised system. *Chemical Science* **2016**, *7* (7), 4548-4556.

156. Kieslich, G.; Sun, S.; Cheetham, A. K., Solid-state principles applied to organic-inorganic perovskites: new tricks for an old dog. *Chemical Science* **2014**, *5* (12), 4712-4715.
157. Kieslich, G.; Sun, S.; Cheetham, A. K., An extended Tolerance Factor approach for organic-inorganic perovskites. *Chemical Science* **2015**, *6* (6), 3430-3433.
158. Poglitsch, A.; Weber, D., Dynamic disorder in methylammoniumtrihalogenoplumbates (II) observed by millimeter-wave spectroscopy. *The Journal of Chemical Physics* **1987**, *87* (11), 6373-6378.
159. Even, J.; Pedesseau, L.; Katan, C.; Kepenekian, M.; Lauret, J.-S.; Saponi, D.; Deleporte, E., Solid-state physics perspective on hybrid perovskite semiconductors. *The Journal of Physical Chemistry C* **2015**, *119* (19), 10161-10177.
160. Pan, Y.-Y.; Su, Y.-H.; Hsu, C.-H.; Huang, L.-W.; Kaun, C.-C., The electronic structure of organic-inorganic hybrid perovskite solar cell: a first-principles analysis. *Computational Materials Science* **2016**, *117*, 573-578.
161. Lindblad, R.; Jena, N. K.; Philippe, B.; Oscarsson, J.; Bi, D.; Lindblad, A.; Mandal, S.; Pal, B.; Sarma, D. D.; Karis, O.; Siegbahn, H.; Johansson, E. M. J.; Odelius, M.; Rensmo, H., Electronic structure of $\text{CH}_3\text{NH}_3\text{PbX}_3$ perovskites: dependence on the halide moiety. *The Journal of Physical Chemistry C* **2015**, *119* (4), 1818-1825.
162. Park, J.-S.; Choi, S.; Yan, Y.; Yang, Y.; Luther, J. M.; Wei, S.-H.; Parilla, P.; Zhu, K., Electronic structure and optical properties of α - $\text{CH}_3\text{NH}_3\text{PbBr}_3$ perovskite single crystal. *The Journal of Physical Chemistry Letters* **2015**, *6* (21), 4304-4308.
163. Brenner, T. M.; Egger, D. A.; Kronik, L.; Hodes, G.; Cahen, D., Hybrid organic-inorganic perovskites: low-cost semiconductors with intriguing charge-transport properties. *Nature Reviews Materials* **2016**, *1*, 15007.
164. Wenger, B.; Nayak, P. K.; Wen, X.; Kesava, S. V.; Noel, N. K.; Snaith, H. J., Consolidation of the optoelectronic properties of $\text{CH}_3\text{NH}_3\text{PbBr}_3$ perovskite single crystals. *Nature Communications* **2017**, *8*, 590.
165. Park, N.-G., Perovskite solar cells: an emerging photovoltaic technology. *Materials Today* **2015**, *18* (2), 65-72.
166. Wood, D. L.; Tauc, J., Weak absorption tails in amorphous semiconductors. *Physical Review B* **1972**, *5* (8), 3144-3151.
167. Castelli, I. E.; García-Lastra, J. M.; Thygesen, K. S.; Jacobsen, K. W., Bandgap calculations and trends of organometal halide perovskites. *APL Materials* **2014**, *2* (8), 081514.
168. Leguy, A. M. A.; Azarhoosh, P.; Alonso, M. I.; Campoy-Quiles, M.; Weber, O. J.; Yao, J.; Bryant, D.; Weller, M. T.; Nelson, J.; Walsh, A.; van Schilfgaarde, M.; Barnes, P. R. F., Experimental and theoretical optical properties of methylammonium lead halide perovskites. *Nanoscale* **2016**, *8* (12), 6317-6327.
169. Weller, M. T.; Weber, O. J.; Frost, J. M.; Walsh, A., Cubic perovskite structure of black formamidinium lead iodide, α - $[\text{HC}(\text{NH}_2)_2]\text{PbI}_3$, at 298 K. *The Journal of Physical Chemistry Letters* **2015**, *6* (16), 3209-3212.

170. Hao, F.; Stoumpos, C. C.; Chang, R. P. H.; Kanatzidis, M. G., Anomalous band gap behavior in mixed Sn and Pb perovskites enables broadening of absorption spectrum in solar cells. *Journal of the American Chemical Society* **2014**, *136* (22), 8094-8099.
171. Im, J.; Stoumpos, C. C.; Jin, H.; Freeman, A. J.; Kanatzidis, M. G., Antagonism between spin-orbit coupling and steric effects causes anomalous band gap evolution in the perovskite photovoltaic materials $\text{CH}_3\text{NH}_3\text{Sn}_{1-x}\text{Pb}_x\text{I}_3$. *The Journal of Physical Chemistry Letters* **2015**, *6* (17), 3503-3509.
172. Takahashi, Y.; Obara, R.; Lin, Z.-Z.; Takahashi, Y.; Naito, T.; Inabe, T.; Ishibashi, S.; Terakura, K., Charge-transport in tin-iodide perovskite $\text{CH}_3\text{NH}_3\text{SnI}_3$: origin of high conductivity. *Dalton Transactions* **2011**, *40* (20), 5563-5568.
173. Sadhanala, A.; Ahmad, S.; Zhao, B.; Giesbrecht, N.; Pearce, P. M.; Deschler, F.; Hoyer, R. L. Z.; Gödel, K. C.; Bein, T.; Docampo, P.; Dutton, S. E.; De Volder, M. F. L.; Friend, R. H., Blue-Green Color Tunable Solution Processable Organolead Chloride-Bromide Mixed Halide Perovskites for Optoelectronic Applications. *Nano Letters* **2015**, *15* (9), 6095-6101.
174. Mitzi, D. B.; Liang, K., Synthesis, resistivity, and thermal properties of the cubic perovskite $\text{NH}_2\text{CH}=\text{NH}_2\text{SnI}_3$ and related systems. *Journal of Solid State Chemistry* **1997**, *134* (2), 376-381.
175. Choi, H.; Jeong, J.; Kim, H.-B.; Kim, S.; Walker, B.; Kim, G.-H.; Kim, J. Y., Cesium-doped methylammonium lead iodide perovskite light absorber for hybrid solar cells. *Nano Energy* **2014**, *7*, 80-85.
176. Anaya, M.; Lozano, G.; Calvo, M. E.; Míguez, H., ABX_3 Perovskites for Tandem Solar Cells. *Joule* **2017**, *1* (4), 769-793.
177. Hutter, E. M.; Eperon, G. E.; Stranks, S. D.; Savenije, T. J., Charge carriers in planar and meso-structured organic-inorganic perovskites: mobilities, lifetimes, and concentrations of trap states. *The Journal of Physical Chemistry Letters* **2015**, *6* (15), 3082-3090.
178. Oga, H.; Saeki, A.; Ogomi, Y.; Hayase, S.; Seki, S., Improved understanding of the electronic and energetic landscapes of perovskite solar cells: high local charge carrier mobility, reduced recombination, and extremely shallow traps. *Journal of the American Chemical Society* **2014**, *136* (39), 13818-13825.
179. Heo, J. H.; Song, D. H.; Han, H. J.; Kim, S. Y.; Kim, J. H.; Kim, D.; Shin, H. W.; Ahn, T. K.; Wolf, C.; Lee, T.-W.; Im, S. H., Planar $\text{CH}_3\text{NH}_3\text{PbI}_3$ perovskite solar cells with constant 17.2% average power conversion efficiency irrespective of the scan rate. *Advanced Materials* **2015**, *27* (22), 3424-3430.
180. Wehrenfennig, C.; Liu, M.; Snaith, H. J.; Johnston, M. B.; Herz, L. M., Charge-carrier dynamics in vapour-deposited films of the organolead halide perovskite $\text{CH}_3\text{NH}_3\text{PbI}_{3-x}\text{Cl}_x$. *Energy & Environmental Science* **2014**, *7* (7), 2269-2275.

181. Zhao, Y.; Nardes, A. M.; Zhu, K., Solid-state mesostructured perovskite $\text{CH}_3\text{NH}_3\text{PbI}_3$ solar cells: charge transport, recombination, and diffusion length. *The Journal of Physical Chemistry Letters* **2014**, *5* (3), 490-494.
182. Zheng, K.; Židek, K.; Abdellah, M.; Messing, M. E.; Al-Marri, M. J.; Pullerits, T., Trap states and their dynamics in organometal halide perovskite nanoparticles and bulk crystals. *The Journal of Physical Chemistry C* **2016**, *120* (5), 3077-3084.
183. Stoumpos, C. C.; Kanatzidis, M. G., The renaissance of halide perovskites and their evolution as emerging semiconductors. *Accounts of Chemical Research* **2015**, *48* (10), 2791-2802.
184. Deng, Y.; Dong, Q.; Bi, C.; Yuan, Y.; Huang, J., Air-stable, efficient mixed-cation perovskite solar cells with Cu electrode by scalable fabrication of active layer. *Advanced Energy Materials* **2016**, *6* (11), 1600372.
185. Im, J.-H.; Lee, C.-R.; Lee, J.-W.; Park, S.-W.; Park, N.-G., 6.5% efficient perovskite quantum-dot-sensitized solar cell. *Nanoscale* **2011**, *3* (10), 4088-4093.
186. Kojima, A.; Teshima, K.; Shirai, Y.; Miyasaka, T., Organometal halide perovskites as visible-light sensitizers for photovoltaic cells. *Journal of the American Chemical Society* **2009**, *131* (17), 6050-6051.
187. Wu, Y.; Islam, A.; Yang, X.; Qin, C.; Liu, J.; Zhang, K.; Peng, W.; Han, L., Retarding the crystallization of PbI_2 for highly reproducible planar-structured perovskite solar cells via sequential deposition. *Energy & Environmental Science* **2014**, *7* (9), 2934-2938.
188. Seo, J.; Park, S.; Chan Kim, Y.; Jeon, N. J.; Noh, J. H.; Yoon, S. C.; Seok, S. I., Benefits of very thin PCBM and LiF layers for solution-processed p-i-n perovskite solar cells. *Energy & Environmental Science* **2014**, *7* (8), 2642-2646.
189. Eperon, G. E.; Burlakov, V. M.; Docampo, P.; Goriely, A.; Snaith, H. J., Morphological control for high performance, solution-processed planar heterojunction perovskite solar cells. *Advanced Functional Materials* **2014**, *24* (1), 151-157.
190. Song, Z.; Wathage, S. C.; Phillips, A. B.; Tompkins, B. L.; Ellingson, R. J.; Heben, M. J., Impact of processing temperature and composition on the formation of methylammonium lead iodide perovskites. *Chemistry of Materials* **2015**, *27* (13), 4612-4619.
191. Wang, Q.; Shao, Y.; Dong, Q.; Xiao, Z.; Yuan, Y.; Huang, J., Large fill-factor bilayer iodine perovskite solar cells fabricated by a low-temperature solution-process. *Energy & Environmental Science* **2014**, *7* (7), 2359-2365.
192. Zhao, Y.; Zhu, K., Efficient planar perovskite solar cells based on 1.8 eV band gap $\text{CH}_3\text{NH}_3\text{PbI}_2\text{Br}$ nanosheets via thermal decomposition. *Journal of the American Chemical Society* **2014**, *136* (35), 12241-12244.
193. Heo, J. H.; Song, D. H.; Im, S. H., Planar $\text{CH}_3\text{NH}_3\text{PbBr}_3$ hybrid solar cells with 10.4% power conversion efficiency, fabricated by controlled crystallization in the spin-coating process. *Advanced Materials* **2014**, *26* (48), 8179-8183.

194. Tsai, H.; Nie, W.; Cheruku, P.; Mack, N. H.; Xu, P.; Gupta, G.; Mohite, A. D.; Wang, H.-L., Optimizing composition and morphology for large-grain perovskite solar cells via chemical control. *Chemistry of Materials* **2015**, *27* (16), 5570-5576.
195. Chen, Y.; Zhao, Y.; Liang, Z., Non-thermal annealing fabrication of efficient planar perovskite solar cells with inclusion of NH₄Cl. *Chemistry of Materials* **2015**, *27* (5), 1448-1451.
196. Liang, P.-W.; Liao, C.-Y.; Chueh, C.-C.; Zuo, F.; Williams, S. T.; Xin, X.-K.; Lin, J.; Jen, A. K. Y., Additive enhanced crystallization of solution-processed perovskite for highly efficient planar-heterojunction solar cells. *Advanced Materials* **2014**, *26* (22), 3748-3754.
197. Li, X.; Ibrahim Dar, M.; Yi, C.; Luo, J.; Tschumi, M.; Zakeeruddin, S. M.; Nazeeruddin, M. K.; Han, H.; Grätzel, M., Improved performance and stability of perovskite solar cells by crystal crosslinking with alkylphosphonic acid ω-ammonium chlorides. *Nature Chemistry* **2015**, *7*, 703-711.
198. Jeon, N. J.; Noh, J. H.; Kim, Y. C.; Yang, W. S.; Ryu, S.; Seok, S. I., Solvent engineering for high-performance inorganic-organic hybrid perovskite solar cells. *Nature Materials* **2014**, *13* (9), 897-903.
199. Ahn, N.; Son, D.-Y.; Jang, I.-H.; Kang, S. M.; Choi, M.; Park, N.-G., Highly reproducible perovskite solar cells with average efficiency of 18.3% and best efficiency of 19.7% fabricated via Lewis base adduct of lead(II) iodide. *Journal of the American Chemical Society* **2015**, *137* (27), 8696-8699.
200. Xiao, M.; Huang, F.; Huang, W.; Dkhissi, Y.; Zhu, Y.; Etheridge, J.; Gray-Weale, A.; Bach, U.; Cheng, Y.-B.; Spiccia, L., A fast deposition-crystallization procedure for highly efficient lead iodide perovskite thin-film solar cells. *Angewandte Chemie* **2014**, *126* (37), 10056-10061.
201. Liang, K.; Mitzi, D. B.; Prikas, M. T., Synthesis and characterization of organic-inorganic perovskite thin films prepared using a versatile two-step dipping technique. *Chemistry of Materials* **1998**, *10* (1), 403-411.
202. Xiao, Z.; Bi, C.; Shao, Y.; Dong, Q.; Wang, Q.; Yuan, Y.; Wang, C.; Gao, Y.; Huang, J., Efficient, high yield perovskite photovoltaic devices grown by interdiffusion of solution-processed precursor stacking layers. *Energy & Environmental Science* **2014**, *7* (8), 2619-2623.
203. Chen, Q.; Zhou, H.; Hong, Z.; Luo, S.; Duan, H.-S.; Wang, H.-H.; Liu, Y.; Li, G.; Yang, Y., Planar heterojunction perovskite solar cells via vapor-assisted solution process. *Journal of the American Chemical Society* **2014**, *136* (2), 622-625.
204. Hao, F.; Stoumpos, C. C.; Liu, Z.; Chang, R. P. H.; Kanatzidis, M. G., Controllable perovskite crystallization at a gas-solid interface for hole conductor-free solar cells with steady power conversion efficiency over 10%. *Journal of the American Chemical Society* **2014**, *136* (46), 16411-16419.

205. Era, M.; Hattori, T.; Taira, T.; Tsutsui, T., Self-organized growth of PbI₂-based layered perovskite quantum well by dual-source vapor deposition. *Chemistry of Materials* **1997**, *9* (1), 8-10.
206. Liu, M.; Johnston, M. B.; Snaith, H. J., Efficient planar heterojunction perovskite solar cells by vapour deposition. *Nature* **2013**, *501*, 395-398.
207. Li, G.; Ho, J. Y. L.; Wong, M.; Kwok, H.-S., Low cost, high throughput and centimeter-scale fabrication of efficient hybrid perovskite solar cells by closed space vapor transport. *Physica status solidi (RRL) – Rapid Research Letters* **2016**, *10* (2), 153-157.
208. Leyden, M. R.; Ono, L. K.; Raga, S. R.; Kato, Y.; Wang, S.; Qi, Y., High performance perovskite solar cells by hybrid chemical vapor deposition. *Journal of Materials Chemistry A* **2014**, *2* (44), 18742-18745.
209. Shen, P.-S.; Chen, J.-S.; Chiang, Y.-H.; Li, M.-H.; Guo, T.-F.; Chen, P., Low-pressure hybrid chemical vapor growth for efficient perovskite solar cells and large-area module. *Advanced Materials Interfaces* **2016**, *3* (8), 1500849.
210. Mitzi, D. B.; Prikas, M. T.; Chondroudis, K., Thin film deposition of organic–inorganic hybrid materials using a single source thermal ablation technique. *Chemistry of Materials* **1999**, *11* (3), 542-544.
211. Longo, G.; Gil-Escrig, L.; Degen, M. J.; Sessolo, M.; Bolink, H. J., Perovskite solar cells prepared by flash evaporation. *Chemical Communications* **2015**, *51* (34), 7376-7378.
212. Chondroudis, K.; Mitzi, D. B.; Brock, P., Effect of Thermal Annealing on the Optical and Morphological Properties of (AETH)PbX₄ (X = Br, I) Perovskite Films Prepared Using Single Source Thermal Ablation. *Chemistry of Materials* **1999**, *12* (1), 169-175.
213. Deng, K.; Li, L., Advances in the application of atomic layer deposition for organometal halide perovskite solar cells. *Advanced Materials Interfaces* **2016**, *3* (21), 1-10.
214. Sutherland, B. R.; Hoogland, S.; Adachi, M. M.; Kanjanaboos, P.; Wong, C. T. O.; McDowell, J. J.; Xu, J.; Voznyy, O.; Ning, Z.; Houtepen, A. J.; Sargent, E. H., Perovskite thin films via atomic layer deposition. *Advanced Materials* **2015**, *27* (1), 53-58.
215. Hsiao, S.-Y.; Lin, H.-L.; Lee, W.-H.; Tsai, W.-L.; Chiang, K.-M.; Liao, W.-Y.; Ren-Wu, C.-Z.; Chen, C.-Y.; Lin, H.-W., Efficient all-vacuum deposited perovskite solar cells by controlling reagent partial pressure in high vacuum. *Advanced Materials* **2016**, *28* (32), 7013-7019.
216. Yin, J.; Qu, H.; Cao, J.; Tai, H.; Li, J.; Zheng, N., Vapor-assisted crystallization control toward high performance perovskite photovoltaics with over 18% efficiency in the ambient atmosphere. *Journal of Materials Chemistry A* **2016**, *4* (34), 13203-13210.
217. Momblona, C.; Gil-Escrig, L.; Bandiello, E.; Hutter, E. M.; Sessolo, M.; Lederer, K.; Blochwitz-Nimoth, J.; Bolink, H. J., Efficient vacuum deposited p-i-n and n-i-p perovskite solar cells employing doped charge transport layers. *Energy & Environmental Science* **2016**, *9* (11), 3456-3463.

218. Comin, R.; Walters, G.; Thibau, E. S.; Voznyy, O.; Lu, Z.-H.; Sargent, E. H., Structural, optical, and electronic studies of wide-bandgap lead halide perovskites. *Journal of Materials Chemistry C* **2015**, *3* (34), 8839-8843.
219. Yang, Y.; Yang, M.; Li, Z.; Crisp, R.; Zhu, K.; Beard, M. C., Comparison of recombination dynamics in $\text{CH}_3\text{NH}_3\text{PbBr}_3$ and $\text{CH}_3\text{NH}_3\text{PbI}_3$ perovskite films: influence of exciton binding energy. *The Journal of Physical Chemistry Letters* **2015**, *6* (23), 4688-4692.
220. Johnston, M. B.; Herz, L. M., Hybrid Perovskites for Photovoltaics: Charge-Carrier Recombination, Diffusion, and Radiative Efficiencies. *Accounts of Chemical Research* **2016**, *49* (1), 146-154.
221. Herz, L. M., Charge-Carrier Dynamics in Organic-Inorganic Metal Halide Perovskites. *Annual Review of Physical Chemistry* **2016**, *67* (1), 65-89.
222. Milot, R. L.; Eperon, G. E.; Snaith, H. J.; Johnston, M. B.; Herz, L. M., Temperature-dependent charge-carrier dynamics in $\text{CH}_3\text{NH}_3\text{PbI}_3$ perovskite thin films. *Advanced Functional Materials* **2015**, *25* (39), 6218-6227.
223. Yin, W.-J.; Shi, T.; Yan, Y., Unusual defect physics in $\text{CH}_3\text{NH}_3\text{PbI}_3$ perovskite solar cell absorber. *Applied Physics Letters* **2014**, *104* (6), 063903.
224. Kim, J.; Lee, S.-H.; Lee, J. H.; Hong, K.-H., The role of intrinsic defects in methylammonium lead iodide perovskite. *The Journal of Physical Chemistry Letters* **2014**, *5* (8), 1312-1317.
225. Snaith, H. J.; Abate, A.; Ball, J. M.; Eperon, G. E.; Leijtens, T.; Noel, N. K.; Stranks, S. D.; Wang, J. T.-W.; Wojciechowski, K.; Zhang, W., Anomalous Hysteresis in Perovskite Solar Cells. *The Journal of Physical Chemistry Letters* **2014**, *5* (9), 1511-1515.
226. Jacobs, D. A.; Wu, Y.; Shen, H.; Barugkin, C.; Beck, F. J.; White, T. P.; Weber, K.; Catchpole, K. R., Hysteresis phenomena in perovskite solar cells: the many and varied effects of ionic accumulation *Physical Chemistry Chemical Physics* **2017**, *19* (4), 3094-3103.
227. Wu, Y.; Shen, H.; Walter, D.; Jacobs, D.; Duong, T.; Peng, J.; Jiang, L.; Cheng, Y.-B.; Weber, K., On the origin of hysteresis in perovskite solar cells. *Advanced Functional Materials* **2016**, *26* (37), 6807-6813.
228. Lee, J.-W.; Kim, S.-G.; Bae, S.-H.; Lee, D.-K.; Lin, O.; Yang, Y.; Park, N.-G., The interplay between trap density and hysteresis in planar heterojunction perovskite solar cells. *Nano Letters* **2017**, *17* (7), 4270-4276.
229. Uratani, H.; Yamashita, K., Charge carrier trapping at surface defects of perovskite solar cell absorbers: a first-principles study. *The Journal of Physical Chemistry Letters* **2017**, *8* (4), 742-746.
230. Chen, H.-W.; Sakai, N.; Ikegami, M.; Miyasaka, T., Emergence of hysteresis and transient ferroelectric response in organo-lead halide perovskite solar cells. *The Journal of Physical Chemistry Letters* **2015**, *6* (1), 164-169.
231. Shockley, W.; Queisser, H. J., Detailed balance limit of efficiency of p-n junction solar cells. *Journal of Applied Physics* **1961**, *32* (3), 510-519.

232. Manser, J. S.; Kamat, P. V., Band filling with free charge carriers in organometal halide perovskites. *Nature Photonics* **2014**, *8*, 737-743.
233. Sha, W. E. I.; Ren, X.; Chen, L.; Choy, W. C. H., The efficiency limit of $\text{CH}_3\text{NH}_3\text{PbI}_3$ perovskite solar cells. *Applied Physics Letters* **2015**, *106* (22), 221104.
234. Rühle, S., Tabulated values of the Shockley–Queisser limit for single junction solar cells. *Solar Energy* **2016**, *130*, 139-147.
235. Zuo, C.; Bolink, H. J.; Han, H.; Huang, J.; Cahen, D.; Ding, L., Advances in perovskite solar cells. *Advanced Science* **2016**, *3* (7), 1500324.
236. Lee, M. M.; Teuscher, J.; Miyasaka, T.; Murakami, T. N.; Snaith, H. J., Efficient hybrid solar cells based on meso-superstructured organometal halide perovskites. *Science* **2012**, *338* (6107), 643-647.
237. Yoshikawa, K.; Kawasaki, H.; Yoshida, W.; Irie, T.; Konishi, K.; Nakano, K.; Uto, T.; Adachi, D.; Kanematsu, M.; Uzu, H.; Yamamoto, K., Silicon heterojunction solar cell with interdigitated back contacts for a photoconversion efficiency over 26%. *Nature Energy* **2017**, *2*, 17032.
238. Yang, W. S.; Park, B.-W.; Jung, E. H.; Jeon, N. J.; Kim, Y. C.; Lee, D. U.; Shin, S. S.; Seo, J.; Kim, E. K.; Noh, J. H.; Seok, S. I., Iodide management in formamidinium-lead-halide-based perovskite layers for efficient solar cells. *Science* **2017**, *356* (6345), 1376-1379.
239. Chen, H.; Ye, F.; Tang, W.; He, J.; Yin, M.; Wang, Y.; Xie, F.; Bi, E.; Yang, X.; Grätzel, M.; Han, L., A solvent- and vacuum-free route to large-area perovskite films for efficient solar modules. *Nature* **2017**, *550*, 92-95.
240. Bush, K. A.; Palmstrom, A. F.; Yu, Z. J.; Boccard, M.; Cheacharoen, R.; Mailoa, J. P.; McMeekin, D. P.; Hoyer, R. L. Z.; Bailie, C. D.; Leijtens, T.; Peters, I. M.; Minichetti, M. C.; Rolston, N.; Prasanna, R.; Sofia, S.; Harwood, D.; Ma, W.; Moghadam, F.; Snaith, H. J.; Buonassisi, T.; Holman, Z. C.; Bent, S. F.; McGehee, M. D., 23.6%-efficient monolithic perovskite/silicon tandem solar cells with improved stability. *Nature Energy* **2017**, *2*, 17009.
241. Bi, C.; Chen, B.; Wei, H.; DeLuca, S.; Huang, J., Efficient Flexible Solar Cell based on Composition-Tailored Hybrid Perovskite. *Advanced Materials* **2017**, *29* (30), 1605900.
242. Jeon, N. J.; Noh, J. H.; Yang, W. S.; Kim, Y. C.; Ryu, S.; Seo, J.; Seok, S. I., Compositional engineering of perovskite materials for high-performance solar cells. *Nature* **2015**, *517*, 476.
243. Saliba, M.; Matsui, T.; Seo, J.-Y.; Domanski, K.; Correa-Baena, J.-P.; Nazeeruddin, M. K.; Zakeeruddin, S. M.; Tress, W.; Abate, A.; Hagfeldt, A.; Grätzel, M., Cesium-containing triple cation perovskite solar cells: improved stability, reproducibility and high efficiency. *Energy & Environmental Science* **2016**, *9* (6), 1989-1997.
244. Saliba, M.; Matsui, T.; Domanski, K.; Seo, J.-Y.; Ummadisingu, A.; Zakeeruddin, S. M.; Correa-Baena, J.-P.; Tress, W. R.; Abate, A.; Hagfeldt, A.; Grätzel, M., Incorporation of rubidium cations into perovskite solar cells improves photovoltaic performance. *Science* **2016**, *354* (6309), 206-209.

245. McMeekin, D. P.; Sadoughi, G.; Rehman, W.; Eperon, G. E.; Saliba, M.; Höranthner, M. T.; Haghighirad, A.; Sakai, N.; Korte, L.; Rech, B.; Johnston, M. B.; Herz, L. M.; Snaith, H. J., A mixed-cation lead mixed-halide perovskite absorber for tandem solar cells. *Science* **2016**, *351* (6269), 151-155.
246. Kim, H.-S.; Lee, C.-R.; Im, J.-H.; Lee, K.-B.; Moehl, T.; Marchioro, A.; Moon, S.-J.; Humphry-Baker, R.; Yum, J.-H.; Moser, J. E.; Grätzel, M.; Park, N.-G., Lead iodide perovskite sensitized all-solid-state submicron thin film mesoscopic solar cell with efficiency exceeding 9%. *Scientific Reports* **2012**, *2*, 591.
247. Giordano, F.; Abate, A.; Correa Baena, J. P.; Saliba, M.; Matsui, T.; Im, S. H.; Zakeeruddin, S. M.; Nazeeruddin, M. K.; Hagfeldt, A.; Graetzel, M., Enhanced electronic properties in mesoporous TiO₂ via lithium doping for high-efficiency perovskite solar cells. *Nature Communications* **2016**, *7*, 10379.
248. Bishop, J. E.; Mohamad, D. K.; Wong-Stringer, M.; Smith, A.; Lidzey, D. G., Spray-cast multilayer perovskite solar cells with an active-area of 1.5 cm². *Scientific Reports* **2017**, *7*, 7962.
249. Pellet, N.; Gao, P.; Gregori, G.; Yang, T.-Y.; Nazeeruddin, M. K.; Maier, J.; Grätzel, M., Mixed-organic-cation perovskite photovoltaics for enhanced solar-light harvesting. *Angewandte Chemie - International Edition* **2014**, *53* (12), 3151-3157.
250. Edri, E.; Kirmayer, S.; Henning, A.; Mukhopadhyay, S.; Gartsman, K.; Rosenwaks, Y.; Hodes, G.; Cahen, D., Why lead methylammonium triiodide perovskite-based solar cells require a mesoporous electron transporting scaffold (but not necessarily a hole conductor). *Nano letters* **2014**, *14* (2), 1000-4.
251. Docampo, P.; Ball, J. M.; Darwich, M.; Eperon, G. E.; Snaith, H. J., Efficient organometal trihalide perovskite planar-heterojunction solar cells on flexible polymer substrates. *Nature Communications* **2013**, *4*, 2761.
252. Liu, D.; Gangishetty, M. K.; Kelly, T. L., Effect of CH₃NH₃PbI₃ thickness on device efficiency in planar heterojunction perovskite solar cells. *Journal of Materials Chemistry A* **2014**, *2* (46), 19873-19881.
253. Etgar, L.; Gao, P.; Xue, Z.; Peng, Q.; Chandiran, A. K.; Liu, B.; Nazeeruddin, M. K.; Grätzel, M., Mesoscopic CH₃NH₃PbI₃/TiO₂ heterojunction solar cells. *Journal of the American Chemical Society* **2012**, *134* (42), 17396-17399.
254. Kim, J.; Hwang, T.; Lee, S.; Lee, B.; Kim, J.; Jang, G. S.; Nam, S.; Park, B., Solvent and intermediate phase as boosters for the perovskite transformation and solar cell performance. *Scientific Reports* **2016**, *6*, 25648.
255. Cao, D. H.; Stoumpos, C. C.; Malliakas, C. D.; Katz, M. J.; Farha, O. K.; Hupp, J. T.; Kanatzidis, M. G., Remnant PbI₂, an unforeseen necessity in high-efficiency hybrid perovskite-based solar cells? *APL Materials* **2014**, *2* (9), 091101.

256. Roldán-Carmona, C.; Gratia, P.; Zimmermann, I.; Grancini, G.; Gao, P.; Graetzel, M.; Nazeeruddin, M. K., High efficiency methylammonium lead triiodide perovskite solar cells: the relevance of non-stoichiometric precursors. *Energy & Environmental Science* **2015**, *8* (12), 3550-3556.
257. Jacobsson, T. J.; Correa-Baena, J. P.; Halvani Anaraki, E.; Philippe, B.; Stranks, S. D.; Bouduban, M. E. F.; Tress, W.; Schenk, K.; Teuscher, J.; Moser, J. E.; Rensmo, H.; Hagfeldt, A., Unreacted PbI_2 as a double-edged sword for enhancing the performance of perovskite solar cells. *Journal of the American Chemical Society* **2016**, *138* (32), 10331-10343.
258. Duren, J. K. J. v.; Mihaiilechi, V. D.; Blom, P. W. M.; Woudenberg, T. v.; Hummelen, J. C.; Rispen, M. T.; Janssen, R. A. J.; Wienk, M. M., Injection-limited electron current in a methanofullerene. *Journal of Applied Physics* **2003**, *94* (7), 4477-4479.
259. Brittan, S.; Adhyaksa, G. W. P.; Garnett, E. C., The expanding world of hybrid perovskites: materials properties and emerging applications. *MRS Communications* **2015**, *5* (1), 7-26.
260. Cheylan, S.; Puigdollers, J.; Bolink, H. J.; Coronado, E.; Voz, C.; Alcubilla, R.; Badenes, G., Increased conductivity of a hole transport layer due to oxidation by a molecular nanomagnet. *Journal of Applied Physics* **2008**, *103* (9), 096110.
261. Grill, I.; Aygüler, M. F.; Bein, T.; Docampo, P.; Hartmann, N. F.; Handloser, M.; Hartschuh, A., Charge transport limitations in perovskite solar cells: the effect of charge extraction layers. *ACS Applied Materials and Interfaces* **2017**, *9* (43), 37655-37661.
262. Liu, D.; Li, S.; Zhang, P.; Wang, Y.; Zhang, R.; Sarvari, H.; Wang, F.; Wu, J.; Wang, Z.; Chen, Z. D., Efficient planar heterojunction perovskite solar cells with Li-doped compact TiO_2 layer. *Nano Energy* **2017**, *31*, 462-468.
263. Xu, Z.; Wu, J.; Wu, T.; Bao, Q.; He, X.; Lan, Z.; Lin, J.; Huang, M.; Huang, Y.; Fan, L., Tuning the Fermi level of TiO_2 electron transport layer through europium doping for highly efficient perovskite solar cells. *Energy Technology* **2017**, *5* (10), 1820-1826.
264. Gu, X.; Wang, Y.; Zhang, T.; Liu, D.; Zhang, R.; Zhang, P.; Wu, J.; Chen, Z. D.; Li, S., Enhanced electronic transport in Fe^{3+} -doped TiO_2 for high efficiency perovskite solar cells. *Journal of Materials Chemistry C* **2017**, *5* (41), 10754-10760.
265. Xiang, Y.; Ma, Z.; Zhuang, J.; Lu, H.; Jia, C.; Luo, J.; Li, H.; Cheng, X., Enhanced performance for planar perovskite solar cells with samarium-doped TiO_2 compact electron transport layers. *The Journal of Physical Chemistry C* **2017**, *121* (37), 20150-20157.
266. Zhang, H.; Shi, J.; Xu, X.; Zhu, L.; Luo, Y.; Li, D.; Meng, Q., Mg-doped TiO_2 boosts the efficiency of planar perovskite solar cells to exceed 19%. *Journal of Materials Chemistry A* **2016**, *4* (40), 15383-15389.
267. Chen, W.; Wu, Y.; Yue, Y.; Liu, J.; Zhang, W.; Yang, X.; Chen, H.; Bi, E.; Ashraful, I.; Grätzel, M.; Han, L., Efficient and stable large-area

- perovskite solar cells with inorganic charge extraction layers. *Science* **2015**, *350* (6263), 944-948.
268. Momblona, C.; Malinkiewicz, O.; Roldán-Carmona, C.; Soriano, a.; Gil-Escrig, L.; Bandiello, E.; Scheepers, M.; Edri, E.; Bolink, H. J., Efficient methylammonium lead iodide perovskite solar cells with active layers from 300 to 900 nm. *APL Materials* **2014**, *2* (8), 081504.
269. Jung, M.-C.; Raga, S. R.; Qi, Y., Properties and solar cell applications of Pb-free perovskite films formed by vapor deposition. *RSC Advances* **2016**, *6* (4), 2819-2825.
270. Polander, L. E.; Pahner, P.; Schwarze, M.; Saalfrank, M.; Koerner, C.; Leo, K., Hole-transport material variation in fully vacuum deposited perovskite solar cells. *APL Materials* **2014**, *2* (8), 081503.
271. Kim, B.-S.; Kim, T.-M.; Choi, M.-S.; Shim, H.-S.; Kim, J.-J., Fully vacuum-processed perovskite solar cells with high open circuit voltage using MoO₃/NPB as hole extraction layers. *Organic Electronics* **2015**, *17*, 102-106.
272. Ke, W.; Zhao, D.; Grice, C. R.; Cimaroli, A. J.; Fang, G.; Yan, Y., Efficient fully-vacuum-processed perovskite solar cells using copper phthalocyanine as hole selective layers. *Journal of Materials Chemistry A* **2015**, *3* (47), 23888-23894.
273. Son, D.-Y.; Lee, J.-W.; Choi, Y. J.; Jang, I.-H.; Lee, S.; Yoo, P. J.; Shin, H.; Ahn, N.; Choi, M.; Kim, D.; Park, N.-G., Self-formed grain boundary healing layer for highly efficient CH₃NH₃PbI₃ perovskite solar cells. *Nature Energy* **2016**, *1*, 16081.
274. Jiang, J.; Jin, Z.; Lei, J.; Wang, Q.; Zhang, X.; Zhang, J.; Gao, F.; Liu, S., ITIC surface modification to achieve synergistic electron transport layer enhancement for planar-type perovskite solar cells with efficiency exceeding 20%. *Journal of Materials Chemistry A* **2017**, *5* (20), 9514-9522.
275. Pérez-del-Rey, D.; Boix, P. P.; Sessolo, M.; Hadipour, A.; Bolink, H. J., Interfacial modification for high efficiency vapor phase deposited perovskite solar cells based on metal-oxide buffer layer. *The Journal of Physical Chemistry Letters* **2018**, *9* (5), 1041-1046.
276. Nie, W.; Tsai, H.; Asadpour, R.; Blancon, J.-C.; Neukirch, A. J.; Gupta, G.; Crochet, J. J.; Chhowalla, M.; Tretiak, S.; Alam, M. A.; Wang, H.-L.; Mohite, A. D., High-efficiency solution-processed perovskite solar cells with millimeter-scale grains. *Science* **2015**, *347* (6221), 522-525.
277. Genco, A.; Mariano, F.; Carallo, S.; Guerra, V. L. P.; Gambino, S.; Simeone, D.; Listorti, A.; Colella, S.; Gigli, G.; Mazzeo, M., Fully vapor-deposited heterostructured light-emitting diode based on organo-metal halide perovskite. *Advanced Electronic Materials* **2016**, *2* (3), 1500325.
278. Bi, C.; Shao, Y.; Yuan, Y.; Xiao, Z.; Wang, C.; Gao, Y.; Huang, J., Understanding the formation and evolution of interdiffusion grown organolead halide perovskite thin films by thermal annealing. *Journal of Materials Chemistry A* **2014**, *2* (43), 18508-18514.
279. Lin, Q.; Armin, A.; Nagiri, R. C. R.; Burn, P. L.; Meredith, P., Electro-optics of perovskite solar cells. *Nature Photonics* **2014**, *9*, 106-112.

280. Yang, Y.; Ostrowski, D. P.; France, R. M.; Zhu, K.; van de Lagemaat, J.; Luther, J. M.; Beard, M. C., Observation of a hot-phonon bottleneck in lead-iodide perovskites. *Nature Photonics* **2015**, *10*, 53-59.
281. Yamada, Y.; Nakamura, T.; Endo, M.; Wakamiya, A.; Kanemitsu, Y., Photoelectronic responses in solution-processed perovskite $\text{CH}_3\text{NH}_3\text{PbI}_3$ solar cells studied by photoluminescence and photoabsorption spectroscopy. *IEEE Journal of Photovoltaics* **2015**, *5* (1), 401-405.
282. Sun, S.; Salim, T.; Mathews, N.; Duchamp, M.; Boothroyd, C.; Xing, G.; Sum, T. C.; Lam, Y. M., The origin of high efficiency in low-temperature solution-processable bilayer organometal halide hybrid solar cells. *Energy & Environmental Science* **2014**, *7* (1), 399-407.
283. Saba, M.; Cadelano, M.; Marongiu, D.; Chen, F.; Sarritzu, V.; Sestu, N.; Figus, C.; Aresti, M.; Piras, R.; Geddo Lehmann, A.; Cannas, C.; Musinu, A.; Quochi, F.; Mura, A.; Bongiovanni, G., Correlated electron-hole plasma in organometal perovskites. *Nature Communications* **2014**, *5*, 5049.

Other contributions of the author

Publications

Light-emitting electrochemical cells

1. Shavaleev, N. M.; Xie, G.; Varghese, S.; Cordes, D. B.; Slawin, A. M. Z.; **Momblona, C.**; Ortí, E.; Bolink, H. J.; Samuel, I. D. W.; Zysman-Colman, E., Green phosphorescence and electroluminescence of sulfur pentafluoride-functionalized cationic iridium(III) complexes. *Inorganic Chemistry* **2015**, *54* (12), 5907-5914. (IF: 4.857, Q1).
2. Bünzli, A. M.; Pertegás, A.; **Momblona, C.**; Junquera-Hernández, J. M.; Constable, E. C.; Bolink, H. J.; Ortí, E.; Housecroft, C. E., $[\text{Ir}(\text{C}^{\wedge}\text{N})_2(\text{N}^{\wedge}\text{N})]^+$ emitters containing a naphthalene unit within a linker between the two cyclometallating ligands. *Dalton Transactions* **2016**, *45* (41), 16379-16392. (IF: 4.029, Q1).
3. Martir, D. R.; **Momblona, C.**; Pertegás, A.; Cordes, D. B.; Slawin, A. M. Z.; Bolink, H. J.; Zysman-Colman, E., Chiral iridium(III) complexes in light-emitting electrochemical cells: exploring the impact of stereochemistry on the photophysical properties and device performances. *ACS Applied Materials & Interfaces* **2016**, *8* (49), 33907-33915. (IF: 7.504, Q1).
4. Pal, A. K.; Cordes, D. B.; Slawin, A. M. Z.; **Momblona, C.**; Ortí, E.; Samuel, I. D. W.; Bolink, H. J.; Zysman-Colman, E., Synthesis, properties, and light-emitting electrochemical cell (LEEC) device fabrication of cationic Ir(III) complexes bearing electron-withdrawing groups on the cyclometallating ligands. *Inorganic Chemistry* **2016**, *55* (20), 10361-10376. (IF: 4.857, Q1).
5. Henwood, A. F.; Pal, A. K.; Cordes, D. B.; Slawin, A. M. Z.; Rees, T. W.; **Momblona, C.**; Babaei, A.; Pertegás, A.; Ortí, E.; Bolink, H. J.; Baranoff, E.; Zysman-Colman, E., Blue-emitting cationic iridium(III) complexes featuring pyridylpyrimidine ligands and their use in sky-blue

electroluminescent devices. *Journal of Materials Chemistry C* **2017**, *5* (37), 9638-9650. (IF: 5.256, Q1).

6. Martínez-Alonso, M.; Cerdá, J.; **Momblona, C.**; Pertegás, A.; Junquera-Hernández, J. M.; Heras, A.; Rodríguez, A. M.; Espino, G.; Bolink, H. J.; Ortí, E., Highly stable and efficient light-emitting electrochemical cells based on cationic iridium complexes bearing arylazole ancillary ligands. *Inorganic Chemistry* **2017**, *56* (17), 10298-10310. (IF: 4.857, Q1).

IF = Impact factor (Science Citation Reports, Web of Science), Q = Quartile.

Perovskite solar cells

1. Baumann, A.; Tvingstedt, K.; Heiber, M. C.; Väh, S.; **Momblona, C.**; Bolink, H. J.; Dyakonov V., Persistent photovoltage in methylammonium lead iodide perovskite solar cells. *APL Materials* **2014**, *2* (8), 081501. (IF: 4.335, Q1).
2. Roldán-Carmona, C.; Malinkiewicz, O.; Betancur, R.; Longo, G.; **Momblona, C.**; Jaramillo, F.; Camacho, L.; Bolink, H. J., High efficiency single-junction semitransparent perovskite solar cells. *Energy & Environmental Science* **2014**, *7* (9), 2968-2973. (IF: 29.518, Q1).
3. Sessolo, M.; **Momblona, C.**; Gil-Escrig, L.; Bolink, H. J., Photovoltaic devices employing vacuum-deposited perovskite layers. *MRS Bulletin* **2015**, *40* (8), 660-666. (IF: 5.199, Q1).
4. Wetzelaer, G.-J. A. H.; Scheepers, M.; Sempere, A. M.; **Momblona, C.**; Ávila, J.; Bolink, H. J., Trap-assisted non-radiative recombination in organic-inorganic perovskite solar cells. *Advanced Materials* **2015**, *27* (11), 1837-1841. (IF: 19.791, Q1).
5. El-Hajje, G.; **Momblona, C.**; Gil-Escrig, L.; Ávila, J.; Guillemot, T.; Guillemoles, J.-F.; Sessolo, M.; Bolink, H. J.; Lombez, L., Quantification of spatial inhomogeneity in perovskite solar cells by hyperspectral luminescence imaging. *Energy & Environmental Science* **2016**, *9* (7), 2286-2294. (IF: 29.518, Q1).

6. Gil-Escrig, L.; **Momblona, C.**; Forgács, D.; Pla, S.; Fernández-Lázaro, F.; Sessolo, M.; Sastre-Santos, Á.; Bolink, H. J., Interface engineering in efficient vacuum deposited perovskite solar cells. *Organic Electronics* **2016**, *37*, 396-401. (IF: 3.399, Q1).
7. Gil-Escrig, L.; **Momblona, C.**; Sessolo, M.; Bolink, H. J., Fullerene imposed high open-circuit voltage in efficient perovskite based solar cells. *Journal of Materials Chemistry A* **2016**, *4* (10), 3667-3672. (IF: 8.867, Q1).
8. Calió, L.; **Momblona, C.**; Gil-Escrig, L.; Kazim, S.; Sessolo, M.; Sastre-Santos, Á.; Bolink, H. J.; Ahmad, S., Vacuum deposited perovskite solar cells employing dopant-free triazatruxene as the hole transport layer. *Solar Energy Materials and Solar Cells* **2017**, *163*, 237-241. (IF: 4.784, Q1).
9. Forgács, D.; Gil-Escrig, L.; Pérez-Del-Rey, D.; **Momblona, C.**; Werner, J.; Niesen, B.; Ballif, C.; Sessolo, M.; Bolink, H. J., Efficient Monolithic Perovskite/Perovskite Tandem Solar Cells. *Advanced Energy Materials* **2017**, *7* (8), 1602121. (IF: 16.72, Q1).
10. Forgács, D.; Pérez-del-Rey, D.; Ávila, J.; **Momblona, C.**; Gil-Escrig, L.; Dänekamp, B.; Sessolo, M.; Bolink, H. J., Efficient wide band gap double cation-double halide perovskite solar cells. *Journal of Materials Chemistry A* **2017**, *5* (7), 3203-3207. (IF: 8.867, Q1).
11. Sherkar, T. S.; **Momblona, C.**; Gil-Escrig, L.; Ávila, J.; Sessolo, M.; Bolink, H. J.; Koster, L. J. A., Recombination in perovskite solar cells: significance of grain boundaries, interface traps, and defect ions. *ACS Energy Letters* **2017**, *2* (5), 1214-1222.
12. Sherkar, T. S.; **Momblona, C.**; Gil-Escrig, L.; Bolink, H. J.; Koster, L. J. A., Improving perovskite solar cells: insights from a validated device model. *Advanced Energy Materials* **2017**, *7* (13), 1602432. (IF: 16.72, Q1).
13. Tvingstedt, K.; Gil-Escrig, L.; **Momblona, C.**; Rieder, P.; Kiermasch, D.; Sessolo, M.; Baumann, A.; Bolink, H. J.; Dyakonov, V., Removing leakage and surface recombination in planar perovskite solar cells. *ACS Energy Letters* **2017**, *2* (2), 424-430.

14. Ávila, J.; **Momblona, C.**; Boix, P. P.; Sessolo, M.; Bolink, H. J., Vapor-deposited perovskites: the route to high-performance solar cell production?. *Joule* **2017**, *1* (3), 431-442.
15. Longo, G.; **Momblona, C.**; La-Placa, M.-G.; Gil-Escrig, L.; Sessolo, M.; Bolink, H. J., Fully vacuum-processed wide band gap mixed-halide perovskite solar cells. *ACS Energy Letters* **2018**, *3* (1), 214-219.
16. Gil-Escrig, L.;[‡] **Momblona, C.**; [‡] La-Placa, M.-G.; Boix, P. P.; Sessolo, M.; Bolink, H. J., Vacuum deposited triple-cation mixed-halide perovskite solar cells. *Advanced Energy Materials* **2018**, accepted. ([‡] equally contributed). (IF: 16.72, Q1).

IF = Impact factor (Science Citation Reports, Web of Science), Q = Quartile.

Patents

European Patent. EP3242340A1 / WO2017191265A1

Name: Solar cell.

Authors: Momblona Rincón, María Cristina; Gil-Escrig, Lidón; Sessolo, Michele; Bolink, Jan Hendrik; Blochwitz-Nimoth, Jan; Lederer, Kay.

Priority date: 04.05.2016

Application number: 16172226.9.

Date of publication: 08.11.2017

Applicant: NovaLED GmbH.

Index of Figures

Figure 1. World energy consumption in 2016. ¹	3
Figure 2. a) Structure of the prototype Ir-iTMC: $[\text{Ir}(\text{ppy})_2(\text{bpy})][\text{PF}_6]$ where ppy^- = 2-phenylpyridinate and bpy = 2,2'-bipyridine. ⁴⁸ The HOMO is spatially located on the Ir metal centre and the phenyl rings of the cyclometalated ligands (in orange) and the LUMO is located on the ancillary ligand (in green). Schematic representation of the electronic density contours calculated for the frontier molecular orbitals b) HOMO and c) LUMO of $[\text{Ir}(\text{ppy})_2(\text{bpy})][\text{PF}_6]$ complex. d) Electronic energy-level diagram for a generic Ir-iTMC. MC is metal-centred, LC is ligand-centred, MLCT and LLCT are metal-to-ligand and ligand-to-ligand charge transfer, respectively.....	12
Figure 3. General scheme depicting the different approaches used for tuning the colour emission toward the blue (left) or red (right) of the archetype $[\text{Ir}(\text{ppy})_2(\text{bpy})][\text{PF}_6]$ complex (centre). Up: Energy-level diagram. Bottom: Chemical structure of the $[\text{Ir}(\text{ppy})_2(\text{bpy})][\text{PF}_6]$ complex, where EWG and EDG mean electron-withdrawing groups and electron-donating groups, respectively. Adapted from reference 58.....	14
Figure 4. Schematic layout of a double-layer sandwiched-type LEC.....	16
Figure 5. The Commission Internationale de l'Eclairage (CIE) chromaticity diagram.....	18
Figure 6. Scheme of the potential profile and the electronic and ionic charge distribution in a LEC during steady-state operation. a) Electrochemical doping model (ECD) and b) electrodynamic model (ED). Thick blue line: potential profile. Cyan and red symbols represent the negatively and positively charges, respectively. Orange and yellow regions correspond to high- and low-field regions in the bulk, respectively. Adapted from reference 13.....	19
Figure 7. Chemical structures of the red and near-infrared Ir-iTMC emitters (complexes 1–8) studied in this thesis.....	28

Figure 8. Photograph of the class 10000 cleanroom at the Instituto de Ciencia Molecular (ICMol) of the Universidad de Valencia.....	29
Figure 9. Electroluminescence spectra of a) LECs 1–6 and 8 driven at an average pulsed-current density of 100 A m ⁻² for 1–6 and 400 A m ⁻² for 8 and b) LEC 7 driven at an average pulsed-current density of 400 A m ⁻² . (1000 Hz, 50% duty cycle, block wave).....	35
Figure 10. Left: Time-dependent luminance or irradiance. Right: Time-dependent operating average voltage. a) LECs 1–6 , b) LEC 7 and c) LEC 8 . Devices operated under an average pulsed-current density of 100 A m ⁻² in a) and 400 A m ⁻² in b) and c). (1000 Hz, 50% duty cycle, block wave).....	36
Figure 11. Extended graph of the time-dependent luminance of LECs 1–3 operated under an averaged pulsed-current density of 100 A m ⁻² . (1000 Hz, 50% duty cycle, block wave).....	39
Figure 12. Luminance <i>versus</i> time of LEC 1 operated under different average pulsed-current densities from 300 to 1500 A m ⁻² (1000 Hz, 50% duty cycle, block wave).....	40
Figure 13. Time to reach 100 cd m ⁻² (<i>t</i> ₁₀₀) <i>versus</i> applied current density for LEC 1 . (1000 Hz, 50% duty cycle, block wave).....	42
Figure 14. Crystal structure of ABX ₃ 3D-perovskite. Pb are placed at the centre of the grey octahedrons, lavender spheres represent iodine atoms and green spheres represent the methylammonium cations. Adapted from reference 152.....	48
Figure 15. Schematic representation of a vacuum chamber with two thermal sources.....	54
Figure 16. Schematic energy-level diagram with absorber and adjacent selective charge layers with adequate energy alignment with the absorber.....	58
Figure 17. Schematic representation of the different recombination mechanisms active in perovskites. a) Trap-assisted recombination. b) Bimolecular recombination. c) Auger recombination. VB: valence band, CB: conduction band. Adapted from reference 221.....	59

Figure 18. Typical $J-V$ characteristics of a solar cell.....	61
Figure 19. The maximum power conversion efficiency for a solar cell operated at 298.15 K and illuminated with an AM 1.5 G spectral irradiance (ASTM 173-03) in accordance with standard solar test conditions as a function of the band gap energy. Graph depicted from tabulated data from reference 238.....	62
Figure 20. Schematic layout of single-junction perovskite solar cells. a) Mesoscopic and b) planar $p-i-n$ solar cells. c) Planar and d) mesoscopic $n-i-p$ solar cells. TCO: transparent conductive oxide, HTL: hole transport layer, ETL: electron transport layer.....	63
Figure 21. Scheme of the device layouts studied in this thesis a) ITO/PEDOT:PSS/polyTPD/MAPbI ₃ /PCBM/Au and b) ITO/PEDOT:PSS/dopedpolyTPD/MAPbI ₃ /PCBM/Au.....	68
Figure 22. Percent absorption spectra of vacuum-deposited MAPbI ₃ films with thicknesses ranging from 160 to 900 nm.....	70
Figure 23. X-ray diffraction patterns of perovskite layers with different layer thicknesses.....	71
Figure 24. a) Flat band energy level diagram. b) Cross-section SEM of a device with 900 nm perovskite thick film (in collaboration with Weizmann Institute of Science, Israel).....	72
Figure 25. Thickness dependence of the photovoltaic parameters (J_{sc} , V_{oc} , FF and PCE) extracted from their respective $J-V$ curves.....	73
Figure 26. a) IPCE and b) $J-V$ -curves of ITO/PEDOT:PSS/polyTPD/MAPbI ₃ /PCBM/Au devices with 285 and 900 nm perovskite thickness and ITO/PEDOT:PSS/polyTPD/MAPbI ₃ /PCBM/Au with 900 nm perovskite thickness.....	75
Figure 27. Scheme of the a) $p-i-n$ and b) $n-i-p$ devices studied in this work.....	82

Figure 28. a) XRD diffraction pattern, b) top-view SEM image and c) UV-Vis spectrum of 500 nm thick film of MAPbI ₃ deposited on top of glass.....	85
Figure 29. <i>J-V</i> curve of the <i>p-i-n</i> device with the layout ITO/TaTm/MAPbI ₃ /C ₆₀ /Ag illuminated under 1 sun illumination (100 mW cm ⁻²).....	86
Figure 30. <i>p-i-n</i> solar cell: a) cross-section SEM (scale bar 200 nm) and scheme of the device layout, b) flat-band energy level diagram (EA electron affinity, IP ionization potential of the dopants) and c) chemical structures of the organic molecules and molecular dopants used to prepare the charge transport layers.....	87
Figure 31. a) Absorption spectra of different <i>p</i> -HTLs as a function of F ₆ -TCNNQ dopant concentration, b) absorption spectra of different <i>n</i> -ETLs as a function of PhIm dopant concentration, c) conductivity of the <i>p</i> -HTLs as a function of F ₆ -TCNNQ dopant concentration and d) conductivity of the <i>n</i> -ETLs as a function of PhIm dopant concentration.....	88
Figure 32. <i>p-i-n</i> solar cells operated under 1 sun illumination (100 mW cm ⁻²) as a function of F ₆ -TCNNQ dopant concentration. a) <i>J-V</i> curves, b) external quantum efficiency (EQE _{PV}), c) evolution of the key parameters deduced from the <i>J-V</i> curves (<i>V</i> _{OC} , <i>J</i> _{SC} , FF and PCE) with F ₆ -TCNNQ dopant concentration.....	89
Figure 33: <i>n-i-p</i> devices: a) external quantum efficiency (EQE _{PV}) and b) <i>J-V</i> curves obtained under 1 sun illumination (100 mW cm ⁻²) as a function of PhIm dopant concentration. c) Cross-section SEM image of a representative <i>n-i-p</i> solar cell. d) <i>J-V</i> curve of the champion <i>n-i-p</i> solar cell.....	91
Figure 34. <i>J-V</i> curves obtained under 1 sun illumination (100 mW cm ⁻²) of the champion <i>p-i-n</i> and <i>n-i-p</i> solar cells obtained in this work.....	92
Figure 35. FF dependence on light intensity of a) <i>p-i-n</i> and b) <i>n-i-p</i> at different dopant concentrations of F ₆ -TCNNQ and PhIm, respectively. <i>J-V</i> and	

radiant flux-voltage curves of c) <i>p-i-n</i> and d) <i>n-i-p</i> champion solar cells.....	93
Figure 36. <i>J-V</i> curves obtained under 1 sun illumination (100 mW cm^{-2}) at different scan speeds for a) <i>p-i-n</i> and b) <i>n-i-p</i> solar cells.....	94
Figure 37. a) <i>J-V</i> curves obtained under 1 sun illumination (100 mW cm^{-2}) for <i>p-i-n</i> devices with both undoped charge transport layers (green line) or without one of the undoped charge transport layers (blue and red). b) <i>J-V</i> curves obtained under 1 sun illumination (100 mW cm^{-2}) for <i>n-i-p</i> devices with both undoped charge transport layers (orange line) or without one of the undoped charge transport layers.....	95
Figure 38. <i>J-V</i> curves under 1 sun illumination (100 mW cm^{-2}) for <i>p-i-n</i> devices a) without <i>p</i> -HTL or b) without <i>n</i> -ETL.....	97
Figure 39. Time-dependent V_{OC} , FF, J_{SC} and PCE of a) <i>p-i-n</i> and b) <i>n-i-p</i> solar cells.....	98
Figure 40. Statistics of the PCE measured for <i>p-i-n</i> (green) and <i>n-i-p</i> (red) devices. Green and red solid lines represent the Gaussian distribution fitting for the PCE.....	98

Index of Tables

Table 1. Thin-film photophysical characterization of complexes 1–8 ($\lambda_{\text{exc}} = 320$ nm).....	33
Table 2. Device performance parameters and electroluminescence data obtained for LECs 1–8 operated under pulsed-current driving (1000 Hz, 50% duty cycle, block wave).....	37
Table 3. Key parameters extracted from J – V curves of p - i - n devices with perovskite thickness from 210 to 900 nm.....	74
Table 4. FF values of a device with 400 nm perovskite thick film at different % of light intensity illumination.....	75
Table 5. Key PV performance data extracted from J – V curves of representative p - i - n and n - i - p devices with one of the two undoped charge selective layers or with both undoped layers.....	95

List of abbreviations

0D	Zero-dimensional structure
1D	One-dimensional structure
2D	Two- and quasi-two-dimensional structure
3D	Three-dimensional structure
ALD	Atomic layer deposition
[Bmim][PF ₆]	3-butyl-1-methylimidazolium hexafluorophosphate
bpy	2,2'-bipyridine
btzpy	2-(pyridin-2-yl)benzo[<i>d</i>]thiazole
C ^N	Cyclometalated ligand
CB	Conduction band
CBM	Conduction band minimum
CIE coord.	Commission Internationale de l'Eclairage coordinates
CIGS	Copper indium gallium diselenide
CSVT	Closed space vapour transport
CVD	Chemical vapour deposition
DMF	Dimethylformamide
DMSO	Dimethylsulfoxide
DSSC	Dye-sensitized solar cells
E_b	Exciton binding energy
E_g	Band gap energy
ECD	Electrochemical doping model
ED	Electrodynamic model
EDG	Electron donating group
EDL	Electric double layer
EGL	Energy gap law
EQE	External quantum efficiency
ETL	Electron transport layer
ETM	Electron transport material
EWG	Electron withdrawing group

F ₆ -TCNNQ	2,2'-(Perfluoronaphthalene-2,6-diylidene) dimalononitrile
FA ⁺	Formamidinium cation
FF	Fill factor
FTO	Fluorine doped tin oxide
GBL	γ-butyrolactone
GIXRD	Grazing incident X-ray diffraction
HOMO	Highest-occupied molecular orbital
HTL	Hole transport layer
HTM	Hole transport material
IL	Ionic liquid
IQE	Internal quantum efficiency
Ir-iTMC	Iridium ionic transition-metal complex
ISC	Intersystem crossing
iTMC	Ionic transition-metal complex
ITO	Indium tin oxide
J_{mpp}	Current density at the maximum power point
J_{sc}	Short-circuit current density
LC	Ligand-centred
LEC	Light-emitting electrochemical cell
LED	Light-emitting diode
LFSEs	Ligand-field splitting energies
LLCT	Ligand-to-ligand charge transfer
LUMO	Lowest-unoccupied molecular orbital
MA ⁺	Methylammonium cation
MACl	Methylammonium chloride
MAI	Methylammonium iodide
MAPbI ₃	Methylammonium lead iodide
MC	Metal-centred
MLCT	Metal-to-ligand charge transfer
N [^] N	Ancillary diimide ligand
<i>n</i> -ETL	<i>n</i> -doped electron transport layer

NIR	Near infrared
OLED	Organic light-emitting diode
OPV	Organic photovoltaics
OS	Organic semiconductor
PC	Poly(carbonate)
PCBM	(6,6)-phenyl C ₆₁ -butyric acid methyl ester
PCE	Power conversion efficiency
PE	Power efficiency
PEDOT:PSS	Poly(3,4-ethylenedioxythiophene):polystyrenesulfonate
PhIm	N1,N4-bis(tri- <i>p</i> -tolylphosphoranylidene) benzene-1,4-diamine
<i>p</i> -HTL	<i>p</i> -doped hole transport layer
PL	Photoluminescence
pLEC	Conjugated polymer-based light-emitting electrochemical cell
PLQY	Photoluminescence quantum yield
PMMA	Poly(methyl methacrylate)
polyTPD	Poly(N,N'-bis(4-butylphenyl)-N,N'bis(phenyl)benzidine
PP	Polypropylene
ppy ⁻	2-phenylpyridinate
PS	Poly(styrene)
PSC	Perovskite solar cell
PTFE	Polytetrafluoroethylene
QD-LEC	Quantum dots-based light-emitting electrochemical cell
R2R	Roll-to-roll
SEM	Scanning electron microscopy
SI	International system
SM-LEC	Small molecule-based light-emitting electrochemical cell
SOC	Spin-orbit coupling
SSL	Solid-state lighting
T ₁	Lowest-energy triplet excited state
TaTm	N ₄ ,N ₄ ,N ₄ '',N ₄ ''-tetra([1,1'-biphenyl]-4-yl)-[1,1':4',1''-terphenyl]-4,4''-diamine

TCO	Transparent conductive oxide
TD-DFT	Time-dependent version of the density function theory
TiO ₂	Titanium dioxide
TMC-LEC	Transition metal complex-based light-emitting electrochemical cell
VB	Valence band
VBM	Valence band minimum
V_{mpp}	Voltage at the maximum power point
V_{OC}	Open-circuit voltage
XRD	X-Ray diffraction

Annexes

Highly Stable Red-Light-Emitting Electrochemical Cells

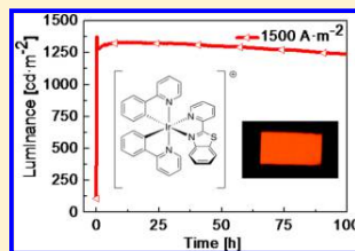
Cathrin D. Ertl,^{S,‡} Cristina Momblona,^{S,†} Antonio Pertegás,[†] José M. Junquera-Hernández,[†] Maria-Grazia La-Placa,[†] Alessandro Prescimone,[‡] Enrique Ortí,[†] Catherine E. Housecroft,^{*,‡} Edwin C. Constable,[‡] and Henk J. Bolink^{*,†,§}

[†]Instituto de Ciencia Molecular, Universidad de Valencia, C/Catedrático José Beltrán 2, ES-46980 Paterna (Valencia), Spain

[‡]Department of Chemistry, University of Basel, Spitalstrasse 51, CH-4056 Basel, Switzerland

Supporting Information

ABSTRACT: The synthesis and characterization of a series of new cyclometalated iridium(III) complexes $[\text{Ir}(\text{ppy})_2(\text{N}^{\wedge}\text{N})][\text{PF}_6]$ in which Hppy = 2-phenylpyridine and $\text{N}^{\wedge}\text{N}$ is (pyridin-2-yl)benzo[*d*]thiazole (L1), 2-(4-(*tert*-butyl)pyridin-2-yl)benzo[*d*]thiazole (L2), 2-(6-phenylpyridin-2-yl)benzo[*d*]thiazole (L3), 2-(4-(*tert*-butyl)-6-phenylpyridin-2-yl)benzo[*d*]thiazole (L4), 2,6-bis(benzo[*d*]thiazol-2-yl)pyridine (L5), 2-(pyridin-2-yl)benzo[*d*]oxazole (L6), or 2,2'-dibenzo[*d*]thiazole (L7) are reported. The single crystal structures of $[\text{Ir}(\text{ppy})_2(\text{L1})][\text{PF}_6] \cdot 1.5\text{SCH}_2\text{Cl}_2$, $[\text{Ir}(\text{ppy})_2(\text{L6})][\text{PF}_6] \cdot \text{CH}_2\text{Cl}_2$, and $[\text{Ir}(\text{ppy})_2(\text{L7})][\text{PF}_6]$ have been determined. The new complexes are efficient red emitters and have been used in the active layers in light-emitting electrochemical cells (LECs). The effects of modifications of the 2-(pyridin-2-yl)benzo[*d*]thiazole ligand on the photoluminescence and LEC performance have been examined. Extremely stable red-emitting LECs are obtained, and when $[\text{Ir}(\text{ppy})_2(\text{L1})][\text{PF}_6]$, $[\text{Ir}(\text{ppy})_2(\text{L2})][\text{PF}_6]$, or $[\text{Ir}(\text{ppy})_2(\text{L3})][\text{PF}_6]$ are used in the active layer, device lifetimes greater than 1000, 6000, and 4000 h, respectively, are observed



1. INTRODUCTION

Lighting is one of the most important needs for daily life. Light-emitting electrochemical cells (LECs) have great potential as light-emitting devices that have emerged over the last 20 years.^{1–11} LECs are simpler than organic light-emitting diodes (OLEDs), because they are typically based on a single layer architecture, whereas OLEDs employ a multilayer stack.¹² The active layer of a LEC consists of an emitter containing ions, using either a polymeric material or an ionic transition-metal complex (iTMC),^{13–15} sandwiched between two air-stable electrodes. This allows for the preparation of novel form factors, such as fibers,¹⁶ and on-chip designs. iTMCs, and particularly iridium-iTMCs, are the most explored type of electroluminescent material in LECs due their phosphorescence emission that allows them to theoretically achieve 100% of luminescence conversion.¹⁷ The operation of LECs depends on the movement of ions, which can lead to a delay in turn-on of light emission after applying a bias. Additionally, the movement of ions eventually also leads to a reduction of luminance. If LECs are to be applied commercially, a combination of fast responses with efficient and stable devices must be accomplished. Since 2004,¹⁸ when Slinker et al. employed the first iridium-iTMC, many types of ligands and substituents have been studied, reporting lifetimes up to 3000 h for orange-emitting LECs.¹⁹ We have shown that this objective is facilitated by operating the device under pulsed current.¹⁴

The stability of LECs, as for OLEDs, depends on the current applied through the device and decreases with increasing current density. This dependency is typically stronger in LECs

because of the increase in ion separation leading to the growing of doped regions²⁰ or to chemical degradation.²¹ Additionally, the efficiency typically decreases with increasing current densities, due to exciton–polaron and exciton–exciton quenching processes. Recently, reports were published showing that the charge carrier balance is improved by adding lithium salts to the light-emitting layer.^{22–24} Many different emission colors have been reported ranging from blue to deep red and even near-infrared, yet few pure red-emitting LECs have been reported.²⁵ This color is important in applications such as signage and automotive. Generally, pure-red LECs under DC operation mode exhibit lifetimes of a few hours.^{8,11,25,26} Tamayo et al. reported a red-emitting complex, $[\text{Ir}(\text{tbutyl-ppy})_2(\text{biq})][\text{PF}_6]$ (tbutyl-ppy[−] = 4'-*tert*-butylphenyl-pyrazolato, biq = 2,2'-biquinoline), that was used in LECs showing a luminance of 7500 cd m^{−2} (no lifetime data were presented).⁸ Zhang et al. also reported a red-LEC using the $[\text{Ir}(\text{ppy})_2(\text{pyoxd})][\text{PF}_6]$ complex (ppy[−] = 2-phenylpyridinate, pyoxd = 2-phenyl-5-(2-pyridyl)-1,3,4-oxadiazole) with an EQE of 9.51%.¹¹ However, the lifetime of the device (time required to reach one-half of the maximum luminance, $t_{1/2}$) under constant-voltage of 5 V was 490 min. Hu et al. introduced in a host–guest configuration an $\text{N}^{\wedge}\text{N}$ ancillary benzoimidazole ligand in $[\text{Ir}(\text{ppy})_2(\text{qIbi})][\text{PF}_6]$ (qIbi = 2-(1-phenyl-1*H*-benzoimidazol-2-yl)quinoline) producing a LEC with a deep red emission.²⁷

Received: December 30, 2016

Published: February 3, 2017

In cyclometalated $[\text{Ir}(\text{C}^{\wedge}\text{N})_2(\text{N}^{\wedge}\text{N})]^+$ complexes, the benzothiazole moiety has previously been used as part of the cyclometalating $\text{C}^{\wedge}\text{N}$ ligand, for example, as 2-phenylbenzo- $[d]$ thiazole.^{28–30} Although complexes of other metal ions coordinated by 2-(pyridin-2-yl)benzo- $[d]$ thiazole (btzpy) have been investigated,^{31,32} there is only one example of an $[\text{Ir}(\text{C}^{\wedge}\text{N})_2(\text{N}^{\wedge}\text{N})]^+$ complex incorporating a related $\text{N}^{\wedge}\text{N}$ domain ($\text{N}^{\wedge}\text{N} = 2$ -(pyridin-2-yl)-4,5-dihydrothiazole); in this example, the focus of attention was on the use of the iridium(III) complex as a photosensitizer for catalytic water reduction.³³

Here, we report a series of LECs using the ionic iridium(III) complex $[\text{Ir}(\text{ppy})_2(\text{btzpy})][\text{PF}_6]$ having ppy^- as the cyclometalating ligand and btzpy as the $\text{N}^{\wedge}\text{N}$ ancillary ligand. The incorporation of substituents, replacement for other ligands, and the role of the heteroatom in the benzothiazole unit are analyzed. All LECs exhibit deep red to infrared electroluminescence. Long lifetimes, even when driven at high current densities, are obtained.

2. EXPERIMENTAL SECTION

Synthesis and Compound Characterization. Starting materials were obtained in reagent grade and used as received. Dry solvents were purchased from Sigma-Aldrich or Acros Organics and used for reactions carried out under inert atmosphere. For all other reactions, solvents used were of reagent grade or distilled. HPLC grade solvents were used for analyses. Column chromatography was performed using Fluka silica gel 60 (0.040–0.063 mm).

One- and two-dimensional NMR spectra were measured on a Bruker Avance III-500 (500 MHz) spectrometer. Chemical shifts are referenced to residual solvent peaks with $\delta(\text{TMS}) = 0$ ppm. Electrospray ionization mass spectra were recorded on a Bruker Esquire 3000^{plus} spectrometer. LC-ESI mass spectra were obtained on a combination of Shimadzu (LC) and Bruker AmaZon X instruments. Elemental analysis was performed on an Elementar Vario Micro Cube instrument, and high resolution ESI mass spectra on a Bruker maXis 4G QTOF spectrometer. FT-IR spectra were recorded on a PerkinElmer Spectrum Two UATR instrument. Absorption spectra were measured on an Agilent 8453 spectrophotometer, and solution emission spectra on a Shimadzu 5301PC spectrofluorophotometer. Solution and powder photoluminescence quantum yields were recorded on a Hamamatsu absolute PL quantum yield spectrometer C11347 Quantaurus QY. Emission spectra of powder samples as well as solution and powder excited-state lifetime measurements were carried out on a Hamamatsu Compact Fluorescence lifetime spectrometer C11367 Quantaurus Tau. Electrochemical measurements were performed using cyclic and square-wave voltammetry on a CH Instruments 900B potentiostat with both glassy carbon and platinum working and platinum auxiliary electrodes; a silver wire was used as a pseudoreference electrode. Dry, purified CH_2Cl_2 was used as solvent, and 0.1 M TBAPF₆ as supporting electrolyte. Ferrocene as internal reference was added at the end of each experiment.

Crystallography. Single crystal structure determination was carried out on a Bruker APEX-II diffractometer. Data reduction, solution, and refinement was done using the programs APEX³⁴ and SHELXL97.³⁵ Structure analysis was done using Mercury v. 3.6.³⁶

Photoluminescence Characterization. The samples for thin-film photoluminescence measurements were done with the same composition and thickness than the emissive layer of LECs. Each complex was mixed with the ionic liquid (IL) 1-butyl-3-methylimidazolium hexafluoridophosphate ($[\text{Bmim}][\text{PF}_6]$) in a 4-to-1 molar ratio. A 100 nm thick film was deposited from a 20 mg mL⁻¹ solution of complexes 1, 5, and 6 in acetonitrile, complexes 2, 3, and 4 in dichloromethane, and complex 7 in methyl ethyl ketone/anisol 3:2, respectively. Prior to deposition, all solutions were filtered with a 0.22 μm pore size filter and spin-coated at 1000 rpm for 30 s in air onto cleaned quartz substrates. As the films obtained from the filtered

solutions of complexes 2 and 4 in the LEC layout were inhomogeneous, a small amount of 2 wt % of PMMA was added to improve the homogeneity of the layer.

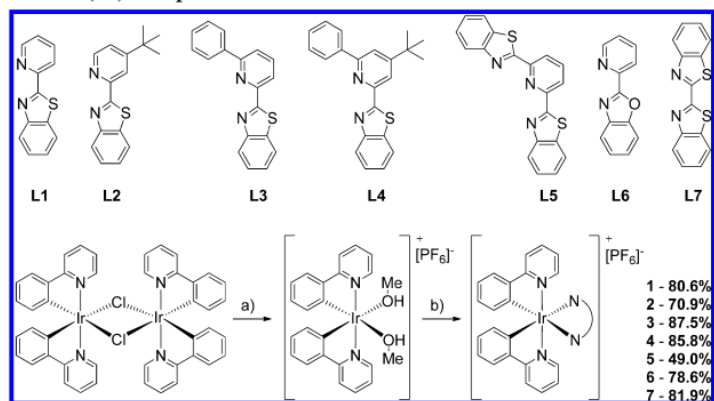
The thin-film photoluminescence spectra and quantum yields were measured in air with a Hamamatsu C9920-02 Absolute PL Quantum Yield Measurement System.

Computational Details. Density functional calculations (DFT) were carried out with the D.01 revision of the Gaussian 09 program package³⁷ using Becke's three-parameter B3LYP exchange-correlation functional^{38,39} together with the 6-31G** basis set for C, H, N, S, and O,⁴⁰ and the "double- ζ " quality LANL2DZ basis set for the Ir element.⁴¹ An effective core potential (ECP) replaces the inner core electrons of Ir leaving the outer core $[(5s)^2(5p)^6]$ electrons and the $(5d)^6$ valence electrons of Ir(III). The geometries of the singlet ground state (S_0) and of the lowest-energy triplet state (T_1) were fully optimized without imposing any symmetry restriction. Phosphorescence emission energies were estimated as the vertical difference between the energy of the minimum of the lowest-energy triplet state and the energy of S_0 at the T_1 optimized geometry. The calculation of the energy of S_0 at the T_1 geometry was performed as an equilibrium single-point calculation with respect to the solvent reaction field/solute electronic density polarization process. All the calculations were performed in the presence of the solvent (dichloromethane). Solvent effects were considered within the self-consistent reaction field (SCRF) theory using the polarized continuum model (PCM) approach.^{42–44} Time-dependent DFT (TD-DFT)^{45–47} calculations of the lowest lying 6 triplets of all systems, and the lowest 40 singlets of 1 and 7, were performed in the presence of the solvent at the minimum-energy geometry optimized for the ground state.

LEC Fabrication. All materials were used as received. Poly(3,4-ethylenedioxythiophene):polystyrenesulfonate (PEDOT:PSS Clevious P VP Al 4083) was purchased from Heraeus. The ionic liquid (IL) 1-butyl-3-methylimidazolium hexafluoridophosphate ($[\text{Bmim}][\text{PF}_6]$) and the poly(methyl methacrylate) (PMMA, $M_w = 120\,000$ g mol⁻¹) were purchased from Sigma-Aldrich. The solvents acetonitrile, dichloromethane, methyl ethyl ketone, and anisol were purchased from Sigma-Aldrich. The photolithography-patterned indium tin oxide (ITO) glass substrates were purchased from Naranjo Substrates (www.naranjosubstrates.com).

LECs were prepared as follows. The substrates were subsequently cleaned with soap, deionized water, and isopropanol in an ultrasonic bath for 5 min each, followed by 20 min of UV-ozone treatment. Onto the clean ITO substrates, an 80 nm thick film of PEDOT:PSS was spin-coated at 1000 rpm for 60 s. The PEDOT:PSS was added from a syringe and filtered with a 0.45 μm pore size filter. The PEDOT:PSS layer was dried at 150 °C for 15 min. On top of it, a 100 nm thick film of the emissive layer was deposited in the same conditions that were described for thin-film photoluminescence samples. In brief, filtered solutions of complex:IL in a 4-to-1 molar ratio were spin-coated in air at 1000 rpm for 30 s and transferred to a glovebox (MBraun, $\text{O}_2 < 0.1$ ppm, $\text{H}_2\text{O} < 0.1$ ppm) for annealing at 100 °C for 1 h. Finally, a 70 nm thick film of aluminum was deposited as top electrode contact using a shadow mask. The active area in all devices is 0.634 cm².

LEC Characterization. LECs using complexes 1–7 were tested by applying pulsed current and by monitoring the voltage and the luminance with a True Color Sensor (MTCsICT Sensor, MAZeT GmbH) using a Lifetime Test System (Botest OLT OLED Lifetime-Test System, Botest System GmbH). The pulsed current consisted of a block wave at 1 kHz frequency with a duty cycle of 50%. LEC with complex 7 was tested by applying pulsed current with the Lifetime Test System and the irradiance was monitored with a sensitive Si-photodiode coupled to an integrating sphere. The peak current density of the pulse was 200 A m⁻² and the average current density was 100 A m⁻² for LECs 1–7. For further understanding of the stability of LEC 1, this device was driven at average current densities of 300, 700, 1250, and 1500 A m⁻². Electroluminescence spectra were recorded using an Avantes fiber optics photospectrometer. All devices were tested without encapsulation and were characterized inside the glovebox at room temperature. For each device configuration, we evaluated eight cells to ensure meaningful statistics.

Scheme 1. Synthesis of Iridium(III) Complexes 1–7^a

^aReaction conditions: (a) AgPF₆, MeOH, room temperature, 2–3.5 h; (b) N^N (L1–L7), MeOH, room temperature, overnight. Reported yields (over two steps) are calculated based on the dimer starting materials.

3. RESULTS AND DISCUSSION

Ligand Synthesis. The chemical structures of ancillary ligands L1–L7 used in this series of complexes are shown in Scheme 1 and the syntheses are detailed in the Supporting Information. 2-(Pyridin-2-yl)benzo[*d*]thiazole (L1), 2-(4-(*tert*-butyl)pyridin-2-yl)benzo[*d*]thiazole (L2), and 2-(pyridin-2-yl)benzo[*d*]oxazole (L6) were prepared by adaptation of a copper-catalyzed coupling reaction described in the literature.⁴⁸ 2,6-Bis(benzo[*d*]thiazol-2-yl)pyridine (L5)⁴⁹ and 2,2'-bibenzo[*d*]thiazole (L7)⁵⁰ were synthesized following reported literature procedures by a condensation reaction of 2-aminothiophenol with 2,6-pyridinedicarboxaldehyde or oxalic acid, respectively. The synthesis of 2-(6-phenylpyridin-2-yl)benzo[*d*]thiazole (L3) and 2-(4-(*tert*-butyl)-6-phenylpyridin-2-yl)benzo[*d*]thiazole (L4) has not yet been reported. Bromination of 2-phenylpyridine and 4-(*tert*-butyl)-2-phenylpyridine with *n*-BuLi/LiDMAE and CBr₄⁵¹ gave 2-bromo-6-phenylpyridine and 2-bromo-4-(*tert*-butyl)-6-phenylpyridine, which were then used in Cu(I)-catalyzed coupling reactions with benzothiazole⁴⁸ to yield the desired products L3 and L4 in moderate yields. Ligands L3 and L4 were characterized by 1D and 2D NMR spectroscopy, LC-ESI mass spectrometry, IR spectroscopy, and elemental analysis. In the mass spectra, the base peaks at *m/z* 289.0 (for L3) and 345.1 (for L4) correspond to the [M+H]⁺ ions.

Synthesis of [Ir(C^N)₂(N^N)]PF₆ Complexes. Cationic iridium complexes of the type [Ir(C^N)₂(N^N)]⁺ are typically synthesized by cleavage of the [Ir(ppy)₂Cl]₂ dimer with the desired N^N ligand in MeOH or CH₂Cl₂/MeOH.^{52–54} Using this method, however, traces of chloride ions can be carried through to the final product, despite using an excess of NH₄PF₆ for ion metathesis. We have recently shown that these chloride impurities are detrimental to device performance.⁵⁵ Therefore, the complexes in this series were prepared via an intermediate solvento complex, formed by the reaction of the iridium dimer with AgPF₆ in MeOH (Scheme 1). During the reaction, AgCl precipitates and is removed by filtration through Celite. The filtrate is concentrated and the solvento intermediate is used immediately without purification or characterization for subsequent transformations. As shown in a series of stable orange emitters, the purity obtained by this synthetic route can

lead to excellent LEC performance, decreasing the risk of chloride ion impurities in the final complexes.⁵⁶ In Scheme 1, the synthetic strategy to complexes 1–7 is shown. Reaction of the [Ir(ppy)₂(MeOH)₂][PF₆]⁺ intermediate with the corresponding N^N ligands L1–L7 in MeOH at room temperature gave the desired iridium complexes in moderate to good yields based on the iridium dimer starting material. All complexes in this series were fully characterized by 1D and 2D NMR spectroscopy, IR spectroscopy, ESI-MS, and elemental analysis. The base peaks in the ESI mass spectra correspond to the [M–PF₆]⁺ cations.

Crystal Structures. Single crystals of 1·1.5CH₂Cl₂, 6·CH₂Cl₂, and 7 were grown by layering CH₂Cl₂ solutions of the complexes with Et₂O. Structures of the complex cations are shown in Figures 1–3, confirming that coordination occurs through the nitrogen atom(s) of the benzothiazole/benzoxazole unit(s) in all three complexes. 1·1.5CH₂Cl₂ and 6·CH₂Cl₂ crystallize in the monoclinic space groups *P*2₁/*c* and *P*2₁/*n*, respectively, whereas 7 crystallizes in the orthorhombic space

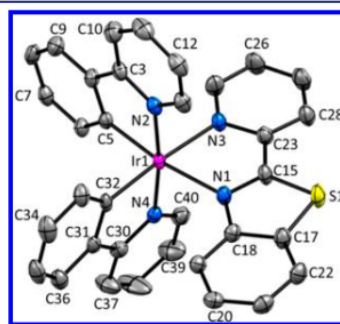


Figure 1. Structure of the Λ -[Ir(ppy)₂(L1)]⁺ cation in 1·1.5CH₂Cl₂. H atoms omitted for clarity and ellipsoids plotted at 50% probability level. Selected bond parameters: Ir1–N1 = 2.172(2), Ir1–N2 = 2.050(2), Ir1–N3 = 2.143(2), Ir1–N4 = 2.041(2), Ir1–C5 = 2.007(3), Ir1–C32 = 2.014(3), S1–C15 = 1.731(3), S1–C17 = 1.742(3) Å; N1–Ir1–N3 = 76.15(9), N2–Ir1–C5 = 80.63(10), N4–Ir1–C32 = 80.65(10), N1–Ir1–C5 = 171.48(9), N2–Ir1–N4 = 172.68(9), N3–Ir1–C32 = 175.40(10), C15–S1–C17 = 88.97(14)^o.

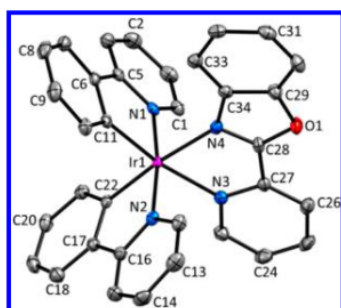


Figure 2. Structure of the Δ -[Ir(ppy)₂(L6)]⁺ cation in 6-CH₂Cl₂. H atoms omitted for clarity and ellipsoids plotted at 50% probability level. Selected bond parameters: Ir1–N1 = 2.044(2), Ir1–N2 = 2.055(2), Ir1–N3 = 2.173(2), Ir1–N4 = 2.140(2), Ir1–C11 = 2.009(3), Ir1–C22 = 2.008(3), O1–C28 = 1.355(4), O1–C29 = 1.394(4) Å; N1–Ir1–C11 = 80.60(11), N2–Ir1–C22 = 80.60(11), N3–Ir1–N4 = 76.33(9), N1–Ir1–N2 = 172.13(9), N3–Ir1–C11 = 170.59(10), N4–Ir1–C22 = 173.90(10), C28–O1–C29 = 103.9(2)^o.

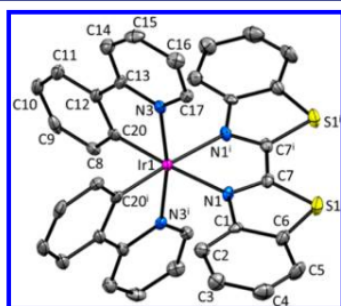


Figure 3. Structure of the Δ -[Ir(ppy)₂(L7)]⁺ cation in 7. H atoms omitted and ellipsoids plotted at 50% probability level. Symmetry code: $i = -x + 1/2, -y + 1/2, z + 1$. Selected bond parameters: Ir1–N1 = 2.176(3), Ir1–N3 = 2.048(2), Ir1–C20 = 2.004(3), S1–C6 = 1.730(4), S1–C7 = 1.718(3) Å; N1–Ir1–N1' = 75.58(14), N3–Ir1–C20 = 80.75(12), N1–Ir1–C20 = 175.83(13), N3–Ir1–N3' = 168.96(15), C6–S1–C7 = 88.77(16)^o.

group *Fdd2*. CH₂Cl₂ solvent molecules are heavily disordered in 1·1.5CH₂Cl₂ and have been removed using the SQUEEZE⁵⁷ method. In 6-CH₂Cl₂, the CH₂Cl₂ solvent molecule is ordered. The asymmetric unit of 7 contains half a cation and half an anion; in each case, the second half is generated by a C₂ rotation axis which is parallel to the *c* axis of the unit cell and runs through the iridium or the phosphorus center, respectively.

For 1·1.5CH₂Cl₂ and 6-CH₂Cl₂, the phenylpyridine ligand, of which the coordinating C atom is *trans* to the benzothiazole/benzoxazole unit, is nearly planar (angles between the ring planes are 3.3 and 2.7^o, respectively). The other ppy cyclometalating ligand (coordinating carbon *trans* to the pyridine ring of the ancillary ligand) shows deviation from planarity, with angles between the ring planes of 8.2 and 10.9^o, respectively. Whereas the L1 ancillary ligand in 1·1.5CH₂Cl₂ is distorted from planarity (angle between the ring planes = 8.2^o), ligand L6 in 6-CH₂Cl₂ does not exhibit the same behavior (angle between the ring planes = 2.2^o). In 7, both the ppy[−] and the L7 ligands are twisted so that the angles between the ring planes amount to 7.1 and 7.5^o, respectively.

Electrochemical Properties. Electrochemical data gained from cyclic voltammetry measurements in CH₂Cl₂ solution are summarized in Table 1; cyclic voltammograms are depicted in

Table 1. Electrochemical Data of Complexes 1–7 in Deaerated CH₂Cl₂ Solutions and Referenced to Fc/Fc⁺ (See Also Figure S1)^a

complex	E_{pa}^{ox} [V] ($E_{pa} - E_{pc}$ [mV])	$E_{1/2}^{red}$ [V] ($E_{pc} - E_{pa}$ [mV])	$\Delta E_{1/2}$ [V]
1	+0.94 (92)	−1.55 (83)	2.49
2	+0.92 (95)	−1.59 (89)	2.51
3	+0.86 ^{qr} (126)	−1.57 (95)	2.43
4	+0.87 ^{qr} (151)	−1.62 (89)	2.49
5	+0.99 ^{ir} , +1.17 ^{ir}	−1.47 (86), −2.30 ^{ir}	2.46
6	+0.92 ^{qr} (114)	−1.61 (104)	2.53
7	+1.01 ^{qr} (144)	−1.27 ^{qr} (123), −2.03 ^{qr} (140)	2.28

^aMeasured using Pt working and counter electrodes, an Ag pseudoreference electrode, and 0.1 M TBAPF₆ as supporting electrolyte at a scan rate of 0.1 V s^{−1}. ir = irreversible, qr = quasi-reversible.

Figure S1. Reduction potentials are similar for complexes 1–4 and 6 (−1.55 to −1.62 V), indicating that reduction takes place mainly on the benzothiazole unit of the ancillary ligand and replacing benzothiazole by benzoxazole does not significantly influence the reduction potential. Both 5 and 7 are more readily reduced than complex 1, with $E_{1/2}^{red}$ shifted by 0.08 and 0.28 V, respectively. The introduction of a second benzothiazole moiety therefore has a pronounced stabilization effect on the LUMO, especially in 7, where the two benzothiazoles are directly linked. A second reduction peak is observed for both complexes, which is not seen for the remaining five compounds within the accessible solvent window. Oxidation potentials are in a close range (+0.86 to +1.01 V), as expected for [Ir(ppy)₂(N^oN)][PF₆] complexes in which the HOMO is located on the iridium center and the cyclometalating ligand. For compound 7, oxidation is shifted to higher potential, which can be explained by the extremely electron-deficient nature of ligand L7, making oxidation of the iridium center more difficult. The opposite trend is seen in 3 and 4, where the introduction of a phenyl group on the ancillary ligand facilitates oxidation. For complex 5, two irreversible oxidation waves are observed, whereas all other complexes exhibit only one reversible to quasi-reversible oxidation.

Photophysical Properties. UV–vis absorption spectra in CH₂Cl₂ solution are shown in Figure 4. All complexes show intense absorption bands in the UV with maxima in the range 254–314 nm, which are ascribed to spin-allowed $\pi \rightarrow \pi^*$ transitions of the ligands. Lower energy bands between 350 and

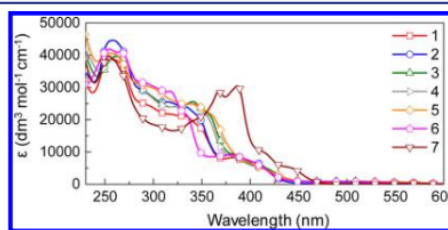


Figure 4. UV–vis absorption spectra in CH₂Cl₂ solution (1.0×10^{-5} mol dm^{−3}) of complexes 1–7.

450 nm correspond to spin-allowed metal-to-ligand ($^1\text{MLCT}$) and ligand-to-ligand charge transfer ($^1\text{LLCT}$) excitations, whereas the low intensity tails above 450 nm arise from spin-forbidden $^3\text{MLCT}$, $^3\text{LLCT}$, and ligand-centered (^3LC) transitions.¹⁴ With the exception of 7, the UV-vis absorption spectra of all complexes in this series are similar. Compound 7 exhibits more intense absorption bands at wavelengths higher than 360 nm compared to the other complexes, with considerably stronger absorption bands extending into the visible region (around 450 nm). This feature is attributed to the ancillary ligand (L7).

Excitation of CH_2Cl_2 solutions of complexes 1–7 gives the photoluminescence spectra shown in Figure 5 with photo-

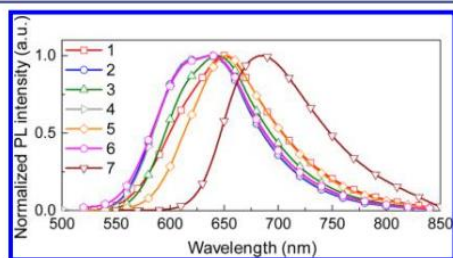


Figure 5. Photoluminescence spectra in CH_2Cl_2 solution (1.0×10^{-5} mol dm^{-3}) of complexes 1–7. $\lambda_{\text{exc}} = 430$ nm for 1–6 and 445 nm for 7.

physical data summarized in Table 2. Emission maxima lie in the red to deep-red region, ranging from 636 to 686 nm. For all complexes, the shapes and positions of the emission bands are independent of the excitation wavelength. Introduction of ligand L1 leads to a 49 nm red-shift of the emission maximum in CH_2Cl_2 when compared to the archetype complex $[\text{Ir}(\text{ppy})_2(\text{bpy})][\text{PF}_6]$ (595 nm, bpy = 2,2'-bipyridine).⁵⁸ This red-shift can be explained by the electron-deficient nature of the benzothiazole moiety, leading to stabilization of the LUMO and as a consequence a smaller energy gap. Replacing the pyridine ring of L1 by another benzothiazole unit (ligand L7) leads to a further 42 nm bathochromic shift of the emission maximum in 7. Substituting L1 with a further benzothiazole group (ligand L5) does not have the same effect as L7; the pendant benzothiazole ring in 5 red-shifts the emission maximum by only 8 nm. Coordination of the benzothiazole to the iridium center is therefore crucial for a substantial bathochromic shift. With the exception of 7, the emission maxima of all complexes in this series are found in a small 16 nm range between 636 and

652 nm, corresponding to red emission. Introduction of a pendant phenyl (3) or benzothiazole ring (5) exerts a negligible influence on the luminescence maximum. An 8 nm blue-shift of the emission band is observed upon *tert*-butyl substitution on the pyridyl ring in complexes 2 and 4. The same effect is observed by changing the benzothiazole to a benzoxazole unit in the ancillary ligand (complex 6). The majority of complexes in this series show broad, unstructured emission profiles, indicating a large charge transfer character of the emissive state. Some vibrational structure is observed in the emission bands of complexes 2 and 6, suggesting that the ^3LC contribution is more pronounced in the emissive state of these two complexes. Photoluminescence quantum yields in solution are generally low (<10%) within this series of complexes (Table 2), but unexceptional for red emitters. A *tert*-butyl substituent on the ancillary ligand in 2 and 4 leads to slightly higher PLQYs of 14.0 and 11.0%, respectively. Lifetimes were determined using biexponential fits in the case of compounds 5 and 6; data are given in Table 2.

Emission spectra of powder samples are depicted in Figure 6; emission maxima, quantum yields, and excited-state lifetimes

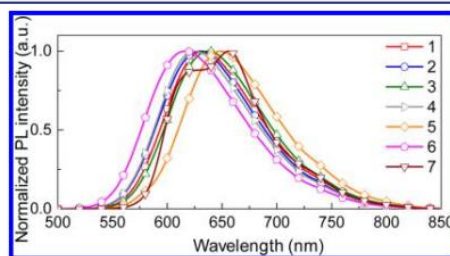


Figure 6. Solid-state photoluminescence spectra of powder samples of complexes 1–7. $\lambda_{\text{exc}} = 280$ nm.

are summarized in Table 2. All complexes exhibit a blue-shift in the range 4–30 nm on going from CH_2Cl_2 solution to the solid state (powder). The largest shift is seen for compound 7; this is also the only complex in this series which has a structured emission profile in the solid state. PLQYs vary from 3.1% for complex 5 to 17.0% for complex 7. Biexponential fits were used for solid state decay curves of all complexes. Average lifetimes lie in the range 185–565 ns, with complex 7 exhibiting not only the highest quantum yield, but also the longest τ_{ave} . Thin films of the complexes combined with $[\text{Bmim}][\text{PF}_6]$ as ionic liquid (4:1 ratio) were spin-coated onto quartz substrates to determine their photophysical properties. For compounds 2

Table 2. Photophysical Properties of Complexes 1–7 (See Also Table S1)

complex	solution ^a			powder			film ^f	
	$\lambda_{\text{em}}^{\text{max}}$ [nm] ^b	$\tau_{1/2}$ [ns] ^{cd}	PLQY [%] ^b	$\lambda_{\text{em}}^{\text{max}}$ [nm] ^d	τ_{ave} [ns] ^{de}	PLQY [%] ^b	$\lambda_{\text{em}}^{\text{max}}$ [nm]	PLQY [%]
1	644	222	7.7	630	277	8.6	645	11.0
2	636	329	14.0	630	305	16.0	642	17.6
3	645	183	6.5	638	214	8.5	651	9.7
4	636	275	11.0	625	287	10.0	626	12.5
5	652	169 ^e	4.1	648	185	3.1	658	5.8
6	636	166 ^e	5.9	616	236	9.7	625	12.3
7	686	126	3.6	656	565	17.0	693	6.7

^aDeaerated CH_2Cl_2 solutions. ^b $\lambda_{\text{exc}} = 266$ nm for 1, 270 nm for 2–4 and 6, 265 nm for 5, and 259 nm for 7. ^cMeasured under an atmosphere of argon. ^d $\lambda_{\text{exc}} = 280$ nm. ^e τ_{ave} (biexponential fits were used for the excited state lifetime determination). ^f $\lambda_{\text{exc}} = 320$ nm.

and 4, 2 wt % poly(methyl methacrylate) (PMMA) was added to increase the quality of the film. The photoluminescence spectra of the different films are depicted in Figure 7 and the

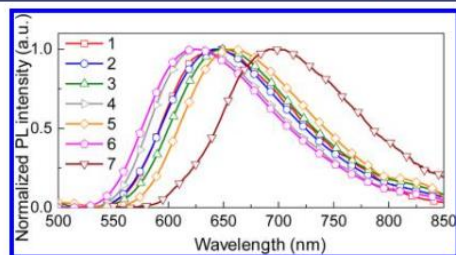


Figure 7. Thin-film photoluminescence spectra of complexes 1–7. $\lambda_{\text{exc}} = 320$ nm.

deduced emission maxima and quantum yields are reported in Table 2. Apart from complex 4, red-shifts in the emission maxima are observed for all complexes on going from powder samples to thin films. A pronounced red-shift of 37 nm is seen for complex 7, resulting in an emission maximum close to the near-infrared region (693 nm). All other complexes exhibit smaller bathochromic shifts ranging from 9 to 15 nm. Interaction of the complexes with the ionic liquid in thin films apparently leads to a slight stabilization of the triplet emissive state and thus a smaller energy gap. The PLQY of the films of all but complex 7 are similar to the values obtained from the powder samples (Table 2). Only for complex 7, the PLQY is significantly lower in film (6.7%) than for the powder sample (17%).

Theoretical Calculations. To obtain a deeper knowledge of the electrochemical and photophysical properties of complexes 1–7, the molecular and electronic structures of

the respective $[\text{Ir}(\text{ppy})_2(\text{N}^{\wedge}\text{N})]^+$ cations, in both ground and excited electronic states, were investigated by means of density functional theory (DFT) calculations at the B3LYP/(6-31G**+LANL2DZ) level in the presence of the solvent (CH_2Cl_2).

The minimum-energy geometries calculated for the $[\text{Ir}(\text{ppy})_2(\text{N}^{\wedge}\text{N})]^+$ cations in their electronic ground state (S_0) reproduce the near-octahedral coordination of the Ir metal and are in good agreement with the X-ray diffraction data presented above for 1, 6, and 7. For these complexes, the $\text{N}^{\wedge}\text{N}$ ligands are predicted to be mainly planar (angle between ring planes = 2.7, 1.9, and 3.8°, respectively). For 3, 4, and 5, the ancillary ligand deviates more from planarity (angle between ring planes = 14.6, 16.0, and 14.3° respectively) to accommodate the pendant phenyl or benzothiazolyl groups. These groups give rise to a face-to-face π -stacking with the phenyl group of the adjacent ppy^- ligand, similar to the intracation stacking observed for $[\text{Ir}(\text{ppy})_2(\text{Phbpy})]^+$ (Phbpy = 6-phenyl-2,2'-bipyridine) and $[\text{Ir}(\text{ppy})_2(\text{Naphbpy})]^+$ (Naphbpy = 6-(2-naphthyl)-2,2'-bipyridine) in previous studies.^{55,59} The centroid–centroid distance between the stacked rings is 3.78, 3.80, and 3.74 Å for 3, 4, and 5, respectively.

Figure 8 compares the energies calculated for the frontier molecular orbitals of complexes 1–7 with those obtained for the archetypal $[\text{Ir}(\text{ppy})_2(\text{bpy})]^+$ complex. The contour plots of the highest-occupied (HOMO) and lowest-unoccupied (LUMO) molecular orbitals show the same topology for all the complexes and only those computed for $[\text{Ir}(\text{ppy})_2(\text{bpy})]^+$, 1, and 7 are depicted in Figure 8 as representative examples. As usually found for $[\text{Ir}(\text{C}^{\wedge}\text{N})_2(\text{N}^{\wedge}\text{N})]^+$ complexes, the HOMO spreads over the iridium center and the phenyl rings of the ppy^- ligands, whereas the LUMO is located over the $\text{N}^{\wedge}\text{N}$ ligand. The energy of the HOMO remains almost constant along the series 1–6 (–5.83 to –5.86 eV), and close to that of

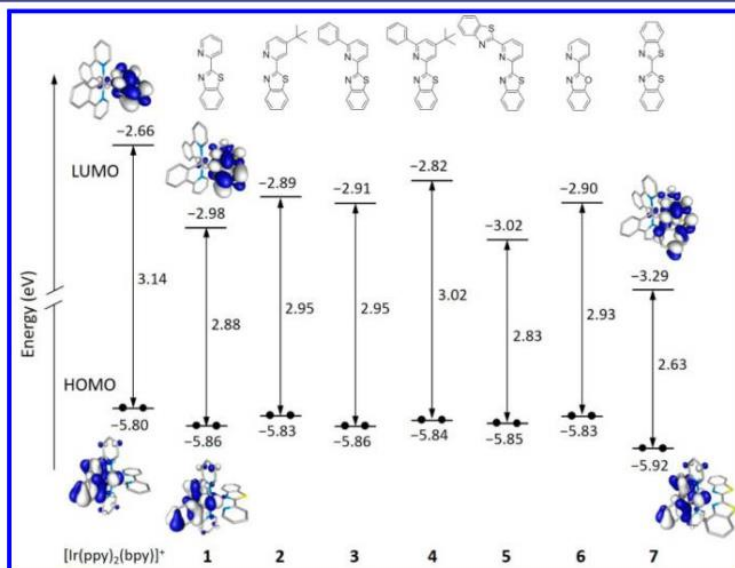


Figure 8. Schematic representation comparing the energies calculated for the frontier molecular orbitals of the archetype complex $[\text{Ir}(\text{ppy})_2(\text{bpy})]^+$ and of complexes 1–7. Isovalue contours (± 0.03 au) of the HOMO and LUMO are included for $[\text{Ir}(\text{ppy})_2(\text{bpy})]^+$, 1, and 7. Hydrogen atoms are omitted for clarity. The chemical structure of the $\text{N}^{\wedge}\text{N}$ ligands is shown in the upper part of the figure.

the archetypal complex (-5.80 eV). This is an expected behavior because all the complexes bear the same C[∞]N ligands and the structural differences are related to the ancillary ligand from which the HOMO has no contribution. Hence, the energy of the HOMO is only indirectly affected as in complex 7, that features a slightly lower HOMO energy (-5.92 eV) due to electron-deficient nature of ligand L7. The theoretical predictions are in good agreement with the very similar oxidation potentials measured for complexes 1–4 and 6, and the higher value recorded for 7. No significant difference is expected for complex 5, for which the measured potential is irreversible.

Regarding the LUMO, its energy undergoes significant changes due to the different structure of the ancillary ligand (see Figure 8). The substitution of the bpy ligand in the reference $[\text{Ir}(\text{ppy})_2(\text{bpy})]^+$ complex by the btzpy ligand incorporating the benzothiazole unit in 1 stabilizes the LUMO by 0.33 eV, passing from -2.66 eV in $[\text{Ir}(\text{ppy})_2(\text{bpy})]^+$ to -2.98 eV in 1. The attachment of additional *tert*-butyl and phenyl groups to the pyridine moiety of btzpy leads to accumulative destabilizations of the LUMO of 2 (-2.89 eV), 3 (-2.91 eV), and 4 (-2.82 eV) compared with 1. Replacing benzothiazole by benzoxazole has a similar small destabilization effect in the LUMO of 6 (-2.90 eV). In contrast, the attachment of a second benzothiazole unit produces a small stabilization of the LUMO of 5 (-3.02 eV). The greatest effect is found for complex 7 (-3.29 eV), for which the pyridine ring is substituted by a second electron-deficient benzothiazole unit, and the LUMO is stabilized by 0.31 eV. The theoretical trends fully support the reduction potentials measured experimentally (Table 1), which present close values for 2, 3, 4, and 6 (around -1.60 V), slightly more negative than 1 (-1.55 V), and less negative values for 5 (-1.47 V) and especially for 7 (-1.27 V).

The HOMO–LUMO energy gaps calculated for 1–7 are in all cases smaller than that computed for the archetype complex (3.14 eV). The largest gap in the family is predicted for complex 4 (3.02 eV), it decreases for complexes 2, 3, and 6, that show gaps around 2.95 eV, and in passing to 1 (2.88 eV) and 6 (2.83 eV), and the smallest gap is predicted for complex 7 (2.63 eV). If emission comes from a triplet excited state originating in the HOMO \rightarrow LUMO excitation, these results justify, in a first approach, the gradual shift to the red experimentally observed for the emission of complexes 1–6, and especially for 7, when compared with $[\text{Ir}(\text{ppy})_2(\text{bpy})]^+$ (Table 2).

To verify the nature of the emitting state, time-dependent DFT (TD-DFT) calculations of the lowest-energy triplet states were performed for the cations of complexes 1–7 at the optimized geometry of S_0 . Table S2 in the Supporting Information compiles the vertical excitation energies and the electronic description computed for the first three triplet excited states. Results for complexes 1–7 mostly present the same pattern. The lowest-lying triplet state (T_1) is mainly described by the HOMO \rightarrow LUMO excitation and has a ${}^3\text{MLCT}/{}^3\text{LLCT}$ nature. The second lowest state (T_2), which also has a ${}^3\text{MLCT}/{}^3\text{LLCT}$ nature, appears 0.3–0.4 eV higher in energy than T_1 and presents some ${}^3\text{LC}$ character (13–22%) due to excitations centered on the ancillary ligand. The third state (T_3) mainly implies the C[∞]N ligands (${}^3\text{LC}$ nature) with some contribution from the metal and is computed more than 0.5 eV above T_1 . The energy differences between these states point to the HOMO \rightarrow LUMO ${}^3\text{MLCT}/{}^3\text{LLCT}$ state as the emissive triplet state for complexes 1–7.

To further confirm the nature of the emitting triplet, the geometry of the lowest-lying triplet state was optimized using the spin-unrestricted UB3LYP approach. Figure 9a summarizes

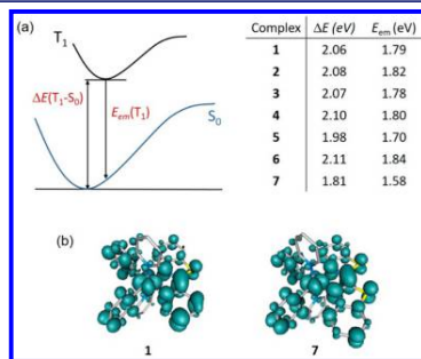


Figure 9. (a) Schematic energy diagram showing the adiabatic energy difference (ΔE) between the S_0 and T_1 states and the emission energy (E_{em}) from T_1 calculated for complexes 1–7. (b) Unpaired-electron spin-density contours (0.002 au) calculated for fully relaxed T_1 states of complexes 1 and 7.

the adiabatic energy difference between S_0 and T_1 (ΔE) and the emission energy (E_{em}) estimated as the vertical energy difference between T_1 and S_0 at the optimized minimum-energy geometry of T_1 . Figure 9b shows the unpaired-electron spin-density distributions computed for the fully relaxed T_1 states of complexes 1 and 7 as representative examples. All the complexes exhibit similar spin density plots spreading the ppy-Ir environment and the N[∞]N ligand (Ir \sim 0.5e, C[∞]N ligands \sim 0.5e, N[∞]N ligand \sim 1.0e) that perfectly match the topology of the HOMO \rightarrow LUMO excitation indicating an electron transfer from the $\text{Ir}(\text{ppy})_2$ moiety to the ancillary ligand. This supports the ${}^3\text{MLCT}/{}^3\text{LLCT}$ nature predicted for the emitting state by the TD-DFT calculations and agrees with the broad and unstructured bands observed in the photoluminescence spectra. The DFT values predicted for E_{em} are in the range 1.58–1.79 eV (Figure 9a) underestimating the experimental emission energies by 0.1–0.2 eV. They correctly reproduce the main experimental trends featuring similar emission energies for complexes 1–4 and 6, a slightly redder emission for 5, and a deeper red emission for 7.

TD-DFT calculations of the lowest-lying singlet excited states were also performed to disentangle the different features observed in the absorption spectra (Figure 4). For complex 7, two relatively intense $S_0 \rightarrow S_n$ electronic transitions are computed at 362 and 373 nm, with oscillator strengths of 0.10 and 0.59 respectively. These transitions originate from $\pi \rightarrow \pi^*$ excitations centered over the 2,2'-bibenzo[*d*]thiazole (L7) ligand. The corresponding transitions for complexes 1–6 are found at higher energies and show lower intensities (for 1: 328 and 335 nm, with oscillator strengths of 0.30 and 0.15, respectively). These differences explain the more intense absorption bands recorded experimentally for 7 at wavelengths higher than 360 nm, which are not observed for the other complexes (Figure 4).

Light-Emitting Electrochemical Cells (LECs). Simple two-layer LECs were prepared to investigate the electro-luminescent properties of complexes 1–7. For clarity, LECs fabricated using complexes 1–7 will be referred as LECs 1–7.

LEC structure is as follows, ITO/PEDOT:PSS/complex(1–7):IL/Al layout, as explained in the Experimental Section. The IL was added to reduce the turn-on time (t_{on}) defined as the time to reach a luminance of 100 cd m^{-2} .⁶⁰

LECs are dynamic devices and are characterized in a different way than OLEDs. In particular, the frequently used luminance and current density versus voltage scans used in OLEDs cannot be used since, due to the slow ionic motion occurring in LECs, they operate in a different manner depending on the scan speeds. Therefore, LECs are generally studied under either fixed voltage or fixed current density over time. As mentioned earlier, our group has shown the benefits of operating the device under pulsed-current driving.^{14,61} In this study, LECs 1–7 were evaluated using a pulsed-current with an average current density of 100 A m^{-2} , consisting of a block wave at a 1000 Hz frequency with a duty cycle of 50%. Using the pulsed driving mode LEC 7 did not produce any electroluminescence. This is most likely related to the poorer film quality of complex 7 resulting from its low solubility. Owing to the poor film quality, the distance between the anode and the cathode is not uniform over the device area which can lead to higher leakage current. A very high current density was indeed observed when operating LEC 7 under a constant-voltage of 4 V, corroborating our hypothesis of high leakage currents (Figure S2).

The electroluminescence (EL) spectra of LECs 1–7 are shown in Figure 10. All the LECs 1–7 emit in the red region.

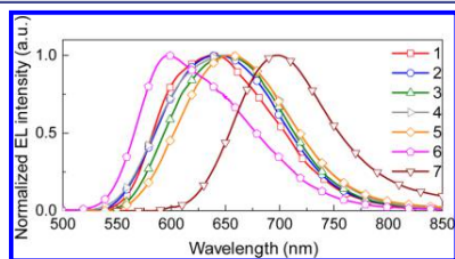


Figure 10. Electroluminescence spectra of LECs 1–7 driven either at an average pulsed-current density of 100 A m^{-2} (1000 Hz, 50% duty cycle, block wave) for 1–6 or constant-voltage of 4 V for 7.

The Commission Internationale de l'Eclairage (CIE) coordinates for LECs 1–6 were determined from the electroluminescence spectra and are collected in Table 3. The EL spectra for LECs 1, 2, 3 and 5 are similar to the PL spectra indicative of the similar excited states being involved in the light emission process. LEC 4 show a red-shift of 22 nm (λ_{em}^{max} EL = 648 nm) and LEC 6 has a blue-shift of 27 nm (λ_{em}^{max} EL = 598

nm), for reasons, currently not yet understood. These electroluminescence spectra are very interesting as up to now only few pure red LECs have been reported.^{25,62–64}

The evolution of the luminance versus time for LECs 1–6 driven at 100 A m^{-2} average pulsed-current density is shown in Figure 11 and the performance key parameters are given in

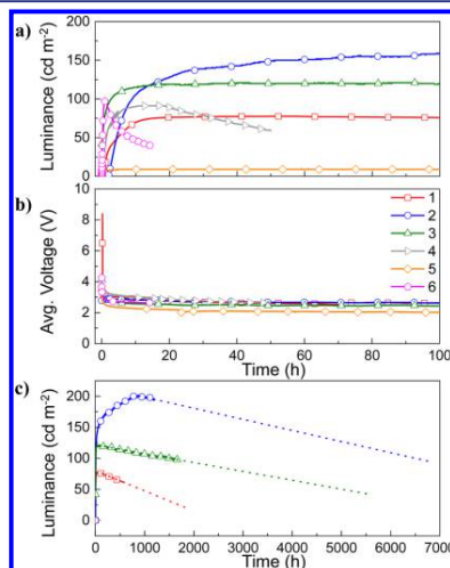


Figure 11. Luminance (a, c) and average voltage (b) versus time of LECs 1–6 operated under an average pulsed-current density of 100 A m^{-2} (1000 Hz, 50% duty cycle, block wave). Panel (c) shows the extrapolation of the luminance to half the initial value for LECs 1–3.

Table 3. LECs 1–6 present the typical behavior under pulsed-current mode operation. The luminance rises while the voltage drops due to the growth of the p- and n-doped regions in the active layer.¹⁴ Once the maximum luminance is attained, the luminance starts to decrease and the operating average voltage remains constant with values between 2.00 and 2.58 V.

LEC 1 presents a maximum luminance of 77 cd m^{-2} after 54 h under operation, which implies that the ionic movement in this system is slow. The device lifetime, expressed by the time to reach one-half of the maximum luminance ($t_{1/2}$), was estimated by extrapolating the luminance curve leading to a value higher than 1000 h. Moreover, LECs 2 and 3 actually show a higher maximum luminance (200 and 119 cd m^{-2}) and

Table 3. Performance Parameters and Electroluminescence Data Obtained for LECs 1–6 Operated under a Pulsed-Current of 100 A m^{-2} (1000 Hz, 50% Duty Cycle, Block Wave)

LEC	$\text{lum}_{max}/\text{cd m}^{-2a}$	t_{on}/h^b	t_{max}/h^c	$t_{1/2}/\text{h}^d$	$\text{efficacy}_{max}/\text{cd A}^{-1e}$	$\text{PE}_{max}/\text{lm W}^{-1f}$	$\text{EQE}_{max}/\%g$	λ_{em}^{max} EL/nm	CIE ^h
1	77	4.6	54	>1000 ⁱ	0.75	0.47	0.70	636	0.6289, 0.3674
2	200	4.3	870	>6000 ⁱ	2.02	1.22	2.00	642	0.6297, 0.3663
3	119	0.2	63	>4500 ⁱ	1.22	0.77	1.49	651	0.6436, 0.3524
4	91	1.3	18	63 ⁱ	1.01	0.51	1.04	648	0.6219, 0.3748
5	9		4.8	>150 ⁱ	0.09	0.06	0.14	655	0.6476, 0.3393
6	97	0.2	0.84	9	0.97	0.54	0.55	598	0.5852, 0.4109

^aMaximum luminance reached. ^b T_{on} Time to reach 50 cd m^{-2} luminance. ^c T_{max} Time to reach the maximum luminance. ^d $T_{1/2}$ Time to reach one-half of the maximum luminance. ^eMaximum efficacy reached. ^fMaximum power efficiency reached. ^gMaximum external quantum efficiency reached. ^hThe Commission Internationale de l'Eclairage (CIE) color coordinates. ⁱExtrapolated values.

further enhanced device stability than LEC 1 (Table 3). The best device of the series (LEC 2) has a $t_{1/2}$ in excess of 6000 h under the operating conditions (average pulsed-current density of 100 A m^{-2}). An extended time-dependent luminance graph for LEC 2 up to 1200 h under operation is depicted in Figure S3. Its turn-on (t_{on}) defined as time to reach 50 cd m^{-2} rises similar to that for LEC 1 (4.6 and 4.3 h for LEC 1 and 2, respectively), yet its luminance continues to increase over a long time, indicating that optimum charge injection and charge balance are only slowly obtained, which could indicate that this slow ionic motion leads to a very slow doping growing over time becoming beneficial for the device lifetime.^{65,66} The higher luminance obtained for LEC 2 is due to the higher PLQY measured for complex 2 (17.6%) compared with complex 1 (11%). LEC 3 incorporating the complex with the pendant phenyl group attached to the $\text{N}^{\wedge}\text{N}$ ligand also shows a higher luminance ($\text{lum}_{\text{max}} = 119 \text{ cd m}^{-2}$ at 63 h) and a longer lifetime (>4500 h) than complex 1 (>1000 h). When increasing the size of the substituents beyond that of complex 3 as in 4 and 5, the corresponding LECs have a significantly reduced stability, they now decay on a time scale of tens of hours. The replacement of the benzothiazole unit (LEC 1) by a benzoxazole (LEC 6) maintains the luminance ($\text{lum}_{\text{max}} = 77$ and 97 cd m^{-2} , respectively), yet produces a detrimental effect in terms of stability ($t_{1/2} > 1000$ and 150 h , respectively). In general, the time to reach the maximum luminance (t_{max}) and t_{on} for LECs 4–6 is almost four times faster than for LECs 1–3, which support the hypothesis that the device lifetime is mainly affected by the growth of the doped zones, which increases the quenching of excitons. LEC 7, as mentioned above, emits in the near-infrared and is not included in Figure 11 because it did not work under pulsed driving operation. The response of LEC 7 under constant-voltage operation is shown in Figure S5. Conclusions are difficult to draw due to the high current density caused probably by the poor film formation, and higher-solubility complexes would be needed to evaluate this type of complexes more carefully.

The current efficiency of LEC 1 is around 0.75 cd A^{-1} and is stable over time. The stability is a result of the stable luminance resulting from the complex and the pulsed-current driving approach. The efficiency is not very high in part due to the emission wavelength, which is only in part visible to the human eye. LECs 2 and 3 are slightly better, as can be observed from their higher luminance values (Table 3), with efficacies of 2.02 and 1.22 cd A^{-1} , respectively.

In view of the deep-red emission wavelength, it is better to express the efficiency as the external quantum efficiency (EQE) defined as

$$\text{EQE} = b\phi/2n^2 \quad (1)$$

where b is the recombination efficiency (equal to 1 for two ohmic contacts), ϕ is the fraction of excitons that decay radiatively, and n is the refractive index of the glass substrate and is equal to 1.5 (the factor $1/2n^2$ accounts for the coupling of light out of the device). As the Ir(III)-based complexes can efficiently harvest both singlet and triplet excitons, ϕ should resemble the PL efficiency. Hence, the efficiency of the device is mainly determined by the PLQY of the iTMC emitter. The maximum EQE that can be obtained with a PLQY of 11% without special outcoupling structures is roughly 2.4%.

Experimentally, this value is not observed, and instead a maximum EQE of 0.70% for LEC 1 was obtained. However, due to the higher luminance achieved for LECs 2 and 3, the

maximum EQE values for LECs 2 and 3 were 2.00 and 1.49%, respectively. Several examples of red-emitting LECs have been reported under constant-voltage operation,^{8,11,67,68} leading to champion peak EQEs of 9.51% with a limited $t_{1/2}$ of 8.2 h.¹¹ To the best of our knowledge, the best device lifetime for red-emitting LECs has been reported under pulsed-current^{69–71} or constant-current^{72,73} operation with a maximum lifetime of 110 h. Hence, the characteristics described here for LECs 1–3 show stabilities ranging from 10 to 60 times longer than those reported previously. These values are exceptional and are only comparable to very few orange emitting LECs operated under the same driving conditions.¹⁹ The performance of the stable red LECs is limited by the moderate luminance and the rather slow response, which is dependent on the applied current and generally linked to the device stability (higher current density leads to lower device lifetime). For this reason, we further investigate how the device stability is affected by increasing the current density.

To do this, a good performing complex obtained in sufficient large quantities is needed to prepare a number of devices to be operated under increasing average current densities. Complex 1 was selected for this more in-depth analysis due to its simple chemical structure. The luminance versus time measured for LEC 1 devices operated using pulsed-current densities (block wave, 1000 Hz, and 50% duty cycle) of 300, 700, 1250, and 1500 A m^{-2} are depicted in Figure 12. The luminance decay is

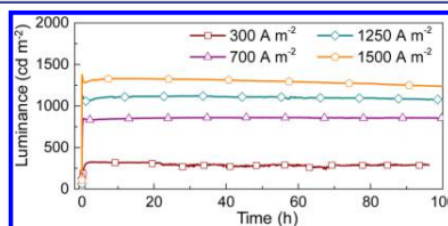


Figure 12. Time-dependent luminance of LEC 1 operated under different pulsed-current densities from 300 to 1500 A m^{-2} .

always very slow and, surprisingly, it does not depend very strongly on the applied current density. As mentioned before, this is remarkable as in electroluminescent devices a strong dependency of the lifetime on the current density is normally observed. There is virtually no luminance decay over the first 100 h (Figure 12) when driven under the pulsed conditions at average current densities of 300 and 700 A m^{-2} , and only a moderate decrease of approximately 10% is observed when the average current density is set at 1250 and 1500 A m^{-2} after 100 h. The luminance decay of the LEC 1 driven at 700 A m^{-2} was followed for a longer time (450 h) resulting in a decay of only 15% (Figure S4). The quasi steady-state luminance that is reached by each device increases linearly in the range from 100 to 700 A m^{-2} . For clarity, the luminance curve for the lower current density (100 A m^{-2}) is not depicted in Figure 12. At higher applied current densities than 700 A m^{-2} , the luminance values still increase but less than linearly. This linear dependence has been previously reported in LEC devices operated in pulse mode at very low current densities. However, this linearity is not usually present at high current densities.⁵⁶ This implies that there is little exciton–exciton or exciton–polaron quenching up to high current densities of 700 A m^{-2} , as this would lead to a sublinear increase, and that the

luminance intensity can be tuned by the current density applied. The time to reach the maximum luminance (Figure S5a) is also affected by the applied average current density and interestingly, the time to reach $100 \text{ cd}\cdot\text{m}^{-2}$ is substantially reduced to the second scale, from 500 s at $300 \text{ A}\cdot\text{m}^{-2}$ to 5 s at $1500 \text{ A}\cdot\text{m}^{-2}$ (Figure 13). For lower current densities it takes

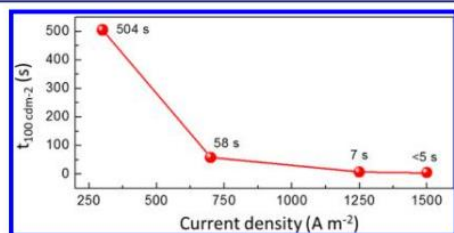


Figure 13. Time to reach $100 \text{ cd}\cdot\text{m}^{-2}$ ($t_{100\text{cd}\cdot\text{m}^{-2}}$) versus applied current densities (pulsed current, 1000 Hz, 50% duty cycle, block wave) for LEC 1.

longer to reach the maximum luminance. This is related to the voltage that is applied, which is lower for lower applied current densities (Figure S5b). Once the maximum luminance is reached, the operating voltage rapidly drops to values in between 2.5 and 2.9 V, depending on the set current density. Herein it is demonstrated the possibility of tuning the luminance levels, fast response with almost no lost in device stability, which is step forward in the demand for red light applications.

4. CONCLUSIONS

In conclusion, a series of ionic iridium(III) complexes using two 2-phenylpyridinate cyclometalating ligands and one 2-(pyridin-2-yl)benzo[d]thiazole based ancillary ($\text{N}^{\wedge}\text{N}$) ligand have been designed, prepared, and fully characterized. These complexes are efficient red emitters and have been used to prepare light-emitting electrochemical cells. The effects of modifying the chemical structure of the 2-(pyridin-2-yl)benzo[d]thiazole ligand and its substitution by 2-(pyridin-2-yl)benzo[d]oxazole and 2,2'-bibenzo[d]thiazole units on the photoluminescence and device performance are carefully studied. Density functional calculations clearly show that these chemical changes only affect the LUMO level leading to important reductions of the HOMO–LUMO energy gap compared to the archetypal $[\text{Ir}(\text{ppy})_2(\text{bpy})]$ complex. The emissive triplet state corresponds in all cases to the HOMO \rightarrow LUMO $^3\text{MLCT}/^3\text{LLCT}$ state. Strikingly, stable red-emitting LECs are obtained. In particular, LECs using the complexes incorporating 2-(pyridin-2-yl)benzo[d]thiazole, 2-(4-(tert-butyl)pyridin-2-yl)benzo[d]thiazole, and 2-(6-phenylpyridin-2-yl)benzo[d]thiazole as ancillary ligands exhibit lifetimes in excess of 1000, 6000, and 4000 h, respectively. This demonstrates that these ligands are very interesting to be further explore in both ionic and neutral iridium-based phosphorescent complexes.

■ ASSOCIATED CONTENT

Supporting Information

The Supporting Information is available free of charge on the ACS Publications website at DOI: 10.1021/jacs.6b13311.

Synthetic details, crystallographic, cyclic voltammetry and photoluminescence data and TD-DFT results, and electroluminescent data (PDF)
Crystal data for 1-1.5 CH_2Cl_2 (CIF)
Crystal data for 6- CH_2Cl_2 (CIF)
Crystal data for 7 (CIF)

■ AUTHOR INFORMATION

Corresponding Authors

*catherine.housecroft@unibas.ch

*henk.bolink@uv.es

ORCID

Henk J. Bolink: 0000-0001-9784-6253

Author Contributions

§C.D.E. and C.M. contributed equally to this work.

Notes

The authors declare no competing financial interest.

■ ACKNOWLEDGMENTS

This work has been supported by the Spanish Ministry of Economy and Competitiveness (MINECO) (MAT2014-55200, CTQ2015-71154-P, and Unidad de Excelencia María de Maeztu MDM-2015-0538), the Generalitat Valenciana (PROMETEO/2016/135), European Feder funds (CTQ2015-71154-P), the Swiss National Science Foundation (Grant Number 200020_144500), the European Research Council (Advanced Grant 267816 LiLo) and the University of Basel. C. M. thanks the MINECO for a predoctoral contract. M.-G.L.-P. thanks the Generalitat Valenciana for her Santiago Grisolia Fellowship.

■ REFERENCES

- Pei, Q.; Yu, G.; Zhang, C.; Yang, Y.; Heeger, A. J. *Science* **1995**, *269*, 1086.
- Lee, J. K.; Yoo, D. S.; Handy, E. S.; Rubner, M. F. *Appl. Phys. Lett.* **1996**, *69*, 1686.
- Gao, F. G.; Bard, A. J. *J. Am. Chem. Soc.* **2000**, *122*, 7426.
- Kalyuzhny, G.; Buda, M.; McNeill, J.; Barbara, P.; Bard, A. J. *J. Am. Chem. Soc.* **2003**, *125*, 6272.
- Rudmann, H.; Shimada, S.; Rubner, M. F. *J. Appl. Phys.* **2003**, *94*, 115.
- Slinker, J.; Bernards, D.; Houston, P. L.; Abruna, H. D.; Bernhard, S.; Malliaras, G. G. *Chem. Commun.* **2003**, 2392.
- Slinker, J. D.; Gorodetsky, A. A.; Lowry, M. S.; Wang, J.; Parker, S.; Rohl, R.; Bernhard, S.; Malliaras, G. G. *J. Am. Chem. Soc.* **2004**, *126*, 2763.
- Tamayo, A. B.; Garon, S.; Sajoto, T.; Djurovich, P. I.; Tsyba, I. M.; Bau, R.; Thompson, M. E. *Inorg. Chem.* **2005**, *44*, 8723.
- Wägberg, T.; Hania, P. R.; Robinson, N. D.; Shin, J.-H.; Matyba, P.; Edman, L. *Adv. Mater.* **2008**, *20*, 1744.
- Tang, S.; Pan, J.; Buchholz, H. A.; Edman, L. *J. Am. Chem. Soc.* **2013**, *135*, 3647.
- Zhang, J.; Zhou, L.; Al-Attar, H. A.; Shao, K.; Wang, L.; Zhu, D.; Su, Z.; Bryce, M. R.; Monkman, A. P. *Adv. Funct. Mater.* **2013**, *23*, 4667.
- Meier, S. B.; Tordera, D.; Pertegás, A.; Roldán-Carmona, C.; Ortí, E.; Bolink, H. *J. Mater. Today* **2014**, *17*, 217.
- Sun, Q.; Li, Y.; Pei, Q. *J. Disp. Technol.* **2007**, *3*, 211.
- Tordera, D.; Meier, S.; Lenes, M.; Costa, R. D.; Ortí, E.; Sarfert, W.; Bolink, H. *J. Adv. Mater.* **2012**, *24*, 897.
- Hu, T.; He, L.; Duan, L.; Qiu, Y. *J. Mater. Chem.* **2012**, *22*, 4206.
- Zhang, Z.; Guo, K.; Li, Y.; Li, X.; Guan, G.; Li, H.; Luo, Y.; Zhao, F.; Zhang, Q.; Wei, B.; Pei, Q.; Peng, H. *Nat. Photonics* **2015**, *9*, 233.

- (17) Henwood, A. F.; Zysman-Colman, E. *Top. Curr. Chem.* **2016**, *374*, 36.
- (18) Slinker, J. D.; Gorodetsky, A. A.; Lowry, M. S.; Wang, J.; Parker, S.; Rohl, R.; Bernhard, S.; Malliaras, G. G. *J. Am. Chem. Soc.* **2004**, *126*, 2763.
- (19) Tordera, D.; Pertegas, A.; Shavaleev, N. M.; Scopelliti, R.; Orti, E.; Bolink, H. J.; Baranoff, E.; Gratzel, M.; Nazeeruddin, M. K. *J. Mater. Chem.* **2012**, *22*, 19264.
- (20) Tordera, D.; Frey, J.; Vonlanthen, D.; Constable, E.; Pertegas, A.; Orti, E.; Bolink, H. J.; Baranoff, E.; Nazeeruddin, M. K. *Adv. Energy Mater.* **2013**, *3*, 1338.
- (21) AlTal, F.; Gao, J. *Org. Electron.* **2015**, *18*, 1.
- (22) Lin, K.-Y.; Bastatas, L. D.; Suhr, K. J.; Moore, M. D.; Holliday, B. J.; Minary-Jolandan, M.; Slinker, J. D. *ACS Appl. Mater. Interfaces* **2016**, *8*, 16776.
- (23) Suhr, K. J.; Bastatas, L. D.; Shen, Y.; Mitchell, L. A.; Holliday, B. J.; Slinker, J. D. *ACS Appl. Mater. Interfaces* **2016**, *8*, 8888.
- (24) Bandiello, E.; Sessolo, M.; Bolink, H. J. *J. Mater. Chem. C* **2016**, *4*, 10781.
- (25) Rodriguez-Redondo, J. L.; Costa, R. D.; Orti, E.; Sastre-Santos, A.; Bolink, H. J.; Fernandez-Lazaro, F. *Dalton Trans.* **2009**, 9787.
- (26) Costa, R. D.; Orti, E.; Bolink, H. J.; Graber, S.; Schaffner, S.; Neuberger, M.; Housecroft, C. E.; Constable, E. C. *Adv. Funct. Mater.* **2009**, *19*, 3456.
- (27) Hu, T.; Duan, L.; Qiao, J.; He, L.; Zhang, D.; Wang, L.; Qiu, Y. *Synth. Met.* **2013**, *163*, 33.
- (28) Lo, K. K.-W.; Li, C.-K.; Lau, J. S.-Y. *Organometallics* **2005**, *24*, 4594.
- (29) Yuan, Y.-J.; Yu, Z.-T.; Chen, X.-Y.; Zhang, J.-Y.; Zou, Z.-G. *Chem. - Eur. J.* **2011**, *17*, 12891.
- (30) Lo, K. K.-W.; Leung, S.-K.; Pan, C.-Y. *Inorg. Chim. Acta* **2012**, *380*, 343.
- (31) Choudhary, C. K.; Choudhary, R. K.; Mishra, L. K. *Complexes of rhodium(III), palladium(II) and platinum(II) with 2-(2'-pyridyl) benzthiazole*; Indian Chemical Society: Calcutta, INDE, 2002.
- (32) Richardson, C.; Keene, F. R.; Steel, P. J. *Aust. J. Chem.* **2008**, *61*, 183.
- (33) Gärtner, F.; Cozzula, D.; Losse, S.; Boddien, A.; Anilkumar, G.; Junge, H.; Schulz, T.; Marquet, N.; Spannenberg, A.; Gladiali, S.; Beller, M. *Chem. - Eur. J.* **2011**, *17*, 6998.
- (34) APEX2, version 2, User Manual, M86-E01078; Bruker Analytical X-ray Systems: Madison, WI, 2006
- (35) Betteridge, P. W.; Carruthers, R. I.; Cooper, K.; Prout, D. J.; Watkin, J. *J. Appl. Crystallogr.* **2003**, *36*, 1487.
- (36) Betteridge, P. W.; Carruthers, J. R.; Cooper, R. I.; Prout, K.; Watkin, D. J. *J. Appl. Crystallogr.* **2003**, *36*, 1487.
- (37) Frisch, M. J.; Trucks, G. W.; Schlegel, H. B.; Scuseria, G. E.; Robb, M. A.; Cheeseman, J. R.; Scalmani, G.; Barone, V.; Mennucci, B.; Petersson, G. A.; Nakatsuji, H.; Caricato, M.; Li, X.; Hratchian, H. P.; Izmaylov, A. F.; Bloino, J.; Zheng, G.; Sonnenberg, J. L.; Hada, M.; Ehara, M.; Toyota, K.; Fukuda, R.; Hasegawa, J.; Ishida, M.; Nakajima, T.; Honda, Y.; Kitao, O.; Nakai, H.; Vreven, T.; Montgomery, J. A., Jr.; Peralta, J. E.; Ogliaro, F.; Bearpark, M. J.; Heyd, J.; Brothers, E. N.; Kudin, K. N.; Staroverov, V. N.; Kobayashi, R.; Normand, J.; Raghavachari, K.; Rendell, A. P.; Burant, J. C.; Iyengar, S. S.; Tomasi, J.; Cossi, M.; Rega, N.; Millam, N. J.; Klene, M.; Knox, J. E.; Cross, J. B.; Bakken, V.; Adamo, C.; Jaramillo, J.; Gomperts, R.; Stratmann, R. E.; Yazyev, O.; Austin, A. J.; Cammi, R.; Pomelli, C.; Ochterski, J. W.; Martin, R. L.; Morokuma, K.; Zakrzewski, V. G.; Voth, G. A.; Salvador, P.; Dannenberg, J. J.; Dapprich, S.; Daniels, A. D.; Farkas, Ö.; Foresman, J. B.; Ortiz, J. V.; Cioslowski, J.; Fox, D. J. *Gaussian 09*, revision D.01, Gaussian, Inc.: Wallingford, CT, 2009.
- (38) Lee, C.; Yang, W.; Parr, R. G. *Phys. Rev. B: Condens. Matter Mater. Phys.* **1988**, *37*, 785.
- (39) Becke, A. D. *J. Chem. Phys.* **1993**, *98*, 5648.
- (40) Francl, M. M.; Pietro, W. J.; Hehre, W. J.; Binkley, J. S.; Gordon, M. S.; DeFrees, D. J.; Pople, J. A. *J. Chem. Phys.* **1982**, *77*, 3654.
- (41) Hay, P. J.; Wadt, W. R. *J. Chem. Phys.* **1985**, *82*, 299.
- (42) Tomasi, J.; Persico, M. *Chem. Rev.* **1994**, *94*, 2027.
- (43) Cramer, C. S.; Truhlar, D. G. In *Solvent Effects and Chemical Reactivity*; Tapia, O., Bertran, J., Eds.; Kluwer: Dordrecht, 1996; pp 1–80.
- (44) Tomasi, J.; Mennucci, B.; Cammi, R. *Chem. Rev.* **2005**, *105*, 2999.
- (45) Casida, M. E.; Jamorski, C.; Casida, K. C.; Salahub, D. R. *J. Chem. Phys.* **1998**, *108*, 4439.
- (46) Jamorski, C.; Casida, M. E.; Salahub, D. R. *J. Chem. Phys.* **1996**, *104*, 5134.
- (47) Petersilka, M.; Gossmann, U. J.; Gross, E. K. U. *Phys. Rev. Lett.* **1996**, *76*, 1212.
- (48) Do, H.-Q.; Khan, R. M. K.; Daugulis, O. *J. Am. Chem. Soc.* **2008**, *130*, 15185.
- (49) Carlson, L. J.; Welby, J.; Zebrowski, K. A.; Wilk, M. M.; Giroux, R.; Ciancio, N.; Tanski, J. M.; Bradley, A.; Tyler, L. A. *Inorg. Chim. Acta* **2011**, *365*, 159.
- (50) Rai, C.; Braunwarth, J. B. *J. Org. Chem.* **1961**, *26*, 3434.
- (51) Vandromme, L.; Reißig, H.-U.; Gröper, S.; Rabe, J. P. *Eur. J. Org. Chem.* **2008**, *2008*, 2049.
- (52) Tordera, D.; Bünzli, A. M.; Pertegas, A.; Junquera-Hernández, J. M.; Constable, E. C.; Zampese, J. A.; Housecroft, C. E.; Orti, E.; Bolink, H. J. *Chem. - Eur. J.* **2013**, *19*, 8597.
- (53) Neve, F.; Crispini, A.; Campagna, S.; Serroni, S. *Inorg. Chem.* **1999**, *38*, 2250.
- (54) Costa, R. D.; Orti, E.; Tordera, D.; Pertegas, A.; Bolink, H. J.; Graber, S.; Housecroft, C. E.; Sachno, L.; Neuberger, M.; Constable, E. C. *Adv. Energy Mater.* **2011**, *1*, 282.
- (55) Schneider, G. E.; Bolink, H. J.; Constable, E. C.; Ertl, C. D.; Housecroft, C. E.; Pertegas, A.; Zampese, J. A.; Kanitz, A.; Kessler, F.; Meier, S. B. *Dalton Trans.* **2014**, *43*, 1961.
- (56) Bünzli, A. M.; Constable, E. C.; Housecroft, C. E.; Prescimone, A.; Zampese, J. A.; Longo, G.; Gil-Escrig, L.; Pertegas, A.; Orti, E.; Bolink, H. J. *Chem. Sci.* **2015**, *6*, 2843.
- (57) Spek, A. L. *Acta Crystallogr., Sect. D: Biol. Crystallogr.* **2009**, *65*, 148.
- (58) Constable, E. C.; Neuberger, M.; Rösel, P.; Schneider, G. E.; Zampese, J. A.; Housecroft, C. E.; Monti, F.; Armaroli, N.; Costa, R. D.; Orti, E. *Inorg. Chem.* **2013**, *52*, 885.
- (59) Bolink, H. J.; Coronado, E.; Costa, R. D.; Orti, E.; Sessolo, M.; Graber, S.; Doyle, K.; Neuberger, M.; Housecroft, C. E.; Constable, E. C. *Adv. Mater.* **2008**, *20*, 3910.
- (60) Parker, S. T.; Slinker, J. D.; Lowry, M. S.; Cox, M. P.; Bernhard, S.; Malliaras, G. G. *Chem. Mater.* **2005**, *17*, 3187.
- (61) Shavaleev, N. M.; Scopelliti, R.; Gratzel, M.; Nazeeruddin, M. K.; Pertegas, A.; Roldan-Carmona, C.; Tordera, D.; Bolink, H. J. *J. Mater. Chem. C* **2013**, *1*, 2241.
- (62) Bolink, H. J.; Coronado, E.; Costa, R. D.; Gaviña, P.; Orti, E.; Tatay, S. *Inorg. Chem.* **2009**, *48*, 3907.
- (63) Ho, C.-C.; Chen, H.-F.; Ho, Y.-C.; Liao, C.-T.; Su, H.-C.; Wong, K.-T. *Phys. Chem. Chem. Phys.* **2011**, *13*, 17729.
- (64) Ross, D. A. W.; Scattergood, P. A.; Babaei, A.; Pertegas, A.; Bolink, H. J.; Elliott, P. I. P. *Dalton Trans.* **2016**, *45*, 7748.
- (65) Meier, S. B.; Hartmann, D.; Tordera, D.; Bolink, H. J.; Winnacker, A.; Sarfert, W. *Phys. Chem. Chem. Phys.* **2012**, *14*, 10886.
- (66) AlTal, F.; Gao, J. *Org. Electron.* **2015**, *18*, 1.
- (67) He, L.; Qiao, J.; Duan, L.; Dong, G.; Zhang, D.; Wang, L.; Qiu, Y. *Adv. Funct. Mater.* **2009**, *19*, 2950.
- (68) Xu, W.-J.; Liu, S.-J.; Ma, T.-C.; Zhao, Q.; Pertegas, A.; Tordera, D.; Bolink, H. J.; Ye, S.-H.; Liu, X.-M.; Sun, S.; Huang, W. *J. Mater. Chem.* **2011**, *21*, 13999.
- (69) Constable, E. C.; Housecroft, C. E.; Schneider, G. E.; Zampese, J. A.; Bolink, H. J.; Pertegas, A.; Roldan-Carmona, C. *Dalton Trans.* **2014**, *43*, 4653.
- (70) Weber, M. D.; Adam, M.; Tykewski, R. R.; Costa, R. D. *Adv. Funct. Mater.* **2015**, *25*, S066.
- (71) Weber, M. D.; Wittmann, J. E.; Burger, A.; Malcıoğlu, O. B.; Segarra-Martí, J.; Hirsch, A.; Coto, P. B.; Bockstedte, M.; Costa, R. D. *Adv. Funct. Mater.* **2016**, *26*, 6737.

(72) Hasan, K.; Donato, L.; Shen, Y.; D. Slinker, J.; Zysman-Colman, E. *Dalton Trans.* **2014**, *43*, 13672.

(73) Suhr, K. J.; Bastatas, L. D.; Shen, Y.; Mitchell, L. A.; Frazier, G. A.; Taylor, D. W.; Slinker, J. D.; Holliday, B. J. *Dalton Trans.* **2016**, *45*, 17807.

Supporting Information

Highly Stable Red-Light-Emitting Electrochemical Cells

Cathrin D. Ertl,^{1,‡} Cristina Momblona,^{1,†} Antonio Pertegás,[†] José M. Junquera-Hernández,[†] Maria-Grazia La-Placa,[†] Alessandro Prescimone,[‡] Enrique Ortí,[†] Catherine E. Housecroft,^{*,‡} Edwin C. Constable,[‡] and Henk J. Bolink^{*,†}

[†]Instituto de Ciencia Molecular, Universidad de Valencia, C/ Catedrático José Beltrán 2, ES-46980 Paterna (Valencia), Spain

[‡]Department of Chemistry, University of Basel, Spitalstrasse 51, CH-4056 Basel, Switzerland

1) Contributed equally to this work.

* Email: catherine.housecroft@unibas.ch, henk.bolink@uv.es

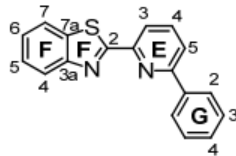
CONTENTS

Synthetic details	S2
Crystallography	S10
Cyclic voltammetry	S10
Photoluminescence data	S11
TD-DFT results	S12
Electroluminescence data	S13
References	S14

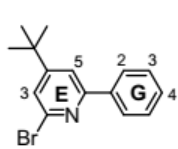
Synthetic details

2-Bromo-6-phenylpyridine,¹ 4-(*tert*-butyl)-2-phenylpyridine,² 2-(pyridin-2-yl)benzo[*d*]thiazole (**L1**),³ 2,2'-bibenzo[*d*]thiazole (**L7**),^{4,5} 2-bromo-4-(*tert*-butyl)pyridine,⁶ and 2,6-bis(benzo[*d*]thiazol-2-yl)pyridine (**L5**)⁷ were synthesized according to literature procedures and their ¹H NMR spectroscopic data matched those reported. Adaptation of the reported synthesis of 2-(pyridin-2-yl)benzo[*d*]thiazole (**L1**)³ gave 2-(4-(*tert*-butyl)pyridin-2-yl)benzo[*d*]thiazole (**L2**)⁸ and 2-(pyridin-2-yl)benzo[*d*]oxazole (**L6**)⁹ and their ¹H NMR spectroscopic data were compared to those described in the literature. [Ir(ppy)₂Cl]₂ was synthesized according to the standard method^{10,11} and ¹H NMR spectroscopic data matched those reported in the literature.¹²

2-(6-Phenylpyridin-2-yl)benzo[*d*]thiazole (**L3**)

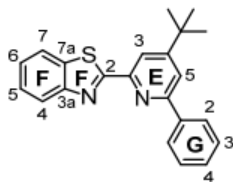
 2-(6-Phenylpyridin-2-yl)benzo[*d*]thiazole (**L3**) was synthesized by adaptation of a literature procedure.³ Benzothiazole (110 μL, 135 mg, 0.971 mmol), 2-bromo-6-phenylpyridine (455 mg, 1.94 mmol), CuI (17.9 mg, 94.0 μmol), phenanthroline monohydrate (19.1 mg, 96.4 μmol), K₃PO₄ (412 mg, 1.94 mmol) and dry DMF (0.8 mL) were added to a microwave vial, purged with N₂, sealed and heated at 120 °C overnight. The mixture was let to cool to room temperature. H₂O (50 mL) and EtOAc (50 mL) were added to the mixture and the layers were separated. The aqueous layer was extracted with EtOAc (3 × 50 mL), the combined organic layers were washed with brine (100 mL), dried over Na₂SO₄ and the solvent was removed under reduced pressure. The crude product was purified by column chromatography (silica, cyclohexane/EtOAc 6:1), the solvent removed and the residue washed with *n*-pentane to yield 2-(6-phenylpyridin-2-yl)benzo[*d*]thiazole (**L3**) as an off-white solid (143 mg, 0.496 mmol, 51.1%). M.p. 129.3 °C. ¹H NMR (500 MHz, CDCl₃) δ/ppm 8.31 (dd, *J* = 7.6, 1.0 Hz, 1H, H^{E3}), 8.20–8.15 (m, 2H, H^{G2}), 8.12 (*pseudo*-dt, *J* = 8.3, 0.9 Hz, 1H, H^{F4}), 7.97 (ddd, *J* = 8.0, 1.1, 0.6 Hz, 1H, H^{F7}), 7.92 (*pseudo*-t, *J* = 7.7 Hz, 1H, H^{E4}), 7.85 (dd, *J* = 7.9, 1.0 Hz, 1H, H^{E5}), 7.56–7.50 (overlapping m, 3H, H^{F5+G3}), 7.50–7.45 (m, 1H, H^{G4}), 7.43 (ddd, *J* = 8.2, 7.2, 1.2 Hz, 1H, H^{F6}). ¹³C{¹H} NMR (126 MHz, CDCl₃) δ/ppm 170.4 (C^{F2}), 157.1 (C^{E6}), 154.5 (C^{F3a}), 151.2 (C^{E2}), 138.3 (C^{G1}), 138.0 (C^{E4}), 136.5 (C^{F7a}), 129.6 (C^{G4}), 129.0 (C^{G3}), 127.1 (C^{G2}), 126.3 (C^{F5}), 125.7 (C^{F6}), 123.7 (C^{F4}), 122.1 (C^{F7}), 121.8 (C^{E5}), 119.0 (C^{E3}). IR (solid, $\tilde{\nu}/\text{cm}^{-1}$) 2982 (w), 1589 (w), 1566 (m), 1509 (w), 1447 (s), 1435 (m), 1319 (m), 1270 (w), 1250 (w), 1237 (w), 1183 (w), 1155 (w), 1083 (m), 1028 (w), 988 (m), 946 (w), 922 (w), 870 (w), 811 (m), 786 (w), 757 (s), 732 (s), 691 (s), 667 (m), 623 (m), 587 (w), 574 (w), 531 (w), 486 (w), 432 (m). LC-ESI-MS *m/z* 289.0 [*M*+H]⁺ (calc. 289.1). Found C 74.67, H 4.43, N 10.01; C₁₈H₁₂N₂S requires C 74.97, H 4.19, N 9.71%.

2-Bromo-4-(*tert*-butyl)-6-phenylpyridine



2-Bromo-4-(*tert*-butyl)-6-phenylpyridine was synthesized by adaptation of a literature procedure.¹ A solution of *n*-BuLi (1.6 mol L⁻¹ in *n*-hexane, 16.0 mL, 12.0 g, 25.6 mmol) was added dropwise to a solution of 2-(dimethylamino)ethanol (1.30 mL, 1.15 g, 13.0 mmol) in dry *n*-hexane (10 mL) at 0 °C. After stirring for 30 min at 0 °C, a solution of 4-(*tert*-butyl)-2-phenylpyridine (879 mg, 4.16 mmol) in dry *n*-hexane (5 mL) was added dropwise. The mixture was stirred for 1 h at 0 °C and then cooled to -78 °C before adding a solution of CBr₄ (4.86 g, 14.7 mmol) in dry *n*-hexane (10 mL). The reaction mixture was stirred for 1 h at -78 °C before it was allowed to warm to room temperature and stirred for 3 d. H₂O (100 mL) was added and the mixture was extracted with *t*-BME (3 × 100 mL). The combined organic layers were dried over Na₂SO₄ and concentrated under reduced pressure. The residue was purified by column chromatography (silica, cyclohexane-1% EtOAc) to yield 2-bromo-4-(*tert*-butyl)-6-phenylpyridine as a light brown solid (892 mg, 3.07 mmol, 73.9%). M.p. 47.7 °C. ¹H NMR (500 MHz, CDCl₃) δ/ppm 7.98–7.94 (m, 2H, H^{G2}), 7.64 (d, *J* = 1.5 Hz, 1H, H^{E5}), 7.49–7.40 (overlapping m, 3H, H^{G3+G4}), 7.40 (d, *J* = 1.5 Hz, 1H, H^{E3}), 1.36 (s, 9H, H^{tBu}). ¹³C{¹H} NMR (126 MHz, CDCl₃) δ/ppm 163.8 (C^{E4}), 158.5 (C^{E6}), 142.6 (C^{E2}), 138.3 (C^{G1}), 129.4 (C^{G4}), 128.7 (C^{G3}), 127.1 (C^{G2}), 123.5 (C^{E3}), 116.7 (C^{E5}), 35.2 (C^{C(CH3)3}), 30.5 (C^{C(CH3)3}). IR (solid, $\tilde{\nu}$ /cm⁻¹) 3045 (w), 2968 (m), 2869 (w), 1590 (s), 1579 (m), 1530 (s), 1498 (m), 1477 (m), 1455 (w), 1415 (m), 1385 (s), 1367 (m), 1296 (m), 1240 (m), 1201 (w), 1184 (w), 1156 (m), 1128 (w), 1066 (m), 1029 (w), 1002 (w), 986 (w), 918 (w), 871 (m), 854 (m), 794 (m), 769 (s), 758 (s), 688 (s), 639 (s), 534 (w), 461 (w). LC-ESI-MS *m/z* 290.0 [M+H]⁺ (calc. 290.1). Found C 61.92, H 5.42, N 5.02; C₁₅H₁₆BrN requires C 62.08, H 5.56, N 4.83%.

2-(4-(*tert*-Butyl)-6-phenylpyridin-2-yl)benzo[*d*]thiazole (L4)



2-(4-(*tert*-Butyl)-6-phenylpyridin-2-yl)benzo[*d*]thiazole (**L4**) was synthesized by adaptation of a literature procedure.³ Benzothiazole (100 μL, 123 mg, 0.883 mmol), 2-bromo-4-(*tert*-butyl)-6-phenylpyridine (495 mg, 1.71 mmol), CuI (17.2 mg, 90.3 μmol), phenanthroline monohydrate (17.6 mg, 88.8 μmol), K₃PO₄ (361 mg, 1.70 mmol) and dry DMF (0.8 mL) were added to a microwave vial, purged with N₂, sealed and heated at 120 °C overnight. The mixture was let to cool to room temperature, diluted with EtOAc (100 mL), filtered through Celite® and washed with EtOAc (50 mL). The combined filtrate was washed with H₂O (100 mL), dried over Na₂SO₄ and the solvent removed under reduced pressure. The crude product was purified by column chromatography (silica, cyclohexane-5% EtOAc) and the solvent removed. *n*-Hexane was added to the residue, the mixture was sonicated and the solid removed by filtration. The solid was dissolved with EtOAc/CH₂Cl₂ and the solvent removed to yield 2-(4-(*tert*-butyl)-6-phenylpyridin-2-yl)benzo[*d*]thiazole (**L4**) as an off-white solid (164 mg, 0.476 mmol, 53.9%). M.p. 158.7 °C. ¹H NMR (500 MHz, CDCl₃) δ/ppm 8.36 (d, *J* = 1.6 Hz, 1H, H^{E3}), 8.17–8.15 (m, 2H, H^{G2}), 8.13 (*pseudo*-dt, *J* =

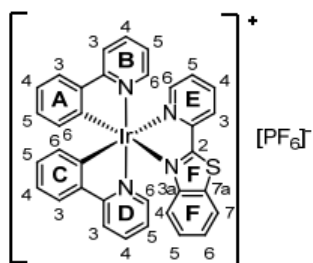
S3

8.2, 0.9 Hz, 1H, H^{F4}), 7.97 (ddd, $J = 8.0, 1.2, 0.7$ Hz, 1H, H^{F7}), 7.85 (d, $J = 1.7$ Hz, 1H, H^{E5}), 7.56–7.49 (overlapping m, 3H, H^{F5+G3}), 7.49–7.45 (m, 1H, H^{G4}), 7.42 (ddd, $J = 8.1, 7.2, 1.1$ Hz, 1H, H^{F6}), 1.47 (s, 9H, H^{Bu}). ¹³C{¹H} NMR (126 MHz, CDCl₃) δ /ppm 171.1 (C^{F2}), 162.4 (C^{E4}), 157.3 (C^{E6}), 154.4 (C^{F3a}), 151.1 (C^{E2}), 139.0 (C^{G1}), 136.5 (C^{F7a}), 129.4 (C^{G4}), 129.0 (C^{G3}), 127.2 (C^{G2}), 126.3 (C^{F5}), 125.6 (C^{F6}), 123.6 (C^{F4}), 122.1 (C^{F7}), 119.2 (C^{E5}), 116.4 (C^{E3}), 35.5 (C^{C(CH3)3}), 30.9 (C^{C(CH3)3}). IR (solid, $\tilde{\nu}$ /cm⁻¹) 2962 (w), 1595 (m), 1544 (m), 1472 (w), 1426 (m), 1392 (m), 1313 (m), 1233 (m), 1110 (w), 1024 (w), 927 (w), 879 (m), 779 (m), 756 (s), 730 (s), 696 (s), 649 (m), 588 (w), 533 (w). LC-ESI-MS m/z 345.1 [$M+H$]⁺ (calc. 345.1). Found C 76.35, H 5.97, N 8.33; C₂₂H₂₀N₂S requires C 76.71, H 5.85, N 8.13%.

General procedure for the synthesis of iridium(III) complexes

[Ir(ppy)₂Cl]₂ and AgPF₆ were suspended in MeOH (15–25 mL) and stirred at room temperature for 2–3.5 h. The mixture was filtered through Celite® and washed with MeOH. The filtrate was concentrated under reduced pressure to yield [Ir(C^N)₂(MeOH)₂][PF₆] which was neither purified nor characterized. Ancillary ligand (**L1–7**) and MeOH (5–10 mL) were added immediately to the solvento intermediate and the mixture stirred at room temperature overnight. The resulting orange-red precipitate was filtered off, redissolved in CH₂Cl₂ and concentrated under reduced pressure. The crude product was purified by column chromatography (silica) and the solvent removed. The residue was dissolved in little CH₂Cl₂ and precipitated with Et₂O and/or *n*-hexane. Where necessary, the complex was dissolved in little CH₂Cl₂, layered with toluene and *n*-hexane and stored in the refrigerator overnight. The resulting precipitation was filtered off and dried under vacuum. The reported yields (over two steps) were calculated based on the iridium dimer starting material.

Complex 1

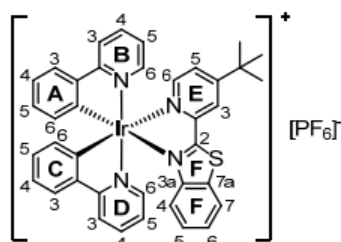


[Ir(ppy)₂Cl]₂ (100 mg, 0.0933 mmol) and AgPF₆ (51.4 mg, 0.203 mmol) in MeOH (20 mL), 2 h 45 min at room temperature. Addition of 2-(pyridin-2-yl)benzo[*d*]thiazole (**L1**) (39.7 mg, 0.187 mmol) and MeOH (10 mL). Purification by column chromatography (silica, CH₂Cl₂ changing to CH₂Cl₂–1% MeOH) and precipitation with Et₂O. Complex **1** was isolated as an orange solid (129 mg, 0.151 mmol, 80.6%). ¹H NMR (500 MHz, CD₂Cl₂)

δ /ppm 8.45 (*pseudo*-dt, $J = 8.0, 1.0$ Hz, 1H, H^{E3}), 8.20 (*pseudo*-td, $J = 7.8, 1.5$ Hz, 1H, H^{E4}), 8.08 (ddd, $J = 8.3, 1.1, 0.7$ Hz, 1H, H^{F7}), 8.02–7.96 (overlapping m, 2H, H^{D3+E6}), 7.93 (*pseudo*-dt, $J = 8.4, 1.1$ Hz, 1H, H^{B3}), 7.80 (ddd, $J = 8.2, 7.4, 1.5$ Hz, 1H, H^{D4}), 7.80–7.72 (overlapping m, 3H, H^{A3+B4+C3}), 7.62 (*pseudo*-dt, $J = 5.9, 1.1$ Hz, 1H, H^{D6}), 7.56–7.51 (overlapping m, 2H, H^{E5+F6}), 7.47 (*pseudo*-dt, $J = 5.9, 1.2$ Hz, 1H, H^{B6}), 7.24 (ddd, $J = 8.4, 7.2, 1.2$ Hz, 1H, H^{F5}), 7.14 (*pseudo*-td, $J = 7.6, 1.2$ Hz, 1H,

H^{A4}), 7.11 (*pseudo*-td, $J = 7.6, 1.2$ Hz, 1H, H^{C4}), 7.03–6.98 (overlapping m, 2H, H^{A5+B5}), 6.98–6.94 (overlapping m, 3H, H^{C5+D5+F4}), 6.41 (dd, $J = 7.7, 1.2$ Hz, 1H, H^{A6}), 6.25 (dd, $J = 7.8, 1.2$ Hz, 1H, H^{C6}). ¹³C{¹H} NMR (126 MHz, CD₂Cl₂) δ /ppm 170.0 (C^{F2}), 168.4 (C^{D2}), 167.9 (C^{B2}), 152.3 (C^{E2}), 151.5 (C^{E6}), 151.2 (C^{F3a}), 150.2 (C^{D6}), 149.2 (C^{B6}), 147.54 (C^{C1}), 147.52 (C^{A1}), 144.7 (C^{A2}), 144.2 (C^{C2}), 140.5 (C^{E4}), 138.92 (C^{D4}), 138.85 (C^{B4}), 134.8 (C^{F7a}), 132.8 (C^{A6}), 131.7 (C^{C6}), 131.4 (C^{C5}), 131.1 (C^{A5}), 129.9 (C^{E5}), 129.3 (C^{F5}), 129.0 (C^{F6}), 126.9 (C^{E3}), 125.6 (C^{C3}), 125.5 (C^{A3}), 124.2 (C^{D5}), 123.9 (C^{B5}), 123.7 (2C, C^{C4+F7}), 123.5 (C^{A4}), 123.3 (C^{F4}), 120.6 (C^{D3}), 120.3 (C^{B3}). IR (solid, $\tilde{\nu}$ /cm⁻¹) 3045 (w), 1608 (m), 1584 (m), 1563 (w), 1479 (s), 1458 (w), 1440 (m), 1421 (m), 1323 (w), 1269 (m), 1229 (w), 1165 (m), 1065 (w), 1031 (m), 1008 (w), 835 (s), 794 (m), 757 (s), 739 (s), 730 (s), 713 (m), 670 (m), 631 (m), 556 (s), 477 (w). UV/Vis (CH₂Cl₂, 1.0×10^{-5} mol dm⁻³) λ /nm (ϵ /dm³ mol⁻¹ cm⁻¹) 255 (39 000), 295 sh (24 000), 330 (21 000), 350 sh (17 000), 382 (8300), 410 sh (5600). Emission (CH₂Cl₂, 1.0×10^{-5} mol dm⁻³, $\lambda_{exc} = 266$ nm) $\lambda_{em}^{max} = 644$ nm. ESI-MS m/z 713.4 [M-PF₆]⁺ (calc. 713.1). Found C 47.16, H 2.97, N 6.76; C₃₄H₂₄F₆IrN₄PS·0.5H₂O requires C 47.11, H 2.91, N 6.46%.

Complex 2



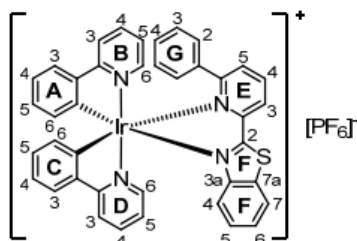
[Ir(ppy)₂Cl]₂ (100 mg, 0.0933 mmol) and AgPF₆ (51.9 mg, 0.205 mmol) in MeOH (20 mL), 2 h at room temperature. Addition of 2-(4-(*tert*-butyl)pyridin-2-yl)benzo[*d*]thiazole (**L2**) (50.1 mg, 0.187 mmol) and MeOH (10 mL). Purification by column chromatography (silica, CH₂Cl₂ changing to CH₂Cl₂–1% MeOH) and precipitation with Et₂O. Complex **2** was isolated as an orange solid (121 mg, 0.133 mmol, 70.9%). ¹H

NMR (500 MHz, CD₂Cl₂) δ /ppm 8.26 (dd, $J = 2.0, 0.6$ Hz, 1H, H^{E3}), 8.08 (*pseudo*-dt, $J = 8.2, 0.9$ Hz, 1H, H^{F7}), 7.98 (*pseudo*-dt, $J = 8.3, 1.2$ Hz, 1H, H^{B3}), 7.93 (*pseudo*-dt, $J = 8.0, 0.9$ Hz, 1H, H^{D3}), 7.87 (dd, $J = 5.9, 0.6$ Hz, 1H, H^{E6}), 7.80 (ddd, $J = 8.3, 7.5, 1.5$ Hz, 1H, H^{B4}), 7.78–7.73 (overlapping m, 3H, H^{A3+C3+D4}), 7.62 (ddd, $J = 5.8, 1.5, 0.7$ Hz, 1H, H^{B6}), 7.54 (ddd, $J = 8.3, 7.2, 1.1$ Hz, 1H, H^{F6}), 7.51–7.46 (overlapping m, 2H, H^{D6+E5}), 7.24 (ddd, $J = 8.5, 7.2, 1.2$ Hz, 1H, H^{F5}), 7.14 (*pseudo*-td, $J = 7.6, 1.2$ Hz, 1H, H^{C4}), 7.10 (*pseudo*-td, $J = 7.6, 1.2$ Hz, 1H, H^{A4}), 7.04–6.94 (overlapping m, 5H, H^{A5+B5+C5+D5+F4}), 6.40 (dd, $J = 7.7, 1.2$ Hz, 1H, H^{C6}), 6.25 (dd, $J = 7.6, 1.2$ Hz, 1H, H^{A6}), 1.43 (s, 9H, H^{tBu}). ¹³C{¹H} NMR (126 MHz, CD₂Cl₂) δ /ppm 170.3 (C^{F2}), 168.5 (C^{D2}), 167.9 (C^{B2}), 165.6 (C^{E4}), 152.1 (C^{E2}), 151.2 (C^{F3a}), 151.0 (C^{E6}), 150.3 (C^{B6}), 149.2 (C^{D6}), 147.9 (C^{C1}), 147.7 (C^{A1}), 144.8 (C^{C2}), 144.2 (C^{A2}), 138.84 (C^{B4/D4}), 138.82 (C^{B4/D4}), 134.6 (C^{F7a}), 132.8 (C^{C6}), 131.6 (C^{A6}), 131.4 (C^{A5}), 131.1 (C^{C5}), 129.3 (C^{F5}), 129.0 (C^{F6}), 127.3 (C^{E5}), 125.51 (C^{A3/C3}), 125.50 (C^{A3/C3}), 124.1 (C^{B5}), 123.9 (C^{D5}), 123.71 (C^{E3}), 123.67 (C^{F7}), 123.66 (C^{A4}), 123.4 (C^{C4}), 123.3 (C^{F4}), 120.5 (C^{B3}), 120.3 (C^{D3}), 36.3 (C^{E4-C(CH3)3}), 30.5 (C^{E4-C(CH3)3}). IR (solid, $\tilde{\nu}$ /cm⁻¹) 2963 (w), 1609 (m), 1584 (m), 1563 (w), 1479 (m), 1440 (w), 1423 (m), 1369 (w), 1326 (w), 1269 (w), 1247 (w), 1228 (w), 1165 (w), 1065 (w), 1033 (m), 834 (s), 794 (m), 757 (s), 730 (m), 709 (w), 670 (w), 631 (w), 556 (s), 462 (w), 418 (m). UV/Vis (CH₂Cl₂,

S5

1.0×10^{-5} mol dm⁻³) λ /nm (ϵ /dm³ mol⁻¹ cm⁻¹) 258 (45 000), 314 (26 000), 348 sh (20 000), 381 (9500), 410 sh (6300). Emission (CH₂Cl₂, 1.0×10^{-5} mol dm⁻³, $\lambda_{\text{exc}} = 270$ nm) $\lambda_{\text{em}}^{\text{max}} = 638$ nm. ESI-MS m/z 769.2 [M -PF₆]⁺ (calc. 769.2). Found C 49.41, H 3.72, N 6.39; C₃₈H₃₂F₆IrN₄PS·0.5H₂O requires C 49.45, H 3.60, N 6.07%.

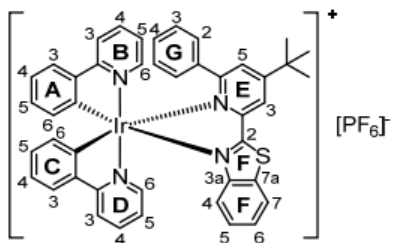
Complex 3



[Ir(ppy)₂Cl]₂ (100 mg, 0.0933 mmol) and AgPF₆ (62.1 mg, 0.246 mmol) in MeOH (20 mL), 3 h 15 min at room temperature. Addition of 2-(6-phenylpyridin-2-yl)benzo[*d*]thiazole (**L3**) (55.5 mg, 0.192 mmol) and MeOH (10 mL). Purification by column chromatography (silica, CH₂Cl₂ changing to CH₂Cl₂-1% MeOH) and precipitation with Et₂O. Complex **3** was isolated as an orange solid (152

mg, 0.163 mmol, 87.5%). ¹H NMR (500 MHz, CD₂Cl₂) δ /ppm 8.48 (dd, $J = 7.9, 1.3$ Hz, 1H, H^{E3}), 8.25 (*pseudo-t*, $J = 7.8$ Hz, 1H, H^{E4}), 8.03 (ddd, $J = 8.3, 1.1, 0.5$ Hz, 1H, H^{F7}), 7.92 (*pseudo-dt*, $J = 5.9, 1.1$ Hz, 1H, H^{B6}), 7.90–7.82 (overlapping m, 2H, H^{B3+B4}), 7.77–7.70 (overlapping m, 2H, H^{D3+D4}), 7.53–7.45 (overlapping m, 3H, H^{C3+E5+F6}), 7.42 (*pseudo-dt*, $J = 5.9, 1.1$ Hz, 1H, H^{D6}), 7.21 (dd, $J = 7.8, 1.3$ Hz, 1H, H^{A3}), 7.16–7.07 (overlapping m, 2H, H^{D5+F5}), 7.04–6.98 (overlapping m, 3H, H^{B5+C4+G4}), 6.86 (*pseudo-td*, $J = 7.5, 1.4$ Hz, 1H, H^{C5}), 6.82–6.75 (overlapping m, 3H, H^{F4+G3}), 6.62 (*pseudo-td*, $J = 7.6, 1.2$ Hz, 1H, H^{A4}), 6.53 (br, 2H, H^{G2}), 6.41 (*pseudo-td*, $J = 7.4, 1.3$ Hz, 1H, H^{A5}), 6.10 (dd, $J = 7.8, 1.1$ Hz, 1H, H^{C6}), 5.59 (dd, $J = 7.7, 1.1$ Hz, 1H, H^{A6}). ¹³C{¹H} NMR (126 MHz, CD₂Cl₂) δ /ppm 171.5 (C^{F2}), 169.1 (C^{B2}), 167.8 (C^{D2}), 167.0 (C^{E6}), 152.9 (C^{E2}), 151.6 (C^{F3a}), 150.4 (C^{B6}), 149.4 (C^{D6}), 148.3 (C^{A1}), 144.1 (2C, C^{C1+C2}), 143.4 (C^{A2}), 140.5 (C^{E4}), 138.8 (C^{D4}), 138.7 (C^{B4}), 137.6 (C^{G1}), 134.7 (C^{F7a}), 132.0 (C^{E5}), 131.7 (C^{C6}), 131.4 (C^{A6}), 130.7 (C^{C5}), 130.3 (C^{A5}), 129.8 (C^{G4}), 128.8 (C^{F5}), 128.6 (C^{F6}), 128.5 (C^{G3}), 127.8 (C^{G2}), 126.0 (C^{E3}), 125.4 (C^{A3}), 125.1 (C^{C3}), 124.0 (C^{D5}), 123.6 (C^{C4}), 123.4 (C^{F7}), 123.2 (C^{F4}), 123.1 (C^{B5}), 121.8 (C^{A4}), 120.7 (C^{B3}), 120.2 (C^{D3}). IR (solid, $\tilde{\nu}$ /cm⁻¹) 3055 (w), 1608 (m), 1585 (m), 1563 (m), 1479 (m), 1459 (w), 1440 (m), 1424 (m), 1326 (w), 1270 (w), 1228 (w), 1180 (w), 1165 (w), 1064 (w), 1031 (w), 836 (s), 756 (s), 729 (s), 699 (m), 670 (m), 630 (m), 556 (s), 418 (m). UV/Vis (CH₂Cl₂, 1.0×10^{-5} mol dm⁻³) λ /nm (ϵ /dm³ mol⁻¹ cm⁻¹) 261 (40 000), 271 sh (39 000), 340 (26 000), 355 sh (22 000), 420 sh (4500). Emission (CH₂Cl₂, 1.0×10^{-5} mol dm⁻³, $\lambda_{\text{exc}} = 270$ nm) $\lambda_{\text{em}}^{\text{max}} = 642$ nm. ESI-MS m/z 789.1 [M -PF₆]⁺ (calc. 789.2). Found C 51.03, H 3.33, N 6.32; C₄₀H₂₈F₆IrN₄PS·0.5H₂O requires C 50.95, H 3.10, N 5.94%.

Complex 4



[Ir(ppy)₂Cl]₂ (120 mg, 0.112 mmol) and AgPF₆ (77.6 mg, 0.307 mmol) in MeOH (25 mL), 3 h at room temperature. Addition of 2-(4-*tert*-butyl)-6-phenylpyridin-2-yl)benzo[*d*]thiazole (**L4**) (77.8 mg, 0.226 mmol) and MeOH (5 mL). Purification by column chromatography (silica, CH₂Cl₂ changing to CH₂Cl₂-1% MeOH) and precipitation with *n*-hexane. Complex **4** was isolated as an orange solid

(190 mg, 0.192 mmol, 85.8%). ¹H NMR (500 MHz, CD₂Cl₂) δ/ppm 8.32 (d, *J* = 2.0 Hz, 1H, H^{E3}), 8.04 (*pseudo*-dt, *J* = 8.2, 1.0 Hz, 1H, H^{F7}), 7.90–7.83 (overlapping m, 3H, H^{B3+B4+B6}), 7.78–7.71 (overlapping m, 2H, H^{D3+D4}), 7.51 (dd, *J* = 7.9, 1.3 Hz, 1H, H^{C4}), 7.50–7.46 (overlapping m, 2H, H^{D6+F6}), 7.43 (d, *J* = 2.0 Hz, 1H, H^{E5}), 7.22 (dd, *J* = 7.8, 1.3 Hz, 1H, H^{A3}), 7.13 (ddd, *J* = 8.5, 7.2, 1.2 Hz, 1H, H^{F5}), 7.12–7.05 (m, 1H, H^{D5}), 7.04–6.97 (overlapping m, 3H, H^{B5+C4+G4}), 6.86 (*pseudo*-td, *J* = 7.5, 1.4 Hz, 1H, H^{C5}), 6.82–6.74 (overlapping m, 3H, H^{F4+G3}), 6.63 (*pseudo*-td, *J* = 7.5, 1.2 Hz, 1H, H^{A4}), 6.54 (br, 2H, H^{G2}), 6.41 (*pseudo*-td, *J* = 7.5, 1.4 Hz, 1H, H^{A5}), 6.09 (dd, *J* = 7.8, 1.1 Hz, 1H, H^{C6}), 5.57 (dd, *J* = 7.7, 1.1 Hz, 1H, H^{A6}), 1.47 (s, 9H, H^{tBu}). ¹³C {¹H} NMR (126 MHz, CD₂Cl₂) δ/ppm 171.7 (C^{F2}), 169.1 (C^{B2}), 168.0 (C^{D2}), 166.7 (C^{E6}), 165.5 (C^{E4}), 152.8 (C^{E2}), 151.6 (C^{F3a}), 150.3 (C^{B6}), 149.4 (C^{D6}), 148.4 (C^{A1}), 144.5 (C^{C1}), 144.1 (C^{C2}), 143.3 (C^{A2}), 138.8 (C^{D4}), 138.7 (C^{B4}), 137.8 (C^{G1}), 134.4 (C^{F7a}), 131.8 (C^{C6}), 131.4 (C^{A6}), 130.7 (C^{C5}), 130.4 (C^{A5}), 129.7 (C^{G4}), 129.1 (C^{E5}), 128.9 (C^{F5}), 128.6 (C^{F6}), 128.5 (C^{G3}), 127.9 (C^{G2}), 125.4 (C^{A3}), 125.2 (C^{C3}), 123.8 (C^{D5}), 123.5 (C^{B5}), 123.4 (C^{F7}), 123.3 (C^{F4}), 123.1 (C^{E3}), 123.0 (C^{C4}), 121.8 (C^{A4}), 120.6 (C^{B3}), 120.3 (C^{D3}), 36.2 (C^{C(CH3)3}), 30.5 (C^{C(CH3)3}). IR (solid, $\tilde{\nu}$ /cm⁻¹) 2959 (w), 1608 (m), 1585 (m), 1541 (w), 1479 (m), 1440 (w), 1424 (m), 1349 (w), 1319 (w), 1270 (w), 1249 (w), 1165 (w), 1064 (w), 1031 (w), 902 (w), 876 (m), 834 (s), 756 (s), 729 (m), 697 (m), 669 (w), 656 (w), 630 (w), 556 (s). UV/Vis (CH₂Cl₂, 1.0 × 10⁻⁵ mol dm⁻³) λ/nm (ε/dm³ mol⁻¹ cm⁻¹) 261 (40 000), 270 sh (38 000), 339 (25 000), 355 sh (21 000), 385 (8400), 420 sh (4100). Emission (CH₂Cl₂, 1.0 × 10⁻⁵ mol dm⁻³, λ_{exc} = 270 nm) λ_{em}^{max} = 636 nm. ESI-MS *m/z* 845.1 [*M*-PF₆]⁺ (calc. 845.2). Found C 53.70, H 4.03, N 5.82; C₄₄H₃₆F₆IrN₄PS requires C 53.38, H 3.67, N 5.66%.

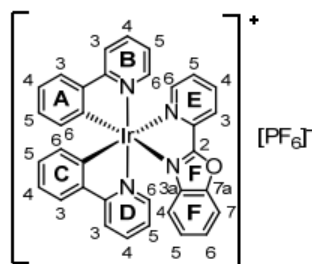
Complex 5



[Ir(ppy)₂Cl]₂ (150 mg, 0.140 mmol) and AgPF₆ (88.1 mg, 0.348 mmol) in MeOH (25 mL), 2 h at room temperature. Addition of 2,6-bis(benzo[*d*]thiazol-2-yl)pyridine (**L5**) (98.0 mg, 0.284 mmol) and MeOH (10 mL). Purification by column chromatography (silica, CH₂Cl₂ changing to CH₂Cl₂-1% MeOH), layering with toluene/*n*-hexane and

subsequent precipitation with *n*-hexane from a CH₂Cl₂ solution. Complex **5** was isolated as a dark red solid (136 mg, 0.137 mmol, 49.0%). ¹H NMR (500 MHz, CD₂Cl₂) δ/ppm 8.66 (br, 1H, H^{D6}), 8.60 (dd, *J* = 7.9, 1.2 Hz, 1H, H^{E3}), 8.31 (*pseudo-t*, *J* = 7.8 Hz, 1H, H^{E4}), 8.10 (dd, *J* = 8.2, 1.0 Hz, 1H, H^{F7}), 7.91–7.77 (overlapping m, 4H, H^{B3+B4+D3+D4}), 7.75 (dd, *J* = 7.8, 1.1 Hz, 1H, H^{E5}), 7.71 (d, *J* = 8.1 Hz, 1H, H^{G4/G7}), 7.68 (dd, *J* = 8.2, 1.1 Hz, 1H, H^{G4/G7}), 7.64 (dd, *J* = 7.8, 1.4 Hz, 1H, H^{C3}), 7.55–7.45 (overlapping m, 3H, H^{B6+F6+G5/G6}), 7.41 (ddd, *J* = 8.3, 7.2, 1.2 Hz, 1H, H^{G5/G6}), 7.24 (ddd, *J* = 7.3, 5.8, 1.8 Hz, 1H, H^{D5}), 7.18–7.06 (overlapping m, 2H, H^{A3+F5}), 7.02 (*pseudo-td*, *J* = 7.5, 1.2 Hz, 1H, H^{C4}), 6.97 (*pseudo-td*, *J* = 6.3, 2.0 Hz, 1H, H^{B5}), 6.79 (*pseudo-td*, *J* = 7.5, 1.4 Hz, 1H, H^{C5}), 6.66 (d, *J* = 8.6 Hz, 1H, H^{F4}), 6.21 (*pseudo-t*, *J* = 7.5 Hz, 1H, H^{A4}), 5.96 (dd, *J* = 7.8, 1.1 Hz, 1H, H^{C6}), 5.67 (*pseudo-t*, *J* = 7.2 Hz, 1H, H^{A5}), 5.36 (d, *J* = 7.6 Hz, 1H, H^{A6}). ¹³C{¹H} NMR (126 MHz, CD₂Cl₂) δ/ppm 170.6 (C^{F2}), 168.6 (C^{B2}), 167.3 (C^{D2}), 162.9 (C^{G2}), 157.4 (C^{E6}), 153.8 (C^{E2}), 153.1 (C^{G3a/G7a}), 151.7 (C^{F3a}), 148.9 (C^{B6}), 145.5 (C^{A1}), 144.3 (C^{C2}), 143.4 (C^{C1}), 142.9 (C^{A2}), 141.1 (C^{E4}), 138.90 (2C, C^{B3/B4+D3/D4}), 138.88 (2C, C^{B3/B4+D3/D4}), 137.3 (C^{G3a/G7a}), 134.9 (C^{F7a}), 132.7 (C^{A6}), 131.83 (C^{C6/E5}), 131.81 (C^{C6/E5}), 130.8 (C^{C5}), 129.1 (C^{F5}), 129.0 (C^{F6}), 128.9 (C^{A5}), 127.6 (C^{E3}), 127.1 (C^{G5/G6}), 126.8 (C^{G5/G6}), 125.2 (C^{C3}), 124.6 (C^{G4/G7}), 124.0 (C^{A3}), 123.62 (C^{C4/F7}), 123.60 (C^{C4/F7}), 123.43 (C^{B5/F4}), 123.38 (C^{B5/F4}), 123.3 (C^{D5}), 122.2 (C^{G4/G7}), 121.4 (C^{A4}), 120.3 (C^{B3/B4}), 119.8 (C^{D3/D4}). IR (solid, $\tilde{\nu}$ /cm⁻¹) 3058 (w), 1608 (m), 1584 (m), 1564 (w), 1480 (m), 1459 (w), 1439 (w), 1423 (m), 1319 (w), 1270 (w), 1230 (w), 1180 (w), 1165 (w), 1119 (w), 1063 (w), 1031 (w), 983 (w), 835 (s), 756 (s), 728 (s), 669 (m), 630 (m), 556 (s), 420 (m). UV/Vis (CH₂Cl₂, 1.0 × 10⁻⁵ mol dm⁻³) λ/nm (ε/dm³ mol⁻¹ cm⁻¹) 255 (41 000), 261 sh (40 000), 300 sh (30 000), 340 (25 000), 365 sh (19 000), 420 sh (4100). Emission (CH₂Cl₂, 1.0 × 10⁻⁵ mol dm⁻³, λ_{exc} = 265 nm) λ_{em}^{max} = 652 nm. ESI-MS *m/z* 846.0 [M-PF₆]⁺ (calc. 846.1). HR ESI-MS *m/z* 846.1340 (calc. 846.1332). Satisfactory elemental analysis could not be obtained.

Complex 6

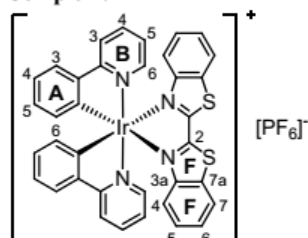


[Ir(ppy)₂Cl]₂ (149 mg, 0.139 mmol) and AgPF₆ (91.6 mg, 0.362 mmol) in MeOH (25 mL), 3.5 h at room temperature. Addition of 2-(pyridin-2-yl)benzo[*d*]oxazole (**L6**) (56.6 mg, 0.288 mmol) and MeOH (10 mL). Purification by column chromatography (silica, CH₂Cl₂ changing to CH₂Cl₂-1% MeOH) and precipitation with Et₂O. Complex **6** was isolated as an orange solid (184 mg, 0.219 mmol, 78.6%).

¹H NMR (500 MHz, CD₂Cl₂) δ/ppm 8.52 (*pseudo-dt*, *J* = 7.9, 1.0 Hz, 1H, H^{E3}), 8.25 (*pseudo-td*, *J* = 7.8, 1.5 Hz, 1H, H^{E4}), 8.05 (*pseudo-dt*, *J* = 5.4, 1.1 Hz, 1H, H^{E6}), 7.99 (*pseudo-dt*, *J* = 8.3, 1.1 Hz, 1H, H^{B3}), 7.93 (*pseudo-dt*, *J* = 8.3, 1.0 Hz, 1H, H^{D3}), 7.86–7.81 (overlapping m, 2H, H^{B4+F7}), 7.80–7.75 (overlapping m, 4H, H^{A3+B6+C3+D4}), 7.64 (ddd, *J* = 7.8, 5.4, 1.3 Hz, 1H, H^{E5}), 7.58 (ddd, *J* = 8.7, 7.5, 1.2 Hz, 1H, H^{F6}), 7.54 (*pseudo-dt*, *J* = 5.8, 1.1 Hz, 1H, H^{D6}), 7.26 (ddd, *J* = 8.4, 7.5, 1.0 Hz, 1H, H^{F5}), 7.16 (*pseudo-td*, *J* = 7.5, 1.2 Hz, 1H, H^{C4}), 7.12 (*pseudo-td*, *J* = 7.6, 1.2 Hz, 1H, H^{A4}), 7.05 (ddd, *J* = 7.4, 5.9, 1.4 Hz, 1H, H^{D5}), 7.02–6.96 (overlapping

m, 3H, H^{A5+B5+C5}), 6.46 (dd, $J = 7.7, 1.3$ Hz, 1H, H^{C6}), 6.39 (*pseudo*-dt, $J = 8.1, 0.9$ Hz, 1H, H^{F4}), 6.37 (dd, $J = 7.7, 1.2$ Hz, 1H, H^{A6}). ¹³C{¹H} NMR (126 MHz, CD₂Cl₂) δ /ppm 168.4 (C^{D2}), 168.1 (C^{B2}), 166.8 (C^{F2}), 152.3 (C^{E6}), 152.1 (C^{F7a}), 150.2 (C^{B6}), 149.5 (C^{D6}), 148.3 (C^{A1}), 145.0 (C^{C2}), 144.53 (C^{C1}), 144.46 (C^{A2}), 144.0 (C^{E2}), 140.6 (C^{E4}), 139.01 (C^{B4}), 138.98 (C^{D4}), 137.9 (C^{F3a}), 132.9 (C^{C6}), 132.1 (C^{A6}), 131.3 (C^{A5}), 131.0 (C^{E5}), 130.8 (C^{C5}), 129.6 (C^{F6}), 128.1 (C^{F5}), 126.8 (C^{E3}), 125.6 (C^{C3}), 125.2 (C^{A3}), 124.17 (C^{BS/D5}), 124.15 (C^{BS/D5}), 123.7 (2C, C^{A4+C4}), 120.5 (C^{B3}), 120.2 (C^{D3}), 119.4 (C^{F4}), 113.2 (C^{F7}). IR (solid, $\tilde{\nu}$ /cm⁻¹) 3054 (w), 1608 (m), 1584 (m), 1565 (w), 1542 (w), 1479 (m), 1439 (m), 1423 (m), 1393 (m), 1304 (w), 1269 (w), 1229 (w), 1164 (w), 1142 (w), 1108 (w), 1093 (w), 1065 (w), 1032 (w), 1019 (w), 836 (s), 792 (m), 755 (s), 698 (w), 670 (w), 646 (w), 631 (w), 556 (s), 494 (w), 434 (w), 418 (m). UV/Vis (CH₂Cl₂, 1.0×10^{-5} mol dm⁻³) λ /nm (ϵ /dm³ mol⁻¹ cm⁻¹) 254 (42 000), 266 (41 000), 295 sh (31 000), 317 (29 000), 335 sh (21 000), 378 (9100), 410 sh (5700). Emission (CH₂Cl₂, 1.0×10^{-5} mol dm⁻³, $\lambda_{exc} = 270$ nm) $\lambda_{em}^{max} = 636$ nm. ESI-MS m/z 697.1 [$M-PF_6$]⁺ (calc. 697.2). Found C 48.19, H 3.26, N 6.89; C₃₄H₂₄F₆IrN₄OP·0.5H₂O requires C 48.00, H 2.96, N 6.59%.

Complex 7



[Ir(ppy)₂Cl]₂ (59.9 mg, 0.0559 mmol) and AgPF₆ (39.3 mg, 0.155 mmol) in MeOH (15 mL), 3 h at room temperature. Addition of 2,2'-bibenzo[*d*]thiazole (**L7**) (30.0 mg, 0.112 mmol) and MeOH (5 mL). Purification by column chromatography (silica, CH₂Cl₂ changing to CH₂Cl₂-2% MeOH) and precipitation with Et₂O.

Complex **7** was isolated as an orange-red solid (83.7 mg, 0.0920

mmol, 81.9%). ¹H NMR (500 MHz, CD₂Cl₂) δ /ppm 8.12 (*pseudo*-dt, $J = 8.2, 0.7$ Hz, 2H, H^{E7}), 7.95 (*pseudo*-dt, $J = 8.1, 0.9$ Hz, 2H, H^{B3}), 7.80–7.74 (overlapping m, 4H, H^{A3+B4}), 7.63–7.55 (overlapping m, 4H, H^{B6+E6}), 7.28 (ddd, $J = 8.4, 7.1, 1.2$ Hz, 2H, H^{E5}), 7.19 (*pseudo*-td, $J = 7.6, 1.2$ Hz, 2H, H^{A4}), 7.02 (*pseudo*-td, $J = 7.5, 1.4$ Hz, 2H, H^{A5}), 6.96 (ddd, $J = 7.4, 5.8, 1.4$ Hz, 2H, H^{B5}), 6.86 (*pseudo*-dt, $J = 8.9, 0.8$ Hz, 2H, H^{E4}), 6.34 (dd, $J = 7.8, 1.1$ Hz, 2H, H^{A6}). ¹³C{¹H} NMR (126 MHz, CD₂Cl₂) δ /ppm 168.1 (C^{B2}), 163.3 (C^{E2}), 151.0 (C^{E3a}), 150.2 (C^{B6}), 144.9 (C^{A1}), 144.8 (C^{A2}), 139.0 (C^{B4}), 136.1 (C^{E7a}), 132.4 (C^{A6}), 131.2 (C^{A5}), 129.9 (C^{E5}), 129.7 (C^{E6}), 125.6 (C^{A3}), 124.2 (C^{B5}), 124.00 (C^{A4}), 123.97 (C^{E7}), 123.6 (C^{E4}), 120.5 (C^{B3}). IR (solid, $\tilde{\nu}$ /cm⁻¹) 3093 (w), 1603 (m), 1587 (m), 1562 (w), 1477 (m), 1460 (m), 1441 (w), 1422 (m), 1409 (w), 1326 (m), 1297 (w), 1271 (w), 1257 (m), 1163 (m), 1134 (w), 1085 (w), 1073 (w), 1025 (m), 870 (m), 834 (s), 772 (s), 760 (s), 748 (s), 727 (m), 709 (m), 671 (m), 630 (w), 600 (w), 557 (s), 492 (w), 419 (m). UV/Vis (CH₂Cl₂, 1.0×10^{-5} mol dm⁻³) λ /nm (ϵ /dm³ mol⁻¹ cm⁻¹) 254 (40 000), 338 sh (19 000), 367 (29 000), 387 (30 000), 415 sh (9800), 445 sh (4800). Emission (CH₂Cl₂, 1.0×10^{-5} mol dm⁻³, $\lambda_{exc} = 259$ nm) $\lambda_{em}^{max} = 686$ nm. ESI-MS m/z 769.1 [$M-PF_6$]⁺ (calc. 769.1). Found C 47.35, H 2.91, N 6.50; C₃₆H₂₄F₆IrN₄PS₂ requires C 47.31, H 2.65, N 6.13%.

Crystallography

Solvent molecules were badly disordered in complex **1** and the SQUEEZE¹³ procedure was used; residual electron density corresponds to 1.5 CH₂Cl₂ per formula unit.

1·1.5CH₂Cl₂, C_{35.50}H₂₇Cl₃F₆Ir₁N₄P₁S₁, *M* = 985.24, yellow block, monoclinic, space group *P*2₁/*c*, *a* = 14.4951(15), *b* = 13.7676(14), *c* = 18.7348(19) Å, β = 106.359(3)°, *U* = 3587.4(6) Å³, *Z* = 4, *D_c* = 1.82 Mg m⁻³, μ(Cu-Kα) = 10.8 mm⁻¹, *T* = 123 K. Total 33781 reflections, 6209 unique, *R*_{int} = 0.022. Refinement of 6169 reflections (424 parameters) with *I* > 2σ (*I*) converged at final *R*₁ = 0.0243 (*R*₁ all data = 0.0244), *wR*₂ = 0.0546 (*wR*₂ all data = 0.0547), *gof* = 0.9999. CCDC 1062206.

6·CH₂Cl₂, C₃₅H₂₆Cl₂F₆Ir₁N₄O₁P₁, *M* = 926.70, red block, monoclinic, space group *P*2₁/*n*, *a* = 14.6181(15), *b* = 13.8956(14), *c* = 16.9244(17) Å, β = 107.448(2)°, *U* = 3279.6(6) Å³, *Z* = 4, *D_c* = 1.877 Mg m⁻³, μ(Cu-Kα) = 10.478 mm⁻¹, *T* = 123 K. Total 19957 reflections, 5966 unique, *R*_{int} = 0.022. Refinement of 5956 reflections (451 parameters) with *I* > 2σ (*I*) converged at final *R*₁ = 0.0256 (*R*₁ all data = 0.0257), *wR*₂ = 0.0556 (*wR*₂ all data = 0.0556), *gof* = 0.9994. CCDC 1515402.

7, C₃₄H₂₄F₆Ir₁N₆P₁S₂, *M* = 917.92, red block, orthorhombic, space group *Fdd*2, *a* = 12.2991(19), *b* = 13.340(2), *c* = 40.350(7) Å, *U* = 6620.3(18) Å³, *Z* = 8, *D_c* = 1.842 Mg m⁻³, μ(Cu-Kα) = 10.068 mm⁻¹, *T* = 123 K. Total 10929 reflections, 2564 unique, *R*_{int} = 0.030. Refinement of 2553 reflections (228 parameters) with *I* > 2σ (*I*) converged at final *R*₁ = 0.0170 (*R*₁ all data = 0.0171), *wR*₂ = 0.0405 (*wR*₂ all data = 0.0405), *gof* = 0.9244. CCDC 1515401.

Cyclic Voltammetry

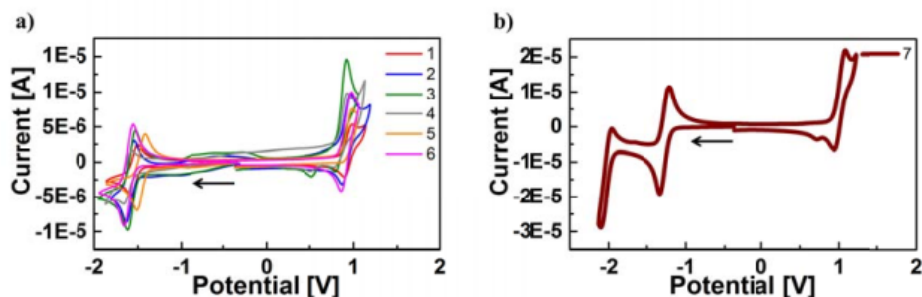


Figure S1. Cyclic voltammograms of complexes **1–6** (a) and **7** (b) with respect to Fc/Fc⁺, measured in CH₂Cl₂ solution; Pt working and counter electrodes, Ag pseudo-reference electrode, 0.1 M TBAPF₆ supporting electrolyte, scan rate = 0.1 V s⁻¹. The arrow indicates the initial scanning direction.

Photoluminescence data

Table S1. Detailed excited-state lifetime data of complexes **1–7** in de-aerated CH₂Cl₂ solution and as powder samples. τ_{ave} = average lifetime.

Complex	Solution ^{a,b}			Powder ^b		
	τ_{ave} [ns]	τ_1 [ns] (A_1)	τ_2 [ns] (A_2)	τ_{ave} [ns]	τ_1 [ns] (A_1)	τ_2 [ns] (A_2)
1	222	---	---	277	206 (6796)	397 (2094)
2	329	---	---	305	224 (5183)	370 (3953)
3	183	---	---	214	148 (5424)	266 (3743)
4	275	---	---	287	184 (5148)	346 (4752)
5	169	139 (6306)	274 (917)	185	109 (4892)	229 (4022)
6	166	143 (6297)	237 (1185)	236	113 (2466)	253 (7659)
7	126	---	---	565	340 (2834)	613 (7404)

^a Measured in de-aerated CH₂Cl₂ solution under an atmosphere of argon. ^b $\lambda_{\text{exc}} = 280$ nm. Biexponential fits were used for the excited state lifetime determination of all powder samples and solution samples of **5** and **6**, according to the equation $\tau_{\text{ave}} = \sum A_i \tau_i / \sum A_i$ (A_i = pre-exponential factor of the lifetime). Monoexponential fits were used for the remaining complexes (no τ_1 and τ_2 reported).

TD-DFT results

Table S2. Lowest triplet excited states (T_n) calculated at the TD-DFT B3LYP/(6-31G**+LANL2DZ) level for complexes **1** to **7** in CH_2Cl_2 solution. Vertical excitation energies (E), dominant monoexcitations with contributions (within parentheses) larger than 10%, nature of the monoexcitation, and description of the excited state are summarized. H and L denote HOMO and LUMO, respectively.

Complex	State	E (eV)	Monoexcitations	Nature	Description
1	T_1	2.17	H \rightarrow L (98)	$d_x(\text{Ir}) + \pi_{\text{C}^{\wedge}\text{N}} \rightarrow \pi_{\text{N}^{\wedge}\text{N}}^*$	$^3\text{MLCT}^{\beta}\text{LLCT}$
	T_2	2.50	H-2 \rightarrow L (31)	$d_x(\text{Ir}) + \pi_{\text{C}^{\wedge}\text{N}} \rightarrow \pi_{\text{N}^{\wedge}\text{N}}^*$	$^3\text{MLCT}^{\beta}\text{LLCT}$
			H-3 \rightarrow L (20) H-6 \rightarrow L (20)	$d_x(\text{Ir}) + \pi_{\text{C}^{\wedge}\text{N}} + \pi_{\text{N}^{\wedge}\text{N}} \rightarrow \pi_{\text{N}^{\wedge}\text{N}}^*$	$^3\text{MLCT}^{\beta}\text{LLCT}^{\beta}\text{LC}(\text{N}^{\wedge}\text{N})$ $^3\text{LC}(\text{N}^{\wedge}\text{N})$
T_3	2.75	H \rightarrow L+1 (65)	$d_x(\text{Ir}) + \pi_{\text{C}^{\wedge}\text{N}} \rightarrow \pi_{\text{C}^{\wedge}\text{N}}^*$	$^3\text{LC}(\text{C}^{\wedge}\text{N})^{\beta}\text{MLCT}$	
2	T_1	2.24	H \rightarrow L (98)	$d_x(\text{Ir}) + \pi_{\text{C}^{\wedge}\text{N}} \rightarrow \pi_{\text{N}^{\wedge}\text{N}}^*$	$^3\text{MLCT}^{\beta}\text{LLCT}$
	T_2	2.55	H-2 \rightarrow L (29)	$d_x(\text{Ir}) + \pi_{\text{C}^{\wedge}\text{N}} \rightarrow \pi_{\text{N}^{\wedge}\text{N}}^*$	$^3\text{MLCT}^{\beta}\text{LLCT}$
			H-3 \rightarrow L (20) H-6 \rightarrow L (22)	$d_x(\text{Ir}) + \pi_{\text{C}^{\wedge}\text{N}} + \pi_{\text{N}^{\wedge}\text{N}} \rightarrow \pi_{\text{N}^{\wedge}\text{N}}^*$	$^3\text{MLCT}^{\beta}\text{LLCT}^{\beta}\text{LC}(\text{N}^{\wedge}\text{N})$ $^3\text{LC}(\text{N}^{\wedge}\text{N})$
T_3	2.75	H \rightarrow L+1 (65)	$d_x(\text{Ir}) + \pi_{\text{C}^{\wedge}\text{N}} \rightarrow \pi_{\text{C}^{\wedge}\text{N}}^*$	$^3\text{LC}(\text{C}^{\wedge}\text{N})^{\beta}\text{MLCT}$	
3	T_1	2.22	H \rightarrow L (93)	$d_x(\text{Ir}) + \pi_{\text{C}^{\wedge}\text{N}} \rightarrow \pi_{\text{N}^{\wedge}\text{N}}^*$	$^3\text{MLCT}^{\beta}\text{LLCT}$
	T_2	2.57	H-3 \rightarrow L (43)	$d_x(\text{Ir}) + \pi_{\text{C}^{\wedge}\text{N}} + \pi_{\text{N}^{\wedge}\text{N}} \rightarrow \pi_{\text{N}^{\wedge}\text{N}}^*$	$^3\text{MLCT}^{\beta}\text{LLCT}^{\beta}\text{LC}(\text{N}^{\wedge}\text{N})$
			H-6 \rightarrow L (14)	$\pi_{\text{N}^{\wedge}\text{N}} \rightarrow \pi_{\text{N}^{\wedge}\text{N}}^*$	$^3\text{LC}(\text{N}^{\wedge}\text{N})$
T_3	2.72	H \rightarrow L+1 (57)	$d_x(\text{Ir}) + \pi_{\text{C}^{\wedge}\text{N}} \rightarrow \pi_{\text{C}^{\wedge}\text{N}}^*$	$^3\text{LC}(\text{C}^{\wedge}\text{N})^{\beta}\text{MLCT}$	
4	T_1	2.29	H \rightarrow L (91)	$d_x(\text{Ir}) + \pi_{\text{C}^{\wedge}\text{N}} \rightarrow \pi_{\text{N}^{\wedge}\text{N}}^*$	$^3\text{MLCT}^{\beta}\text{LLCT}$
	T_2	2.63	H-3 \rightarrow L (41)	$d_x(\text{Ir}) + \pi_{\text{C}^{\wedge}\text{N}} + \pi_{\text{N}^{\wedge}\text{N}} \rightarrow \pi_{\text{N}^{\wedge}\text{N}}^*$	$^3\text{MLCT}^{\beta}\text{LLCT}^{\beta}\text{LC}(\text{N}^{\wedge}\text{N})$
			H-6 \rightarrow L (14)	$\pi_{\text{N}^{\wedge}\text{N}} \rightarrow \pi_{\text{N}^{\wedge}\text{N}}^*$	$^3\text{LC}(\text{N}^{\wedge}\text{N})$
T_3	2.72	H \rightarrow L+1 (58)	$d_x(\text{Ir}) + \pi_{\text{C}^{\wedge}\text{N}} \rightarrow \pi_{\text{C}^{\wedge}\text{N}}^*$	$^3\text{LC}(\text{C}^{\wedge}\text{N})^{\beta}\text{MLCT}$	
5	T_1	2.10	H \rightarrow L (95)	$d_x(\text{Ir}) + \pi_{\text{C}^{\wedge}\text{N}} \rightarrow \pi_{\text{N}^{\wedge}\text{N}}^*$	$^3\text{MLCT}^{\beta}\text{LLCT}$
	T_2	2.50	H-2 \rightarrow L (25)	$d_x(\text{Ir}) + \pi_{\text{C}^{\wedge}\text{N}} \rightarrow \pi_{\text{N}^{\wedge}\text{N}}^*$	$^3\text{MLCT}^{\beta}\text{LLCT}$
			H-3 \rightarrow L (36) H-9 \rightarrow L (13)	$d_x(\text{Ir}) + \pi_{\text{C}^{\wedge}\text{N}} + \pi_{\text{N}^{\wedge}\text{N}} \rightarrow \pi_{\text{N}^{\wedge}\text{N}}^*$	$^3\text{MLCT}^{\beta}\text{LLCT}^{\beta}\text{LC}(\text{N}^{\wedge}\text{N})$ $^3\text{LC}(\text{N}^{\wedge}\text{N})$
T_3	2.69	H \rightarrow L+1 (41)	$d_x(\text{Ir}) + \pi_{\text{C}^{\wedge}\text{N}} \rightarrow \pi_{\text{C}^{\wedge}\text{N}}^*$	$^3\text{LC}(\text{C}^{\wedge}\text{N})^{\beta}\text{MLCT}$	
		H \rightarrow L+2 (26)	$d_x(\text{Ir}) + \pi_{\text{C}^{\wedge}\text{N}} \rightarrow \pi_{\text{C}^{\wedge}\text{N}}^*$	$^3\text{LC}(\text{C}^{\wedge}\text{N})^{\beta}\text{MLCT}$	
6	T_1	2.22	H \rightarrow L (98)	$d_x(\text{Ir}) + \pi_{\text{C}^{\wedge}\text{N}} \rightarrow \pi_{\text{N}^{\wedge}\text{N}}^*$	$^3\text{MLCT}^{\beta}\text{LLCT}$
	T_2	2.58	H-2 \rightarrow L (34)	$d_x(\text{Ir}) + \pi_{\text{C}^{\wedge}\text{N}} \rightarrow \pi_{\text{N}^{\wedge}\text{N}}^*$	$^3\text{MLCT}^{\beta}\text{LLCT}$
			H-3 \rightarrow L (23) H-6 \rightarrow L (19)	$d_x(\text{Ir}) + \pi_{\text{C}^{\wedge}\text{N}} + \pi_{\text{N}^{\wedge}\text{N}} \rightarrow \pi_{\text{N}^{\wedge}\text{N}}^*$	$^3\text{MLCT}^{\beta}\text{LLCT}^{\beta}\text{LC}(\text{N}^{\wedge}\text{N})$ $^3\text{LC}(\text{N}^{\wedge}\text{N})$
T_3	2.75	H \rightarrow L+1 (67)	$d_x(\text{Ir}) + \pi_{\text{C}^{\wedge}\text{N}} \rightarrow \pi_{\text{C}^{\wedge}\text{N}}^*$	$^3\text{LC}(\text{C}^{\wedge}\text{N})^{\beta}\text{MLCT}$	
7	T_1	1.91	H \rightarrow L (96)	$d_x(\text{Ir}) + \pi_{\text{C}^{\wedge}\text{N}} \rightarrow \pi_{\text{N}^{\wedge}\text{N}}^*$	$^3\text{MLCT}^{\beta}\text{LLCT}$
	T_2	2.18	H-2 \rightarrow L (50)	$d_x(\text{Ir}) + \pi_{\text{C}^{\wedge}\text{N}} + \pi_{\text{N}^{\wedge}\text{N}} \rightarrow \pi_{\text{N}^{\wedge}\text{N}}^*$	$^3\text{MLCT}^{\beta}\text{LLCT}^{\beta}\text{LC}(\text{N}^{\wedge}\text{N})$
			H-4 \rightarrow L (23) H-6 \rightarrow L (16)	$d_x(\text{Ir}) + \pi_{\text{C}^{\wedge}\text{N}} + \pi_{\text{N}^{\wedge}\text{N}} \rightarrow \pi_{\text{N}^{\wedge}\text{N}}^*$	$^3\text{MLCT}^{\beta}\text{LLCT}^{\beta}\text{LC}(\text{N}^{\wedge}\text{N})$ $^3\text{LC}(\text{N}^{\wedge}\text{N})$
T_3	2.48	H-3 \rightarrow L (65)	$d_x(\text{Ir}) + \pi_{\text{C}^{\wedge}\text{N}} + p_{\text{d}(s)} \rightarrow \pi_{\text{N}^{\wedge}\text{N}}^*$	$^3\text{MLCT}^{\beta}\text{LLCT}^{\beta}\text{LC}(\text{N}^{\wedge}\text{N})$	

Electroluminescence data

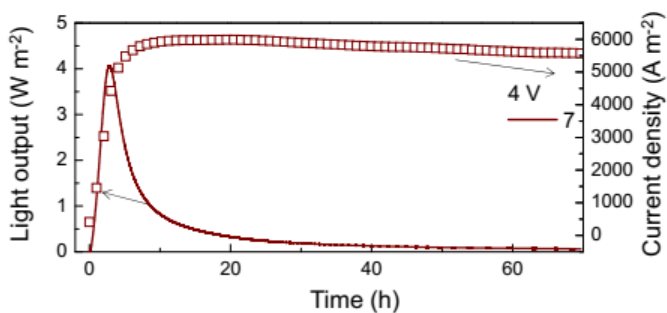


Figure S2. Irradiance and current density *versus* time for LEC 7 operated under a constant-voltage driving of 4 V.

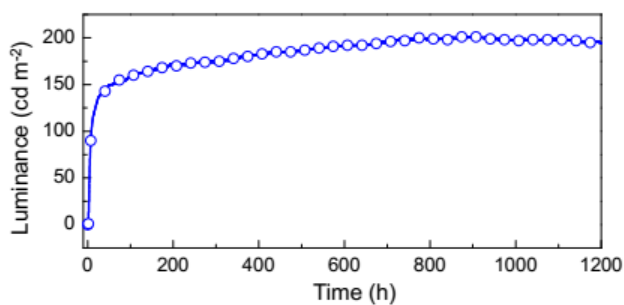


Figure S3. Time-dependent luminance for LEC 2 up to 1200 h operated under an average pulsed current density of $100 \text{ A} \cdot \text{m}^{-2}$ (1000 Hz, 50% duty cycle, block wave).

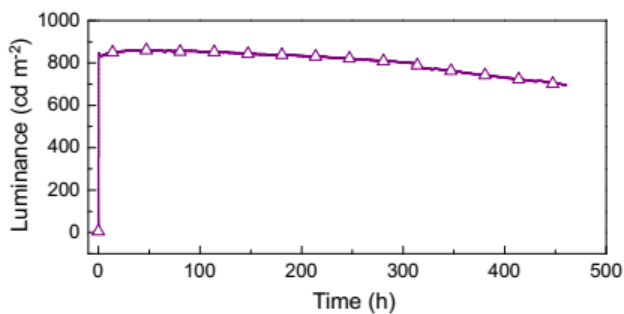


Figure S4. Time-dependent luminance for LEC 1 up to 450 h operated under an average pulsed current density of $700 \text{ A} \cdot \text{m}^{-2}$ (1000 Hz, 50% duty cycle, block wave).

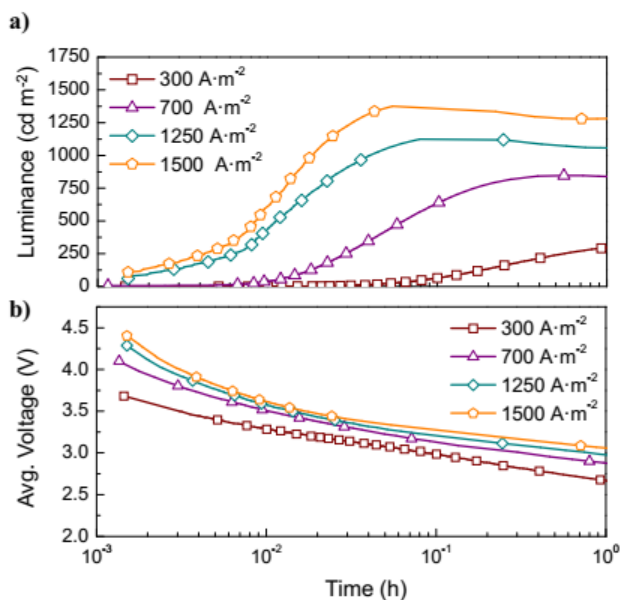


Figure S5. Time-dependent luminance (a) and average voltage (b) for LEC 1 operated under different average pulsed current densities of 300, 700, 1250, and 1500 A·m⁻² (1000 Hz, 50% duty cycle, block wave).

References

- (1) Vandromme, L.; Reißig, H.-U.; Gröper, S.; Rabe, J. P. *Eur. J. Org. Chem.* **2008**, 2049.
- (2) Seiple, I. B.; Su, S.; Rodriguez, R. A.; Gianatassio, R.; Fujiwara, Y.; Sobel, A. L.; Baran, P. S. *J. Am. Chem. Soc.* **2010**, *132*, 13194.
- (3) Do, H.-Q.; Kashif Khan, R. M.; Daugulis, O. *J. Am. Chem. Soc.* **2008**, *130*, 15185.
- (4) Rai, C.; Braunwarth, J. B. *J. Org. Chem.* **1961**, *26*, 3434.
- (5) Zhu, M.; Fujita, K.; Yamaguchi, R. *Chem. Commun.* **2011**, *47*, 12876.
- (6) Peters, M.; Breinbauer, R. *Tetrahedron Lett.* **2010**, *51*, 6622.
- (7) Carlson, L. J.; Welby, J.; Zebrowski, K. A.; Wilk, M. M.; Giroux, R.; Ciancio, N.; Tanski, J. M.; Bradley, A.; Tyler, L. A. *Inorg. Chim. Acta* **2011**, *365*, 159.
- (8) Ojwach, S. O.; Westman, G.; Darkwa, J. *Polyhedron* **2007**, *26*, 5544.
- (9) Wu, M.; Hu, X.; Liu, J.; Liao, Y.; Deng, G.-J. *Org. Lett.* **2012**, *14*, 2722.
- (10) Garces, F. O.; King, K. A.; Watts, R. J. *Inorg. Chem.* **1988**, *27*, 3464.
- (11) Sprouse, S.; King, K. A.; Spellane, P. J.; Watts, R. J. *J. Am. Chem. Soc.* **1984**, *106*, 6647.
- (12) Rachford, A. A.; Ziessel, R.; Bura, T.; Retailleau, P.; Castellano, F. N. *Inorg. Chem.* **2010**, *49*, 3730.
- (13) Speck, A. L. *Acta Crystallogr. Sect. D* **2009**, *65*, 148.

Cite this: *RSC Adv.*, 2017, 7, 31833

Simple design to achieve red-to-near-infrared emissive cationic Ir(III) emitters and their use in light emitting electrochemical cells†

 Amlan K. Pal,^a David B. Cordes,^b Alexandra M. Z. Slawin,^b Cristina Momblona,^c Antonio Pertegás,^c Enrique Ortí,^b Henk J. Bolink^{b,*c} and Eli Zysman-Colman^{b,*a}
Received 6th June 2017
Accepted 13th June 2017

DOI: 10.1039/c7ra06347d

rsc.li/rsc-advances

Two cationic Ir(III) complexes bearing 2-phenylpyridinato cyclometalating ligands and bithiazole-type ancillary ligands have been synthesized and optoelectronically characterised. These emitters exhibit unusually deep red-to-near-infrared emission at room temperature, thereby rendering them as attractive emitters in solution-processed light emitting electrochemical cell (LEEC) electroluminescent devices.

Near-infrared- (NIR-) emitting compounds are an important subclass of luminescent materials due to their potential applications in sensors, night-vision displays, optical cosmetology, telecommunication and photodynamic therapies.¹ The most studied NIR-dyes in these contexts comprise semiconductor quantum dots,² lanthanoid complexes,³ organic small-molecule dyes⁴ and transition metal complexes.^{1a,b,5} With rich photo-physical behaviour, the NIR-emitting transition metal complexes are attractive candidates for solid-state lighting (SSL), as, with access to the triplet state, 100% of the electrically generated excitons can be harvested. Iridium complexes are well known phosphors for SSL due to their relatively short excited-state lifetimes, high photoluminescence quantum yields (Φ_{PL}) and remarkable colour tunability, particularly across the visible spectrum.⁶ While stable green and yellow emissive iridium complexes are relatively well documented and have been successfully incorporated into electroluminescent (EL) devices, there is a dearth of examples of red-to-NIR emissive iridium complexes.^{1a,b,7} Cationic Ir complexes of the form $[\text{Ir}(\text{C}^{\wedge}\text{N})_2(\text{N}^{\wedge}\text{N})]^+$ (where $\text{C}^{\wedge}\text{N}$ = cyclometalating ligand and $\text{N}^{\wedge}\text{N}$ = ancillary ligand) are the most widely studied class of emitters for LEECs.^{1b} In these charged complexes, the highest occupied molecular orbital (HOMO) typically resides on both the $\text{C}^{\wedge}\text{N}$ ligand and metal, while the lowest unoccupied molecular orbital (LUMO) resides on the $\text{N}^{\wedge}\text{N}$ ligand.⁸ The

common strategies of achieving red-to-NIR emission ($\lambda_{\text{em}} > 620$ nm) include: (a) destabilisation of the HOMO through introduction of electron-donating substituents^{7a,9} onto the $\text{C}^{\wedge}\text{N}$ ligands and/or stabilisation of the $\text{N}^{\wedge}\text{N}$ ligand-based LUMO by incorporation of electron-withdrawing substituents,¹⁰ and (b) introduction of π -conjugated systems either on one or both of the $\text{C}^{\wedge}\text{N}$ or $\text{N}^{\wedge}\text{N}$ ligands¹¹ thereby decreasing the HOMO–LUMO gap. Based on these principles, several charged red-to-NIR emitting Ir(III) complexes have been reported, a representative selection of which are shown in Chart 1 (sections a and b).^{7a,9}

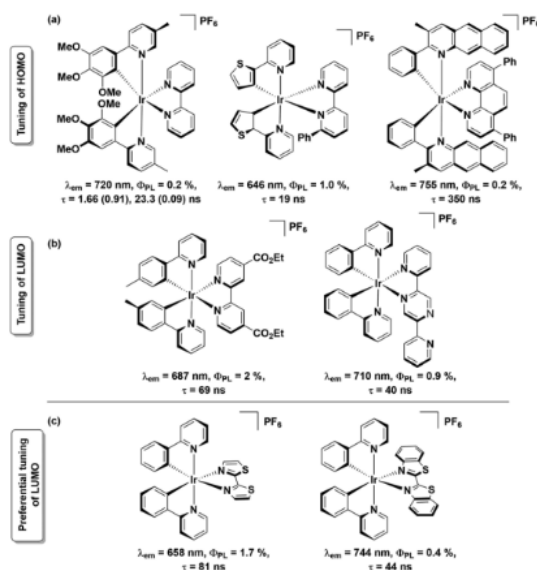


Chart 1 Strategies of achieving red-to-NIR emissive cationic Ir(III) complexes by (a) destabilisation of HOMO (top row), (b) stabilisation of LUMO (middle row). Complexes in current study are shown in (c) bottom row.

^aOrganic Semiconductor Centre, EaStCHEM School of Chemistry, University of St Andrews, St Andrews, Fife KY16 9ST, UK. E-mail: eli.zysman-colman@st-andrews.ac.uk; Web: <http://www.zysman-colman.com>

^bEaStCHEM School of Chemistry, University of St Andrews, St Andrews, Fife KY16 9ST, UK

^cInstituto de Ciencia Molecular, Universidad de Valencia, C/Catedrático José Beltrán 2, 46100 Paterna, Spain

† Electronic supplementary information (ESI) available: Synthetic, crystallographic, optoelectronic and DFT studies. CCDC 1538393 and 1538394. For ESI and crystallographic data in CIF or other electronic format see DOI: 10.1039/c7ra06347d

Of the strategies outlined above, that involving LUMO stabilization is the most underexplored, despite its potential to produce red-to-NIR emissive cationic Ir(III) complexes.^{10,11} In this context, herein, we report the syntheses of two red-to-NIR cationic Ir(III) complexes, [Ir(ppy)₂(L1)]⁺[PF₆]⁻, **1**, and [Ir(ppy)₂(L2)]⁺[PF₆]⁻, **2**, possessing remarkably simple ligand architectures. These complexes bear 2-phenylpyridinato-C²,N' as the C[∧]N ligand and strongly π-accepting ligands 2,2'-bithiazole (**L1**) and 2,2'-bibenzo[d]thiazole (**L2**) as the N[∧]N ligands (Chart 1c). Coincident with the present study, complex **2** was recently reported by Ertl *et al.*,¹² though no Light Emitting Electrochemical Cell (LEEC) device data was reported. Herein, the optoelectronic properties of complexes **1** and **2** are reported along with the LEEC device performance.

Ligands **L1** and **L2** were synthesized by Pd-catalysed homocoupling of 2-bromothiazole or 2-bromobenzothiazole, respectively, in moderate yields (41% for **L1** and 51% for **L2**, ESI[†]).¹³ Complexes **1** and **2** were obtained by cleavage of the [Ir(ppy)₂Cl]₂ dimer in the presence of 2.3 equiv. of the corresponding ancillary ligands followed by an anion metathesis with aqueous NH₄PF₆ in 91% and 95%, respectively (ESI[†]). Ligands **L1** and **L2** and complexes **1** and **2** were characterised by ¹H and ¹³C NMR spectroscopy, HRMS, melting point determination and elemental analyses. The ¹H and ¹³C NMR spectra confirmed the inherent C₂ symmetry present in both **1** and **2** (Fig. S1–S4, ESI[†]). Single crystal XRD studies of **1** and **2** corroborated the microanalysis and the geometry of the complexes (Fig. S5, Tables S1 and S2, ESI[†]).

In both crystal structures, the coordinatively saturated Ir(III) ions occupy a distorted octahedral geometry. The C[∧]N carbon atoms are mutually *cis* disposed, similar to the solid-state structure of [Ir(ppy)₂(bpy)]⁺, **R1** (where bpy = 2,2'-bipyridine).¹⁴ The ancillary ligands coordinate in a bidentate N',N'-mode through the hard N-donors instead of the soft S-donors. The Ir–C[∧]N bond distances [ranging from 2.003(7) to 2.007(6) Å in **1** and 2.009(4) to 2.009(5) Å in **2**] are similar to those observed in **R1** [ranging from 2.004(4) to 2.025(4) Å]. The Ir–N[∧]N bond distances are likewise similar across the three complexes [ranging from 2.046(5) to 2.048(5) Å in **1**, 2.049(4) to 2.058(4) Å in **2** and 2.042(3) to 2.048(3) Å in **R1**]. The Ir–N[∧]N length [2.148(6) to 2.149(6) Å in **1** and 2.180(4) to 2.195(4) Å in **2**] resemble closely those in **R1** [2.129(3) to 2.137(3) Å in **2**].

The electrochemical properties of **1** and **2** were monitored by cyclic- (CV) and differential pulse- (DPV) voltammetry and the CV and DPV traces in MeCN are shown in Fig. S6 (ESI[†]). The detailed CV data *vs.* SCE (E_c/E_a = 0.38 V in MeCN)¹⁵ are

summarized in Table S3 (ESI[†]) while only first redox potentials are listed in Table 1. In the anodic scan, complexes **1** and **2** exhibit quasi-reversible mono-electronic oxidation processes at 1.24 V and 1.37 V, respectively. These oxidation processes are assigned to the Ir(III)/(IV) redox couple with contributions from the C[∧]N ligands, assignments supported by DFT calculations (Fig. S7[†]). While the oxidation potential of complex **1** (E_{1/2}^{OX} = 1.24 V) is similar to that of **R1** (E_{1/2}^{OX} = 1.27 V),¹⁶ that of complex **2** (E_{1/2}^{OX} = 1.37 V) is anodically shifted by 100 mV compared to **R1**, which aligns with the stabilized nature of the calculated HOMO of **2** (E_{HOMO} = -5.80 eV) compared to that found in **1** (E_{HOMO} = -5.58 eV) and **R1** (E_{HOMO} = -5.56 eV). The more positive oxidation potential accounted for complex **2** is probably due to the modulation of the electron density of the Ir(III) ion by **L2** as the latter is a better π-acceptor than **L1** or 2,2'-bpy and thereby rendering the Ir(III) centre more electron deficient compared to that in complex **1**.

Upon scanning to negative potential, complex **1** exhibits two quasi-reversible one-electron reduction processes up to -2 V, while three other irreversible and quasi-reversible reduction waves could also be observed at higher negative potentials. Complex **2**, on the other hand, displayed four mono-electronic quasi-reversible waves up to -3 V (Table S3 and Fig. S5, ESI[†]). DFT calculations show that the calculated LUMOs of **1** and **2** are localized on the N[∧]N ligand and therefore the first reduction processes are ascribed to radical anion formation on the ancillary ligand. The first reduction potentials for **1** and **2** (E_{1/2}^{Red} = -1.15 V for **1** and -0.82 V for **2**) are anodically shifted by 230 mV and 560 mV, respectively, compared to that for **R1**, demonstrating the significantly stronger π-accepting nature of ligands **L1** and **L2** compared to bpy. The CV data mirrors the DFT results, which show significant LUMO stabilization from **R1** (E_{LUMO} = -2.31 eV) to **1** (E_{LUMO} = -2.76 eV) to **2** (E_{LUMO} = -3.07 eV). The trend in the calculated decreasing HOMO–LUMO gap from **R1** (3.25 eV) to **1** (2.82 eV) to **2** (2.73 eV) is in good agreement to the decreasing redox gap observed for **R1** (2.65 V) to **1** (2.38 V) to **2** (2.19 V). The second quasi-reversible and third irreversible reductions (Table S3, ESI[†]) of complex **1** could be ascribed to the reductions of the pyridine moiety of the C[∧]N ligand based on the coarse approximation that both the LUMO+1 and LUMO+2 reside on the C[∧]N ligand as predicted by DFT calculations (Fig. S7, ESI[†]) and similar assignments are also valid for the second and third quasi-reversible reductions of complex **2** (Table S3, ESI[†]).

Table 1 Optoelectronic properties of **1**, **2** and **R1** in degassed MeCN^a

	λ _{em} /nm	Φ _{PL} /%	τ _e /μs	k _t /10 ⁵ s ⁻¹	k _{nr} /10 ⁵ s ⁻¹	E _{1/2} ^{OX} /V (ΔE _p , mV)	E _{1/2} ^{Red} /V (ΔE _p , mV)
1	658	1.72	0.081	0.21	123.2	1.24 (110)	-1.15 (74)
2	744	0.35	0.044	0.08	227.2	1.37 (169)	-0.82 (88)
R1 ^b	602	9.29	0.275	3.4	33	1.27	-1.38

^a Φ_{PL} measured at 298 K using [Ru(bpy)₃]Cl₂ (Φ_{PL} = 4% in H₂O, aerated) as the reference.¹⁹ k_t = Φ_{PL}/τ_e and k_{nr} = (1 - Φ_{PL})/τ_e. CV values are *vs.* SCE.¹⁵ ΔE_p = |E_{pa} - E_{pc}|, where E_{pa} = anodic peak potential and E_{pc} = cathodic peak potential; E_{1/2} = (E_{pa} + E_{pc})/2. A silver wire was used as the pseudoreference electrode; a glassy-carbon electrode was used for the working electrode and a Pt electrode was used as the counter electrode.

^b Φ_{PL} measured at 298 K using [Ru(bpy)₃](PF₆)₂ (Φ_{PL} = 9.5% in MeCN) as the reference.²⁰

The UV-vis absorption spectra of complexes **1** and **2** were obtained in dry MeCN and the values are tabulated in Table S4.† Overlays of experimentally observed and theoretically predicted absorption data by TD-DFT are shown in Fig. S8 (ESI†). The UV region is dominated by spin allowed $^1\pi \rightarrow \pi^*$ transitions in both ligand moieties centered around 240–280 nm (Tables S4 and S5, ESI†). For complex **2**, singlet ligand-centered $\pi \rightarrow \pi^*$ transitions (1LC) extend up to 407 nm, as predicted by TD-DFT, due to increased conjugation in **L2** (Table S5†). The set of absorption bands clustered around 315 nm in **1** are significantly red-shifted in **2** at ca. 363 nm. The character of these band in **1** is an admixture of singlet metal-to-ligand charge transfer (1MLCT) from $Ir(d\pi) \rightarrow ppy(\pi^*)$ and ppy -based 1LC transitions while in **2** the nature of these transitions is more CT in character and comprises 1MLCT from $Ir(d\pi) \rightarrow L2(\pi^*)$ and singlet ligand-to-ligand charge transfer (1LLCT) from $ppy(\pi) \rightarrow L2(\pi^*)$, as suggested by TD-DFT. The greater CT character coupled with the lower lying LUMO is responsible for this large bathochromic shift. The lowest energy absorption maxima for **1** and **2** appear at 500 nm and 599 nm, respectively. These bands are assigned as a mixture of spin-allowed and spin-forbidden 1MLCT / 3MLCT and ligand-to-ligand charge transfer (1LLCT / 3LLCT) transitions. These hypochromic bands at lower energy are the result of poor spatial overlap between the HOMO and LUMO and are typical for cationic Ir complexes.^{6,17} Concomitant to the larger calculated HOMO–LUMO gap for **1** ($\Delta E = 2.82$ eV) than **2** ($\Delta E = 2.73$ eV) (Fig. S7†), the absorption onset of **2** is also red-shifted by 99 nm (3.31×10^3 cm⁻¹) compared to that of **1**. The UV-vis absorption spectrum of complex **2** in CH₂Cl₂ solution exhibits intense absorption bands extending into the visible region (around 450 nm), as observed by Ertl *et al.*¹² The observed red-shift of 149 nm of the lowest energy transition of complex **2** in comparison to the study of Ertl *et al.* is presumably because of the solvent polarity where the MeCN used in this study stabilises both Frontier MOs, perhaps more pronounced for the LUMO. In comparison to **R1** (lowest-energy $\lambda_{max}^{abs} = 420$ nm),¹⁶ both complexes show significantly red-shifted absorption spectra.

The steady-state emission spectra of **1** and **2** were recorded in degassed MeCN at 298 K and are shown in Fig. S9 (ESI†). The photophysical data are summarised in Table 1. The emission profiles are broad and featureless, indicative of mixed 3CT emission, as also observed by Ertl *et al.*¹² The spin density distribution of the excited-state corroborates this assignment (Fig. S9 and S10†). The emission maximum ($\lambda_{max}^{em} = 744$ nm) of complex **2** is red-shifted by 86 nm (1.76×10^3 cm⁻¹) compared to that of complex **1** ($\lambda_{max}^{em} = 658$ nm). The DFT predicted emission maxima for **1** ($\lambda_{DFT}^{em} = 712$ nm) and **2** ($\lambda_{DFT}^{em} = 761$ nm) also follow the observed trend in emission maxima of complexes **1** and **2**, with relative errors of 7.6% and 2.2%, respectively. The emission maxima of **1** and **2** are significantly red-shifted compared to that of **R1** ($\lambda_{max}^{em} = 602$ nm).¹⁶ In comparison to the observed emission maximum at 686 nm in CH₂Cl₂ solution of complex **2** by Ertl *et al.*,¹² the same for complex **2** is red-shifted by 58 nm in our study, which is because of the effect of solvent polarity in emission.¹⁸ With the exception of the cationic Ir(III) complex bearing 3-methyl-2-phenylbenzo[*g*]

quinolinato C^N ligands reported by Tao *et al.*^{7a} (Chart 1a), complex **2** is, to the best of our knowledge, the most red-shifted emitting cationic Ir(III) complex.^{7a,9–11} The Φ_{PL} in degassed MeCN of **1** and **2** are 1.7% and 0.4%, respectively (Table 1). The corresponding excited-state lifetimes, τ_e , are very short at 81 and 44 ns, for **1** and **2**, respectively. The lower Φ_{PL} and shorter τ_e values compared to **R1** are a stark consequence of energy-gap law as evidence by the associated ~4-fold (for **1**) and 7-fold (for **2**) increase in the non-radiative decay rate constant, k_{nr} , compared to that in **R1**. The observed Φ_{PL} and τ_e values of complex **2** in CH₂Cl₂ solution, reported by Ertl *et al.*, are 3.6% and 126 ns, respectively.¹² The lower Φ_{PL} and τ_e values in our study compared to the study of Ertl *et al.* is again due to a consequence of energy-gap law for a NIR emitter like **2**.

The emission maxima of the thin films of **1** and **2** mixed with 1-butyl-3-methylimidazolium hexafluorophosphate, [Bmim][PF₆] are 658 and 707 nm, respectively ($\lambda_{exc} = 320$ nm). The thin film Φ_{PL} values of 14% and 5% for **1** and **2**, respectively, are enhanced compared to solution values. The PL spectra and photophysical data of the films are displayed in Fig. S11 and Table S9 (ESI†).

Light emitting electrochemical cells (LEECs) were prepared and the electroluminescence properties of the complexes were evaluated. The preparation of LEECs were done by spin-coating on pre-cleaned ITO substrates, which were first coated with a 80 nm thick film of PEDOT:PSS. The active layer was then deposited from dichloromethane solution. Recently, a first attempt was done for the LEEC fabrication with complex **2**.¹² At that time, the bad film morphology led to poor LEEC performance. In this work, a different solvent was used to improve the film morphology of the emissive layer. Here, the complex was dissolved in dichloromethane, which led to good films completely covering the substrates after spin-coating. After the active layer deposition, the top electrode (70 nm thick film of aluminium) was thermally evaporated. The fabricated LEECs were measured using a pulsed current driving (1 kHz, 50% duty cycle and block wave). The current densities applied to the LEECs were 800 and 1600 A m⁻², which corresponds to an average current density of 400 and 800 A m⁻², respectively, as a function of the duty cycle. For simplicity, the LEECs fabricated with **1** and **2** are called LEEC-1 and LEEC-2.

The luminance for LEEC-1 or light output for LEEC-2 and average voltage *versus* time measured under average current density of 400 A m⁻² is depicted in Fig. 1 while the measurements at 800 A m⁻² are shown in Fig. S12 (ESI†). In the inset of Fig. 1, the electroluminescence (EL) spectrum of each LEEC is shown and all the device data are summarized in Table S11 for LEEC-1 and Table S12 for LEEC-2, respectively (ESI).† LEEC-1 exhibits a red electroluminescence centred at 661 nm while LEEC-2 shows a near-infrared emission at 705 nm, in both cases, in good agreement with the PL spectra registered in thin film (658 nm for **1** and 707 nm for **2**). The applied voltage rapidly diminishes due to the ionic motion over operation, which decreases the electrical resistance. As this characteristic is directly related with the ionic mobility, generally, the time to reach the maximum light emission (t_{max}) in LEECs varies from seconds to hours. Despite the similarity structure of complexes

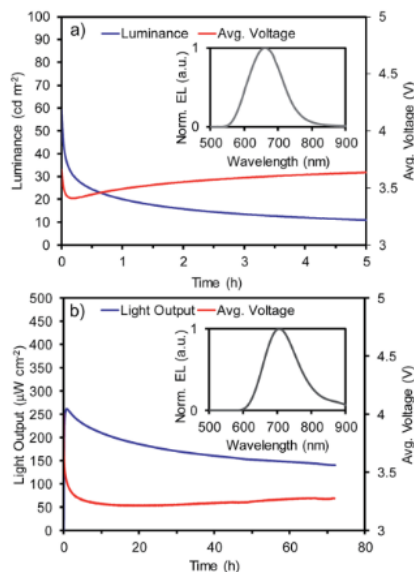


Fig. 1 Device performance versus time and electroluminescence (inset) for (a) LEEC-1 and (b) LEEC-2 under a pulsed current of 400 A m⁻² (average current density), 1 kHz and 50% of duty cycle.

1 and **2** as well as the presence of the same counter-anion (PF₆), t_{max} is significantly shorter for LEEC-1 (<5 seconds) than LEEC-2 (0.8 and 4.3 hours for 400 and 800 A m⁻², respectively). Moreover, differences are observed between LEEC-1 and LEEC-2 when comparing the device lifetime, usually defined as the time to reach one-half of the maximum light emission ($t_{1/2}$). While LEEC-1 shows a $t_{1/2}$ of 0.3 hours, LEEC-2 was significantly more stable at above 80 hours. The differences observed seem to be related to the presence of the annulated benzenes in the ancillary ligand. A possible explanation is related to the larger cation in complex **2**, which reduces the ionic movement in the active layer during operation. LEEC-2 exhibits an improved efficiency compared to that based on **1**. While LEEC-1 achieved an external quantum efficiency (EQE) of 0.23% and 0.13%, LEEC-2 reached 0.37% and 0.30% at 400 and 800 A m⁻², respectively. Hence, the efficiency of LEEC-1 is more strongly affected by increasing the current density than LEEC-2. Thus, the slower ionic movement in LEEC-2 leads to more balanced carrier. To the best of our knowledge, only a few examples of near-infrared emitting LEECs have been reported, generally with low EQE (EQE < 0.1%)⁶ due to the energy gap law. Recently, new examples have overcome the EQE of 1%,^{5d,21} but none of these is based on a cationic iridium complex as the emitter. Considering the low emission quantum yield of complex **2** (0.4%) and the high current density applied (up to 800 A m⁻²) the achieved efficiencies for LEEC-2 are very impressive and close to the theoretical achievable one assuming a typical light outcoupling of 20%.

In summary, we demonstrate dramatic red-shifted emission for both **1** and **2** as a function of the use of strongly π -accepting bithiazole-type ancillary ligands compared to the archetype

complex **R1**. Notably, to the best of our knowledge, complex **2** displays the most red-shifted emission maximum for a cationic iridium complex, especially considering the simplicity of the ligand structure and synthesis. LEEC devices show deep red and NIR emission using **1** and **2**, respectively. LEEC-2 shows improved efficiency compared to LEEC-1 and represents the first example of a NIR LEEC employing a cationic iridium complex emitter. Current efforts are focussed on pushing the emission even further into the near-IR through addition of strongly conjugated C^N ligands.

Acknowledgements

We are grateful to the University of St Andrews and EPSRC for financial support from grant EP/M02105X/1. We thank the EPSRC UK National Mass Spectrometry Facility at Swansea University for analytical services. We thank Umicore AG for the gift of IrCl₃. We also thank the Spanish Ministry of Economy and Competitiveness (MINECO) via the Unidad de Excelencia María de Maeztu MDM-2015-0538, MAT2014-55200, CTQ2015-71154-P and PCIN-2015-255, the Generalitat Valenciana (Prometeo/2016/135) and European FEDER funds (CTQ2015-71154-P). C. M. thanks MINECO for her predoctoral contract.

References

- (a) A. Barbieri, E. Bandini, F. Monti, V. K. Praveen and N. Armaroli, *Top. Curr. Chem.*, 2016, **374**, 47; (b) A. F. Henwood and E. Zysman-Colman, *Chem. Commun.*, 2017, **53**, 807–826; (c) J. Yello, S. A. Perez, G. Yello, J. Zajac, A. Donaire, G. Viguera, V. Novohradsky, C. Janiak, V. Brabec and J. Ruiz, *Chem. Commun.*, 2016, **52**, 14165–14168; (d) G. Qian and Z. Y. Wang, *Chem.-Asian J.*, 2010, **5**, 1006–1029.
- C. Wang, X. Gao and X. Su, *Anal. Bioanal. Chem.*, 2010, **397**, 1397–1415.
- S. V. Eliseeva and J. C. Bunzli, *Chem. Soc. Rev.*, 2010, **39**, 189–227.
- (a) E. Zysman-Colman, S. S. Ghosh, G. Xie, S. Varghese, M. Chowdhury, N. Sharma, D. B. Cordes, A. M. Z. Slawin and I. D. W. Samuel, *ACS Appl. Mater. Interfaces*, 2016, **8**, 9247–9253; (b) J. O. Escobedo, O. Rusin, S. Lim and R. M. Strongin, *Curr. Opin. Chem. Biol.*, 2010, **14**, 64–70; (c) O. A. Melville, B. H. Lessard and T. P. Bender, *ACS Appl. Mater. Interfaces*, 2015, **7**, 13105–13118.
- (a) A. K. Pal, S. Serroni, N. Zaccheroni, S. Campagna and G. S. Hanan, *Chem. Sci.*, 2014, **5**, 4800–4811; (b) H. Xiang, J. Cheng, X. Ma, X. Zhou and J. J. Chruma, *Chem. Soc. Rev.*, 2013, **42**, 6128–6185; (c) D. A. Ross, P. A. Scattergood, A. Babaei, A. Pertegas, H. J. Bolink and P. I. Elliott, *Dalton Trans.*, 2016, **45**, 7748–7757; (d) J. H. Hsu and H. C. Su, *Phys. Chem. Chem. Phys.*, 2016, **18**, 5034–5039; (e) B. N. Bideh, C. Roldan-Carmona, H. Shahroosvand and M. K. Nazeeruddin, *J. Mater. Chem. C*, 2016, **4**, 9674–9679.
- A. F. Henwood and E. Zysman-Colman, *Top. Curr. Chem.*, 2016, **374**, 36.

- 7 (a) R. Tao, J. Qiao, G. Zhang, L. Duan, L. Wang and Y. Qiu, *J. Phys. Chem. C*, 2012, **116**, 11658–11664; (b) D. Ma, T. Tsuboi, Y. Qiu and L. Duan, *Adv. Mater.*, 2017, **29**, 1603253.
- 8 The reported complex is $[(ppy-F_2)_2Ir(dtBubpy)]^+$, where $ppy-F_2$ is 2,4-difluorophenylpyridinato. H. J. Bolink, E. Coronado, R. n. D. Costa, N. Lardiés and E. Orti, *Inorg. Chem.*, 2008, **47**, 9149–9151.
- 9 (a) K. Hasan, A. K. Bansal, I. D. W. Samuel, C. Roldán-Carmona, H. J. Bolink and E. Zysman-Colman, *Sci. Rep.*, 2015, **5**, 12325; (b) A. M. Bünzli, H. J. Bolink, E. C. Constable, C. E. Housecroft, J. M. Junquera-Hernandez, M. Neuburger, E. Orti, A. Pertegás, J. J. Serrano-Perez, D. Tordera and J. A. Zampese, *Dalton Trans.*, 2014, **43**, 738–750.
- 10 (a) L. Donato, C. E. McCusker, F. N. Castellano and E. Zysman-Colman, *Inorg. Chem.*, 2013, **52**, 8495–8504; (b) J. L. Rodríguez-Redondo, R. D. Costa, E. Orti, A. Sastre-Santos, H. J. Bolink and F. Fernandez-Lazaro, *Dalton Trans.*, 2009, 9787–9793; (c) D. Ma, L. Duan and Y. Qiu, *J. Mater. Chem. C*, 2016, **4**, 5051–5058.
- 11 (a) Y. Li, N. Dandu, R. Liu, Z. Li, S. Kilina and W. Sun, *J. Phys. Chem. C*, 2014, **118**, 6372–6384; (b) A. M. Bünzli, E. C. Constable, C. E. Housecroft, A. Prescimone, J. A. Zampese, G. Longo, L. Gil-Escrig, A. Pertegás, E. Orti and H. J. Bolink, *Chem. Sci.*, 2015, **6**, 2843–2852; (c) X. Zhu, L. Lystrom, S. Kilina and W. Sun, *Inorg. Chem.*, 2016, **55**, 11908–11919.
- 12 C. D. Ertl, C. Momblona, A. Pertegás, J. M. Junquera-Hernández, M.-G. La-Placa, A. Prescimone, E. Orti, C. E. Housecroft, E. C. Constable and H. J. Bolink, *J. Am. Chem. Soc.*, 2017, **139**, 3237–3248.
- 13 B. Fu, C.-Y. Wang, B. D. Rose, Y. Jiang, M. Chang, P.-H. Chu, Z. Yuan, C. Fuentes-Hernandez, B. Kippelen, J.-L. Brédas, D. M. Collard and E. Reichmanis, *Chem. Mater.*, 2015, **27**, 2928–2937.
- 14 R. D. Costa, E. Orti, H. J. Bolink, S. Graber, S. Schaffner, M. Neuburger, C. E. Housecroft and E. C. Constable, *Adv. Funct. Mater.*, 2009, **19**, 3456–3463.
- 15 V. V. Pavlishchuk and A. W. Addison, *Inorg. Chim. Acta*, 2000, **298**, 97–102.
- 16 For examples see: S. Ladouceur, D. Fortin and E. Zysman-Colman, *Inorg. Chem.*, 2011, **50**, 11514–11526.
- 17 Y.-C. Chiu, J.-Y. Hung, Y. Chi, C.-C. Chen, C.-H. Chang, C.-C. Wu, Y.-M. Cheng, Y.-C. Yu, G.-H. Lee and P.-T. Chou, *Adv. Mater.*, 2009, **21**, 2221–2225.
- 18 M. A. Haidekker, T. P. Brady, D. Lichlyter and E. A. Theodorakis, *Bioorg. Chem.*, 2005, **33**, 415–425.
- 19 H. Ishida, S. Tobita, Y. Hasegawa, R. Katoh and K. Nozaki, *Coord. Chem. Rev.*, 2010, **254**, 2449–2458.
- 20 S. Ladouceur and E. Zysman-Colman, *Eur. J. Inorg. Chem.*, 2013, **2013**, 2985–3007.
- 21 (a) C.-C. Ho, H.-F. Chen, Y.-C. Ho, C.-T. Liao, H.-C. Su and K.-T. Wong, *Phys. Chem. Chem. Phys.*, 2011, **13**, 17729–17736; (b) C.-L. Lee, C.-Y. Cheng and H.-C. Su, *Org. Electron.*, 2014, **15**, 711–720.

Simple Design to Achieve Red-to-Near-infrared Emissive Cationic Ir(III) Emitters and their use in Light Emitting Electrochemical Cells

Amlan K. Pal,^a David B. Cordes,^b Alexandra M. Z. Slawin,^b Cristina Momblona,^c Antonio Pertegás,^c
Enrique Ortí,^c Henk J. Bolink^c and Eli Zysman-Colman^{*a}

^aOrganic Semiconductor Centre, EaStCHEM School of Chemistry, University of St Andrews, St Andrews, Fife, UK, KY16 9ST, Fax: +44-1334 463808; Tel: +44-1334 463826; E-mail: eli.zysman-colman@st-andrews.ac.uk;

URL: <http://www.zysman-colman.com>

^bEaStCHEM School of Chemistry, University of St. Andrews, St. Andrews, KY16 9ST, Fife, United Kingdom

^cInstituto de Ciencia Molecular, Universidad de Valencia, C/J. Beltran 2, 46980 Paterna, Spain

Table of Contents:

Experimental section.....	S2-S8
NMR spectra of complexes.....	S10-S11
X-ray Crystallographic section.....	S12-S13
Electrochemistry.....	S14-S15
DFT calculations and UV-vis study.....	S15-S18
Steady-state emission profiles and spin densities.....	S17
XYZ Coordinates of DFT optimized structures.....	S18-S22
Photoluminescence in thin film.....	S24
Device characteristics.....	S25-S26
Notes and References.....	S26-S27

Experimental Section

General Synthetic Procedures. Commercial chemicals were used as supplied. All reactions were performed using standard Schlenk techniques under an inert (N₂) atmosphere. Purification and handling of all compounds were carried out under air. All products were stored in the dark. Freshly distilled anhydrous toluene was obtained from a Pure Solv™ solvent purification system (Innovative Technologies). Chromatography was performed on columns with an i.d. of 25–30 mm on silica gel (Geduran® Silicagel 60, 40–63 μm; Merck). The progress of reactions and the elution of products were followed by TLC (silica gel on aluminum sheets, SiliaPlate™ TLC Plates, Silicycle, 250 μm with indicator F-254). Compounds were visualised under UV light. ¹H and ¹³C NMR spectra were recorded with Bruker AVANCE II spectrometer (500 MHz for ¹H; 125 MHz for ¹³C). The following abbreviations have been used for multiplicity assignments: “s” for singlet, “d” for doublet, “t” for triplet, “p” for pentet, “m” for multiplet, and “br” for broad. ¹H NMR spectra were referenced to the solvent peak. Melting points (Mp) were recorded using open-end capillaries on an Electrothermal melting point apparatus IA9200 and are uncorrected. The heating rate was 0.5 or 1.0 °C/min. High-resolution mass spectra were recorded by EPSRC National Mass Spectrometry Service Centre, Swansea University. Elemental analyses were performed by Mr. Stephen Boyer, London Metropolitan University.

Photophysical measurements. All samples were prepared in HPLC grade acetonitrile (MeCN) with varying concentrations on the order of μM. Absorption spectra were recorded at RT using a Shimadzu UV-1800 double beam spectrophotometer. Molar absorptivity determination was verified by linear least-squares fit of values obtained from at least five independent solutions at varying concentrations with absorbance ranging from 6.88×10^{-1} to 3.19×10^2 μM.

The sample solutions for the emission spectra were prepared in N₂-degassed (20 minutes) HPLC grade MeCN using an in-house designed quartz cuvette. Steady-state and time-resolved emission spectra were recorded at room temperature using a Gilden fluoroSENS fluorimeter. The samples were excited at the absorption maxima of the dominant low-energy ¹MLCT/³MLCT band as indicated in Table S4. Excited state lifetimes were measured by time correlated single photon counting (TCSPC) with an Edinburgh Instruments FLS980 fluorimeter using a pulsed diode laser (exciting at 378 nm) and PL emission was detected at the corresponding steady-state emission maximum for each complex. The PL decays were fitted to a single exponential decay function. Emission quantum yields were determined using the optically dilute method.¹ A stock solution with absorbance of *ca.* 1.1 was prepared and then four dilutions were prepared with dilution factors of 43.2, 21, 13.7 and 10 to obtain solutions with absorbances of *ca.* 0.025, 0.050, 0.075 and 0.1, respectively. The Beer-Lambert law was found to be linear at the concentrations of the solutions. The emission spectra were then measured after the solutions were rigorously degassed with solvent-saturated N₂ gas for 20 minutes prior to spectrum acquisition. For each sample, linearity between absorption and emission intensity was verified through linear regression analysis and additional measurements were acquired until the Pearson regression factor (R^2) for the linear fit of the data set surpassed 0.9. Individual relative quantum yield values were calculated for each solution and the values reported represent the slope value. The equation $\Phi_s = \Phi_r(A_r/A_s)(I_s/I_r)(n_s/n_r)^2$ was used to calculate the relative quantum yield of each of the sample, where Φ_r is the absolute quantum yield of the reference, n is the refractive index of the solvent, A is the absorbance at the excitation wavelength, and I is the integrated area under the corrected emission curve. The subscripts s and r refer to the sample and reference, respectively. An aerated solution of [Ru(bpy)₃]Cl₂ in water ($\Phi_r = 0.04$) was used as the external reference.²

The samples for thin-film photoluminescence (PL) measurements were done with the same composition and thickness than the emissive layer of LEECs. Each complex was mixed with the ionic liquid (IL) 1-butyl-3-methylimidazolium hexafluorophosphate [Bmim][PF₆] in a 4-to-1 molar ratio (iTMC:IL) and deposited onto a quartz plate. A Hamamatsu absolute quantum yield C9920 instrument was used for the steady-state emission spectra and determination of photoluminescence quantum yields of the doped thin-films. A Hamamatsu Compact fluorescence lifetime spectrometer C11367 instrument was used to determine the excited state lifetimes of the doped thin-films.

Electrochemistry measurements. Cyclic voltammetry (CV) measurements were performed in N₂-purged HPLC grade acetonitrile at room temperature with an electrochemical analyzer potentiostat model 620E from CH Instruments interfaced to a PC at a sweep rate of 100 mV/s. Differential pulse voltammetry (DPV) was conducted with an increment potential of 0.004 V and a pulse amplitude, width, and period of 50 mV, 0.05, and 0.5 s, respectively. Solutions for CV and DPV were prepared in MeCN and degassed with MeCN-saturated N₂ bubbling for about 10 min prior to scanning. Tetra(*n*-butyl)ammonium hexafluorophosphate (TBAPF₆; *ca.* 0.1 M in MeCN) was used as the supporting electrolyte. A silver wire was used as the pseudoreference electrode; a glassy-carbon electrode was used for the working electrode and a Pt wire was used as the counter electrode. The redox potentials are reported relative to a standard calomel electrode (SCE) electrode with a ferrocenium/ferrocene (Fc⁺/Fc) redox couple as an internal reference (0.38 V vs SCE).³

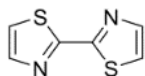
Experimental uncertainties are as follows: absorption maxima, ±2 nm; molar absorption coefficient, 10%; redox potentials, ±10 mV; emission maxima, ±3 nm; emission lifetimes, ±10%; luminescence quantum yields, ±10%.

Device preparation. LEECs were prepared on top of a patterned indium tin oxide (ITO, 15 Ω square⁻¹) coated glass substrate (www.naranjosubstrates.com) previously cleaned as follows: a)

sonication with soap, b) deionized water, c) isopropanol, and d) UV-O₃ lamp for 20 min. The thickness of the films was determined with an Ambios XP-1 profilometer. Prior to the deposition of the emitting layer, a 80 nm thick film of poly(3,4-ethylenedioxythiophene):poly-(styrenesulfonate) (PEDOT:PSS) (CLEVIOS™ P VP AI 4083, aqueous dispersion, 1.3–1.7% solid content, Heraeus) was coated in order to avoid the formation of pinholes and to increase the reproducibility of the cells. The emitting layer (100 nm) was prepared by spin-coating of a dichloromethane solution consisting of the iTMC with the addition of the ionic liquid (IL) 1-butyl-3-methylimidazolium hexafluorophosphate [Bmim][PF₆] (> 98.5%, Sigma-Aldrich) in a 4:1 molar ratio (iTMC:IL). For obtaining a good layer morphology, after adding the dichloromethane solution the substrate was covered during spinning. This fact slowed down the evaporation of the solvent and lead to more homogeneous and better-quality film. The devices were then transferred to an inert atmosphere glovebox (< 0.1 ppm O₂ and H₂O, MBraun). Finally, a layer (70 nm) of aluminium (the top electrode) was thermally evaporated onto the devices using an Edwards Auto500 evaporator integrated in the inert atmosphere glovebox. The area of the device was 6.5 mm². The devices were not encapsulated and were characterized inside the glovebox at room temperature.

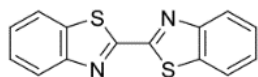
Device characterization. The device lifetime was measured by applying a pulsed current and monitoring the voltage *versus* time with a Botest OLT OLED Lifetime-Test System. The radiance was monitored using an integrating sphere (UDT Instruments, model 2525LE) coupled to a Radiometric Sensor (UDT Instruments, model 247) and an optometer (UDT Instruments, model S370). The electroluminescent (EL) spectra were measured using an Avantes AvaSpec-2048 Fiber Optic Spectrometer during device lifetime measurement. The peak current density of the pulse was 800 and 1600 A m⁻² and the average current density is determined by multiplying the peak current density by the time-on time and dividing by the total cycle time 50%.

2,2'-Bithiazole, L1.



2-Bromothiazole (2.00 g, 12.20 mmol, 1 equiv.), *N,N'*-diisopropylethylamine (DIPEA) (2.13 mL, 12.20 mmol, 1 equiv.), *n*-Bu₄NBr (1.97 g, 6.10 mmol, 0.50 equiv.) and Pd(OAc)₂ (0.14 g, 0.61 mmol, 0.05 equiv., 0.06 mol%) were dissolved in nitrogen-degassed toluene (35 mL). The mixture was heated to reflux for 20 h, after which time distilled water (50 mL) was added to the dark-brown solution before cooling down the solution to room temperature. The mixture was stirred at room temperature and dichloromethane (100 mL) was added. The organic layer was carefully separated and this procedure was repeated one more time with additional dichloromethane (50 mL). The organic layers were combined and evaporated to dryness to give dark brown oil. To this oil was added diethylether (200 mL) and the mixture was sonicated for 30 min. The ether solution was carefully decanted out and evaporated to dryness to afford the product as dark-orange microcrystalline solid. **Yield:** 0.85 g, 41%. **Mp:** 96-99 °C. **¹H NMR (500 MHz, CDCl₃) δ (ppm):** 7.45 (d, *J* = 3.21 Hz, 1 H), 7.90 (d, *J* = 3.21 Hz, 1 H). **¹³C NMR (126 MHz, CD₃CN) δ (ppm):** 161.79, 144.05, 121.12. Characterisation data match that reported in literature.⁴

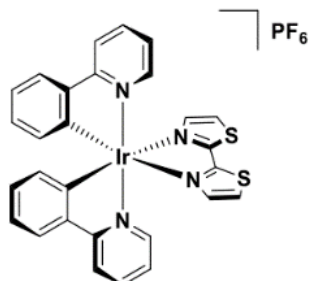
2,2'-bibenzo[d]thiazole, L2.



2-Bromobenzthiazole (2.00 g, 9.34 mmol, 1 equiv.), *N,N'*-diisopropylethylamine (DIPEA) (1.63 mL, 9.34 mmol, 1 equiv.), *n*-Bu₄NI (1.73 g, 4.67 mmol, 0.50 equiv.) and Pd(OAc)₂ (0.21 g, 0.93 mmol, 0.1 equiv., 0.09 mol%) were dissolved in nitrogen-degassed toluene (35 mL). The mixture was heated to reflux for 20 h, after which time distilled water (50 mL) was added to the dark-brown solution before cooling down the solution to room temperature. The mixture was stirred at room temperature and dichloromethane (100 mL) was added. The organic layer was carefully separated and this procedure was repeated one more time with additional dichloromethane (50 mL). The organic layers were combined and evaporated to dryness to give dark brown oil. To this oil was added diethylether (200 mL) and the mixture was sonicated for 30 min. The ether solution was carefully decanted out and evaporated to dryness to afford the product as dark-orange microcrystalline solid. **Yield:** 1.27 g, 51%. **Mp:** 238-241 °C (dec.). **¹H NMR (500 MHz, CDCl₃) δ (ppm):** 8.17 (d, *J* = 8.27 Hz, 1H), 7.99

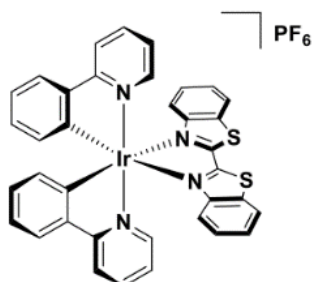
(d, $J = 8.05$ Hz, 1H), 7.57 (t, $J = 7.72$ Hz, 1H), 7.50 (t, $J = 7.67$ Hz, 1H). ^{13}C NMR (126 MHz, CD_3CN) δ (ppm): 161.68, 153.69, 135.94, 127.00, 126.79, 124.23, 122.20. Characterisation data match that reported in literature.⁵

Bis(2-phenylpyridinato- C^2,N')(2,2'-bithiazole- N',N')iridium(III) hexafluorophosphate, 1.



A 100 mL round-bottomed flask was charged with tetrakis[2-phenylpyridinato- N,C^2]-bis(μ -chloro)diiridium(III) (0.100 g, 0.092 mmol, 1 equiv.) and 2,2'-bithiazole (0.033 g, 0.193 mmol, 2.1 equiv.). An aliquot of a mixture of dichloromethane and methanol (40 mL, 1:1, v/v) was added to the flask and the solution was degassed with nitrogen. The solution was heated to reflux under a nitrogen atmosphere for 20 h. The solution was cooled down to room temperature and the solvent was evaporated to dryness under reduced pressure to afford a red solid. Purification by flash column chromatography (silica, dichloromethane/methanol, 95:5, v/v) and subsequent anion metathesis by addition of an aliquot of saturated aqueous solution of KPF_6 afforded the product as an orange-yellow solid. The Crystals of suitable X-ray quality were grown by slow diffusion of diethylether into a concentrated solution of the title compound in dichloromethane. **Yield:** 0.138 g, 91%. **Mp:** 345-348 °C (dec.) **R_f:** 0.48 (dichloromethane/methanol, 95:5, v/v on silica). ^1H NMR (500 MHz, CD_3CN) δ (ppm): 6.26 - 6.32 (m, 1 H), 6.90 (td, $J = 7.48, 1.28$ Hz, 1 H), 7.03 (ddd, $J = 7.85, 7.21, 1.18$ Hz, 1 H), 7.08 (ddd, $J = 7.37, 5.88, 1.28$ Hz, 1 H), 7.23 (d, $J = 3.42$ Hz, 1 H), 7.60 (dd, $J = 5.77, 0.64$ Hz, 1 H), 7.78 (dd, $J = 7.80, 1.18$ Hz, 1 H), 7.84 - 7.89 (m, 1 H) 7.92 (d, $J = 3.21$ Hz, 1 H), 8.04 (dd, $J = 8.12, 0.85$ Hz, 1 H). ^{13}C NMR (126 MHz, CD_3CN) δ (ppm): 168.27, 162.71, 150.91, 147.63, 145.24, 142.75, 139.54, 132.53, 130.98, 128.60, 125.61, 124.56, 123.56, 120.56. **HR NSI⁺ MS:** $[\text{M-PF}_6]^+$ **Calculated:** ($\text{C}_{28}\text{H}_{20}\text{N}_4\text{S}_2\text{Ir}$) 669.0758; **Found:** 669.0744. **Anal. Calcd.** for $\text{C}_{28}\text{H}_{20}\text{N}_4\text{F}_6\text{PS}_2\text{Ir}$: C, 41.33; H, 2.48; N, 6.88; Found: C, 41.95; H, 2.72; N, 6.82.

Bis(2-phenylpyridinato- C^2,N')(2,2'-bibenzo[d]thiazole- N',N')iridium(III) hexafluorophosphate,
2.



A 100 mL round-bottomed flask was charged with tetrakis[2-phenylpyridinato- N,C^2]-bis(μ -chloro)diiridium(III) (0.100 g, 0.092 mmol, 1 equiv.) and 2,2'-bibenzo[d]thiazole (0.057 g, 0.211 mmol, 2.3 equiv.). An aliquot of a mixture of dichloromethane and methanol (40 mL, 1:1, v/v) was added to the flask and the solution was degassed with nitrogen. The solution was heated to reflux under a nitrogen atmosphere for 20 h. The solution was cooled down to room temperature and the solvent was evaporated to dryness under reduced pressure to afford a brownish-red solid. Purification by flash column chromatography (silica, dichloromethane/methanol, 95:5, v/v) and subsequent anion metathesis by addition of an aliquot of aqueous saturated solution of KPF_6 afforded the product as a red solid. The Crystals of suitable X-ray quality were grown by slow diffusion of diethylether into a concentrated solution of the title compound in dichloromethane. **Yield:** 0.160 g, 95%. **Mp:** 388-390 °C (dec.) **R_f:** 0.45 (dichloromethane/methanol, 95:5, v/v on silica). **¹H NMR (500 MHz, CD₃CN) δ (ppm):** 8.20 (dt, $J = 8.3, 1.0$ Hz, 1H), 8.03 (dt, $J = 8.2, 1.1$ Hz, 1H), 7.86 – 7.78 (m, 2H), 7.72 (ddd, $J = 5.8, 1.5, 0.8$ Hz, 1H), 7.57 (ddd, $J = 8.3, 7.2, 1.1$ Hz, 1H), 7.24 (ddd, $J = 8.5, 7.2, 1.2$ Hz, 1H), 7.15 (td, $J = 7.6, 1.2$ Hz, 1H), 6.98 (dtd, $J = 7.4, 5.5, 1.4$ Hz, 2H), 6.83 (dt, $J = 8.6, 0.9$ Hz, 1H), 6.32 (dd, $J = 7.7, 1.2$ Hz, 1H). **¹³C NMR (126 MHz, CD₃CN) δ (ppm):** 167.90, 164.67, 151.64, 151.38, 145.94, 145.63, 139.71, 136.86, 132.67, 131.17, 129.80, 129.72, 125.88, 124.83, 124.79, 124.14, 123.27, 120.70. **HR NSI⁺ MS: [M-PF₆]⁺ Calculated:** (C₃₆H₂₄N₄S₂Ir) 769.1065; **Found:** 769.1061. **Anal. Calcd.** for C₃₆H₂₄N₄F₆PS₂Ir: C, 47.31; H, 2.65; N, 6.13; Found: C, 47.17; H, 2.84; N, 6.17.

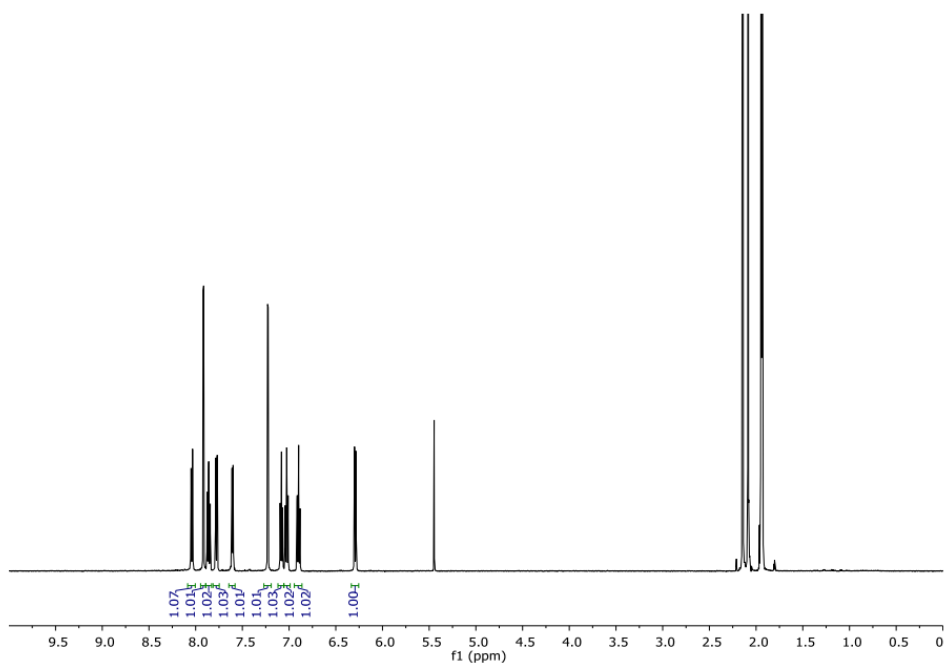


Fig. S1: ^1H NMR spectrum of complex **1** in CD_3CN at 500 MHz at r.t. (peak at ~ 5.3 ppm corresponds to residual DCM in CD_3CN).

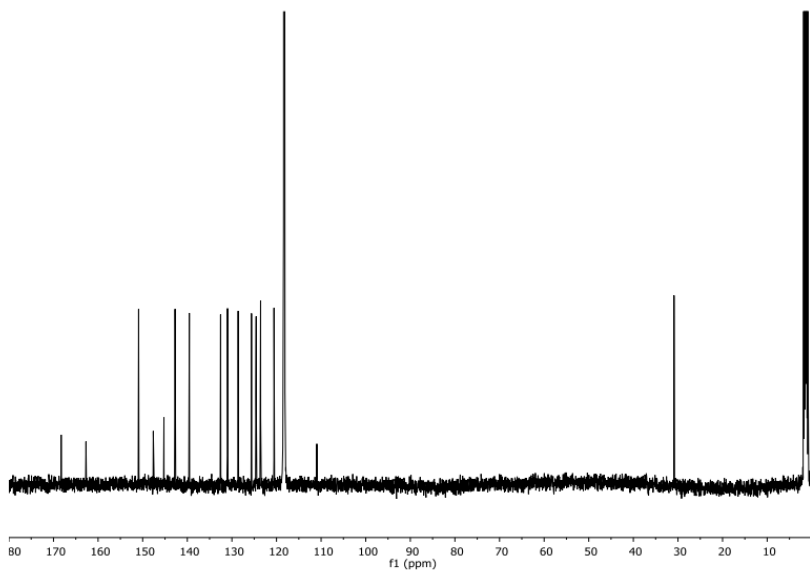


Fig. S2: ^{13}C NMR spectrum of complex **1** in CD_3CN at 500 MHz at r.t. (peak at ~ 30 ppm corresponds to residual DCM in CD_3CN).

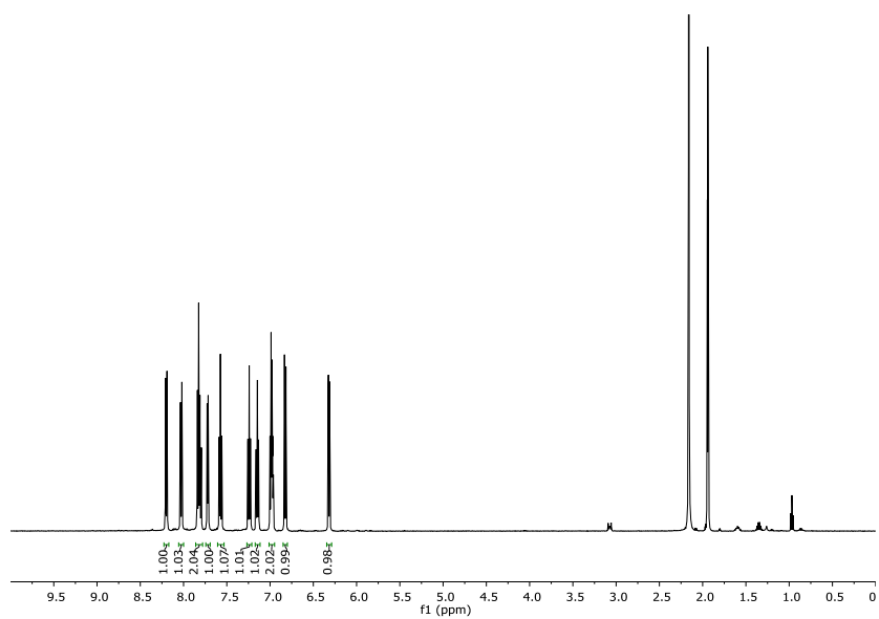


Fig. S3: ^1H NMR spectrum of complex **2** in CD_3CN at 500 MHz at r.t.

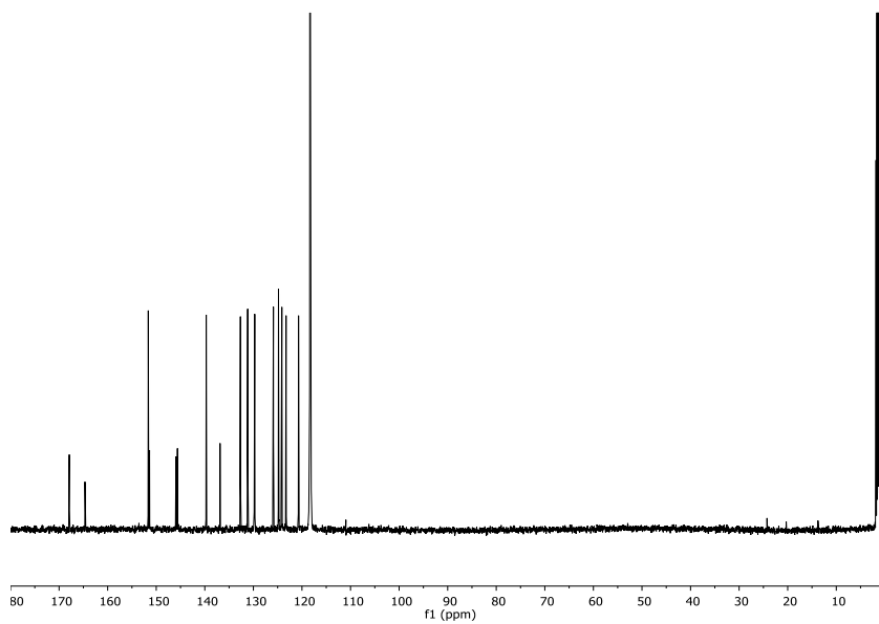


Fig. S4: ^{13}C NMR spectrum of complex **2** in CD_3CN at 500 MHz at r.t.

X-Ray Crystallography

Single crystals were grown by vapour diffusion of diethyl ether into either concentrated CH₂Cl₂ solution (**1**) or concentrated MeCN solution (**2**). Data were collected at 173 K (**1**) or 93 K (**2**) on a Rigaku FR-X Ultrahigh brilliance Microfocus RA generator/confocal optics with Rigaku XtaLAB P200 system, using Mo K α radiation ($\lambda = 0.71075 \text{ \AA}$). Intensity data were collected using ω steps accumulating area detector images spanning at least a hemisphere of reciprocal space. All data were corrected for Lorentz polarization effects, and a multiscan absorption correction was applied by using CrystalClear.⁶ Structures were solved by Patterson methods (PATTY)⁷ and refined by full-matrix least-squares against F² (SHELXL-2013).⁸ Non-hydrogen atoms were refined anisotropically, and hydrogen atoms were refined using a riding model. All calculations were performed using the CrystalStructure interface.⁹

Table S1. Crystal Data and Structure Refinement

compound	1	2
empirical formula	C ₂₈ H ₂₀ F ₆ IrN ₄ PS ₂	C ₃₈ H ₂₇ F ₆ IrN ₅ PS ₂
fw	813.80	954.97
cryst syst	orthorhombic	orthorhombic
lattice	Primitive	Primitive
space group	<i>Pbca</i> (#61)	<i>Pca21</i> (#29)
a [Å]	10.8949(11)	24.377(3)
b [Å]	15.8728(15)	9.1545(10)
c [Å]	33.006(4)	15.859(2)
α [°]	90	90
β [°]	90	90
γ [°]	90	90
vol [Å ³]	5707.8(10)	3539.1(7)
Z	8	4
ρ (calc) [Mg/m ³]	1.894	1.792
μ [cm ⁻¹]	49.599	40.154
F(000)	3152.00	1872.00
cryst	orange, chip	red, prism
cryst size [mm ³]	0.06 × 0.03 × 0.01	0.20 × 0.10 × 0.10
θ range	2.240 – 25.371°	2.377 – 25.315°
reflns collected	64336	17647
indep reflns (R _{int})	5220 (0.0622)	6135 (0.0256)
max/min transm	0.952 / 0.875	0.669 / 0.517
data/restraints/params	5220 / 0 / 379	6135 / 1 / 479
GOF on F ²	1.097	0.841
final R indices	R1 = 0.0336,	R1 = 0.0185,
[I > 2 σ (I)]	wR2 = 0.0571	wR2 = 0.0360
R indices	R1 = 0.0743,	R1 = 0.0200,
(all data)	wR2 = 0.0725	wR2 = 0.0362
largest diff. peak/hole [e/Å ³]	0.85 / -0.70	0.57 / -0.34

Table S2. Comparison of observed bond distances and angles in complexes **1** and **2** with values calculated for these complexes.^a

Compound	Bond Length (Å)			Angle (°)		
		Obs. (X-ray)	Calc. (DFT)		Obs. (X-ray)	Calc. (DFT)
1	Ir1-N25 _{N^oN}	2.148(6)	2.245	N1 _{C^oN} -Ir1-C8 _{C^oN}	80.6(2)	79.99
	Ir1-N31 _{N^oN}	2.149(6)	2.245	N13 _{C^oN} -Ir1-C20 _{C^oN}	80.7(2)	80.00
	Ir1-N1 _{C^oN}	2.048(5)	2.090	N25 _{N^oN} -Ir1-N31 _{N^oN}	75.3(2)	74.19
	Ir1-N13 _{C^oN}	2.046(5)	2.090			
	Ir1-C8 _{C^oN}	2.007(6)	2.025			
	Ir1-C20 _{C^oN}	2.003(7)	2.025			
2	Ir1-N1 _{C^oN}	2.058(4)	2.089	N1 _{C^oN} -Ir1-C8 _{C^oN}	80.62(17)	80.01
	Ir1-N13 _{C^oN}	2.049(4)	2.089	N13 _{C^oN} -Ir1-C20 _{C^oN}	80.45(17)	80.01
	Ir1-N25 _{N^oN}	2.180(4)	2.285	N25 _{N^oN} -Ir1-N35 _{N^oN}	76.00(14)	74.09
	Ir1-N35 _{N^oN}	2.195(4)	2.285			
	Ir1-C8 _{C^oN}	2.009(4)	2.025			
	Ir1-C20 _{C^oN}	2.009(5)	2.025			

^aRestricted DFT geometry optimizations of [**1**]⁺ and [**2**]⁺ (B3LYP/SBKJC-VTZ[Ir]6-31G**[C,H,N,S]).

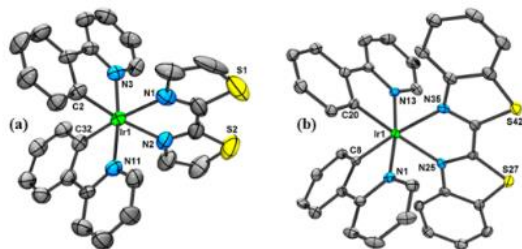


Fig. S5: Perspective views of complexes (a) **1** and (b) **2**. Ellipsoids correspond to a 50% probability level. Anions, co-crystallised solvent molecule (in **2**) and H-atoms have been omitted for clarity.

Electrochemistry

Table S3. Redox potentials of complexes **1** and **2** and the benchmark complex $[\text{Ir}(\text{ppy})_2(\text{bpy})]^+$, **R1** (where bpy = 2,2'-bipyridine) in degassed MeCN at 298 K.^a

Cmpd	$E_{1/2}^{\text{Ox}}$ (V)	$E_{1/2}^{\text{Red}}$ (V)	$\Delta E_{\text{redox}}^b$ (V)	E_{HOMO} (eV) ^c	E_{LUMO} (eV) ^c	$\Delta E_{ \text{LUMO-HOMO} }$ (eV) ^c
1	1.24(110)	-1.15(74), -1.73(293), -2.13(irr), -2.29(213), -2.83(irr)	2.38	-5.58	-2.76	2.82
2	1.37(169)	-0.82(88), -1.46(89), -2.37(103), -2.66(171)	2.19	-5.80	-3.07	2.73
R1 ^d	1.27	-1.38	2.65	-5.56	-2.31	3.25

^aPotentials are in volts (V) vs. SCE for acetonitrile solutions, 0.1 M in $[\text{n-Bu}_4\text{N}]\text{PF}_6$, recorded at room temperature at a sweep rate of 100 mV/s using a glassy carbon electrode as a working electrode, a platinum wire as a counter electrode and a silver wire as a reference electrode. The difference between cathodic, E_{pc} , and anodic, E_{pa} , peak potentials, ΔE_{p} , (millivolts) is given in parentheses. ^b ΔE_{redox} is the difference (V) between first oxidation and first reduction potentials. ^cDFT calculated energy in eV. ^dRedox potentials are from ref 10.

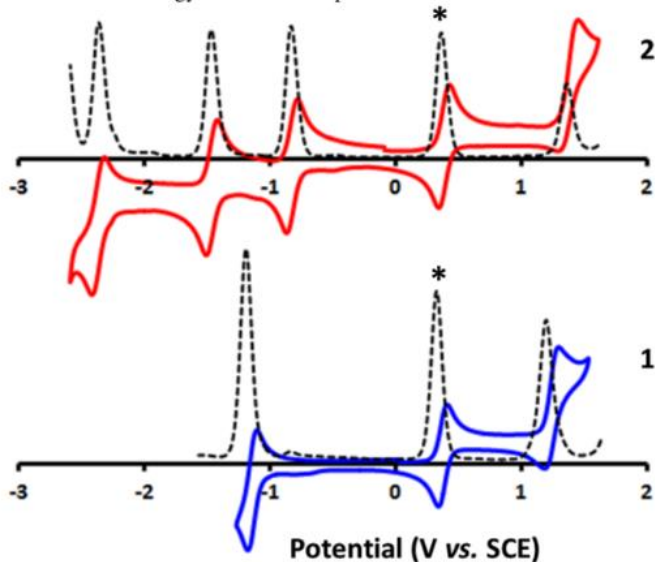


Fig. S6: Cyclic voltammogram (bold lines) and differential pulse voltammogram (dotted lines) of complexes **1** and **2** in degassed MeCN at r.t at a scan rate of 100 mV/s. Wave denoted with an asterix at 0.38 V corresponds to Fc/Fc⁺ couple.

DFT Calculations:

All calculations were performed with the Gaussian09, revision D.01¹¹ suite of programs employing the DFT method, the Becke three-parameter hybrid functional,¹² and Lee-Yang-Parr's gradient-corrected correlation functional (B3LYP).¹³ Singlet and triplet ground state geometry optimizations and single point energy calculations for [1]⁺, [2]⁺ and [R1]⁺ were carried out at the (R)B3LYP and (U)B3LYP levels, using their respective crystallographic structures as starting points. All elements except Iridium were assigned the 6-31G(d,p) basis set.¹⁴ The double- ζ quality SBKJC VDZ ECP basis set¹⁵ with an effective core potential was employed for the Ir(III)-ion. Vertical electronic excitations based on (R)B3LYP-optimized geometries were computed for [1]⁺, [2]⁺ and [R1]⁺ using the TD-DFT formalism^{16a,b} in acetonitrile using conductor-like polarizable continuum model (CPCM).^{17a-c} Vibrational frequency calculations were performed to ensure that the optimized geometries represent the local minima and there are only positive eigenvalues. The electronic distribution and localization of the singlet excited states were visualized using the electron density difference maps (ED-DMs).¹⁸ *Gausssum 2.2* and *Chemission v3.8*¹⁹ were employed to visualize the absorption spectra (simulated with Gaussian distribution with a full-width at half maximum (fwhm) set to 3000 cm⁻¹) and to calculate the fractional contributions of various groups to each molecular orbital. All calculated structures and Kohn-Sham orbitals were visualized with ChemCraft.²⁰

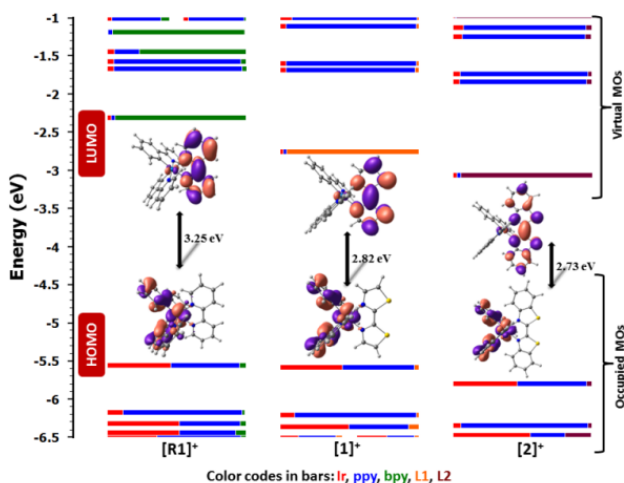


Fig. S7: Calculated frontier MO energies of $[\mathbf{R1}]^+$, $[\mathbf{1}]^+$ and $[\mathbf{2}]^+$, obtained from DFT [(rb3lyp/SBKJC-VDZ for Ir(III)) and (6-31g** for C,H,N,S)] with CPCM(MeCN) and 0.05 eV threshold of degeneracy. Kohn-Sham MOs of $[\mathbf{R1}]^+$, $[\mathbf{1}]^+$ and $[\mathbf{2}]^+$ are also shown (contours are isovalued at 0.03).

Table S4. UV-vis absorption data of complexes **1** and **2** (in degassed MeCN at room temperature) and benchmark complex **R1**.

Compound	$\lambda_{\text{abs}}/\text{nm}$ ($\epsilon \times 10^4 \text{ M}^{-1}\text{cm}^{-1}$)
1	252 (4.14), 265 (3.76), 303 (2.34), 318 (2.41), 333 (2.25), 377 (1.01), 466 (0.09), 500 (0.07)
2	251 (3.92), 343 (1.98), 363 (2.64), 379 (2.82), 407 (1.03), 433 (0.50), 549 (0.06), 599 (0.03)
R1 ^a	265 (4.17), 310 (1.29), 375 (0.60), 420 (0.26)

^aFrom ref. 10 in MeCN.

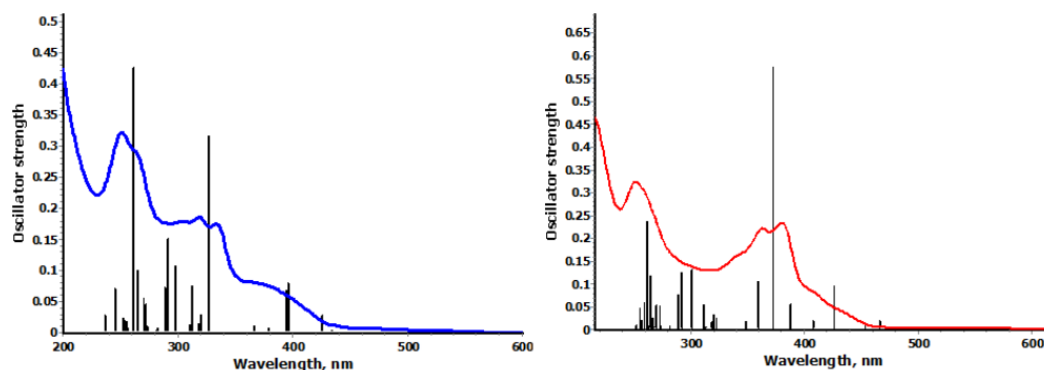


Fig. S8: Overlay of experimental UV-vis absorption spectra (curved lines) of complexes **1** and **2** with their predicted transitions (vertical bars) calculated by singlet TD-DFT at room temperature in MeCN.

Table S5. Selected transitions from TD-DFT calculations of $[\mathbf{1}]^+$ in the singlet ground state (B3LYP/SBKJC-VDZ[Ir]6-31G**[C,H,N,S], CPCM (MeCN)).

state	$\lambda_{\text{abs}}/\text{nm}$ (TD-DFT)	$\lambda_{\text{abs}}/\text{nm}$ ($\epsilon \times 10^4 \text{ M}^{-1}\text{cm}^{-1}$) [expt.]	f (TD-DFT)	Major transition(s)	character
44	245	252 (4.14)	0.0707	H-12->L (72%)	L1 (π) to L1 (π^*)
33	262	265 (3.76)	0.4271	H-6->L+1 (32%), H-1->L+4 (34%)	L1 (π) to ppy(π^*) (minor) + ppy(π) to ppy(π^*) (major)

S16

18	291	303 (2.34)	0.1506	H-4->L+1 (67%)	ppy(π) to ppy(π^*) (major) + Ir(d π) to ppy(π^*) (minor)
14	312	318 (2.41)	0.0762	H-1->L+2 (71%)	ppy(π) to ppy(π^*)
9	327	333 (2.25)	0.3175	H-6->L (76%)	L1 (π) to L1 (π^*)
4	396	377 (1.01)	0.0801	H-3->L (82%)	ppy(π) to L1 (π^*) (major) + Ir(d π) to L1 (π^*) (minor)
2	434	466 (0.09)	0.0047	H-4->L (15%), H-2->L (81%)	ppy(π) to L1 (π^*) (major) + Ir(d π) to L1 (π^*) (minor)
1	578	500 (0.07)	0.0001	H->L (99%)	ppy(π) to L1 (π^*) (major) + Ir(d π) to L1 (π^*) (minor)

Table S6. Selected transitions from TD-DFT calculations of $[2]^+$ in the singlet ground state (B3LYP/SBKJC-VDZ[Ir]6-31G**[C,H,N,S], CPCM (MeCN)).

state	$\lambda_{\text{abs}}/\text{nm}$ (TD-DFT)	$\lambda_{\text{abs}}/\text{nm}$ ($\epsilon \times 10^4 \text{ M}^{-1} \text{ cm}^{-1}$) [expt.]	f (TD-DFT)	Major transition(s)	character
43	261	251 (3.92)	0.2385	H-7->L+1 (46%), H-1->L+4 (36%)	L2 (π) to ppy(π^*) (major) + ppy(π) to ppy(π^*) (minor)
10	359	343 (1.98)	0.1065	H-7->L (92%)	ppy(π) to ppy(π^*)
8	372	363 (2.64)	0.5763	H-6->L (91%)	L2 (π) to L2 (π^*)
6	388	379 (2.82)	0.0191	H-5->L (97%)	ppy(π) to L2 (π^*)
5	408	407 (1.03)	0.0201	H-4->L (96%)	ppy(π) to L2 (π^*)
4	426	433 (0.50)	0.0965	H-3->L (93%)	Ir(d π) to L2 (π^*) (major) + ppy(π) to L2 (π^*) (minor)
2	466	549 (0.06)	0.0194	H-2->L (92%)	Ir(d π) to L2 (π^*) (major) + ppy(π) to L2 (π^*) (minor)
1	608	599 (0.03)	0.0001	H->L (99%)	Ir(d π) to L2 (π^*) (minor) + ppy(π) to L2 (π^*) (major)

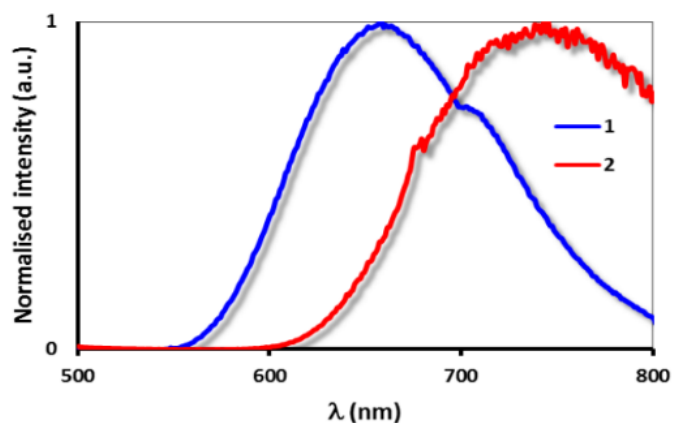


Fig. S9: Emission profiles of complexes **1** and **2** at r.t. in degassed MeCN ($\lambda_{\text{exc}} = 360$ nm). The shoulder at ~ 700 nm of complex **1** is due to instrumental artefact.

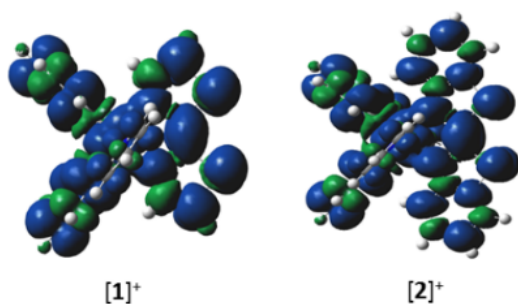


Fig. S10: Triplet spin density distributions of complexes **1** and **2**, obtained from DFT [(UB3LYP/SBKJC-VDZ for Ir(III)) and (6-31g** for C,H,N,S)] with CPCM(MeCN). Contours are isovalued at 0.004.

Table S7. Optimized Atomic coordinates obtained from DFT calculations of $[1]^+$.

Center Number	Atomic Number	Atomic Type	Coordinates (Angstroms)		
			X	Y	Z
1	77	0	0.163546	0.000108	0.000315
2	16	0	-4.162633	-1.069762	1.440592
3	16	0	-4.165051	1.055742	-1.443292
4	7	0	-1.626674	-0.770934	1.115220
5	7	0	-1.628373	0.765264	-1.115997
6	7	0	0.297520	-1.845705	-0.971581
7	7	0	0.289706	1.847220	0.971093
8	6	0	-2.796112	-0.424437	0.588496
9	6	0	1.587459	0.894539	-1.128493

10	6	0	1.899298	-2.223467	0.750219
11	6	0	-1.784511	1.565552	-2.220300
12	1	0	-0.905302	1.923656	-2.739621
13	6	0	-2.797057	0.414968	-0.590117
14	6	0	-0.275042	-3.431375	-2.677996
15	1	0	-0.861378	-3.664224	-3.559309
16	6	0	0.628688	-4.348185	-2.132226
17	1	0	0.763297	-5.325927	-2.583904
18	6	0	-0.291525	3.432305	2.675176
19	1	0	-0.880109	3.663716	3.555368
20	6	0	-3.082797	1.829765	-2.552554
21	1	0	-3.461813	2.425962	-3.370346
22	6	0	2.825245	2.992939	-1.471498
23	1	0	3.051807	4.013881	-1.178522
24	6	0	1.189076	-2.727209	-0.423416
25	6	0	2.833943	-2.983848	1.473758
26	1	0	3.064605	-4.003792	1.180495
27	6	0	1.357781	-3.992621	-1.006700
28	1	0	2.066894	-4.688005	-0.574525
29	6	0	3.471299	2.444476	-2.573209
30	1	0	4.193595	3.032842	-3.129785
31	6	0	1.892335	2.229642	-0.748793
32	6	0	1.178682	2.731624	0.423475
33	6	0	-0.408113	-2.194748	-2.066512
34	1	0	-1.086056	-1.443654	-2.453473
35	6	0	-1.781014	-1.571794	2.219364
36	1	0	-0.901031	-1.927059	2.739327
37	6	0	1.589155	-0.889706	1.130373
38	6	0	2.258629	0.366132	-2.240169
39	1	0	2.068091	-0.654297	-2.556810
40	6	0	1.341732	3.998183	1.005893
41	1	0	2.048860	4.695862	0.574167
42	6	0	3.476436	-2.433737	2.576742
43	1	0	4.200075	-3.019838	3.133964
44	6	0	2.256705	-0.359579	2.243391
45	1	0	2.061903	0.659952	2.560388
46	6	0	-3.078680	-1.840296	2.550611
47	1	0	-3.456340	-2.437803	3.368074
48	6	0	3.186174	1.129259	-2.953799
49	1	0	3.694308	0.693504	-3.809761
50	6	0	0.609588	4.352024	2.129973
51	1	0	0.739814	5.330677	2.580962
52	6	0	-0.418911	2.194621	2.064631
53	1	0	-1.094522	1.441284	2.451284
54	6	0	3.185986	-1.119823	2.957841
55	1	0	3.691290	-0.682844	3.814854

Table S8. Optimized Atomic coordinates obtained from DFT calculations of [2]⁺.

Center Number	Atomic Number	Atomic Type	Coordinates (Angstroms)		
			X	Y	Z
1	77	0	-0.000039	-0.443672	0.000012
2	16	0	-1.690076	3.966726	0.278033
3	16	0	1.690509	3.966470	-0.278860
4	7	0	-1.347756	1.380480	0.281447
5	7	0	1.347790	1.380264	-0.282068
6	7	0	-0.640471	-0.566355	-1.984569
7	7	0	0.640423	-0.565548	1.984605
8	6	0	-0.710388	2.526461	0.132681
9	6	0	1.377681	-1.918760	-0.165387
10	6	0	-2.042766	-2.246307	-1.046019
11	6	0	2.700498	1.580623	-0.534644
12	6	0	0.710599	2.526356	-0.133436
13	6	0	-0.614337	0.057848	-4.299824
14	1	0	-0.192106	0.678899	-5.081302
15	6	0	-1.616101	-0.879927	-4.566129
16	1	0	-1.999551	-1.006930	-5.573577
17	6	0	0.614570	0.059820	4.299556
18	1	0	0.192407	0.681255	5.080768
19	6	0	3.083519	2.944895	-0.568442
20	6	0	3.044128	-3.231233	1.078549
21	1	0	3.553478	-3.473577	2.006617
22	6	0	-1.618013	-1.492761	-2.224492
23	6	0	-3.044489	-3.231373	-1.077380
24	1	0	-3.553889	-3.474029	-2.005341
25	6	0	-2.114475	-1.652944	-3.526816
26	1	0	-2.887199	-2.387824	-3.716441
27	6	0	3.392823	-3.910524	-0.083363
28	1	0	4.164634	-4.672996	-0.057908
29	6	0	2.042538	-2.246048	1.046763
30	6	0	1.617937	-1.491891	2.224901
31	6	0	-0.157061	0.181194	-2.997003
32	1	0	0.623627	0.884444	-2.734768
33	6	0	-2.700413	1.581080	0.534049

34	6	0	-1.377918	-1.918547	0.166008
35	6	0	1.740361	-2.628209	-1.318928
36	1	0	1.247629	-2.420875	-2.263389
37	6	0	2.114574	-1.651393	3.527239
38	1	0	2.887333	-2.386160	3.717143
39	6	0	-3.393312	-3.910078	0.084837
40	1	0	-4.165230	-4.672453	0.059704
41	6	0	-1.740745	-2.627394	1.319872
42	1	0	-1.248032	-2.419653	2.264253
43	6	0	-3.083209	2.945427	0.567742
44	6	0	2.735944	-3.608067	-1.280578
45	1	0	2.998194	-4.142208	-2.189807
46	6	0	1.616355	-0.877824	4.566218
47	1	0	1.999955	-1.004302	5.573674
48	6	0	0.157147	0.182519	2.996725
49	1	0	-0.623571	0.885645	2.734244
50	6	0	-2.736445	-3.607148	1.281940
51	1	0	-2.998809	-4.140826	2.191407
52	6	0	3.665281	0.583200	-0.759065
53	6	0	4.974820	0.973162	-0.999575
54	1	0	5.730825	0.214745	-1.174517
55	1	0	4.685648	4.380889	-0.831629
56	6	0	4.402669	3.334070	-0.809608
57	6	0	5.342839	2.331653	-1.022514
58	6	0	-3.665363	0.583827	0.758535
59	6	0	-4.974826	0.974019	0.999056
60	1	0	-5.730967	0.215752	1.174061
61	1	0	-4.685112	4.381694	0.830820
62	6	0	-4.402307	3.334823	0.808893
63	6	0	-5.342631	2.332580	1.021890
64	1	0	3.378370	-0.460322	-0.746447
65	1	0	6.376002	2.604212	-1.212268
66	1	0	-3.378623	-0.459738	0.745984
67	1	0	-6.375749	2.605301	1.211645

Table S9. Optimized Atomic coordinates obtained from DFT calculations of $[\mathbf{R1}]^+$.

Center	Atomic	Atomic	Coordinates (Angstroms)
--------	--------	--------	-------------------------

Number	Number	Type	X	Y	Z
1	6	0	1.645524	-0.688774	1.057703
2	6	0	1.320067	1.218175	-1.032447
3	6	0	2.222796	-0.137520	2.211030
4	1	0	1.846155	0.797719	2.613898
5	6	0	3.291034	-0.764800	2.857217
6	1	0	3.720901	-0.312640	3.747010
7	6	0	3.816617	-1.964200	2.365846
8	1	0	4.647486	-2.447030	2.870206
9	6	0	3.268253	-2.533329	1.222396
10	1	0	3.680281	-3.464416	0.844339
11	6	0	2.193928	-1.905623	0.568290
12	6	0	1.565831	-2.440136	-0.638807
13	6	0	1.955433	-3.602778	-1.321922
14	1	0	2.790331	-4.184159	-0.950100
15	6	0	1.282716	-4.001547	-2.467842
16	1	0	1.588189	-4.899063	-2.996419
17	6	0	0.212332	-3.231855	-2.933308
18	1	0	-0.339289	-3.502846	-3.826171
19	6	0	-0.136796	-2.093040	-2.224658
20	1	0	-0.952689	-1.456824	-2.545225
21	6	0	2.080424	0.902389	-2.168379
22	1	0	2.068618	-0.107292	-2.567060
23	6	0	2.870601	1.864109	-2.802624
24	1	0	3.450060	1.589489	-3.679985
25	6	0	2.927532	3.174083	-2.315621
26	1	0	3.543765	3.917749	-2.810645
27	6	0	2.190680	3.516310	-1.188065
28	1	0	2.240613	4.533969	-0.811902
29	6	0	1.393959	2.551805	-0.546563
30	6	0	0.593260	2.834717	0.643099
31	6	0	0.535887	4.062341	1.321455
32	1	0	1.123101	4.897798	0.960164
33	6	0	-0.258653	4.203842	2.449746
34	1	0	-0.297848	5.152955	2.974968
35	6	0	-1.002092	3.109305	2.901832
36	1	0	-1.633226	3.172453	3.780784
37	6	0	-0.913563	1.918133	2.198851
38	1	0	-1.460999	1.037232	2.511089

39	6	0	-1.900456	1.419959	-2.056745
40	1	0	-0.957028	1.844808	-2.382242
41	6	0	-3.108470	1.778067	-2.646994
42	1	0	-3.121403	2.499035	-3.456734
43	6	0	-4.281373	1.195352	-2.170066
44	1	0	-5.244039	1.451434	-2.600683
45	6	0	-4.204200	0.278913	-1.125118
46	1	0	-5.110080	-0.172072	-0.739661
47	6	0	-2.957420	-0.042927	-0.575757
48	6	0	-2.788209	-1.004546	0.542640
49	6	0	-3.847824	-1.742675	1.082589
50	1	0	-4.849591	-1.642508	0.684025
51	6	0	-3.610310	-2.620788	2.136564
52	1	0	-4.426278	-3.197443	2.560187
53	6	0	-2.314095	-2.747369	2.632403
54	1	0	-2.082220	-3.419419	3.451069
55	6	0	-1.302571	-1.990340	2.049826
56	77	0	0.057818	0.007896	-0.000030
57	7	0	0.513916	-1.701840	-1.110213
58	7	0	-0.142352	1.775660	1.101989
59	7	0	-1.821540	0.531206	-1.050982
60	7	0	-1.528197	-1.139113	1.033636
61	1	0	-0.274624	-2.049828	2.390996

Photoluminescence in thin film:

Table S10. Photophysical properties of complex **1** and **2** in doped thin film.^a

Thin film	$\lambda_{\text{em}} / \text{nm}^b$	$\Phi_{\text{PL}} / \%^c$	τ / ns^d
1 : [Bmim][PF ₆]	658	14	257
2 : [Bmim][PF ₆]	707	5	117

^aPhotophysical properties measured on a quartz/thin film. ^b $\lambda_{\text{exc}} = 320 \text{ nm}$. ^c Φ_{PL} measured using an integrating sphere. ^d $\lambda_{\text{exc}} = 340 \text{ nm}$.

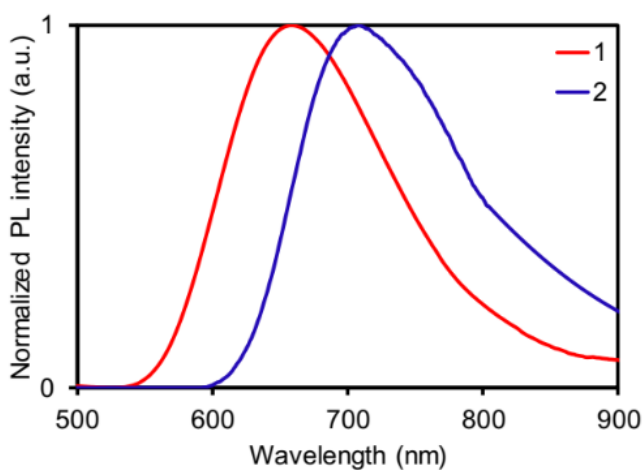


Fig. S11: Photoluminescence spectrum for **1** and **2** in thin film: **Quartz / 1 or 2:[Bmim][PF₆]** upon excitation at 320 nm. [Bmim][PF₆] is 1-butyl-3-methylimidazolium hexafluorophosphate.

Device characteristics:

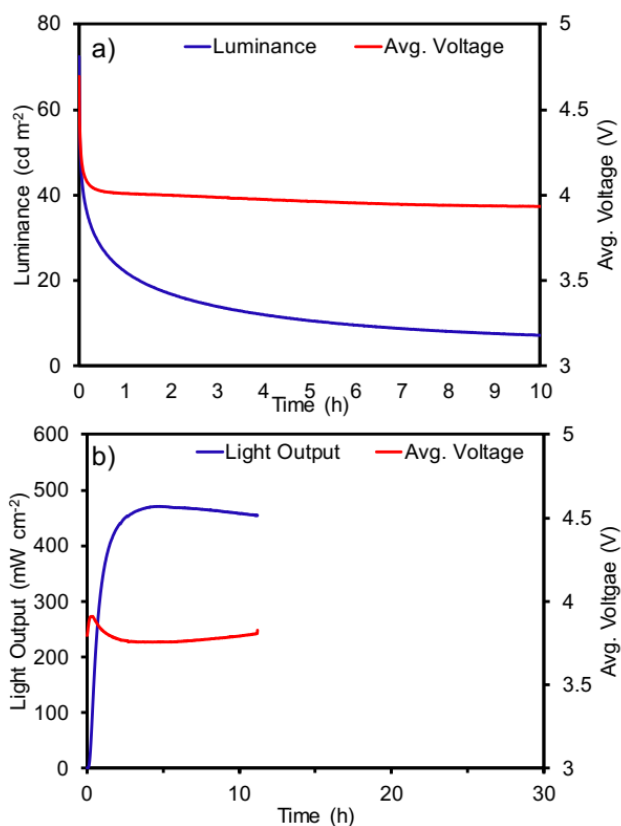


Fig. S12: Device performance *versus* time (a) LEEC-1 and (b) LEEC-2 under a pulsed current of 800 A m⁻² (average current density), 1KHz and 50% of duty cycle.

Table S11: Device performance for LEEC-1 under pulsed current of 400 and 800 A m⁻² (average current density).

Device	PC / A m ⁻²	Luminance _{max} ^a / cd m ⁻²	t _{1/2} ^b / h	EQE _{max} ^c / %	λ _{em} ^{max} EL / nm	CIE ^d
LEEC-1	400	59	0.24	0.23	661	0.65, 0.34
	800	72	0.15	0.13		

^aMaximum luminance. ^bTime to reach one-half of the maximum luminance. ^cMaximum external quantum efficiency. ^dCommission internationale de l'Éclairage.

Table S12: Device performance for LEEC-2 under pulsed current of 400 and 800 A m⁻².

Device	PC / A m ⁻²	Light output _{max} ^a / μW cm ⁻²	t _{1/2} ^b / h	EQE _{max} ^c / %	λ _{em} ^{max} EL / nm
LEEC-2	400	262	80	0.37	705
	800	471	>80	0.33	

^aMaximum light output. ^bTime to reach one-half of the maximum light output. ^cMaximum external quantum efficiency.

References:

1. G. A. Crosby, J. N. Demas, *J. Phys. Chem.* 1971, **75**, 991.
2. W. H. Melhuish, *J. Phys. Chem.*, 1961, **65**, 229–235.
3. V. V. Pavlishchuk and A. W. Addison, *Inorg. Chim. Acta*, 2000, **298**, 97.
4. B. Fu, C.-Y. Wang, B. D. Rose, Y. Jiang, M. Chang, P.-H. Chu, Z. Yuan, C. Fuentes-Hernandez, B. Kippelen, J.-L. Bredas, D. M. Collard, E. Reichmanis, *Chem. Mater.*, 2015, **27**, 2928-2937.
5. M. Zhu, K.-I. Fujita, R. Yamaguchi, *Chem. Commun.*, 2011, **47**, 12876.
6. *CrystalClear-SM Expert v. 2.1*; Rigaku Americas, The Woodlands, Texas, USA and Rigaku Corporation, Tokyo, Japan, **2010-2014**.
7. Beurskens, P. T.; Beurskens, G.; de Gelder, R.; Garcia-Granda, S.; Gould, R. O.; Israel, R.; Smits, J. M. M., *DIRDIF-99. DIRDIF-99*; University of Nijmegen, The Netherlands, **1999**.
8. Sheldrick, G., *Acta Crystallogr., Sect. C: Cryst. Struct. Commun.* **2015**, *71*, 3.
9. *CrystalStructure v4.1*; The Woodlands, Texas, USA and Rigaku Corporation, Tokyo, Japan, **2014**.
10. S. Ladouceur, D. Fortin, E. Zysman-Colman, *Inorg. Chem.*, 2011, **50**, 11514-11526.
11. M. J. Frisch, G. W. Trucks, H. B. Schlegel, G. E. Scuseria, M. A. Robb, J. R. Cheeseman, G. Scalmani, V. Barone, B. Mennucci, G. A. Petersson, H. Nakatsuji, M. Caricato, X. Li, H. P. Hratchian, A. F. Izmaylov, J. Bloino, G. Zheng, J. L. Sonnenberg, M. Hada, M. Ehara, K. Toyota, R. Fukuda, J. Hasegawa, M. Ishida, T. Nakajima, Y. Honda, O. Kitao, H. Nakai, T. Vreven, J. A. Montgomery, Jr., J. E. Peralta, F. Ogliaro, M. Bearpark, J. J. Heyd, E. Brothers, K. N. Kudin, V. N. Staroverov, T. Keith, R. Kobayashi, J. Normand, K. Raghavachari, A. Rendell, J. C. Burant, S. S. Iyengar, J. Tomasi, M. Cossi, N. Rega, J. M. Millam, M. Klene, J. E. Knox, J. B. Cross, V. Bakken, C. Adamo, J. Jaramillo, R. Gomperts, R. E. Stratmann, O. Yazyev, A. J. Austin, R. Cammi, C. Pomelli, J. W. Ochterski, R. L. Martin, K. Morokuma, V. G. Zakrzewski, G. A. Voth, P. Salvador, J. J. Dannenberg, S. Dapprich, A. D. Daniels, O.

- Farkas, J. B. Foresman, J. V. Ortiz, J. Cioslowski, and D. J. Fox, Gaussian, Inc., Wallingford CT, 2013.
12. A. D. Becke, *J. Chem. Phys.*, 1993, **98**, 5648–5652.
 13. C. Lee, W. Yang, R. G. Parr, *Phys. Rev. B: Condens. Matter*, 1988, **37**, 785–789.
 14. A. D. McLean, G. S. Chandler, *J. Chem. Phys.*, 1980, **72**, 5639–5648.
 15. J. S. Binkley, J. A. Pople, W. J. Hehre, *J. Am. Chem. Soc.*, 1980, **102**, 939.
 16. (a) M. E. Casida, C. Jamorski, K. C. Casida, D. R. Salahub, *J. Chem. Phys.*, 1998, **108**, 4439–4449. (b) R. E. Stratmann, G. E. Scuseria, M. J. Frisch, *J. Chem. Phys.*, 1998, **109**, 8218–8224.
 17. (a) M. Cossi, N. Rega, G. Scalmani, V. Barone, *J. Comput. Chem.*, 2003, **24**, 669–681. (b) M. Cossi, V. Barone, *J. Chem. Phys.*, 2001, **115**, 4708–4717. (c) V. Barone, M. Cossi, *J. Phys. Chem. A*, 1998, **102**, 1995–2001.
 18. W. R. Browne, N. M. O’Boyle, J. J. McGarvey, J. G. Vos, *Chem. Soc. Rev.*, 2005, **34**, 641–663.
 19. Chemissian v4.42, © Skripnikov Lenoid 2005-2015; www.chemissian.com.
 20. D. A. Zhurko, G. A. Zhurko, ChemCraft 1.5; Plimus: San Diego, CA. Available at <http://www.chemcraftprog.com>.

Efficient methylammonium lead iodide perovskite solar cells with active layers from 300 to 900 nm

C. Momblona,¹ O. Malinkiewicz,¹ C. Roldán-Carmona,^{1,2} A. Soriano,¹
 L. Gil-Escrig,¹ E. Bandiello,¹ M. Scheepers,¹ E. Edri,³ and H. J. Bolink^{1,a}

¹Instituto de Ciencia Molecular, Universidad de Valencia, C/Catedrático J. Beltrán 2, 46980 Paterna, Valencia, Spain

²Department of Physical Chemistry and Applied Thermodynamics, University of Córdoba, Campus Rabanales, Ed. C3, 14014, Córdoba, Spain

³Department of Materials and Interfaces, Weizmann Institute of Science, Herzl St. 34, Rehovot 76100, Israel

(Received 1 May 2014; accepted 2 July 2014; published online 16 July 2014)

Efficient methylammonium lead iodide perovskite-based solar cells have been prepared in which the perovskite layer is sandwiched in between two organic charge transporting layers that block holes and electrons, respectively. This configuration leads to stable and reproducible devices that do not suffer from strong hysteresis effects and when optimized lead to efficiencies close to 15%. The perovskite layer is formed by using a dual-source thermal evaporation method, whereas the organic layers are processed from solution. The dual-source thermal evaporation method leads to smooth films and allows for high precision thickness variations. Devices were prepared with perovskite layer thicknesses ranging from 160 to 900 nm. The short-circuit current observed for these devices increased with increasing perovskite layer thickness. The main parameter that decreases with increasing perovskite layer thickness is the fill factor and as a result optimum device performance is obtained for perovskite layer thickness around 300 nm. However, here we demonstrate that with a slightly oxidized electron blocking layer the fill factor for the solar cells with a perovskite layer thickness of 900 nm increases to the same values as for the devices with thin perovskite layers. As a result the power conversion efficiencies for the cells with 300 and 900 nm are very similar, 12.7% and 12%, respectively. © 2014 Author(s). All article content, except where otherwise noted, is licensed under a Creative Commons Attribution 3.0 Unported License. [<http://dx.doi.org/10.1063/1.4890056>]

Thin film photovoltaic devices hold great promise to reduce the dependencies on fossil energy. Solid state methylammonium lead halide perovskites solar cells are attracting much attention due to their ease of preparation, low cost, and high efficiencies.^{1,2} The hybrid organic-inorganic methylammonium lead iodide perovskites have been studied extensively since many years and have been recognized for their excellent semiconducting properties.^{3,4} After the seminal work of Miyasaka *et al.*⁵ tremendous progress in the performance of methylammonium lead iodide perovskite based solar cells has been obtained.^{6–11} Most high efficiency perovskite solar cells reported until now use a (mesoscopic) metal oxide such as Al₂O₃, TiO₂, or ZrO₂ requiring a high temperature sintering process. However, an increasing number of works in which the inverted approach is used are appearing. In these devices, the holes are extracted via the transparent conductor poly(3,4-ethylenedioxythiophene):poly(styrenesulfonic acid) (PEDOT:PSS) situated on top of the transparent bottom electrode.^{12–14} Recently, we have improved the performance of such inverted devices by sandwiching an evaporated CH₃NH₃PbI₃ perovskite in between organic electron and hole blocking

^aAuthor to whom correspondence should be addressed. Electronic mail: henk.bolink@uv.es.



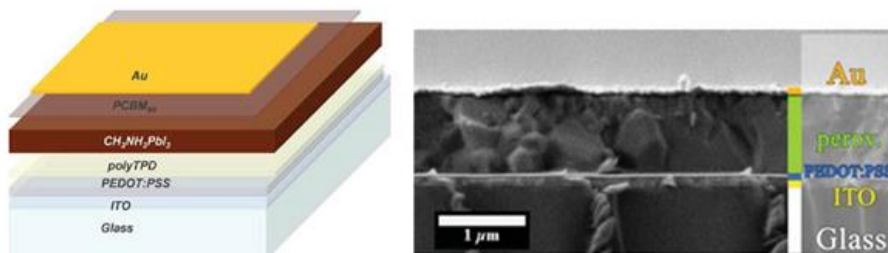


FIG. 1. (a) Schematic presentation of the device layout and (b) SEM cross section image of a device with a perovskite layer thickness of 900 nm. The polyTPD and PCBM₆₀ cannot be discerned due to their low thickness.

layers. This configuration leads to stable and reproducible devices that do not suffer from strong hysteresis effects and when optimized lead to efficiencies close to 15%.¹⁵

Recently, reports have appeared that mention a long charge carrier diffusion length in methylammonium lead iodide perovskite.^{16–18} Probably related to that is the observation of a low recombination efficiency of electrons and holes in this material.¹⁹ However, depending on the type of perovskite and its preparation method, very different diffusion lengths, ranging from 100 to 1000 nm, have been reported.

If the longer diffusion lengths hold in real devices one would expect an almost thickness independent performance up to thicknesses equal to the diffusion lengths. To date, most of the perovskite solar cells reported in literature use perovskite layers with thicknesses in the range of 200–400 nm, well below 1 μm. We are aware of only one reference where a thickness dependence study was performed to determine the optimal perovskite layer thickness on PEDOT:PSS on fluorine doped tin oxide (FTO) based glass substrates. From that study, an optimum short-circuit current density (J_{sc}) was found for a perovskite layer thickness of around 450 nm.²⁰ Additionally, Kelly presented a study on the effect of perovskite thicknesses in a ZnO/CH₃NH₃PbI₃/OMTAD device configuration at the HOPV14 conference in Lausanne, he found an optimum J_{sc} for devices having a perovskite thicknesses in the range of 300–400 nm.²¹ Both studies used solution processed perovskites layers which are reported to have slightly different properties than vacuum deposited ones. Using our smooth evaporated perovskite films we have prepared perovskite solar cells sandwiched in between organic hole- and electron-blocking layers with perovskite layer thicknesses ranging from 160 to 900 nm. The dual-source thermal evaporation method used to prepare the perovskite layers allows for high precision thickness variations. We show that the J_{sc} of the solar cells increases with increasing perovskite layer thickness, fast up to 300 nm and more slowly for devices with layers going from 300 to 900 nm. However, due to a decreasing fill factor (FF) for cells with perovskite layers in excess of 300 nm the power conversion efficiency (PCE) is reduced for the thicker devices. However, partially oxidation of the poly[N,N'-bis(4-butylphenyl)-N,N'-bis(phenyl)benzidine (polyTPD) electron blocking/hole transporting layer in cells with a 900 nm perovskite layer leads to a recovery of the fill factor and efficiency, reaching similar values as those obtained for the thin perovskite layer based solar cells. This demonstrates that with non-limiting organic layers, the cell performance is rather independent on perovskite layer thickness in between 300 and 900 nm.

The device layout used in this study is shown in Figure 1 and consists of two selective layers situated on both sides of the perovskite layer. To block the electrons and allow holes to reach the anode a thin layer of polyTPD or doped-polyTPD was used. To block holes and allow the electrons to reach the cathode (Au) [6,6]-phenyl C61-butyric acid methylester (PCBM₆₀), was used. The indium-tin oxide (ITO) (anode) acts as the hole-collecting contact and the Au (cathode) as the top electron-collecting electrode. Au was selected as it resulted in better performing and more stable devices compared to devices employing other top contact electrodes. A layer of 80 nm of PEDOT:PSS was spin-coated (1200 rpm, 30 s) onto a pre-patterned-ITO containing glass substrate and thermally annealed at 150 °C during 15 min. This layer smoothens the substrate and acts as a hole transporter. Next the polyTPD or doped-polyTPD solution was spin-coated (3000 rpm, 30 s)

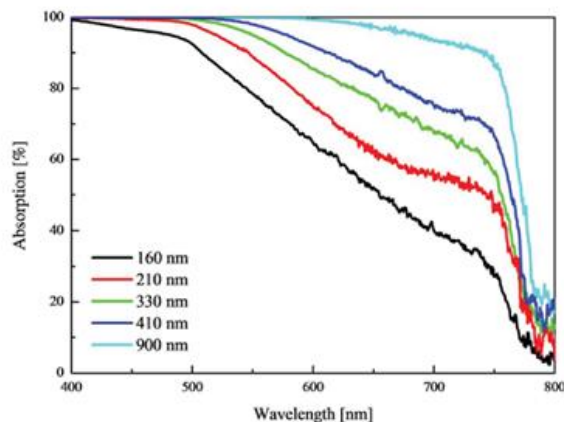


FIG. 2. Absorption spectrum for perovskite thicknesses from 160 to 900 nm.

to obtain a 20 nm thin film. The perovskite was deposited by co-evaporating the two starting materials PbI_2 and $\text{CH}_3\text{NH}_3\text{I}$ in a high vacuum chamber. The thickness of the layers was verified using absorbance and by a stylus profilometer (Ambios X1). Then, a thin layer of 20 nm of PCBM_{60} was deposited using a meniscus coater and a coating speed of 2.5 mm/s.²² The final stack was covered by 60 nm of Au as the top electrode layer using a vacuum evaporation process. A cross section scanning electron microscopy (SEM) image of a cell with a perovskite layer thickness of 900 nm is shown in Figure 1, where all the layers, except the thin blocking layers, are visible.

The percentage of absorption of the different perovskite layer thicknesses is shown in Figure 2. All films showed an onset of the photocurrent generation at 790 nm, in good agreement with the band gap value (1.55 eV) of the $\text{CH}_3\text{NH}_3\text{PbI}_3$, similar to those reported previously for this material.²³ This broad absorption extends from the visible to the near-IR region. Moreover, the absorption increases almost linearly with the perovskite layer thickness. These spectra were taken on glass substrates, which were also used as the blank. When incorporated into a solar cell, the transmission of the front electrode (ITO) should be taken into account as well as the reflectance at the top Au mirror electrode, which leads to a second pass of the light through the perovskite layer. However, from this figure it is clear that just a single pass of the light through a film with a thickness of 210 nm, leads to more than 50% absorption.

X-ray diffraction analysis of the different thickness perovskite layers is depicted in Fig. S1 of the supplementary material.²⁴ Slight variations in the diffraction patterns of the different perovskite films are observed. These slight changes are also observed within a series of perovskite layers with a single thickness. Such changes, however, do not lead to large variations of performance as it is evidenced by the narrow statistics that are presented also in Fig. S2 of the supplementary material where an average of 5 to 10 cells are displayed.²⁴

As the numbers of photo-generated carriers is related to the number of absorbed photons one expects that J_{sc} increases with increasing layer thickness until all the light is absorbed. With no losses, the remaining parameters, open circuit voltage (V_{oc}) and FF are expected to remain unchanged. Figure 3 summarizes graphically the solar cell performance as a function of perovskite layer thickness. The key performance parameters of the solar cells obtained from the current-density (J) voltage (V) sweeps under 1 sun illumination are plotted versus perovskite layer thickness.

As expected the J_{sc} increases with increasing perovskite layer thickness. It increases rapidly with the perovskite layer thickness from 200 to 300 nm and it continues to increase slowly with further incrementing perovskite layers thickness. Hence, there is still a significant gain in absorption of the sunlight when going from perovskite layers of 200–400 nm. This implies that one cannot simply double the absorption data obtained for a thin film to a device with a mirror top electrode (Fig. 2), but has to take into account the total stack reflectance and absorbance. The increase in J_{sc}

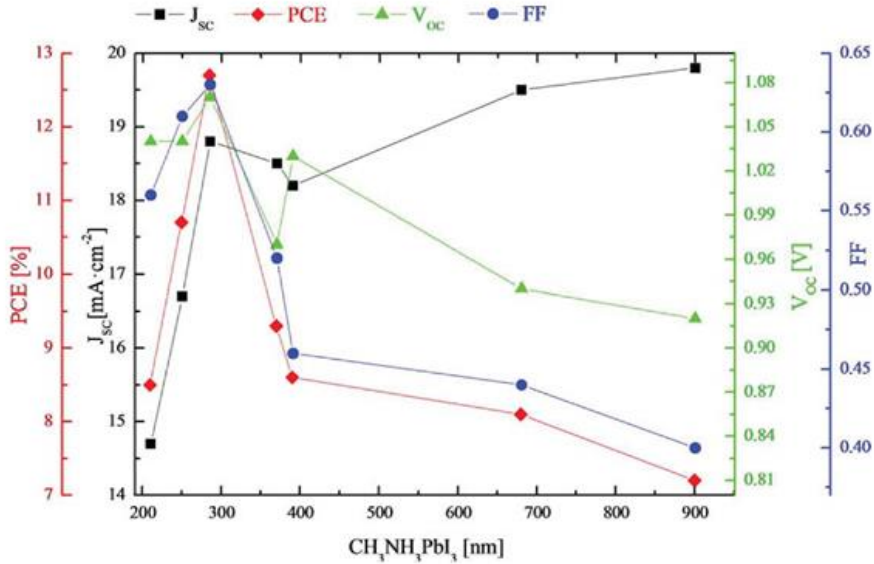


FIG. 3. J_{sc} , V_{oc} , FF, and PCE values as a function of perovskite thickness. For clarity the statistics are not shown in this plot, but are present in the version of this plot in Figure S2 of the supplementary material.²⁴

TABLE I. FF values of thick devices at different % of light intensity irradiation.

1 sun intensity [%]	FF
100	48.7
50	52.6
20	55.9
10	58.6
1	63.4

for a device with a perovskite layer of 400 nm to that with a perovskite layer thickness of 900 nm is only around 5%. At the same time, 20% more light is absorbed, and while more free carriers are generated due to increase in light absorbance, the collection efficiency is lower in the thicker device. The V_{oc} is constant for devices with a perovskite layer thickness from 200 to 400 nm. It decreases by nearly 10% for devices with a thicker perovskite layer. The main parameter that is negatively affected by the increase of the perovskite layer thickness is the FF, which drops strongly for devices with a perovskite layer thickness in excess of 300 nm. As a result of the decreasing FF the PCE also decreases with increasing perovskite layer thicknesses. Statistical data is presented in Fig. S2 of the supplementary material.²⁴

The decrease in FF is only observed at high light intensity, when this is reduced the FF improves and reaches values similar to the best (thin perovskite layer) devices at 1% of 1 sun (Table I) and Fig S3 of the supplementary material.²⁴ Hence, with lower charge carrier densities, due to the lower illumination intensity, the FF increases and reaches values similar to what is observed for devices with perovskite layer thickness lower than 300 nm. This implies that the reduction of the fill factor is not primarily related to the increased path length for the charge carriers, i.e., series resistance in the absorber layer. Yet it appears to be related to the efficiency of charge extraction. This can be due to, e.g., the lower hole mobilities in the polyTPD compared to that of holes in the perovskite layers, and can also be related to smaller built in voltage in the thicker devices. From previous work on

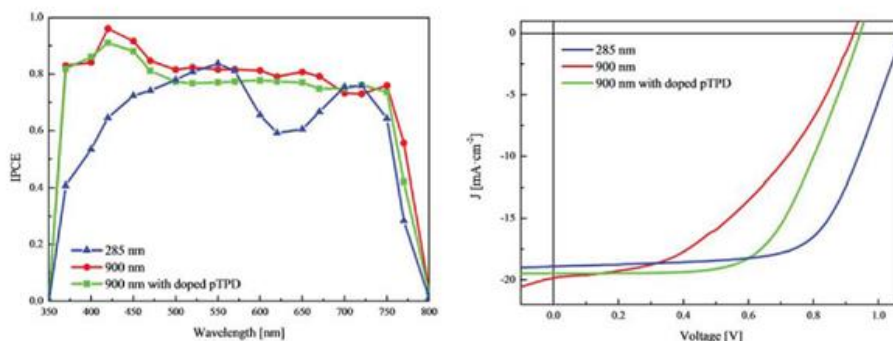


FIG. 4. (a) IPCE curves and (b) photocurrent density versus voltage under 1 sun illumination, for a thin, a thick, and a thick device with doped hole transporting layer.

organic light-emitting diodes (OLEDs) it is known that the conductivity of the polyTPD increases superlinearly when it is partially oxidized (doped).²⁵ Yet, high doping levels may hamper the layer's ability to block electrons, therefore, for this study we replaced the pristine polyTPD with a slightly oxidized version polyTPD (0.05% oxidized). Using this doped electron blocking/hole transporting layer solar cells were prepared with perovskite layer thickness of 900 nm (Fig. 4).

With this partially oxidized polyTPD layer the FF of the solar cells at 1 sun light intensity is recovered and reaches values similar of the devices with perovskite layers up to 400 nm (Table II). The V_{oc} seems not to be affected by the doping of the polyTPD and remains almost the same as with the undoped thick cell (slightly below 1 V). Due to the slightly higher J_{sc} , the slightly lower V_{oc} and similar FF, the PCE of the solar cells with perovskite layer thicknesses of 285 and 900 nm reaches 12.7% and 12.0%, respectively. This is yet another example of the high electronic quality of organic-inorganic lead halide perovskite materials. It can be attributed to the large charge carrier diffusion lengths observed in solution processed $\text{CH}_3\text{NH}_3\text{PbI}_3$ perovskite. As mentioned in these studies the observed diffusion lengths depend on the preparation method, therefore, it is possible that in evaporated $\text{CH}_3\text{NH}_3\text{PbI}_3$ perovskite layer even larger diffusion length of charge carriers are present. The effect of the doped polyTPD layer on cells employing a thinner perovskite layer was negligible (Fig. S4 of the supplementary material).²⁴

Our device architecture employing PEDOT:PSS and ITO as the anode and Au as the cathode, the built-in potential is expected to be small in view of the small off set in work functions of these two electrodes (5.0 and 5.1 eV, respectively). However, it is known that the interactions of metals and organics can change the effective work functions. This built-in potential assists in the separation of electrons to one direction and holes to the opposite one. Using capacitance voltage scans an estimate of the flat band potential around 1 V was obtained, confirming the presence of a built-in potential (Fig. S5 of the supplementary material).²⁴ Following the p-i-n model suggested to describe how these devices work, increasing the doping in the selective contacts leads to an increase in the built-in potential in the absorber. This can explain the large difference in FF between low and high light intensities for the thick devices: at low light intensity, most of the built in potential is still present leading to high FF; at high light intensities the bands are flatter and hence the lower FF. This will not be so in thin devices as the electric field is larger (the potential difference being the same, yet the layer being thinner). Another support for this hypothesis we find in the dark J-V of the various devices (Fig. S6 of the supplementary material), where the diode onset is shifted to higher voltages when the polyTPD in the thick device is doped.²⁴ Our results demonstrate that the solar cell performance is high over a wide range of thicknesses (300–900 nm) simplifying large area processing requirements, hence facilitating industrial production scales.

To conclude, methylammonium lead iodide perovskite solar cells have been prepared with a wide range of active layer thicknesses. With undoped hole transport layers the best performances are obtained for solar cells with a perovskite layer thickness around 300 nm, reaching a PCE of 12.7%

TABLE II. Current density–voltage data of ITO/PEDOT:PSS/polyTPD/CH₃NH₃PbI₃/PCBM₆₀/Au at different perovskite thicknesses.

CH ₃ NH ₃ PbI ₃ [nm]	J _{sc} [mA/cm ²]	V _{oc} [V]	FF [%]	PCE [%]
210	14.7	1.04	0.56	8.6
250	16.7	1.04	0.61	10.6
285	18.8	1.07	0.63	12.7
370	18.5	0.97	0.52	9.3
390	18.2	1.03	0.46	8.6
680	19.5	0.94	0.44	8.1
900	19.8	0.92	0.4	7.2
900 ^a	19.5	0.94	0.65	12.0

^aThis device corresponds to ITO/ PEDOT:PSS/doped-polyTPD (0.05% AgSbF₆)/CH₃NH₃PbI₃/PCBM₆₀/Au configuration.

in this series. However, if the hole transport materials is slightly doped by adding a small amount of an oxidant to it, the solar cell performance is almost independent on perovskite layer thickness. For a device with a perovskite layer thickness of 900 nm, a PCE of 12% was obtained only slightly below that of the best device with a perovskite layer thickness of 300 nm. These results demonstrate that the carriers generated in this layer do not suffer from recombination losses even in such very thick layers, corroborating earlier reports of long carrier diffusion lengths.

All chemicals and solvents used were obtained from Sigma-Aldrich and used as received unless stated otherwise. ITO covered glass substrates were purchased from NaranjoSubstrates. PEDOT:PSS CLEVIOS P VP Al 4083 was purchased from Hereaus Holding and used as received. Poly[N,N'-bis(4-butylphenyl)-N,N'-bis(phenyl)benzidine (polyTPD) was purchased from American Dye Source and [6,6]-phenyl C61-butyric acid methylester (PCBM₆₀) from Solenne B.V. Both of them were used as received. For their application they were dissolved in chlorobenzene solutions (7 mg ml⁻¹ and 10 mg ml⁻¹, respectively). Doped-poly(TPD) corresponds to 7 mg ml⁻¹ of polyTPD with a 0.05 molar% in AgSbF₆ purchased from Sigma-Aldrich. Solutions were freshly prepared before using. PbI₂ was purchased from Sigma-Aldrich and CH₃NH₃I was synthesized following the procedure previously reported.²⁶ In short, CH₃NH₃I was synthesized by reacting 26 ml of methylamine (40 wt.% in water) and 10 ml of hydroiodic acid (57 wt.% in water) in a 250 ml round-bottomed flask at 0 °C for 2 h under magnetic stirring. The white precipitate was recovered by evaporation at 50 °C for 1 h. The product was dissolved in ethanol, filtered and recrystallized from diethyl ether and dried at 70 °C in an oven for 24 h. Fresh CH₃NH₃I was synthesized before each set of experiments. Perovskite was synthesized using a vacuum chamber of MBraun integrated in an inert glovebox (MBraun). The starting materials were placed in ceramic crucibles which were heated up from two evaporation sources from Creaphys. The substrates were placed at 20 cm from the top of the ceramic crucibles. A shutter was present below the substrate holder, being closed until the adequate PbI₂/CH₃NH₃I ratio was achieved. At a pressure of 1 × 10⁻⁶ mbar, CH₃NH₃I was heated to 70 °C. Once the sensor reading was stable, PbI₂ was heated until 250 °C to obtain dark brown perovskite layers. The process was followed by three quartz microbalance sensors placed in the chamber. Typically 4 cells of 0.06 cm² are present on each substrate. Up to 5 substrates can be coated with the perovskite in one single co-evaporation step.

All the characterizations, except the UV-Vis absorption spectra and profilometer measurements, were done in a nitrogen filled glove box (<0.01 ppm O₂ and <0.1 ppm H₂O) without exposure to ambient. Absorption measurements were done using a fibre-optics based Aventas Avaspec 2048 spectrometer. J-V curves were recorded in a MiniSun simulator by ECN the Netherlands. During the measurements, the devices were illuminated by a white light halogen lamp and using a mask overlaying the sample which only illuminated the active area of the cells. Before each measurement, the exact light intensity was determined using a calibrated Si reference diode equipped with an infrared cut-off filter (KG-3, Schott). An estimation of the short-circuit current density (J_{sc}) under standard test conditions was calculated by convolving the external quantum efficiency (EQE) spectrum with the AM1.5G reference spectrum, using the premise of a linear dependence of J_{sc} on light intensity.

Current-voltage (J-V) curves were measured using a Keithley 2400 source measure unit. The scan was performed with steps of 0.01 V starting from -0.2 V to 1.1 V with a time delay between each point set to 0.01 s. The perovskite films were characterized by using grazing incidence X-ray diffraction (GIXRD) after its evaporation. The measurements were done at room temperature in the 2θ range 5° – 50° on an Empyrean PAN analytical powder diffractometer, using Cu K α radiation. The capacitance-voltage measurements were performed using a Keithley 4200-SCS parameter analyzer. Voltage sweeps were performed with a step of 0.05 V in the range from -0.8 to $+0.8$ V (33 points for each sweep). The capacitance values were obtained by measuring the impedance of the samples at 1 KHz frequency and with an applied ac voltage of 10 mV rms. During the measurements, the samples were kept inside a Faraday cage, to screen them from external electromagnetic interferences.

This work was supported by the Spanish Ministry of Economy and Competitiveness (MINECO) (MAT2011-24594), the Generalitat Valenciana (Prometo/2012/053). E.B. acknowledges MINECO for an FPI grant. C.R.-C. would like to thank the MINECO for the financial support of this research in the framework of project CTQ2010-17481, the Junta de Andalucía (CICYE) for special financial support (P10-FQM-6703), and the MECED (Spanish Ministry of Education, Culture, and Sport) for a FPU grant.

- ¹ P. Gao, M. Grätzel and M. K. Nazeeruddin, "Organohalide lead perovskites for photovoltaic applications," *Energy Environ. Sci.* (published online).
- ² H. J. Snaith, *J. Phys. Chem. Lett.* **4**(21), 3623–3630 (2013).
- ³ C. R. Kagan, D. B. Mitzi, and C. D. Dimitrakopoulos, *Science* **286**(5441), 945–947 (1999).
- ⁴ A. Poglitsch and D. Weber, *J. Chem. Phys.* **87**(11), 6373–6378 (1987).
- ⁵ A. Kojima, K. Teshima, Y. Shirai, and T. Miyasaka, *J. Am. Chem. Soc.* **131**(17), 6050–6051 (2009).
- ⁶ M. M. Lee, J. Teuscher, T. Miyasaka, T. N. Murakami, and H. J. Snaith, *Science* **338**(6107), 643–647 (2012).
- ⁷ J. M. Ball, M. M. Lee, A. Hey, and H. J. Snaith, *Energy Environ. Sci.* **6**(6), 1739–1743 (2013).
- ⁸ J. Burschka, N. Pellet, S.-J. Moon, R. Humphry-Baker, P. Gao, M. K. Nazeeruddin, and M. Grätzel, *Nature (London)* **499**(7458), 316–319 (2013).
- ⁹ M. Liu, M. B. Johnston, and H. J. Snaith, *Nature (London)* **501**(7467), 395–398 (2013).
- ¹⁰ O. Malinkiewicz, A. Yella, Y. H. Lee, G. M. Espallargas, M. Grätzel, M. K. Nazeeruddin, and H. J. Bolink, *Nat. Photon* **8**(2), 128–132 (2014).
- ¹¹ D. Liu and T. L. Kelly, *Nat. Photon* **8**(2), 133–138 (2014).
- ¹² J.-Y. Jeng, Y.-F. Chiang, M.-H. Lee, S.-R. Peng, T.-F. Guo, P. Chen, and T.-C. Wen, *Adv. Mater.* **25**(27), 3727–3732 (2013).
- ¹³ S. Sun, T. Salim, N. Mathews, M. Duchamp, C. Boothroyd, G. Xing, T. C. Sum, and Y. M. Lam, *Energy Environ. Sci.* **7**(1), 399–407 (2014).
- ¹⁴ Q. Wang, Y. Shao, Q. Dong, Z. Xiao, Y. Yuan, and J. Huang, *Energy Environ. Sci.* **7**, 2359–2365 (2014).
- ¹⁵ O. Malinkiewicz, C. Roldán, A. Soriano, E. Bandiello, L. Camacho, M. K. Nazeeruddin, and H. J. Bolink, *Adv. Energy Mater.* **4**, 1400345 (2014).
- ¹⁶ G. Xing, N. Mathews, S. Sun, S. S. Lim, Y. M. Lam, M. Grätzel, S. Mhaisalkar, and T. C. Sum, *Science* **342**(6156), 344–347 (2013).
- ¹⁷ S. D. Stranks, G. E. Eperon, G. Grancini, C. Menclauou, M. J. P. Alcocer, T. Leijtens, L. M. Herz, A. Petrozza, and H. J. Snaith, *Science* **342**(6156), 341–344 (2013).
- ¹⁸ E. Edri, S. Kirmayer, A. Henning, S. Mukhopadhyay, K. Gartsman, Y. Rosenwaks, G. Hodes, and D. Cahen, *Nano Lett.* **14**(2), 1000–1004 (2014).
- ¹⁹ C. Wehrenfennig, G. E. Eperon, M. B. Johnston, H. J. Snaith, and L. M. Herz, *Adv. Mater.* **26**(10), 1584–1589 (2014).
- ²⁰ P. Docampo, J. M. Ball, M. Darwich, G. E. Eperon, and H. J. Snaith, *Nat. Commun.* **4**, 2761 (2013).
- ²¹ T. Kelly, in proceedings of the HOPV14 conference, Lausanne, 2014.
- ²² O. Malinkiewicz, M. Lenes, H. Brine, and H. J. Bolink, *RSC Adv.* **2**(8), 3335–3339 (2012).
- ²³ T. Baikie, Y. Fang, J. M. Kadro, M. Schreyer, F. Wei, S. G. Mhaisalkar, M. Grätzel, and T. J. White, *J. Mater. Chem. A* **1**(18), 5628–5641 (2013).
- ²⁴ See supplementary material at <http://dx.doi.org/10.1063/1.4890056> for additional information such as x-ray, J-V data, and C-V data.
- ²⁵ S. Cheylan, J. Puigdollers, H. J. Bolink, E. Coronado, C. Voz, R. Alcubilla, and G. Badenes, *J. Appl. Phys.* **103**(9), 096110 (2008).
- ²⁶ L. Etgar, P. Gao, Z. Xue, Q. Peng, A. K. Chandiran, B. Liu, M. K. Nazeeruddin, and M. Grätzel, *J. Am. Chem. Soc.* **134**(42), 17396–17399 (2012).

Supporting Information

Efficient methylammonium lead iodide perovskite solar cells with active layers from 300 to 900 nm.

C. Momblona, O. Malinkiewicz, C. Roldán-Carmona, A. Soriano, L. Gil-Escrig, E. Bandiello, M. Scheepers, E. Edri, and H. J. Bolink^{*})

Content:

1. X-ray diffraction spectrum of different perovskite thicknesses.
2. J_{sc} , V_{oc} , FF and PCE values as a function of perovskite thickness.
3. Dependence of J_{sc} , FF and V_{oc} on percentage of incident light intensity.
4. $J - V$ curve of a 300 nm perovskite thickness device with doped and undoped polyTPD layer.
5. Capacitance voltage curve for a device with a 300 nm perovskite thickness.
6. Dark $J - V$ curves for 300 and 900 nm perovskite thickness devices with doped and undoped polyTPD layer.

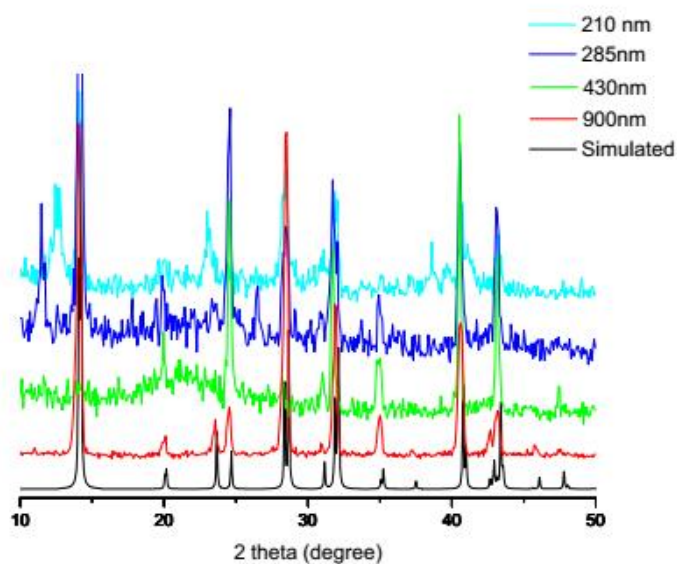


FIG S1. X-ray diffraction spectrum of different perovskite thicknesses. Typically four repeated measurements were collected and merged into a single diffractogram. Pawley refinements, were performed using the TOPAS computer program and revealed an excellent fit to a one-phase model with a tetragonal cell ($a = 8.80(2)$, $c = 12.57(2)$ Å) and space group $I4/ cm$.

REFERENCIAS: (G. S. Pawley, *J. Appl. Cryst.*, 1981, 14, 357-361.

4. Coelho, A. A. TOPAS-Academic, Version 4.1, 2007, see: [http:// www.topas-academic.net](http://www.topas-academic.net))

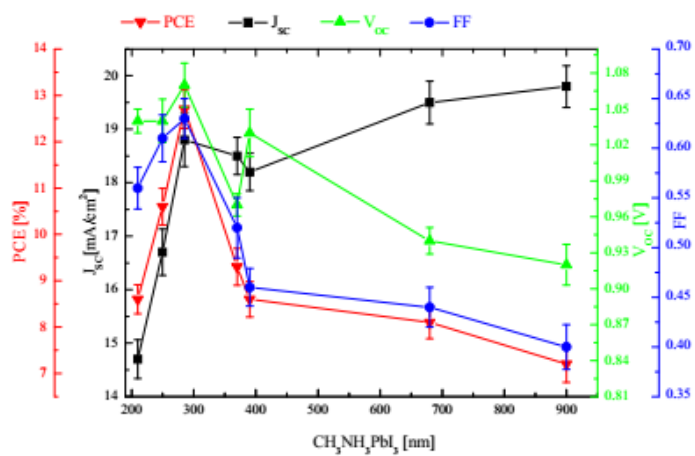


FIG S2. J_{sc}, V_{oc}, FF and PCE values as a function of perovskite thickness with statistical data taken from 5 to 10 cells.

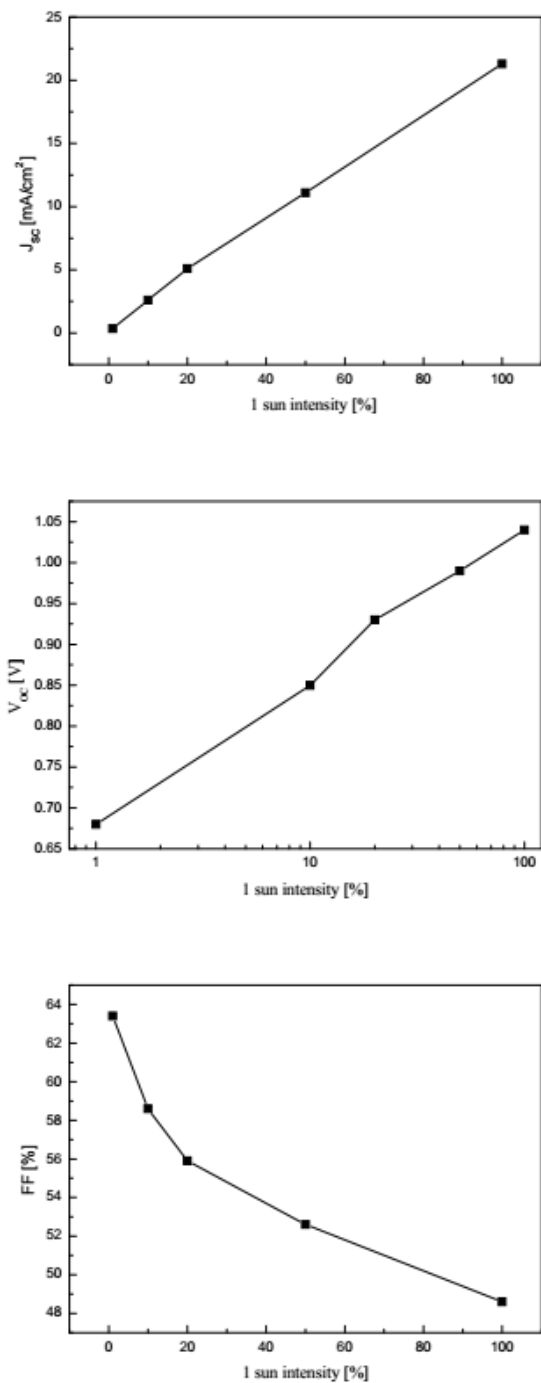


FIG S3. J_{sc} , V_{oc} , FF and PCE values as a function of sun intensity percentage.

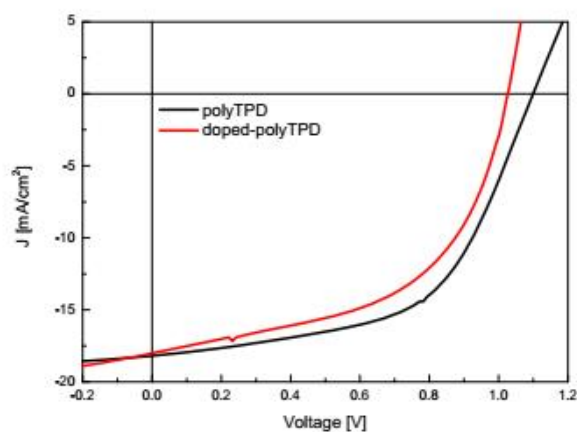


FIG S4. J – V curves for 300 nm perovskite thickness devices with the configuration: a) ITO/PEDOT:PSS/polyTPD/CH₃NH₃PbI₃/PCBM /Au and b) ITO/PEDOT:PSS/doped-polyTPD (0.05% AgSbF₆)/CH₃NH₃PbI₃/PCBM /Au.

TABLE S1. J – V characteristics data of different perovskite thickness devices.

CH ₃ NH ₃ PbI ₃ [nm]	J _{SC} [mA/cm ²]	V _{OC} [V]	FF [%]	PCE [%]
210	14.7	1.04	0.56	8.6
250	16.7	1.04	0.61	10.6
285	18.8	1.07	0.63	12.7
300	18.1	1.10	0.56	11.2
300*	18.0	1.03	0.51	9.6
370	18.5	0.97	0.52	9.3
390	18.2	1.03	0.46	8.6
680	19.5	0.94	0.44	8.1
900	19.8	0.92	0.4	7.2
900*	19.5	0.94	0.65	12.0

* These devices correspond to ITO/ PEDOT:PSS/doped-polyTPD (0.05% AgSbF₆)/CH₃NH₃PbI₃/PCBM₆₀/Au configuration

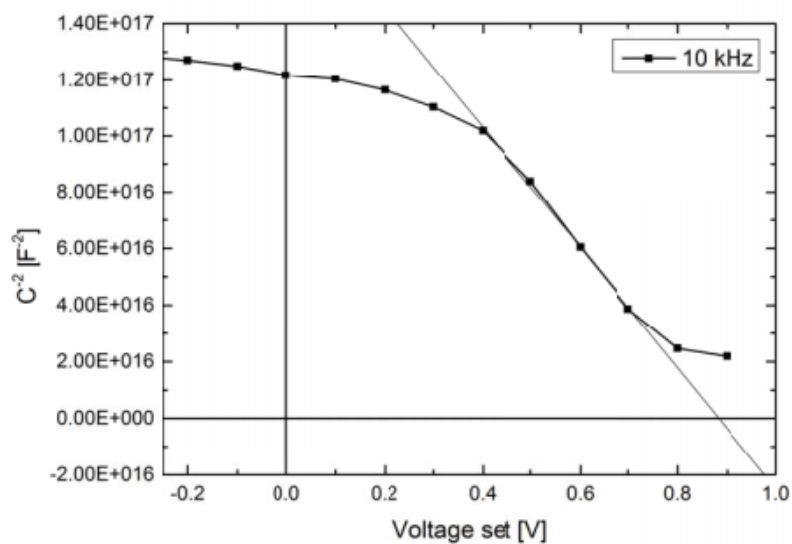


FIG. S5. Capacitance versus voltage for a device with a 300 nm perovskite layer and an undoped polyTPD layer.

The capacitance-voltage measurements were performed using a Keithley 4200-SCS parameter analyzer. Voltage sweeps were performed with a step of 0.05 V in the range from -0.8 to +0.8 V (33 points for each sweep). The capacitance values were obtained by measuring the impedance of the samples at 10 KHz frequency and with an applied ac voltage of 10 mV rms. During the measurements, the samples were kept inside a Faraday cage, to screen them from external electromagnetic interferences.

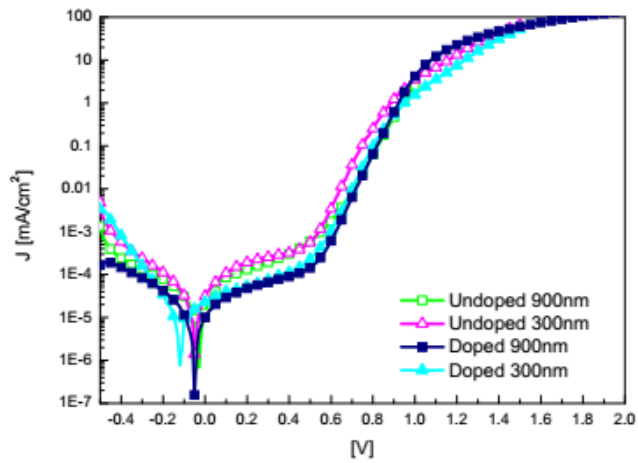


FIG. S6. Current density versus voltage in the dark for thick and thin cells using either doped or an undoped polyTPD layer.



Cite this: *Energy Environ. Sci.*,
2016, 9, 3456

Efficient vacuum deposited p-i-n and n-i-p perovskite solar cells employing doped charge transport layers†

Cristina Momblona,[‡] Lidón Gil-Escrig,[‡] Enrico Bandiello,^a Eline M. Hutter,^b Michele Sessolo,^a Kay Lederer,^c Jan Blochwitz-Nimoth^{*c} and Henk J. Bolink^{*a}

Methylammonium lead halide perovskites have emerged as high performance photovoltaic materials. Most of these solar cells are prepared *via* solution-processing and record efficiencies (>20%) have been obtained employing perovskites with mixed halides and organic cations on (mesoscopic) metal oxides. Here, we demonstrate fully vacuum deposited planar perovskite solar cells by depositing methylammonium lead iodide in between intrinsic and doped organic charge transport molecules. Two configurations, one inverted with respect to the other, p-i-n and n-i-p, are prepared and optimized leading to planar solar cells without hysteresis and very high efficiencies, 16.5% and 20%, respectively. It is the first time that a direct comparison between these two opposite device configurations has been reported. These fully vacuum deposited solar cells, employing doped organic charge transport layers, validate for the first time vacuum based processing as a real alternative for perovskite solar cell preparation.

Received 20th July 2016,
Accepted 20th September 2016

DOI: 10.1039/c6ee02100j

www.rsc.org/ees

Broader context

High efficiency perovskite solar cells are mostly prepared using solution based processes. Solution based processing, if carried out in air on a large area and using benign solvents, can be a very cost-efficient production method. On the other hand, vacuum based coating techniques have a higher initial cost, yet at high production volumes the depreciation of the equipment becomes a small fraction of the total photovoltaic module cost. In fact, vacuum deposition is a widely used technique in the electronic and photovoltaic industry. Additionally, it allows for conformal and additive coatings, which is beneficial for flexible or tandem device structures. As no (toxic) solvents are employed in vacuum processes, ultra-dry films are obtained. In this study, we have prepared planar solar cells employing a 500 nm layer of the CH₃NH₃PbI₃ perovskite absorber, sandwiched in between small molecular weight organic charge transport molecules, using only vacuum based processes. Both of the commonly used perovskite device architectures, p-i-n and n-i-p, in which the polarity of the front contact is inverted with respect to each other have been prepared. By rational combination of intrinsic and molecularly doped charge transport layers, we obtain hysteresis-free planar solar cells with power conversion efficiencies up to 20% for 0.1 cm² and 15% for cell areas close to 1 cm². These results validate vacuum techniques as a production method for high efficiency perovskite solar cells.

Thin-film photovoltaics is a promising technology for low-cost and sustainable renewable energy sources. Organic-inorganic (hybrid) lead halide perovskite solar cells have recently aroused wide interest in photovoltaic applications because of their impressive power conversion efficiencies (PCEs), now exceeding 21%.^{1–3} Importantly, the perovskite thin-film absorber can be deposited using low-cost and abundant starting materials, hence with a large potential for the preparation of inexpensive

photovoltaic devices.⁴ High PCEs are the result of a very high absorption coefficient and mobilities of the photogenerated electrons and holes of the hybrid perovskites.^{5,6} While the use of the archetype perovskite, methylammonium lead iodide (MAPbI₃), can lead to high efficiency devices,^{7,8} a further decrease of the bandgap by incorporation of formamidinium (FA), allows for the harvesting of additional near-infrared photons.⁹ When such a mixed organic cation perovskite is further stabilized by replacing part of the iodide with bromide, and/or by partial cesium incorporation, the champion materials for perovskite cells are obtained.^{3,10–12} Two main solar cell architectures have been used so far. One of them is derived from dye-sensitized solar cells, and consists of a transparent conductive substrate coated with a mesoporous/planar TiO₂ layer (n-type, hence acting as the electron transport layer, ETL) into/onto which the perovskite absorber is applied.^{13–15} A hole

^a Instituto de Ciencia Molecular, Universidad de Valencia, C/Catedrático J. Beltrán 2, 46980 Paterna, Valencia, Spain. E-mail: henk.bolink@uv.es

^b Department of Chemical Engineering, Delft University of Technology, Van der Maasweg 9, 2629 HZ Delft, The Netherlands

^c NOVALED GmbH, Tatzberg 49, 01307 Dresden, Germany. E-mail: jan.bn@novaled.com

† Electronic supplementary information (ESI) available. See DOI: 10.1039/c6ee02100j

‡ These authors contributed equally to this work.

transport layer (HTL, p-type), usually consisting of organic semiconductors, is then deposited on top of the perovskite and the device is completed with an evaporated top electrode. The second common configuration is inverted compared to the one mentioned above, and the conductive substrate is coated with a HTL, followed by the perovskite absorber and an ETL, coated with a suitable evaporated top electrode.^{16,17} While in the perovskite solar cell literature these two device configurations have been referred to as “conventional” and “inverted”, a less confusing nomenclature, n-i-p and p-i-n, will be used throughout this manuscript. Recently, Chen *et al.* demonstrated that the PCE in planar devices can be improved by increasing the conductivity of the metal oxide layers by incorporating heteroatoms with different valences.¹⁸ The increase in the conductivity was limited, however (approximately one order of magnitude), limiting the thickness of the metal oxide layers to 20 nm. An alternative strategy to improve the conductivity of charge transport layers is the use of doped organic semiconductors. These materials have been widely studied for organic light-emitting diodes (OLEDs) and small molecular weight organic solar cells (OPVs). In these applications they have proven to enhance charge carrier injection as well as transport, and more manufacturing oriented properties such as large area uniformity and yield.^{19–21} In doped organic semiconductors the conductivity can be varied over several orders of magnitude by varying the doping concentration, yet without an associated strong increase in the optical absorption of the layer. This is advantageous because it allows the use of rather thick (100 nm) doped layers generating additional freedom to design/fine-tune the device architecture.

Most reported solar cells using a vacuum deposited perovskite layer still employ charge transport layers processed from solution.^{22–24} Fully vacuum deposited perovskite devices would offer the additional advantage of being compatible with temperature-sensitive substrates, allowing for conformal coatings on non-planar substrates and for the straightforward implementation into tandem solar cells.²⁵ Additionally, vacuum processing is an established technique in the electronic industry demonstrating high throughput and reliability.²⁶ In principle, solution processing of the semiconductor can be an inexpensive alternative to vacuum deposition, however, the impact of processing costs is very limited on the overall module price, which is dominated by the material cost. Polander *et al.* were the first to demonstrate fully vacuum deposited cells where open circuit voltages (V_{oc}) as high as 1.1 V were obtained.²⁷ The highest efficiency (15.4%) reported for fully vacuum deposited perovskite solar cells was produced from a device with rather high hysteresis, which used undoped organic molecules as the charge extraction materials.^{28,29}

Here, we present fully vacuum deposited planar perovskite solar cells in which the perovskite layer is sandwiched in between two charge extraction double-layers. The latter consist of a thin layer of pristine organic charge transport molecules and a thicker layer of the same molecules that are partially oxidized (in the case of the hole transporter) or reduced (in the case of the electron transport layer). The partial oxidation or reduction of the charge transport molecules leads to p- and n-type doped layers, respectively, with a significantly enhanced conductivity. These multi-layer solar

cells have been prepared in both the p-i-n and n-i-p architectures, allowing for a direct comparison between these two designs. We demonstrate that the presence of thin undoped layers is beneficial for device performance. Average power conversion efficiencies of 15% and 18% are obtained for the p-i-n and n-i-p architectures, respectively, bringing vacuum deposited perovskite solar cells closer to their solution-processed equivalents.

The MAPbI₃ perovskite thin films were prepared by co-evaporation of the two starting compounds, CH₃NH₃I and PbI₂. Details of the experimental conditions for the perovskite layer have been described previously and are presented in the ESI†²³ Out of the two perovskite precursors, CH₃NH₃I and PbI₂, the first is somewhat complicated to sublime. However, once properly outgassed (using the high vacuum of the evaporation chamber) the material is sublimed similarly to small molecular weight organic molecules, that is, the rate of evaporation is stable as monitored by the microbalance crystal sensors that are positioned in the chamber. These films were characterized using grazing incidence X-ray diffraction (GIXRD), showing the typical diffraction pattern for this material which is independent of the type of under-layer employed (Fig. S1a in the ESI†). Scanning electron microscopy (SEM) images both of the perovskite surface (Fig. S1b in the ESI†) and of the device cross-section (Fig. 1) show a dense packing of crystals, virtually without any pinholes, that have an average domain size of approximately 100 nm. The surface is homogeneous and smooth with a roughness (root mean square), estimated using atomic force microscopy over an area of 25 μm², of only 10.1 nm (Fig. S2 in the ESI†). The optical absorption spectra of these films show the expected MAPbI₃ band-to-band transition at 780 nm and high absorbance over the whole visible spectra (Fig. S1c in the ESI†). The perovskite film formation is very reproducible and the layer properties did not change over a period of 6 months during which the experiments described in this manuscript were performed. Planar diodes were prepared by sandwiching a 500 nm thick perovskite layer in between organic HTLs and ETLs, initially, the former on top of a pre-patterned indium tin oxide (ITO) coated glass substrate and by thermally evaporating a metal top contact on the latter. A vacuum evaporated MAPbI₃ layer of 500 nm was selected as it was shown that almost all sub-bandgap sunlight is absorbed and all the charge carriers can still reach the respective interfaces.³⁰ Both organic charge transport layers were prepared by vacuum sublimation of the corresponding organic molecules to a layer thickness of 10 nm. The hole transport molecule we selected is a derivative of an arylamine, N₄,N₄,N₄′,N₄′-tetra[[1,1′-biphenyl]-4-yl]-[1,1′:4′,1′′-terphenyl]-4,4′′-diamine (TaTm) (Fig. 1) and was chosen due to its very stable sublimation conditions and tendency to form completely amorphous films. The fullerene C₆₀ was selected as the electron transport molecule as it is also easy to sublime and has proven to be an efficient electron acceptor in perovskite solar cells.^{29,31} To ensure sufficient statistics for each device configuration mentioned in this report, at least 2 different devices each containing 4 cells were evaluated, while for top performing configurations at least 5 different devices with a total of 20 cells were characterized. The device area used, defined as the

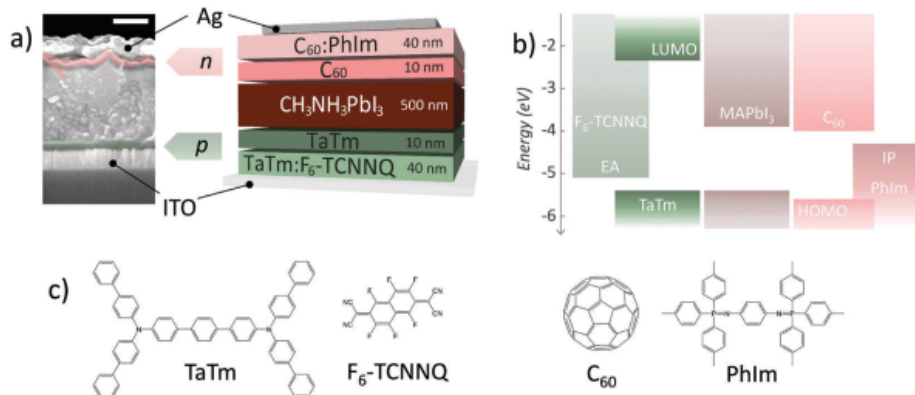


Fig. 1 (a) SEM cross-section and schematics of a completed p-i-n solar cell (scale bar 200 nm). (b) Flat band energy diagrams of the materials employed (the electron affinity, EA, and ionization potential, IP, of the dopants are also reported). (c) Chemical structures of the organic molecules used to prepare the charge transport layers.

aperture of the shadow mask, was 1 mm² and for top performing devices, larger areas of 10, 27 and 85 mm² were also used.

Using the architecture described above, employing single layers of hole and electron extraction molecules (without any electrical dopant), the photovoltaic performance of the diodes under 1 Sun illumination was rather poor, due to a pronounced s-shape of the current density (J) versus voltage (V) curve, leading to poor fill factors (FF) and hence low PCE values (Fig. S3 and Table S1, in the ESI[†]). This indicates that the extraction of the charge carriers is severely hindered, either due to the high resistance of the organic charge transport layers or to the presence of an extraction barrier at the electrode interfaces. To reduce the series resistance of the charge transport layers and to ensure an ohmic contact between them and the electrodes we prepared partially oxidized and reduced HTL and ETL, respectively, by co-evaporation of the charge transport molecules with a suitable reactant (see Fig. 1). This method allows for precise control of the ratios of each molecule in the sublimed film by carefully monitoring the evaporation rate using micro-balance sensors during the evaporation process. Here we selected molecular dopants due to their intrinsic advantages over inorganic reactants,³² *i.e.* the molecular dopants that typically evaporate in a suitable temperature range between 100 °C and 400 °C are less prone to oxidation when handling in air and are more diffusion stable inside the organic layers. For the HTL we used 2,2'-(perfluoronaphthalene-2,6-diylidene) dimalononitrile (F₆-TCNNQ) as the organic dopant whereas for the C₆₀ ETL, *N*₁,*N*₄-bis(tri-*p*-tolylphosphoranylidene)-benzene-1,4-diamine (PhIm) (Fig. 1) was employed. In OPVs, the presence of a thin layer of pure, undoped charge transport molecules in between the doped layers and the light-absorber is often found to be beneficial. Therefore, we used this device architecture (Fig. 1) as the starting point to study the effect of dopant concentration on device performance.

To verify the optimum dopant concentration in the p-HTL we first kept the dopant concentration in the n-ETL constant at 30 wt%. The main effect of an increasing F₆-TCNNQ

concentration is the increase in the FF from 55% for a F₆-TCNNQ concentration of 3 wt% to a maximum of 74% at an F₆-TCNNQ concentration of 11 wt%. This trend reflects the increased conductivity of the p-HTL for increasing doping levels, as measured by depositing co-evaporated films on interdigitated electrodes (Fig. S4 in the ESI[†]). Hence, charges are extracted more efficiently as the p-HTL conductivity increases. The open circuit voltage (V_{oc}) increases as well with increasing F₆-TCNNQ concentration going from 1053 mV to 1082 mV. This effect is likely to be a consequence of a reduction in the charge recombination due to the more efficient charge carrier extraction from the perovskite to the external contacts. The short-circuit current density (J_{sc}), however, decreases when the F₆-TCNNQ concentration is increased. This is due to the higher absorbance of the p-HTL (Fig. S5 in the ESI[†]), diminishing the light intensity reaching the perovskite absorber and hence decreasing the device EQE (Fig. 2a).

Due to this reduction in J_{sc} we found an optimum in the average PCE of 15.4% at a F₆-TCNNQ concentration of 11 wt%. Once established, the optimum dopant concentration in the p-HTL at 11 wt%, the amount of dopant in the n-ETL was varied. The effect of the dopant concentration in the n-ETL on the photovoltaic performance is not very pronounced (Fig. S6a in the ESI[†]). This indicates that in the dopant range studied, the conductivity of the n-ETL is sufficiently high to ensure an efficient electron extraction to the electrodes. Indeed, even for rather low PhIm concentrations, the conductivity of the n-ETL is already higher than that of the p-HTL (Fig. S4 in the ESI[†]) which supports this assumption. Importantly, the efficiency of the p-i-n devices is essentially unvaried (we observe only a small reduction of the FF) when the thickness of the doped transport layers is increased from 40 to 90 nm (Fig. S6b in the ESI[†]).

One of the benefits of vacuum deposition is the insensitivity towards the substrate to be coated, which allows preparation of inverted devices (n-i-p) using the same materials and layers as described above, simply by evaporating them in the reverse order. The only difference is the top metal electrode, Ag for the

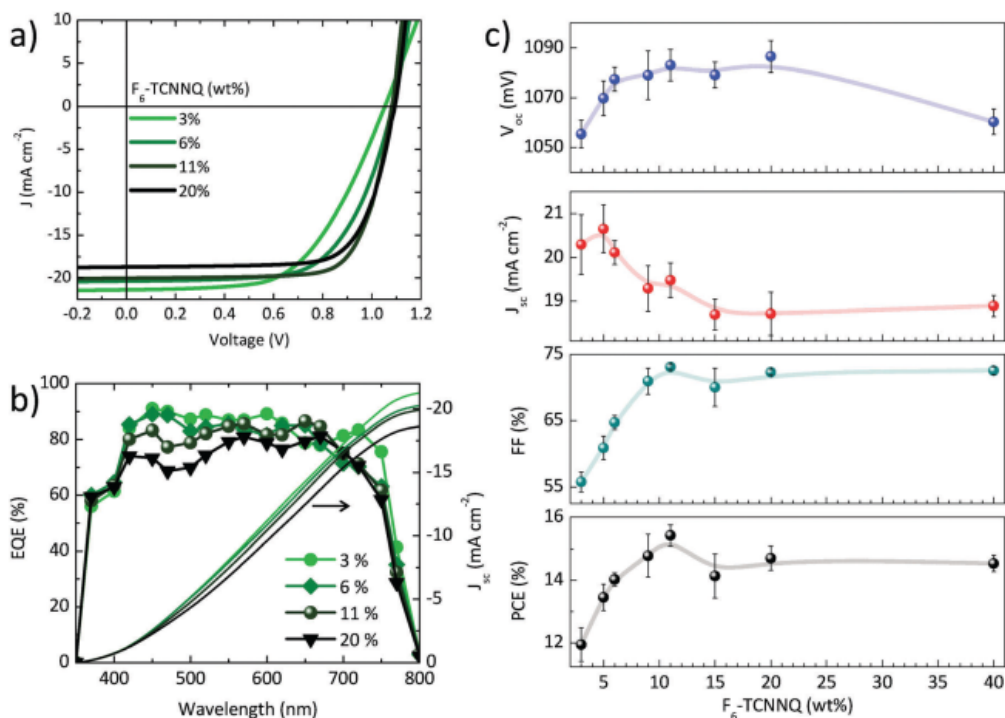


Fig. 2 (a) J - V curves under 100 mW cm^{-2} illumination and (b) external quantum efficiency (EQE) as a function of F_6 -TCNNQ concentration for the p-i-n solar cells (the integrated photocurrent with the AM1.5G solar spectrum is shown on the right axis). (c) Evolution of the key parameters deduced from the J - V curves, V_{oc} , J_{sc} , FF and PCE, as a function of F_6 -TCNNQ concentration.

p-i-n cells and Au for the n-i-p cells (Au was used for its higher work function). The n-i-p devices are particularly interesting as to date most perovskite solar cells in this configuration employ metal oxides as the ETL, and only very few reports used a purely organic electron acceptor below the perovskite layer.²⁹

In Fig. 3, a cross-sectional SEM image of a completed n-i-p solar cell is depicted, showing a dense perovskite film with low roughness and a conformal coating of the thin organic charge transport layers. The J - V characteristics under 100 mW cm^{-2} illumination employing a fixed F_6 -TCNNQ concentration of 11 wt% in the p-HTL and with varying PhIm (n-dopant)

concentrations are shown in Fig. 3b. The J_{sc} increases slightly with increasing PhIm content and reaches an average of 20 mA cm^{-2} for the highest n-dopant concentration. This is a consequence of the reduced C_{60} content and the subsequently reduced optical absorbance of the n-ETL (Fig. S5b in the ESI[†]), here used as the front contact. The higher transmittance is also the origin of the observed increase in the EQE with increasing PhIm content (Fig. 3c). The V_{oc} and FF do not change significantly in the n-dopant range evaluated, maintaining values as high as 1.1 V and 80%, respectively. These parameters lead to PCEs of 18% on average (Fig. S7 in the ESI[†]) with one pixel exceeding 20% for

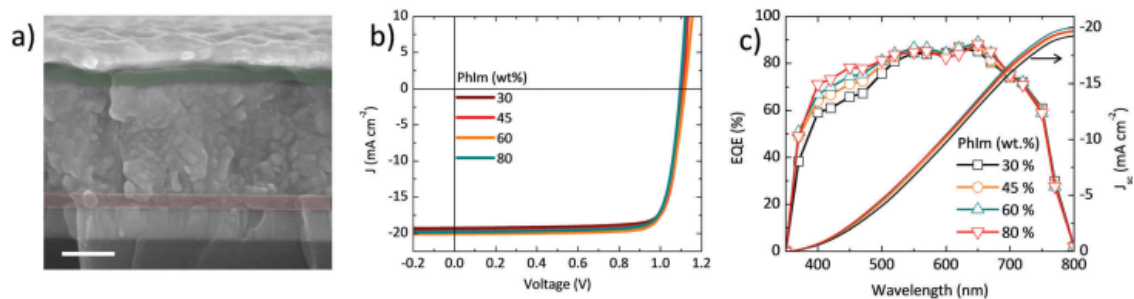


Fig. 3 (a) Cross-sectional SEM image of a completed n-i-p solar cell (scale bar 200 nm). (b) J - V curves under 100 mW cm^{-2} illumination and (c) EQE spectra (the integrated photocurrent with the AM1.5G solar spectrum is shown on the right axis) as a function of PhIm concentration.

the record n-i-p cell (Fig. S8 in the ESI†) obtained with a PhIm concentration of 60 wt%. These efficiency values might be surprising considering the rather small crystal size observed in our MAPbI₃ thin films (50–200 nm), and somehow contradict the accepted view for the need for large crystals in order to have long charge diffusion length and efficient charge collection.³³ Hence, we estimated the charge carrier diffusion length by means of time resolved microwave conductivity (TRMC) measurements on MAPbI₃ films deposited on quartz substrates (see ESI† for details on the characterization). The samples were illuminated with a 650 nm laser, and the excitation intensity was tuned in order to obtain a charge concentration of approximately 10¹⁵ cm⁻³, which is comparable to excitation under standard AM1.5 illumination.³⁴ Under these conditions, the effective mobility was determined to be 3.9 cm² (V s)⁻¹, with a half lifetime of 210 ns (Fig. S9 in the ESI†). Considering these parameters, the charge carrier diffusion length is determined to be ~1.5 μm, in agreement with previous estimations on solution-processed MAPbI₃ films.^{35,36} Besides the impact of the grain size on the carrier diffusion length, the nature of the grain boundaries and defects in perovskite will have a substantial influence as well. Many reports have highlighted that grain boundaries in perovskites are substantially benign, since they do not generate any states within the bandgap of MAPbI₃.³⁷ Such effects might be responsible for the high charge diffusion length observed here, leading to efficient solar cells even with perovskite films composed of relatively small crystals.

Motivated by the high PCE obtained for the n-i-p devices, a series of cells with increasing area (for both the electrode overlap and the shadow mask aperture, see the Experimental part in the ESI† for details) were prepared. The FF decreases with increasing area, causing the PCE to drop from 19.7% to 15.0% when going from 0.1 to 0.85 cm² (Fig. S10 in the ESI†), in agreement with similar larger cells.¹⁸ The performance of the n-i-p solar cells is strongly improved compared to that of the devices in the p-i-n configuration (Fig. S7 in the ESI†), primarily due to an increase in the FF, which is above 80% regardless of the PhIm concentration (Fig. S11b in the ESI†). The reason for the enhanced FF, when going from the p-i-n to the n-i-p configuration, is probably related to the difference in conductivity of the doped charge transporting layers at the front contact. The n-ETL conductivity is two orders of magnitude higher compared to the p-HTL, for the different dopant concentrations evaluated (Fig. S4 in the ESI†). The FF of the p-i-n cells increases at lower light intensities, even for cells using the optimum 11 wt% dopant concentration. Yet, in contrast, in n-i-p devices, the effect of the PhIm dopant concentration on the FF is present only at low illumination intensity, becoming virtually concentration independent when the light intensity increases (Fig. S11a and b in the ESI†). This, therefore, confirms that in the p-i-n configuration a barrier for hole extraction exists, also in agreement with the recent estimation of carrier collection efficiency on vacuum deposited perovskite cells (using solution processed charge transport layers).³⁸ Those devices, besides showing PCEs of approximately 15% (similar to the p-i-n cells presented here), suffered from hindered and spatially inhomogeneous charge

transport, which was suggested to be at the front contact, *i.e.* at the hole transport interface. Measurement of the electroluminescence of the p-i-n devices (Fig. S11c and d in the ESI†) show that the radiant flux saturates at about 1.7 V and then starts to decrease, whereas the n-i-p devices show enhanced electroluminescence with no saturation. This confirms a more efficient and balanced charge carrier injection which translates in a higher FF for the n-i-p devices. The ability to efficiently inject holes when the doped p-HTL is placed in between the HTL and the metal electrode (as in n-i-p devices) can be understood considering that the metal electrode is evaporated on top of the p-HTL which leads to an improved contact (metal atoms slightly penetrate the soft organic layer) and potentially to an increased conductivity. It is worth mentioning that the EQE for electroluminescence of the best performing n-i-p cell is among the highest reported (EQE = 0.36, Fig. S12 in the ESI†) for light-emitting diodes employing MAPbI₃ as the emitting layer.^{12,32} Very small hysteresis between the forward (negative to positive bias) and reverse *J-V* scans was observed only for the p-i-n devices (Fig. S13a in the ESI†), where small fluctuations in the *V*_{oc} and FF were present due to the extraction issues at the ITO/p-HTL contact (the overall variation of the PCE was limited to 0.1%). On the other hand, the n-i-p devices were essentially hysteresis-free, independently of the scan speed used (Fig. S13b and Table S2 in the ESI†).

The initial device configuration with the undoped HTL and ETL in between the perovskite and the doped charge transport layers was chosen to prevent any negative interaction between the radical cations and anions that are present in the doped charge transport layers, and the photogenerated charge carriers in the perovskite. However, it is not obvious whether such a negative interaction in fact occurs, since in perovskites the electrons and holes are spontaneously formed after photon absorption without long living intermediate excitonic states and, additionally, the absorber layer is very thick compared with the organic photovoltaic devices. Therefore, two series of devices without undoped interlayers were prepared and evaluated; the first, without the undoped HTL and the second without the undoped ETL. We first examined the p-i-n configuration, where the dopant concentrations were fixed at the optimum 11 and 30 wt% for the p-HTL and n-ETL, respectively. In Fig. 4b, the *J-V* curves of these two series of devices are compared with the reference cell in which both undoped layers are present. The performance of the devices without the undoped ETL is significantly worse than the reference cell, due to a lower *J*_{sc}, *V*_{oc} and, most pronouncedly, a lower FF. Without the C₆₀ ETL, the perovskite film is in direct contact with the conductive doped n-ETL; therefore electron-hole recombination can occur at this interface causing the simultaneous reduction of all the performance indicators of the solar cells. In contrast, the cells without the undoped TaTm HTL perform only slightly worse compared to the reference cells, with a small reduction in the *J*_{sc} and *V*_{oc}. Most likely, due to the low dopant content and hence low conductivity of the p-HTL (when compared to the n-ETL), this layer can still efficiently confine the electrons in the perovskite absorber and inhibit charge recombination at the

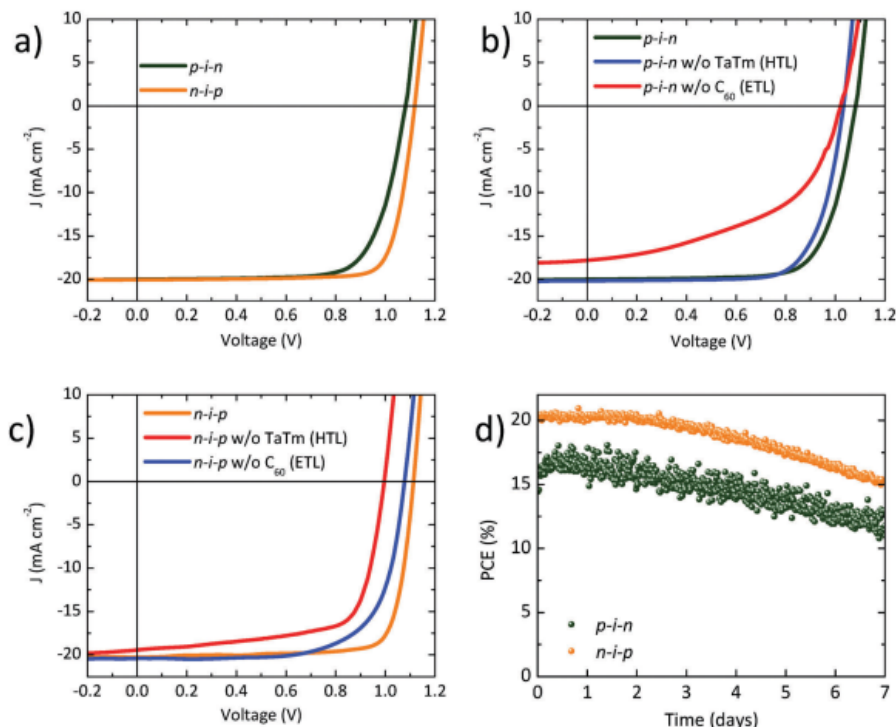


Fig. 4 (a) J - V curves for the n-i-p and p-i-n solar cells under 100 mW cm⁻² illumination. (b) J - V curves under 100 mW cm⁻² illumination for the p-i-n devices without one of the undoped charge transport layers. (c) J - V curves under 100 mW cm⁻² illumination for n-i-p devices without one of the undoped charge transport layers. (d) Stability under approximated 100 mW cm⁻² illumination.

p-HTL/MAPbI₃ interface. The slight decrease in V_{oc} observed upon the removal of the non-doped TaTm layer can be attributed to the lower Fermi level of the p-HTL compared to the highest occupied molecular orbital (HOMO) of TaTm. Additionally, we have studied the effect of the selective removal of one of the doped organic layers on the device performances. As clearly observed in Fig. S14 (ESI[†]), both the doped p-HTL and n-HTL are required to avoid severe charge extraction issues. However, in accordance with previous reports,^{23,24} devices with only a thin layer of pure C₆₀ and no doped layer between the fullerene and the metal show lower (FF especially) but still appreciable photovoltaic behavior. This effect originates from the dipole which is created at the interface between the noble metals (Au and, as in our case, Ag) and C₆₀, enhancing electron extraction.³⁹ Also, in the n-i-p configuration the effect of the undoped charge transport layers was evaluated. Fig. 4c shows the J - V characteristics of the cells without one of the undoped charge transport layers and the reference n-i-p cell. As observed in the p-i-n configuration, the removal of the undoped layers leads to a decrease in device performance. The effect of the removal of the C₆₀ in between the n-ETL and the perovskite substantially reduces the V_{oc} and the FF, while the removal of the undoped HTL has a limited effect on the device performance, in agreement with what was observed for p-i-n devices and with the conductivity trend among the p-HTL and the n-ETL. Hence, independently of the device configurations,

the presence of undoped layers in between the perovskite and the doped charge transport layers is required for high efficiency cells.

To obtain an indication of the stabilities of different cell configurations, they were analyzed during prolonged exposure to white LED light (spectra in Fig. S15 in the ESI[†]). The light intensity was adjusted by setting the J_{sc} of the solar cells equal to the value obtained under 1.5 AM illumination. The temperature of the cells during this test reached approximately 40 °C in the first 10 minutes and remained constant afterwards in part due to the LED lights used that radiate less heat than incandescent lamps. The setup consisted of 8 test positions installed inside a nitrogen filled glovebox (with oxygen and H₂O levels below 1 ppm). All cells were illuminated under short-circuit conditions without encapsulation and positioned within a few days after preparation. At fixed time intervals J - V scans were taken to deduce the key performance indicators of the cells (Fig. S16 in the ESI[†]) from which the evolution of the PCE was derived (Fig. 4d). From our first indicative analysis on the stability, it appears that no substantial difference in the PCE lifetime exists among the p-i-n and n-i-p configurations. However, the parameters causing PCE decay in the p-i-n cells is the current density, which monotonically diminishes during the measured time span, while the performance degradation observed in the n-i-p devices is caused mainly by the decrease of the FF. Interestingly, a lower PhIm doping concentration in the n-ETL of the n-i-p cells was

observed to partially stabilize the cell performance (Fig. S17 in the ESI†). Further optimization of the dopant and charge transport molecules and their ratios is expected to lead to improved stabilities, in analogy to what is obtained in OLEDs and organic small molecular weight PV modules. The implementation of modified perovskite absorbers with a slightly lower bandgap is expected to further enhance the device PCE.

Conclusions

We have demonstrated fully vacuum deposited perovskite solar cells by depositing methylammonium lead iodide in between intrinsic and doped organic charge transport molecules. Two configurations, one inverted with respect to the other, p-i-n and n-i-p, were prepared and optimized leading to planar solar cells without hysteresis and with high efficiencies, 15% and 18% on average, respectively. It is the first time that a direct comparison between these two opposite device configurations has been reported. These fully vacuum deposited solar cells allow fine tuning of the device properties by controlling at will the individual layer thicknesses and composition for specific applications including tandem configurations.

Author contributions

JBN and HJB conceived the idea. CM and LG prepared and characterized the devices. EB collected the SEM images and characterized the devices. MS, KL, JBN and HJB designed and supervised the experiments. All authors analyzed the results. MS and HJB wrote the manuscript.

Acknowledgements

We are grateful to Jorge Ferrando for his assistance with the sample characterization. The Spanish Ministry of Economy and Competitiveness (MINECO) via the Unidad de Excelencia María de Maeztu MDM-2015-0538 and MAT2014-55200, PCIN-2015-255 and the Generalitat Valenciana (Prometeo/2016/135). C. M., E. B. and M. S. thank the MINECO for their pre- and post-doctoral (JdC) contracts.

References

- 1 A. Kojima, K. Teshima, Y. Shirai and T. Miyasaka, *J. Am. Chem. Soc.*, 2009, **131**, 6050–6051.
- 2 M. M. Lee, J. Teuscher, T. Miyasaka, T. N. Murakami and H. J. Snaith, *Science*, 2012, **338**, 643–647.
- 3 W. S. Yang, J. H. Noh, N. J. Jeon, Y. C. Kim, S. Ryu, J. Seo and S. I. Seok, *Science*, 2015, **348**, 1234–1237.
- 4 J. Berry, T. Buonassisi, D. A. Egger, G. Hodes, L. Kronik, Y.-L. Loo, I. Lubomirsky, S. R. Marder, Y. Mastai, J. S. Miller, D. B. Mitzi, Y. Paz, A. M. Rappe, I. Riess, B. Rybtchinski, O. Stafsudd, V. Stevanovic, M. F. Toney, D. Zitoun, A. Kahn, D. Ginley and D. Cahen, *Adv. Mater.*, 2015, **27**, 5102–5112.
- 5 S. D. Stranks, G. E. Eperon, G. Grancini, C. Menelaou, M. J. P. Alcocer, T. Leijtens, L. M. Herz, A. Petrozza and H. J. Snaith, *Science*, 2013, **342**, 341–344.
- 6 D. Shi, V. Adinolfi, R. Comin, M. Yuan, E. Alarousu, A. Buin, Y. Chen, S. Hoogland, A. Rothenberger, K. Katsiev, Y. Losovyj, X. Zhang, P. A. Dowben, O. F. Mohammed, E. H. Sargent and O. M. Bakr, *Science*, 2015, **347**, 519–522.
- 7 C. Roldan-Carmona, P. Gratia, I. Zimmermann, G. Grancini, P. Gao, M. Graetzel and M. K. Nazeeruddin, *Energy Environ. Sci.*, 2015, **8**, 3550–3556.
- 8 Y. Shao, Y. Yuan and J. Huang, *Nat. Energy*, 2016, **1**, 15001.
- 9 N. Pellet, P. Gao, G. Gregori, T.-Y. Yang, M. K. Nazeeruddin, J. Maier and M. Grätzel, *Angew. Chem., Int. Ed.*, 2014, **53**, 3151–3157.
- 10 N. J. Jeon, J. H. Noh, W. S. Yang, Y. C. Kim, S. Ryu, J. Seo and S. I. Seok, *Nature*, 2015, **517**, 476–480.
- 11 M. Saliba, T. Matsui, J.-Y. Seo, K. Domanski, J.-P. Correa-Baena, N. Mohammad K, S. M. Zakeeruddin, W. Tress, A. Abate, A. Hagfeldt and M. Grätzel, *Energy Environ. Sci.*, 2016, **9**, 1989–1997.
- 12 D. Bi, W. Tress, M. I. Dar, P. Gao, J. Luo, C. Renevier, K. Schenk, A. Abate, F. Giordano, J.-P. Correa Baena, J.-D. Decoppet, S. M. Zakeeruddin, M. K. Nazeeruddin, M. Grätzel and A. Hagfeldt, *Sci. Adv.*, 2016, **2**, e1501170.
- 13 J. Burschka, N. Pellet, S.-J. Moon, R. Humphry-Baker, P. Gao, M. K. Nazeeruddin and M. Grätzel, *Nature*, 2013, **499**, 316–319.
- 14 H. Zhou, Q. Chen, G. Li, S. Luo, T.-b. Song, H.-S. Duan, Z. Hong, J. You, Y. Liu and Y. Yang, *Science*, 2014, **345**, 542–546.
- 15 A. Mei, X. Li, L. Liu, Z. Ku, T. Liu, Y. Rong, M. Xu, M. Hu, J. Chen, Y. Yang, M. Grätzel and H. Han, *Science*, 2014, **345**, 295–298.
- 16 J.-Y. Jeng, Y.-F. Chiang, M.-H. Lee, S.-R. Peng, T.-F. Guo, P. Chen and T.-C. Wen, *Adv. Mater.*, 2013, **25**, 3727–3732.
- 17 C.-G. Wu, C.-H. Chiang, Z.-L. Tseng, M. K. Nazeeruddin, A. Hagfeldt and M. Grätzel, *Energy Environ. Sci.*, 2015, **8**, 2725–2733.
- 18 W. Chen, Y. Wu, Y. Yue, J. Liu, W. Zhang, X. Yang, H. Chen, E. Bi, I. Ashraful, M. Grätzel and L. Han, *Science*, 2015, **350**, 944–948.
- 19 K. Walzer, B. Maennig, M. Pfeiffer and K. Leo, *Chem. Rev.*, 2007, **107**, 1233–1271.
- 20 D. J. Gaspar and E. Polikarpov, *OLED Fundamentals: Materials, Devices, and Processing of Organic Light-Emitting Diodes*, CRC Press, 2015.
- 21 I. Salzmann and G. Heimel, *J. Electron Spectrosc. Relat. Phenom.*, 2015, **204**(Part A), 208–222.
- 22 M. Liu, M. B. Johnston and H. J. Snaith, *Nature*, 2013, **501**, 395–398.
- 23 O. Malinkiewicz, A. Yella, Y. H. Lee, G. M. Espallargas, M. Graetzel, M. K. Nazeeruddin and H. J. Bolink, *Nat. Photonics*, 2014, **8**, 128–132.
- 24 Q. Lin, A. Armin, R. C. R. Nagiri, P. L. Burn and P. Meredith, *Nat. Photonics*, 2015, **9**, 106–112.
- 25 M. Kaltenbrunner, G. Adam, E. D. Glowacki, M. Drack, R. Schwodiauer, L. Leonat, D. H. Apaydin, H. Groiss, M. C. Scharber, M. S. White, N. S. Sariciftci and S. Bauer, *Nat. Mater.*, 2015, **14**, 1032–1039.

- 26 L. K. Ono, M. R. Leyden, S. Wang and Y. Qi, *J. Mater. Chem. A*, 2016, **4**, 6693–6713.
- 27 L. E. Polander, P. Pahner, M. Schwarze, M. Saalfrank, C. Koerner and K. Leo, *APL Mater.*, 2014, **2**, 081503.
- 28 B.-S. Kim, T.-M. Kim, M.-S. Choi, H.-S. Shim and J.-J. Kim, *Org. Electron.*, 2015, **17**, 102–106.
- 29 W. Ke, D. Zhao, C. R. Grice, A. J. Cimaroli, G. Fang and Y. Yan, *J. Mater. Chem. A*, 2015, **3**, 23888–23894.
- 30 C. Momblona, O. Malinkiewicz, C. Roldán-Carmona, A. Soriano, L. Gil-Escrig, E. Bandiello, M. Scheepers, E. Edri and H. J. Bolink, *APL Mater.*, 2014, **2**, 081504.
- 31 P.-W. Liang, C.-C. Chueh, S. T. Williams and A. K. Y. Jen, *Adv. Energy Mater.*, 2015, **5**, 1402321.
- 32 A. Genco, F. Mariano, S. Carallo, V. L. P. Guerra, S. Gambino, D. Simeone, A. Listorti, S. Colella, G. Gigli and M. Mazzeo, *Adv. Electron. Mater.*, 2016, **2**, 1500325.
- 33 W. Nie, H. Tsai, R. Asadpour, J.-C. Blancon, A. J. Neukirch, G. Gupta, J. J. Crochet, M. Chhowalla, S. Tretiak, M. A. Alam, H.-L. Wang and A. D. Mohite, *Science*, 2015, **347**, 522–525.
- 34 M. B. Johnston and L. M. Herz, *Acc. Chem. Res.*, 2016, **49**, 146–154.
- 35 E. M. Hutter, G. E. Eperon, S. D. Stranks and T. J. Savenije, *J. Phys. Chem. Lett.*, 2015, **6**, 3082–3090.
- 36 R. L. Milot, G. E. Eperon, H. J. Snaith, M. B. Johnston and L. M. Herz, *Adv. Funct. Mater.*, 2015, **25**, 6218–6227.
- 37 W.-J. Yin, T. Shi and Y. Yan, *Adv. Mater.*, 2014, **26**, 4653–4658.
- 38 G. El-Hajje, C. Momblona, L. Gil-Escrig, J. Avila, T. Guillemot, J.-F. Guillemoles, M. Sessolo, H. J. Bolink and L. Lombez, *Energy Environ. Sci.*, 2016, **9**, 2286–2294.
- 39 S. C. Veenstra, A. Heeres, G. Hadziioannou, G. A. Sawatzky and H. T. Jonkman, *Appl. Phys. A: Mater. Sci. Process.*, 2002, **75**, 661–666.

Supplementary Materials for

High efficiency vacuum deposited p-i-n and n-i-p perovskite solar cells

Cristina Momblona^{1,†}, Lidón Gil-Escrig^{1,†}, Enrico Bandiello¹, Michele Sessolo¹, Kay Lederer²,
Jan Blochwitz-Nimoth^{2*} and Henk J. Bolink^{2*}

¹Instituto de Ciencia Molecular, Universidad de Valencia, C/ Catedrático J. Beltrán 2, 46980
Paterna (Valencia), Spain

²NOVALED GmbH, Tatzberg 49, 01307 Dresden, Germany

*Corresponding author. E-mail: jan.bn@novaled.com and henk.bolink@uv.es

This PDF file includes:

Materials and Methods

Figs. S1 to S16

Materials and Methods

Materials

Photolithographically patterned ITO coated glass substrates were purchased from Naranjo Substrates (www.naranjosubstrates.com). 2,2'-(Perfluoronaphthalene-2,6-diylidene) dimalononitrile (F6-TCNNQ), N₄,N₄,N₄'',N₄''-tetra([1,1'-biphenyl]-4-yl)-[1,1':4',1''-terphenyl]-4,4''-diamine (TaTm) and N₁,N₄-bis(tri-p-tolylphosphoranylidene)benzene-1,4-diamine (PhIm) were provided from Novaled GmbH. Fullerene (C₆₀) was purchased from sigma Aldrich. PbI₂ was purchased from Tokyo Chemical Industry CO (TCI), and CH₃NH₃I (MAI) from Lumtec.

Device preparation

ITO-coated glass substrates were subsequently cleaned with soap, water and isopropanol in an ultrasonic bath, followed by UV-ozone treatment. They were transferred to a vacuum chamber integrated into a nitrogen-filled glovebox (MBraun, H₂O and O₂ < 0.1 ppm) and evacuated to a pressure of 1·10⁻⁶ mbar. The vacuum chamber is equipped with six temperature controlled evaporation sources (Creaphys) fitted with ceramic crucibles. The sources were directed upwards with an angle of approximately 90° with respect to the bottom of the evaporator. The substrate holder to evaporation sources distance is approximately 20 cm. Three quartz crystal microbalance (QCM) sensors are used, two monitoring the deposition rate of each evaporation source and a third one close to the substrate holder monitoring the total deposition rate.

For thickness calibration, we first individually sublimed the charge transport materials and their dopants (TaTm and F₆-TCNNQ, C₆₀ and PhIm). A calibration factor was obtained by comparing

the thickness inferred from the QCM sensors with that measured with a mechanical profilometer (Ambios XP1). Then these materials were co-sublimed at temperatures ranging from 135-160 °C for the dopants to 250 °C for the pure charge transport molecules, and the evaporation rate was controlled by separate QCM sensors and adjusted to obtain the desired doping concentration. In general, the deposition rate for TaTm and C₆₀ was kept constant at 0.8 Å s⁻¹ while varying the deposition rate of the dopants during co-deposition. Pure TaTm and C₆₀ layers were deposited at a rate of 0.5 Å s⁻¹.

For the *p-i-n* configuration, 40 nm of the p-doped hole-transport layer (p-HTL, TaTm:F₆-TCNNQ) capped with 10 nm of the pure TaTm were deposited. Once completed this deposition, the chamber was vented with dry N₂ to replace the p-HTL crucibles with those containing the starting materials for the perovskite deposition, PbI₂ and CH₃NH₃I. The vacuum chamber was evacuated again to a pressure of 10⁻⁶ mbar, and the perovskite films were then obtained by co-deposition of the two precursors. The calibration of the deposition rate for the CH₃NH₃I was found to be difficult due to non-uniform layers and the soft nature of the material which impeded accurate thickness measurements. Hence, the source temperature of the CH₃NH₃I was kept constant at 70 °C and the CH₃NH₃I:PbI₂ ratio was controlled off line using grazing incident x-ray diffraction by adjusting the PbI₂ deposition temperature. The optimum deposition temperatures were found to be 250 °C for the PbI₂ and 70 °C for the CH₃NH₃I. After deposition of a 500 nm thick perovskite film, the chamber was vented and the crucibles replaced with those containing C₆₀ and PhIm, and evacuated again to a pressure of 10⁻⁶ mbar. The devices were completed depositing a film of pure C₆₀ and one of the n-ETL (C₆₀:PhIm), with thicknesses of 10 and 40 nm, respectively. This process of exchanging crucibles was done to evaluate the effect of changes in the organic layer composition for an identical perovskite layer. In one evaporation run

we can prepare 5 substrates (3 by 3 cm) each containing 4 cells. Generally, one substrate was reserved for a reference configuration allowing to evaluate 4 variations in the transport layers per perovskite evaporation. It is also possible to prepare the complete stack without breaking vacuum as we have 6 sources available. Finally the substrates were transferred to a second vacuum chamber where the metal top contact (100 nm thick) was deposited. For *n-i-p* devices, the exact same procedure as described before was used in the inverted order.

Characterization

Grazing incident X-ray diffraction (GIXRD) pattern were collected at room temperature on an Empyrean PANalytical powder diffractometer using the Cu K α 1 radiation. Typically, three consecutive measurements were collected and averaged into single spectra.

The surface morphology of the thin films was analyzed using atomic force microscopy (AFM, Multimode SPM, Veeco, USA). Scanning Electron Microscopy (SEM) images were performed on a Hitachi S-4800 microscope operating at an accelerating voltage of 2 kV over Platinum - metallized samples. Absorption spectra were collected using a fiber optics based Avantes Avaspec2048 Spectrometer.

Characterization of the solar cells was performed as follows. The external quantum efficiency (EQE) was estimated using the cell response at different wavelength (measured with a white light halogen lamp in combination with band-pass filters), where the solar spectrum mismatch is corrected using a calibrated Silicon reference cell (MiniSun simulator by ECN, the Netherlands). The current density-voltage (J-V) characteristics were obtained using a Keithley 2400 source measure unit and under white light illumination, and the short circuit current density was

corrected taking into account the device EQE. The electrical characterization was validated using a solar simulator by Abet Technologies (model 10500 with an AM1.5G xenon lamp as the light source). Before each measurement, the exact light intensity was determined using a calibrated Si reference diode equipped with an infrared cut-off filter (KG-3, Schott). Importantly, no difference in the J-V characteristics was observed as a function of evaluation method. The J-V curves were recorded between -0.2 and 1.2 V with 0.01V steps, integrating the signal for 20 ms after a 10 ms delay. This corresponds to a speed of about 0.3 V s^{-1} . Two different devices layout has been used to test the solar cells configurations, one with four equal areas (0.0653 cm^2 , defined as the overlap between the ITO and the top metal contact) and measured through a shadow masks with 0.01 cm^2 aperture, and a second with increasing areas (0.0897 cm^2 , 0.1522 cm^2 , 0.3541 cm^2 and 0.9524 cm^2) which was characterized using a shadow mask with aperture areas of 0.0484 cm^2 , 0.1024 cm^2 , 0.2704 cm^2 and 0.8464 cm^2 , respectively. For hysteresis study, different scan rates (0.1 , 0.5 and 1 Vs^{-1}) were used, biasing the device from -0.2 to 1.2 V with 0.01 V steps and vice versa. Light intensity dependence measurements were done by placing 0.1, 1, 10, 20, 50% neutral density filters (LOT-QuantumDesign GmbH) between the light source and the device.

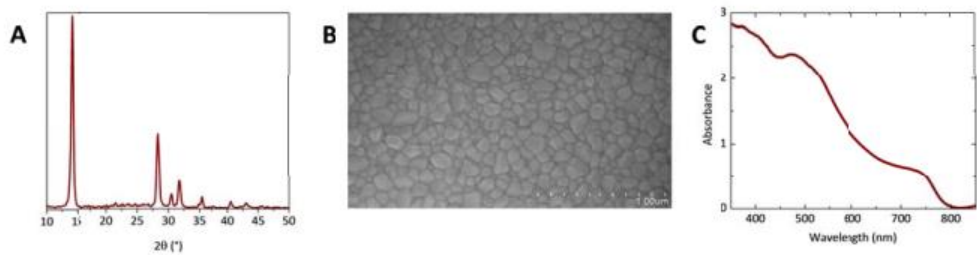


Fig. S1 (A) GIXRD pattern, (B) surface SEM picture and (C) optical absorbance of the vacuum deposited MAPbI_3 thin films used for *p-i-n* and *n-i-p* cells preparation.

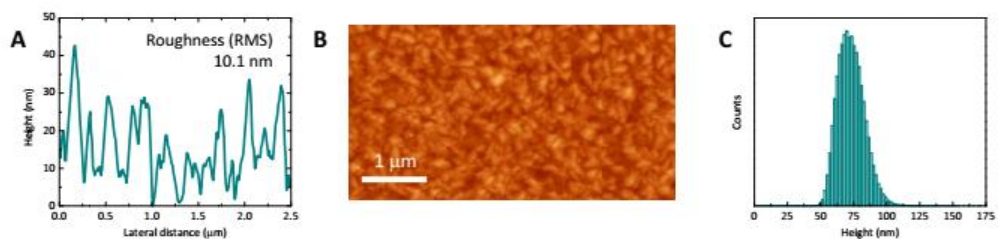


Fig. S2 Atomic force microscopy (AFM) characterization. (A) Surface profile, (B) topography and (C) roughness analysis of the vacuum deposited MAPbI_3 thin films used for *p-i-n* and *n-i-p* cells preparation.

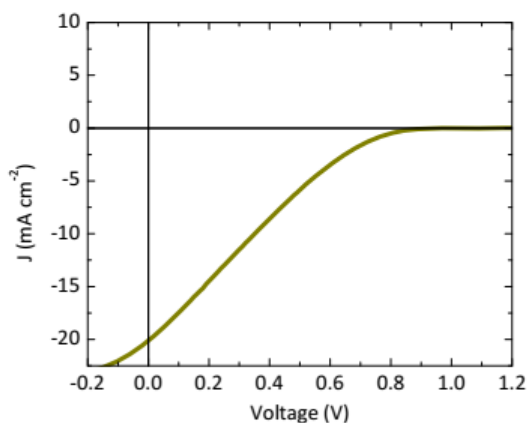


Fig. S3 Electrical characterization of a device without doped layers. J-V scan for a *p-i-n* device with the structure ITO/TaTm (40 nm)/MAPbI₃ (500 nm)/C₆₀ (40 nm)/Ag.

Table S1 Photovoltaic parameters for the main solar cells architecture studied. The effect of the selective removal of the intrinsic charge transport layers is highlighted.

	Device structure	V _{oc} (mV)	J _{sc} (mA cm ⁻²)	FF (%)	PCE (%)
	TaTm/MAPbI ₃ /C ₆₀	1041	20.12	16.8	3.5
<i>p-i-n</i>	p-HTL/TaTm/MAPbI ₃ /C ₆₀ /n-ETL	1082	20.02	73.1	15.8
	p-HTL/MAPbI₃/C₆₀/n-ETL	1033	20.19	73.3	15.3
	p-HTL/TaTm/MAPbI ₃ / n-ETL	1032	17.82	45.0	8.3
<i>n-i-p</i>	n-ETL/C ₆₀ /MAPbI ₃ /TaTm/p-HTL	1115	20.28	79.8	18.0
	n-ETL/MAPbI₃/TaTm/p-HTL	1084	20.45	68.8	15.2
	n-ETL/C ₆₀ /MAPbI ₃ / p-HTL	998	19.44	68.7	13.3

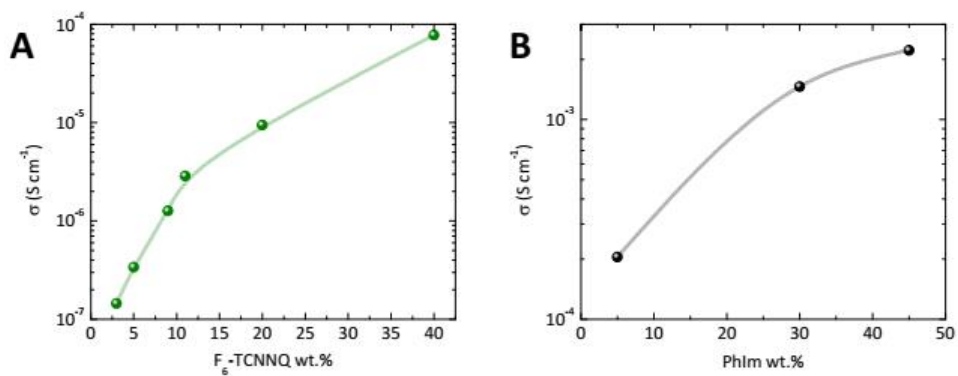


Fig. S4 Conductivity as a function of the dopant concentration for 100 nm thick films of (A) p-HTL (TaTm:F₆-TCNNQ) and (B) n-ETL (C₆₀:PhIm)

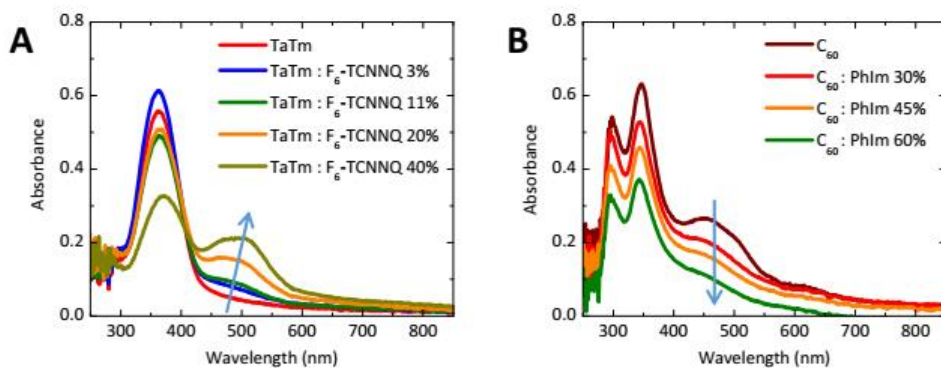


Fig. S5 Optical absorbance as a function of the dopant concentration for 40 nm thick films of (A) p-HTL (TaTm:F₆-TCNNQ) and (B) n-ETL (C₆₀:PhIm).

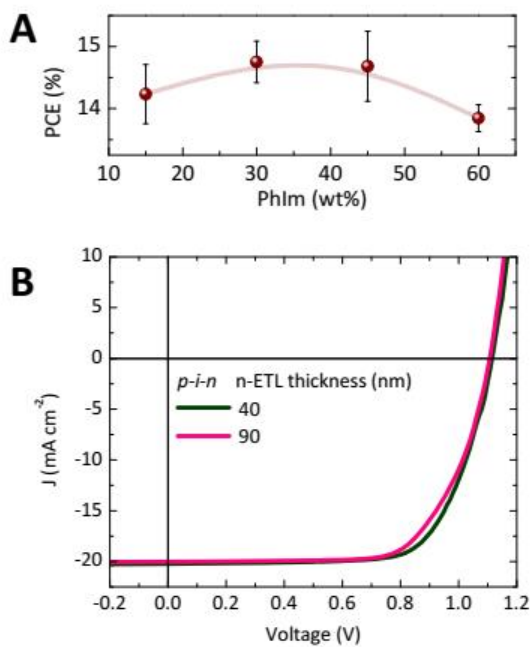


Fig. S6 (A) Trend of the PCE for a series of *p-i-n* cells with increasing concentration of the PhIm dopant in the n-ETL. (B) J-V scans for *p-i-n* devices with increasing thickness of the n-ETL (C₆₀:PhIm).

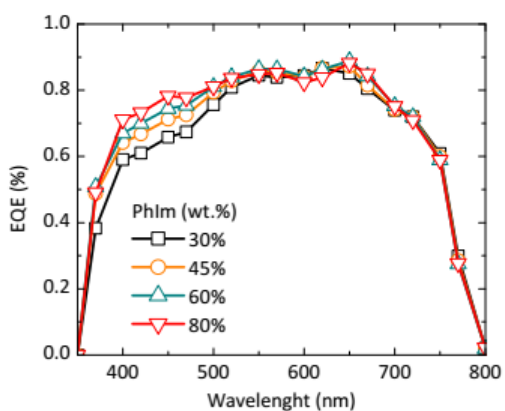


Fig. S7 EQE for a series of *n-i-p* cells with increasing concentration of the PhIm dopant in the n-ETL.

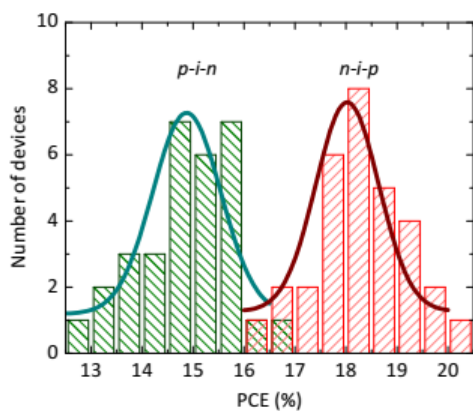


Fig. S8 Statistics of the PCE measured for *p-i-n* (green) and *n-i-p* devices (32 cells for each configuration). Green and red solid lines represent the Gaussian distribution fitting for the PCE.

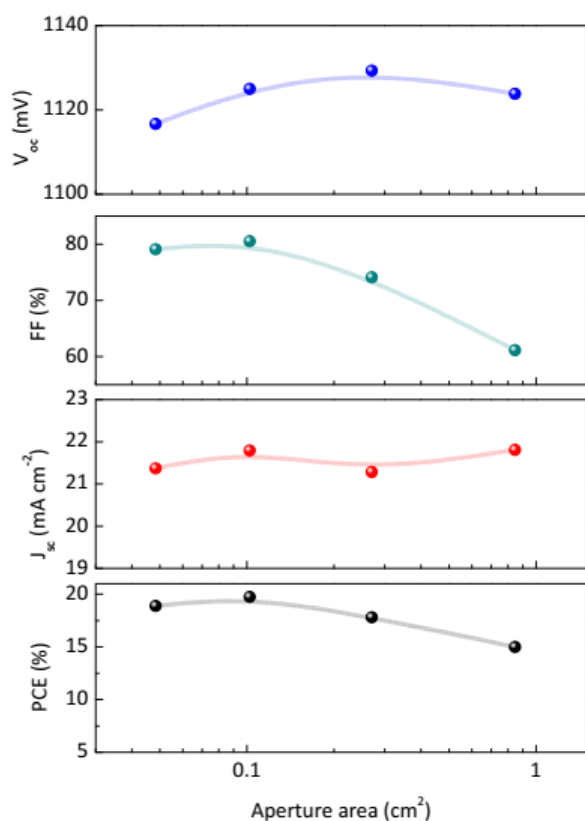


Fig. S9 Performance parameters for *n-i-p* cells as a function of the area. Photovoltaic parameters extracted from *J-V* and EQE measurements for a series of *n-i-p* devices with increasing area, defined as the shadow mask aperture. Note that the area of the ITO/metal is also increasing proportionally.

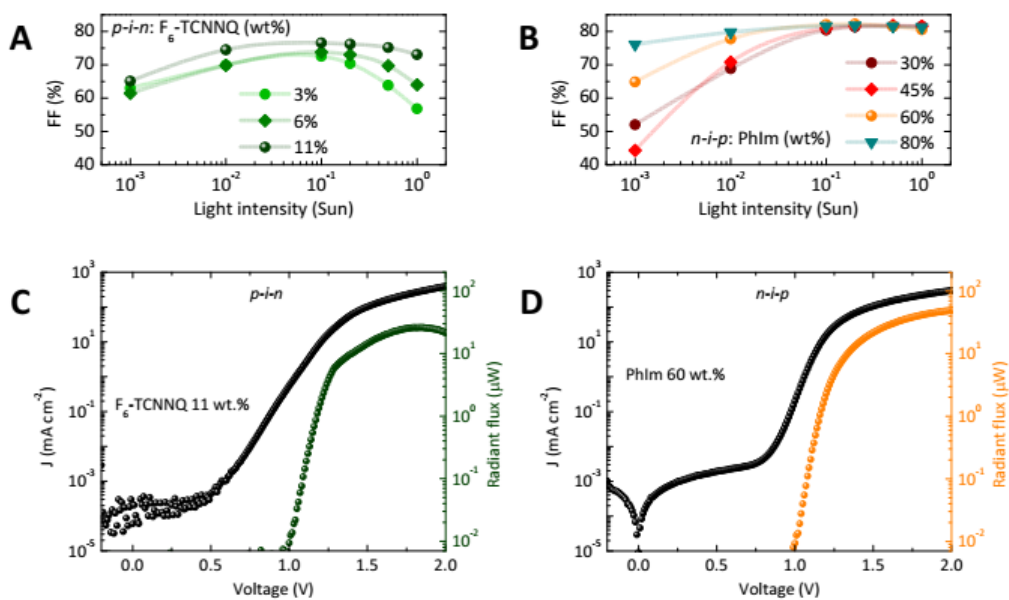


Fig. S10 Light intensity dependence of the measured FF for different doping concentration in the charge transport layer at the front contact for (A) *p-i-n* and (B) *n-i-p* cells. J-V and electroluminescence characteristics for the 2 reference (C) *p-i-n* and (D) *n-i-p* devices.

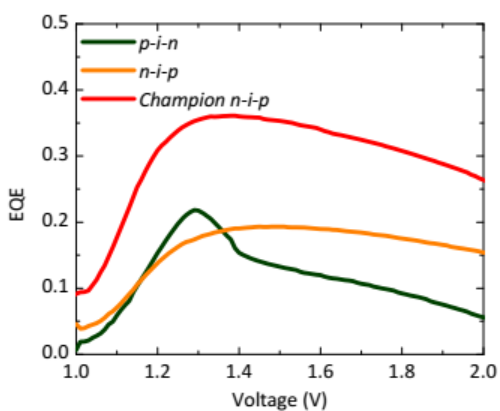


Fig. S11 EQE of electroluminescence for *p-i-n* and *n-i-p* cells. The EQE characteristic for our record PCE *n-i-p* device is shown for comparison.

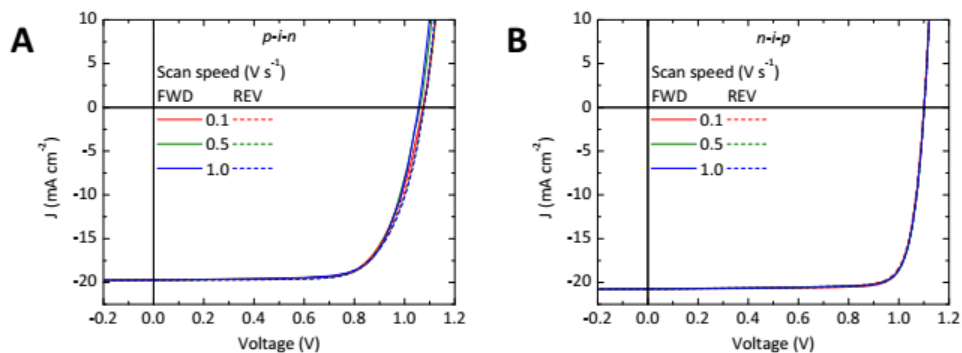


Fig. S12 Characterization of the J-V hysteresis of (A) *p-i-n* and (B) *n-i-p* perovskite solar cells, performed by measuring the current as a function of the bias scan direction at different scan speed.

Table S2 Photovoltaic parameters extracted from the the J-V hysteresis (Fig. S12) for *p-i-n* and *n-i-p* perovskite solar cells, under forward (FWD) and reverse (REV) bias at different scan speed.

Speed		0.1 V s ⁻¹		0.5 V s ⁻¹		1.0 V s ⁻¹	
Direction		FWD	REV	FWD	REV	FWD	REV
<i>p-i-n</i>	V _{oc} (mV)	1073	1076	1061	1077	1056	1075
	J _{sc} (mA cm ⁻²)	19.65	19.64	19.65	19.65	19.63	19.65
	FF (%)	71.0	71.4	72.3	71.1	72.7	71.0
	PCE (%)	15.0	15.1	15.1	15.0	15.1	15.0
<i>n-i-p</i>	V _{oc} (mV)	1101	1100	1102	1101	1101	1102
	J _{sc} (mA cm ⁻²)	20.73	20.73	20.73	20.73	20.73	20.73
	FF (%)	83.0	82.2	82.9	82.7	82.7	82.8
	PCE (%)	19.0	18.7	18.9	18.9	18.9	18.9

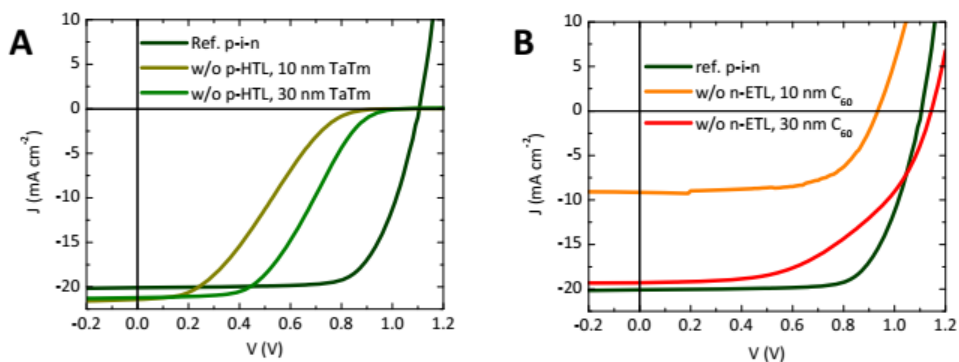


Fig. S13 J-V characteristics of *p-i-n* perovskite devices when the (A) p-HTL of the (B) n-ETL, for different thicknesses of the intrinsic TaTm and C₆₀ transport layer, respectively.

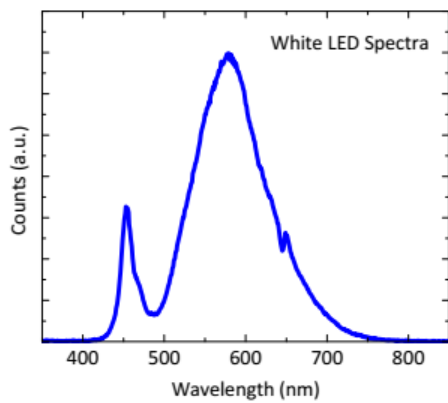


Fig. S14 Optical emission spectra of the white LED used to illuminate the solar cells during lifetime measurements.

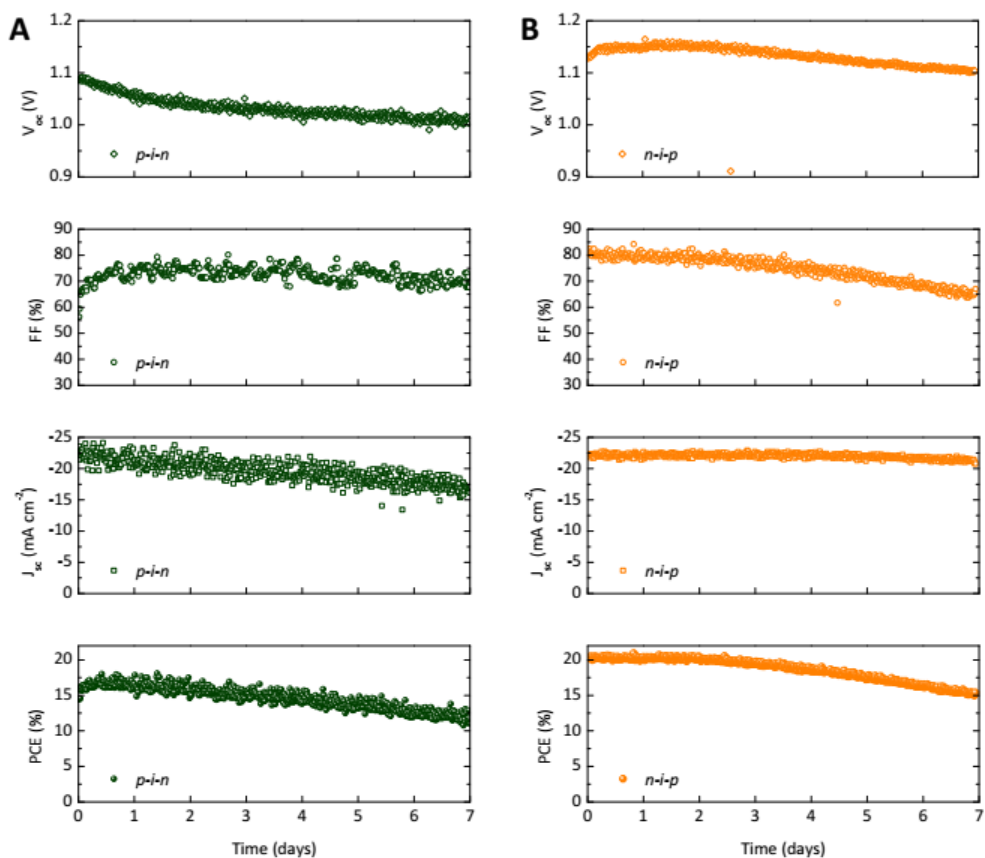


Fig. S15 Comparison of the lifetime of (A) *p-i-n* and (B) *n-i-p* perovskite devices. The photovoltaic parameters are extracted while the cells are kept under continuous illumination at short circuit conditions and with no temperature control.

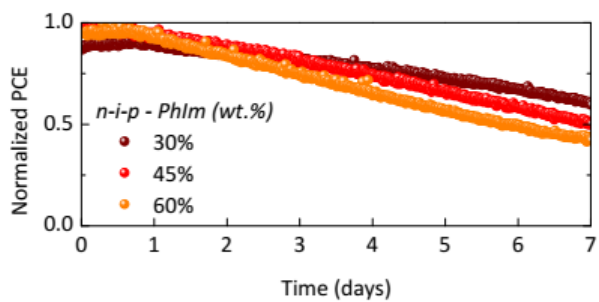


Fig. S16 Evolution of the PCE (normalized here for comparison) for a series of *n-i-p* solar cells with increasing concentration of the PhIm dopant in the n-ETL front contact.